Durham E-Theses

Secondary flow reduction techniques in linear turbine cascades

Biesinger, Thomas Ernst

SECONDARY FLOW REDUCTION TECHNIQUES

IN LINEAR TURBINE CASCADES

Thomas Ernst Biesinger

School of Engineering and Computer Science

University of Durham

Thesis submitted for the degree of
Doctor of Philosophy of the University of Durham

July 1993

- 9 DEC 1993

Declaration

The work contained in this thesis has not been submitted elsewhere for any other degree or qualification, and unless otherwise referenced it is the author's own work.

Für Meine Eltern

Acknowledgements

SECONDARY FLOW REDUCTION TECHNIQUES

IN LINEAR TURBINE CASCADES

Thomas Ernst Biesinger

Abstract

This thesis investigates a novel secondary flow reduction method. The inlet boundary layer to a linear turbine cascade is skewed by injection of air through an upstream slot to oppose regular generated negative streamwise vorticity. Other methods from the pertinent literature are reviewed on a broad basis.

Detailed measurements of the flowfield in the Durham Linear Cascade facility have shown that substantial reductions in secondary flows and losses are possible. If the kinetic energy required for the blowing is taken into account by means of an availability analysis, no net gain in loss is achieved.

Tests are performed at two different angles, of which the higher is typical for film cooling applications, and at a wide range of injection ratios. Calculation of the mixed-out losses show the tangential rather than spanwise momentum of the injected air is more effective in countering the generation of secondary flows.

Computations using a state-of-the-art Navier-Stokes solver indicated shortcomings in modelling a flow governed by complex vortex dynamics. Improvements in the turbulence model and injection geometry could remedy this.

The evaluation of turbulent and laminar production rates obtained without injection helps to explain total pressure loss generation mechanisms. The comparison of calculated and experimental eddy viscosities reveals the inadequacy of the Boussinesq assumption for high turning flows.

The results obtained in this work are relevant to endwall film cooling applications. The tangential injection of air in front of the leading edge provides coolant in an optimum manner whilst possibly reducing secondary losses to a large extent. Disc cooling air, present in a real engine to prevent the ingestion of hot air from the mainstream, could be used to supply the injection.

Contents

List of Figures

List of Tables

Nomenclature

Symbols

A	area		v	velocity
c	coefficient		x	axial direction
E	energy		y	tangential direction
h	enthalpy		z	spanwise direction
$\hbar$	half span			
H_{12}	shape factor $\left(\frac{\delta_1}{\delta_2}\right)$		α	flow angle
l	axial chord length		ε	exergy or availability
m	mass		δ	physical thickness of boundary layer
M	momentum			
n_{12}	power law coefficient $(f_{(\delta_1,\delta_2)})$		δ_1	displacement thickness
p	pressure		δ_2	momentum thickness
r	jet to cascade mass flow ratio $\left(\frac{\dot{m}_j}{\dot{m}_u}\right)$		δ_3	energy thickness
			θ	injection angle
s	pitch		ν	kinematic viscosity
t	injection slot width		ξ	vorticity
T	temperature		ρ	density
u	fluctuating velocity		σ	entropy
U	mean velocity		Ψ	production

Superscripts

$\dot{a}$	time derivative		$\bar{a}$	pitch/mass-averaged value
a'	boundary layer component		$\bar{\bar{a}}$	area/mass-averaged value
a''	excess boundary layer component			

Subscripts

0	stagnation	s	static
		ske	secondary kinetic energy
amb	ambient	t	tangential
b	blown	T	turbulent
d	dynamic	u	upstream
e	exit	ub	unblown
g	gain	x	axial direction
i	inlet	y	tangential direction
j	jet	z	spanwise direction
l	local		
L	laminar	ε	exergy or availability
m	mixed-out	ν	normal
p	stagnation pressure	σ	streamwise

Terminology

Belt is a subscript referring to the positive skew case of Walsh [1987].

Blowing is a synonym for injection.

Jet means physically a jet sheet or blowing layer.

Positive Skew refers to the test case of Walsh [1987].

Slot is a synonym for an axial plane traversed by the 5H-probe, whereas **injection slot** refers to the blowing apparatus.

Tangential is equivalent to pitchwise.

Abbreviations

H_s	Horseshoe suction side leg
H_p	Horseshoe pressure side leg
S_4	Strip at suction side containing endwall material
SS	Suction side of blade
PS	Pressure side of blade

Chapter 1

Introduction

*M*odern high pressure (HP) turbines have to be designed for high efficiency. The contribution of secondary flows to the overall loss is substantial in HP low aspect ratio stages. Apart from higher efficiencies, other improvements such as less disturbed mainstream flow giving more uniform incidence to the next blade row, more easily controllable heat transfer on blade and endwall as well as diminished erosion and reduced wake unsteadiness are brought about by the reduction of secondary flows in turbines. In compressors, benefits arise from prevention of corner stall and build-up of low energy fluid through several stages, blade suction side separation due to passage vortex blockage and improved off-design performance.

In a real machine, film cooling of the blade surface is already common practice. Changes to the blade passage are made possible by the use of 3D design tools. Tip leakage flow investigations are the objective of many current research projects. Prevention of hot air ingestion at the rotor hub by injecting compressor air is investigated alongside disk cavity effects. A typical HP stage embedded in its engine environment is shown in Figure 1.1.

The Durham Linear Cascade is a simplified, large-scale model of a typical row of HP rotor blades. With the absence of a radial pressure gradient and blade profiles adapted to the low speed environment, high turning, 'aft'-loaded design as well as the high aspect ratio[1] (1.8) allows a straightforward investigation of the secondary flows and their production and dissipation mechanisms. A grid was fitted upstream to simulate the high free stream turbulence level of a real machine.
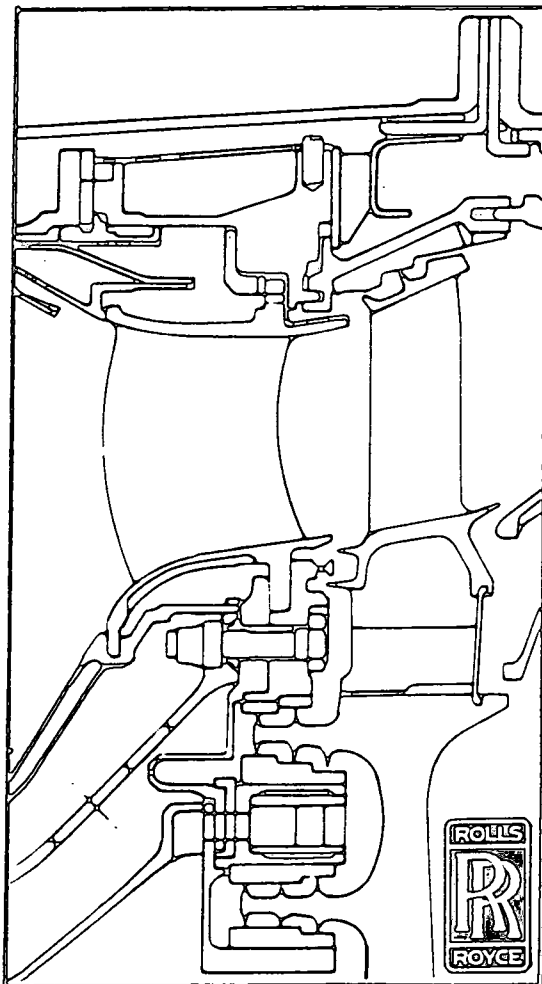
Figure 1.1: High Pressure Turbine Stage of a Jet Engine

The general objective of the present work is to provide a fundamental understanding of the secondary flow and loss dynamics with upstream boundary layer blowing. The aim of the blowing is to reduce secondary flows and losses. Balancing the required power for the blowing with the overall loss reduction provides an insight to its effectiveness, although higher overall gains might be achievable in combination with film cooling. The results could serve as a basis for aero- and thermodynamic testing in annular or real engine environments.

The choice of upstream boundary layer blowing as a secondary loss reduction method was made after a thorough investigation of the literature, which is addressed in the following Chapter 2 together with a description of the fundamentals of secondary flows. Chapter 3 contains a detailed description of the apparatus

---

1 $\frac{blade\ span}{blade\ chord}$

used. Chapter 4 presents the experimental data. Chapter 5 deals with their analysis accounting for the invested blowing energy. Chapter 6 contains the results of simulation runs. Chapter 7 provides an insight into loss production mechanisms due to the generation and decay of turbulence. A summarizing discussion is given in Chapter 8. The final Chapter 9 concludes and proposes future work.

Chapter 2

Secondary Flows, Losses and Reduction Techniques

*A*n overview of secondary flows and their reduction techniques is given. Furthermore, a particular reduction method, which is related to the situation in a real machine, is proposed to form the basis of further experimental and numerical investigation.

2.1 Generation and Definition

Secondary flows in turbomachines are generated when a boundary layer is turned relative to its streamwise direction. The cross passage pressure gradient turns the main stream and is imposed on the low-momentum boundary layer on the hub or casing and causes overturning. A 'passage' vortex develops due to the blades, growing from where the leading edge horseshoe vortex meets the blade suction side, up to the exit plane. All mixing and skin-friction losses associated with secondary flows such as the various loss cores and the formation of a new highly-skewed endwall boundary layer are summarized in what is defined in this

work qualitatively as secondary losses. The loss due to the leading edge horseshoe-vortex and the separation bubble in front of it are strictly not due to secondary flows; but they have small loss values, which are not easily separable. Moreover, there is a small amount of natural growth of the inlet boundary layer up to its separation within the blade passage. These losses are also attributed to the secondary loss. Thus, a net secondary loss can be defined as the difference between loss inherent in the inlet boundary layer and the profile loss from the overall loss (Section 5.3.5). The profile loss may be obtained by using the downstream measured loss at midspan (Table A.2, Appendix) or by a two-dimensional calculation method. Losses associated with suction surface separation bubbles are not included in the above definition but may be part of the profile loss. Losses due to tip leakage require a separate investigation.

Following Denton [1987], the term 'entropy production' rather than 'loss generation' should be used for turbomachines since it forms an integral part of efficiency formulæ expressing irreversibility. For flows with small changes in total pressure and temperature, total pressure loss is proportional to the entropy production as shown by Moore [1983]. In stationary cascades, the total pressure loss is made dimensionless with respect to to the up- or downstream dynamic head.

Losses are generally due to viscous forces, which dissipate energy either directly or by producing turbulence - an intermediate stage to the final dissipation. The direct dissipation is usually small compared to the production of turbulent kinetic energy (Section 7.1). It is therefore possible to relate loss to the production of turbulence (Moore et al. [1985]).

A mixing-loss is defined as the loss being associated with reaching a uniform state in the fluid, which makes the use of a fictitious downstream plane.

2.2   Review of the Literature on Secondary Flows

2.2.1   Theoretical and Empirical Secondary Flow Calculation Methods

Classical Secondary Flow Theories

Squire & Winter [1951] developed one of the first theoretical, inviscid secondary flow calculation methods. The distributed streamwise vorticity at exit is set identical to the inlet normal vorticity multiplied by twice the deflection of the flow; zero inlet streamwise vorticity and low turning is assumed. Their work was followed by Hawthorne [1955], Lakshminarayana & Horlock [1973] and Came & Marsh [1974]. The latter employed Kelvin's circulation theorem to obtain formulæ for the distributed secondary, trailing filament and trailing shed vorticity components at the exit plane when inlet streamwise and normal vorticity components are known (cf. equations (4.2), pg. 44, and (4.3), pg. 50). They assumed a many-bladed cascade so that the surfaces of constant inlet total pressure ('Bernoulli surfaces') are not distorted. The results could be reduced to those of Squire & Winter for low turning. Glynn [1982] and Gregory-Smith & Okan [1991] allowed for the convection of the Bernoulli surfaces, i.e. the influence of the secondary on the primary flow.

The corresponding exit secondary velocity field and exit angle deviations are obtained by solving for a secondary flow stream function using the distributed secondary vorticity (Glynn & Marsh [1980]).

Secondary Loss Prediction Methods

An early secondary loss correlation was developed by Ainley & Mathieson [1951]. Considering a large amount of different experimental data, Dunham [1970] devel-

oped a better correlation, which was in turn improved by other authors.

Gregory-Smith [1982] suggested a simple way of estimating secondary losses without relying on a single correlation. An 'extra' secondary loss, which is estimated to be roughly equal to secondary kinetic energy at exit, was added to the loss of a thin newly formed two-dimensional endwall boundary layer and a triangular loss core. The low momentum material found in the triangular region between a double-peak loss core and the suction side endwall corner was assumed to consist mainly of inlet boundary layer material. The secondary kinetic energy at exit was obtained using the formulæ of Came & Marsh [1974] and Glynn & Marsh [1980].

Okan & Gregory-Smith [1992] incorporated a loss model, which also refers to the amount of secondary kinetic energy produced by secondary flows, into their inviscid prediction code. Fair agreement was obtained between calculation and experiment for a wide range of test cases.

A different approach for estimating the production of secondary loss is the boundary layer integral method (Denton [1987]). It is based on Schlichting's dissipation integral which is used to relate the rise of entropy in a two-dimensional boundary layer to a loss coefficient. This approach seems to be valid since most of the loss is produced by skin fricitional forces very close to the walls. Shortcomings of the method are addressed by Harrison [1989].

2.2.2   Secondary Flow Features in Turbine Cascades

Sieverding [1985] performed a comprehensive review of the physics of secondary flows. Sharma & Butler [1986] describe the leading edge horseshoe vortices, the formation of the passage vortex and corner vortices as well as limiting streamlines (Figure 2.1). Inlet boundary layer material is trapped in the horseshoe vortices of
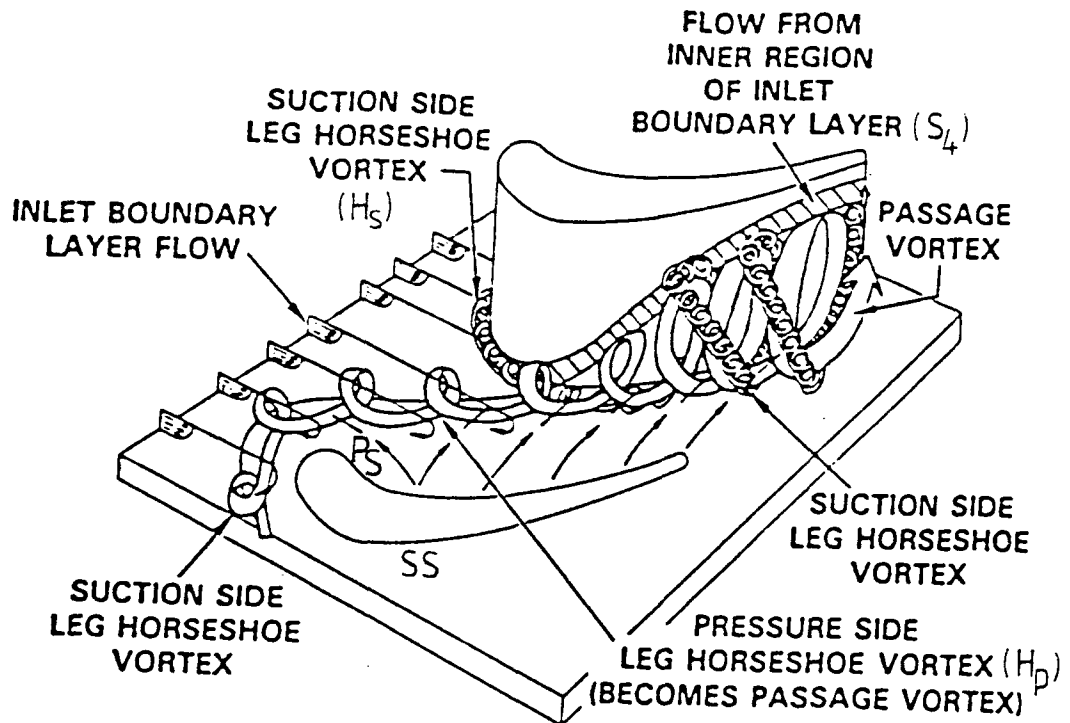
Figure 2.1: Cascade Endwall Flow Structure (after Sharma & Butler [1986])

which the pressure side leg (H_p) develops into the passage vortex. The suction side leg (H_s) may wrap around the passage vortex and a strip[1] (S_4, following the notation of Sieverding [1985]) with endwall material exists at the suction side due to the action of the passage vortex. Figure 2.1 does not show a possible separation bubble on the suction side. In a real machine, the free-stream turbulence level would usually be high enough to prevent separation bubbles. The turbulence grid mounted in the present cascade had the same effect and eliminated an originally observed bubble. The new boundary layer developing underneath the passage vortex is very thin and highly skewed due to the down-wash of the secondary velocities. Hot film investigations (e.g. Harrison [1989]) suggest a laminar nature over large parts of the endwall.

The downstream flow structure usually shows three loss cores: the loss core

---

[1] The distance of the strip from the endwall at the trailing edge may be predicted by a correlation after Sharma [1986].

due to the passage vortex, a loss core associated with S_4 and a region of high loss at the suction side endwall corner connected with the presence of a corner vortex. The downstream distribution of vorticity is augmented by vortex shedding from the blade trailing edge adding on to streamwise and normal vorticity components remaining from within the blade passage. Trailing shed vorticity is due to a spanwise varying blade circulation (or lift, loading), which arise both from a forced vortex design in a real machine and also from secondary flows in cascades. Trailing filament vorticity is created by the interaction of stretched pressure and suction side vortex filaments in the blade wakes; according to Helmholtz' theorem, the circulation of a line vortex remains constant in inviscid flows resulting in a change of vorticity when stretched.

Mixed-out loss calculations are performed in order to be independent of the distance of the downstream measurement plane from the trailing edge and thus provide a basis for comparison of data from various cascade test facilities. A drawback of this method is the mixing out of secondary kinetic energy, which could be beneficial in a downstream blade row. Moore & Adhye [1985] showed that the downstream mixed-out loss roughly equates to the sum of exit loss and secondary kinetic energy. Dejc [1973] suggested the use of a common measuring plane at a downstream distance of the passage throat width. This is reasonable because Gregory-Smith & Cleak [1992] found a dependence of the downstream mixed-out loss on the inlet boundary layer thickness through different amounts of generated secondary kinetic energy.

Langston [1977] and Marchal & Sieverding [1977] found a rapid increase of loss downstream of the throat in their blade passage. They attributed this partly to the fact the loss cores cannot be detected until they have reached a certain size as they grow towards the trailing edge and influence the measurements only gradually.

2.3 Reduction of Secondary Flows

2.3.1 Literature Review on Reduction Techniques

Sieverding [1975] provides an overview of available methods by the year 1975. He identified four different categories, in which achievements might be possible: aerodynamic improvements such as alterations of the turning, blade height, Mach number and loading ('front'/'aft'), profile changes with an increase or decrease in camber (contradictory results were reported), meridional axisymmetric endwall profiling such as the Russian kink and boundary layer fences (the latter two being only effective for cascades with low aspect-ratios, where the secondary flows are more dominant due to an interaction of the hub and tip vortex at midspan). Some of these and other promising techniques are discussed below.

A common method of reducing secondary flows and losses is to accelerate the flow in the rear-ward blade passage by a suitable endwall profile. A consequence is the stretching of the passage vortex already weakened by a reduced blade-to-blade pressure gradient in the forward part of the passage; an 'aft'-loaded blade results. The simplest geometry is to have a smooth step after the passage throat, which is known as the 'Russian kink' (Dejc *et al.* [1973]). Successful tests, mostly in in cascades of low aspect-ratio, including variation/optimization of this idea have been reported in the literature by Morris & Hoare [1975], Kopper & Milano [1980], Horton [1984], Boletis [1985], Moustapha & Williamson [1985] and Atkins [1987]. Axi-symmetric designs can easily be incorporated into state-of-the-art through-flow methods, which account already for a variable annulus geometry.

Another common geometrical method is to introduce compound lean (dihedral) to the blades (e.g. Wang *et al.* [1989], Harrison [1990]). Blade sections are

stacked mostly along a parabola in order to create a radially falling pressure gradient towards midspan. In cascade tests, it has been favoured rather than sweep (Smith & Yeh [1963], Hill & Lewis [1971]), re-cambering (Welua *et al.* [1969]) or variations in the blade chord with a radial variation to account for a spanwise variation in inlet or exit angles. Compound lean reduces downstream mixing losses and spanwise variations of the exit flow angle, decreasing the losses at the endwall and increasing those at midspan. The overall loss remains roughly constant. Compound lean plus endwall profiling configurations are the subject of a computational investigation by Horton [1984].

The extent, location and influence of suction side separation bubbles on secondary flows and losses is not clear from this investigation. The uncertainty persists throughout the most of the literature.

Prümper [1975] performed a vast number of preliminary tests on various reduction techniques such as pressure to suction side slots through the blades, similar bores and tandem configurations, blowing and suction of the boundary layer through holes in the endwall situated upstream and within the passage region, boundary layer fences or grooves positioned either on the endwall or blade surface. His test facility was that of a low aspect-ratio (0.25), full stage turbine with strongly interacting severe secondary flows and a substantial radial pressure gradient. Of all methods, fences mounted on the suction side of the blade rather than the endwall (an optimization was attempted by Kawai *et al.* [1988]) showed the greatest reduction in loss. The fences were tested both on the guide vanes and rotor blades. Fences glued onto the blade surface made tests at characteristic rotor speeds impossible. It is also reported that they might not survive the extreme conditions (high temperature, stresses and rotational speed) found in a real engine. Alternatively, grooves, which provide approximately the same reduction of loss, could be employed but would lead to stress concentrations in the blades. Blowing

of the endwall boundary layer was also found to reduce the losses substantially but could be not pursued because of experimental difficulties. An accounting procedure for the necessary blowing power was not available either.

A 'natural' reduction occurs in axial compressors, where the rotational change in frame of reference from one row to the next skews the inlet boundary layer to oppose the developing secondary flow. This effect gets distorted in the following row since near wall over-turning due to developed secondary flows decreases the skew whereas under-turning increases it (although less effectively because of the greater distance from the wall). In turbines the situation is reversed with the skew enhancing the secondary flows (Boletis *et al.* [1983]). Moore & Richardson [1957] employed a pitchwise-tangential stream of air to model the casing upstream of a compressor rotor cascade. Walsh & Gregory-Smith [1987] and Walsh & Gregory-Smith [1990] used an upstream rotating belt to simulate the hub movement relative to their stationary turbine rotor cascade. There, the negative skew provided by the belt enhanced the secondary flow. The belt was also rotated in the opposite positive direction to simulate the compressor situation. A significant reduction in gross secondary loss (downstream loss coefficient subtracted by profile mixed-out) of 35% was found.

'Balance holes' (rotor disk cavities with big clearance) in the rotor of a steam turbine provide suction of the inlet boundary layer feeding it back into the downstream flow due to the pressure drop from upstream to downstream of the stage. Unsworth & Parker [1991] found them together with fillets, flares and blade lean capable of reducing secondary flows and improving the overall efficiency.

Topunov [1982] conducted a series of tests to reduce losses in turbine cascades and stages. The aspect ratio of his cascade was low (0.84), the inlet turbulence level amounted to as much as 10%. An optimum configuration of blowing through holes in the blade suction side to supply an (incomplete) cooling film was transferred to

the nozzle guide vanes of a whole stage and further tested. The reduction in loss was attributed to the removal of a pulsating laminar separation bubble at the blade suction side[2]. Blowing into the separation bubble through a recess in the vane was found to be more effective, but without accounting for blowing power needed. Suction yielded similar values. It should be noted that the removal of a separation bubble does not necessarily lead to a reduction of the secondary flows and loss as defined in Section 2.1 irrespective of the fact that there seems to be a confusion in the Russian literature about pulsating separation on the blade suction side and secondary flows and the passage vortex (see for example Shkurikhin [1969]).

An exotic way of reducing secondary flows is stated in Russian patent no. SU1089-282/3 [1989]. A 'flexible plate' on the blade suction side or end-wall lifts off while interacting with the secondary vortex and thereby reduces it. Detailed information on these devices is not available. They seem rather impractical.

UK patent applications by Bischoff [1982] and Bischoff [1983] suggest the use of a pitchwise step, similar to Topunov [1975], or a suction side corner fillet ('Bischoffshügel') to reduce the secondary flow losses. The lack of experimental data renders an evaluation impossible. However, the idea of altering the blade passage hints at an inverse design approach, which is discussed below.

Sieverding & Wilputte [1981] evaluated an endwall cooling configuration with one upstream row of holes and two within the passage. A decrease in secondary flows and losses was found for a freestream to coolant total pressure ratio greater than unity. The results cannot easily be transferred to a real machine due to a uniform total temperature. Bario *et al.* [1990] investigated endwall blowing

---

[2]The high turbulence level would usually prevent the separation bubble, so the value for the free-stream level might be an printing error in the translation of the Russian paper and only amount to 1%.

through discrete orifices and rows of holes for different jet to mainstream angles. They reported local re-energization of the endwall boundary layer and diminished overturning as a result of injection through two rows of holes near the blade leading edges. The influence of a cooling air injection through individual holes around the blade surface on secondary flows and the loss distribution was investigated by Yamamoto [1990]. The blowing power is not considered in these investigations.

2.3.2   Categorization, Evaluation and Selection of a Technique

A straightforward categorization of the above techniques is to divide them into *active* and *passive* control methods. Active methods require additional power whereas passive methods do not and so the former might be more effective than the latter, but overall less efficient. Not only the amount of the reduction in loss obtained but also the conditions under which the tests were performed must be considered (e. g. aspect-ratio, linear/annular cascade, full stage).

From a theoretical point of view, the reduction of secondary flows is an inverse design problem. In annular cascade, changes to the blade profile, e.g. thickness or camber, could be introduced to produce whirl distributions, which counteract secondary flows. Although not commonly used, numerical boundary element methods (Brebbia [1984]) extended to viscous flows seem to be suited for inverse design approaches. Another theoretical approach could be the inclusion of the secondary flow reduction problem as an additional constraint to hybrid design optimizer employing expert systems (Section 2.3.3), numerical procedures and genetic algorithms (Tong & Gregory [1990]).

Walsh & Gregory-Smith obtained a remarkable reduction in secondary flows and losses in the Durham Linear Cascade by skewing the upstream inlet boundary layer. Therefore, it was decided for the experimental part of this investigation to

apply endwall boundary layer blowing at inlet of the cascade in the same direction and roughly at a position where root leakage air in a real machine, necessary to prevent ingestion of hot gas (Bindon [1979a]), would be injected. In a real engine, this air exited from a rotating disk cavity and would therefore posses the same swirl direction as the skewed inlet boundary (Dadkhah *et al.* [1992]). However, it might be possible to guide the root leakage air such that it opposed its usual swirl direction and that of the incoming boundary layer. It would then have to counteract the skew already present in the incoming boundary layer and possess an excess momentum to reduce the secondary flow. An investigation of this type would exceed the scope of the present work and is also more suited for annular configurations. Injection of cold air upstream the leading edge could serve endwall film cooling purposes, too.

2.3.3   Optimization of a Technique using Artificial Intelligence

Once a reduction technique has been selected and tested, it is necessary to perform a parameter optimization. Analytical expressions for complex problems are not always available. However, it might be possible to formulate qualitative rules on the effect of parameter changes. If the number of rules and their degree of interference exceeds a certain limit, solution techniques based on artificial intelligence might be useful. Expert-systems, genetic algorithms and neural nets could help to reduce the time required to find an optimum design. Rechenberg [1973] suggested a method of reducing secondary flows in bend pipes by optimizing the shape of the bend, applying 'evolutionary strategies', which are similar to genetic algorithms. The optimum was found experimentally with only a small number of steps.

A general implementation scenario for a rule-based expert system supervising both simulation and experiment as well as deciding on which one to run next, is

suggested in Figure 2.2. Information retrieval and generation of a proposal how to satisfy the overall goal require possibly back- and forward-chaining object-oriented inference engines operating on a rule-base updated by results from a data-base. Abelson *et al.* [1989] developed useful guidelines for setting up a rule-base to prepare, execute and control numerical experiments. A learning feature could be added to improve the rule-base according to penalty functions, which depends on the success or failure of a run, by dropping existing or adding new rules.

In the design of a multi-stage turbine, Tong & Gregory [1990] queried an expert-system, incorporating empirical design rules, before a time-consuming numerical/genetic-algorithm optimization was performed. The success in reducing drastically the turn-around time demonstrates the necessity of overcoming the exclusive use of conventional design methods in turbo-machinery.

Figure 2.2: Blowing Design Optimization by a Rule-Based Expert System

The implementation of a similar scheme as depicted in Figure 2.2 had been initially considered for endwall profiling but was abandoned due to a lack of available experimental and computational data to feed the data-base. With upstream boundary layer blowing, the similar difficulties had been met.

Moreover, the complexity of the suggested approach was thought to exceeded the scope of the project.

Chapter 3

Experimental Setup

F undamental information on the Durham Linear Cascade is provided in Graves [1985], Walsh [1987] and Cleak [1989]. The data acquisition is described in the following as far as it updates or completes the existing apparatus.

3.1 Apparatus

3.1.1 The Durham Linear Cascade Facility

Geometry

The test facility at the University of Durham is that of a low speed, linear, turbine cascade of high aspect ratio. The blades are representative of a high turning HP rotor giving the same loading distribution. The design data is given in Table A.1 (appendix). A schematic of the cascade and the blade profiles with traverse planes is shown in Figures 3.1 and 3.2. New is a 5 mm wide injection slot situated at the previous traverse slot 1 position. The new slot 1 has been moved 8 mm downstream and is about 9% of axial chord upstream of the leading edge (see Figure 3.1) to allow for measurements behind the injection slot.
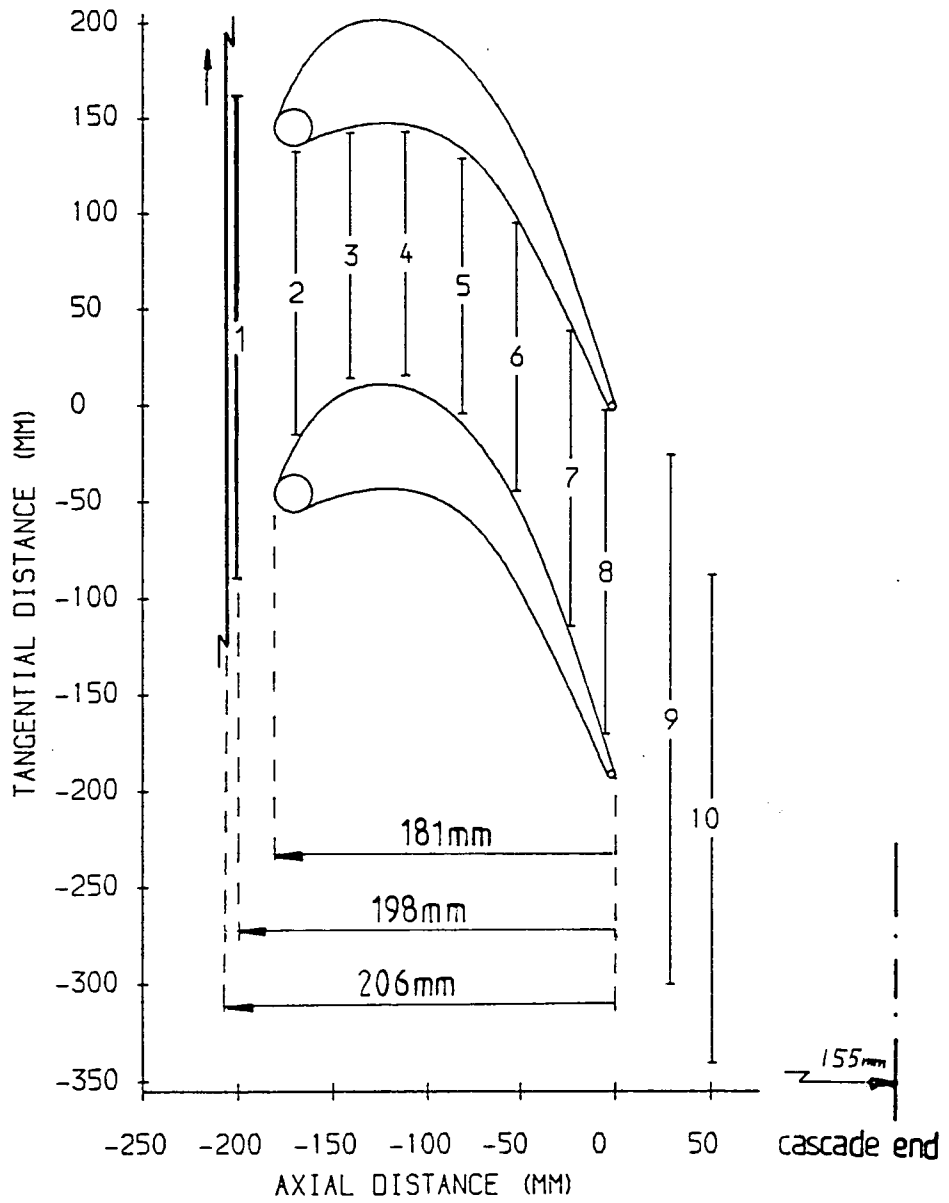
Figure 3.1: Blade Profile with Traverse Planes and Injection Slot Position
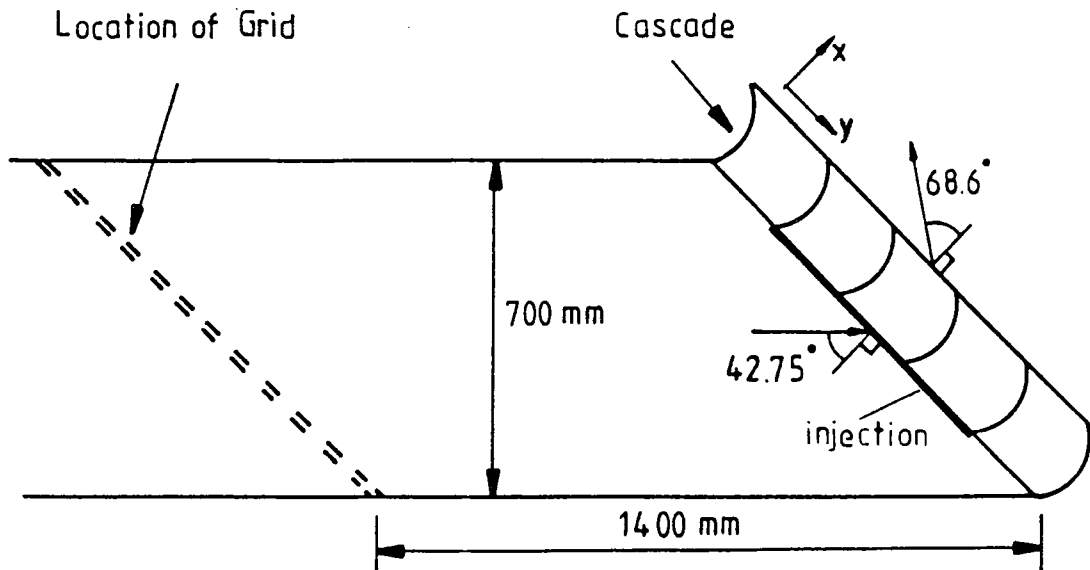
Figure 3.2: Tunnel and Cascade Geometry

Constant Reynolds Number Operation

For low-speed cascades it is necessary to ensure an operation at a constant Reynolds number. This is achieved by a variation of the upstream dynamic head according to a change in the atmospheric conditions and a correction of all measured pressures relative to that. Due to the injection of air upstream of the blade passage but downstream of the tunnel pitot tube while keeping the exit mass flow constant, different corrections to the dynamic head and the measured pressures have to be carried out. A derivation of the correction factors is given in Appendix B.

Inlet Boundary Layer

Inlet boundary layer data is contained in Table 3.1. A numerical integration procedure derives the displacement, momentum and energy thicknesses from upstream measured pitch-averaged data. The displacement thickness is obtained by a cubic interpolation is from the first near wall point of measurement up to midspan

	JGC	TB - 1	TB - 2	TB - 3	TB - 4	TB - 5
δ	40.0-45.0	35.0-40.0	35.0-40.0	40.0-45.0	40.0-45.0	35.0 - 40.0
δ_1	3.557	3.468	3.881	3.979	3.992	4.127
δ_2	3.013	2.873	3.147	3.194	3.283	3.282
δ_3	5.532	5.246	5.741	5.801	6.003	5.958
H_{12}	1.180	1.207	1.233	1.246	1.216	1.258
n_{12}	11.1	9.7	8.6	8.1	9.3	7.7
$c_{p_{0_1}}$	0.0222	0.0204	0.0233	0.0230	0.0259	0.0231

Table 3.1: Boundary Layer at Slot 1 - Area 2

whereas a power law is fit from the wall up to this point to avoid problems with the splines. Momentum and energy thickness integrands possess maxima which are at $0.25v_{up}^2$ and $0.385v_{up}^3$ respectively and those are used instead of zero values at the wall with the cubic fit.

The experimental scatter between the reference conditions presented by Cleak [1989] ('JGC') and measurements on different days of this work ('TB - n') shows the difficulty in matching it to an exact power law profile, of which n_{12} denotes the coefficient obtained from displacement and momentum thickness. The measurements were obtained for a constant upstream bleed (Walsh [1987]). Since the cascade Reynolds number cannot be set very accurately (Appendix B), the bleed off might be influenced and should be monitored and ajusted in the future to obtain more consistent data. A step of 2-3 mm in the endwall in front the sealed injection slot influenced near wall measurements without injection (TB - 1) before it was taped down to about 1 mm and before the slot 1 traverse plane had been moved.

The variation of the measured loss coefficient $c_{p_{0_1}}$ is still within its specified accuracy (Table 3.5, pg. 35) and is thus not significant to the data analysis.

The inlet boundary layer is also influenced by the upstream turbulence grid, which causes a slight acceleration near mid-span seen in pitch-averaged plots of slot 1 (Figure 4.15, pg. 72).

Mass Flow through Cascade

Using standard day values (Table B.1, pg. 190), a representative displacement thickness of $\delta_1 = 3.979$ (Table 3.1) and an inlet flow angle of $\alpha_1 = 45.5°$ (Table A.1, pg. 188), the cascade mass flow is calculated to

$$\dot{m}_{cascade} = \rho v_{up} \sin(\alpha_1)(\hbar - \delta_1)s$$
$$= 0.585 \frac{kg}{s}$$

Experimental values, of which the slot 10 result was used in the data analysis, are given in Table 3.2 for the sealed injection slot. Within the blade passage, accurate results cannot be expected due to the extrapolation through the blade boundary layer to the blade surface. A better agreement in the calculated and measured mass

Slot	1	2	5	8	10
$\dot{m}_{cascade}$	$0.612 \frac{kg}{s}$	$0.578 \frac{kg}{s}$	$0.540 \frac{kg}{s}$	$0.537 \frac{kg}{s}$	$0.600 \frac{kg}{s}$

Table 3.2: Massflow through Cascade

flow at slot 10 is expected indicating the necessity of a future re-calibration of the 5H-probe.

Outlet Flow Angle

The metal angle of the blades is $-68.0°$. The correlation by Ainley & Mathieson [1951] gives

$$\alpha_e = -11.15 + 1.54 \arccos\left(\frac{\Theta}{s}\right) + \frac{4s}{\frac{i^2}{8z}}$$
$$= -68.9°$$

An average value of $-68.6°$ (Figure 4.19, pg. 79) with an error of $\pm 0.5°$ (Table 3.5, pg. 35) is reproduced by the 5H-probe.

Wind Tunnel Resonance

A tunnel resonance frequency of 15.2 Hz was measured by Cleak [1989] using a single hotwire in regions where the turbulence level was low enough not to swamp it. The resonance was thought to be due to an 'organ-pipe' effect giving rise to a standing pressure wave, the wavelength being related to the geometry of the cascade. Accounting for the 'Helmholtz effect', which corrects the wavelength due to the diameter of an open end (Bergmann-Schäfer [1974], pg. 522), and the speed of the cascade flow, a similar result is obtained.

A so far unrevealed feature in the cascade is a range of dominant frequencies between 0.1 and 0.06 Hz found by recording time-dependent total pressure data of the upstream pitot tube via transducer and A/D-converter. Data up to 30 kHz was sampled and a discrete FFT with a Parzen window (Press *et al.* [1988]) was used to obtain the power spectrum. The resonance might be due to a low frequency disturbance in the air supply by the cascade fan and is avoided by updating the upstream pressures together with the probe pressures at their normal recording frequency of about 10 kHz.

3.1.2 Injection Slot

Geometry

The injection slot (Figure 3.3) spans three blade rows, which should give sufficient periodicity for measurements in the centre blade passage (Figure 3.2). It consists of eight vanes per pitch, which were designed to inject air perpendicular to the axial flow direction, i.e. with tangential and spanwise velocity components. Tests have been performed for the two representative blade angles of 15° and 30° measured from the tangential direction. The correlation of Ainley and Mathieson [1951] gave an approximate discharge angle of 20° for the '**low angle**' and about 35°
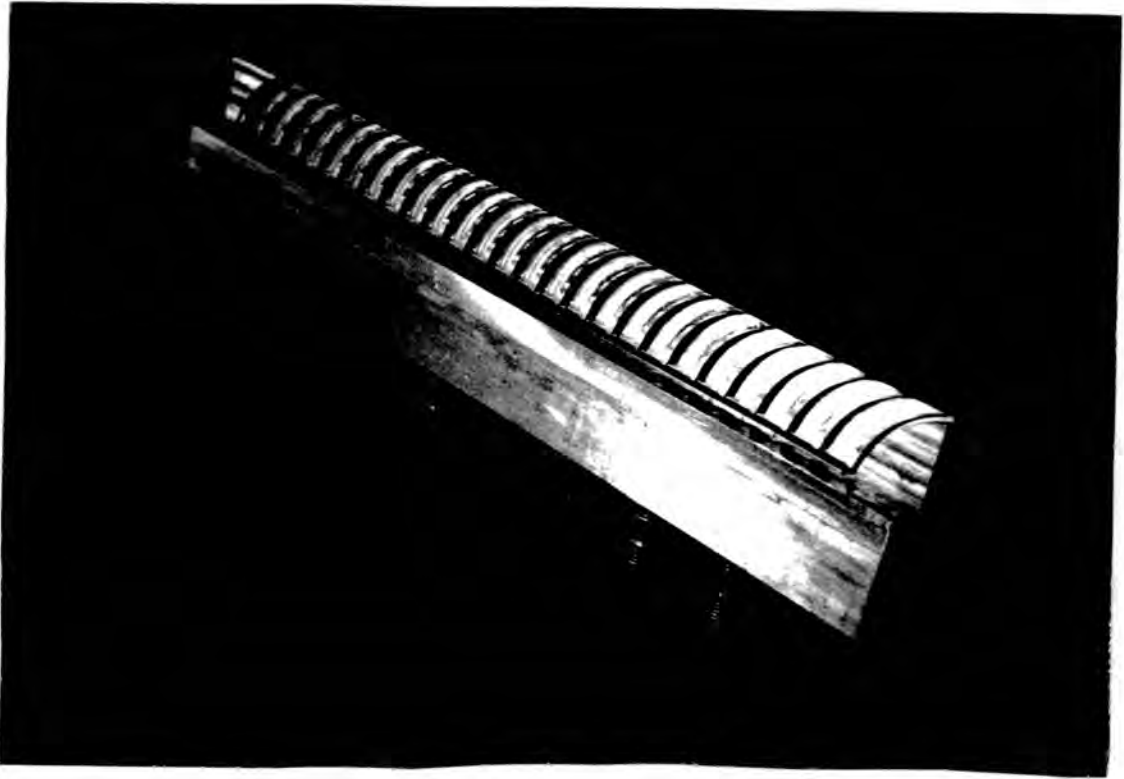
Figure 3.3: Injection Slot

for the '**high angle**'. An uncertainty in the values is due the low aspect-ratio of the injection vanes for which the correlation does not necessarily give accurate results[1]. The vanes, which were designed for non-separated flow past them in order to minimize the wake losses are shown in Figures 3.4 and 3.5.

The geometry of the injection slot is shown Figure 3.6. The first design had a sharp right-angled edge on the downstream side, which was thought to give raise to separation and recirculation behind the jet as seen by Bindon [1979b]. Thus, a rounded edge downstream of the injection is used to prevent recirculation, but it gives rise to an uncertainty in the area of injection. The vane trailing edges lie above the start of the radius of curvature, this being a compromise between guiding the injected air, preventing the downstream separation and accepting small variations in the area of injection. A theoretical value per blade pitch is obtained by

---

[1]An *in situ* measurement of the pitchwise varying discharge angle was not attempted due to experimental difficulties.
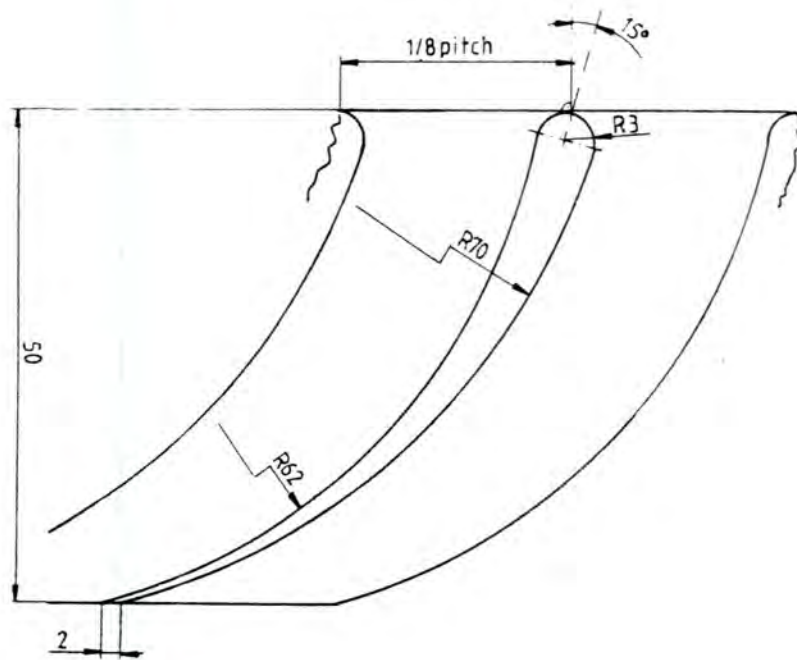
Figure 3.4: Guide Vane for Injection Slot at 15°
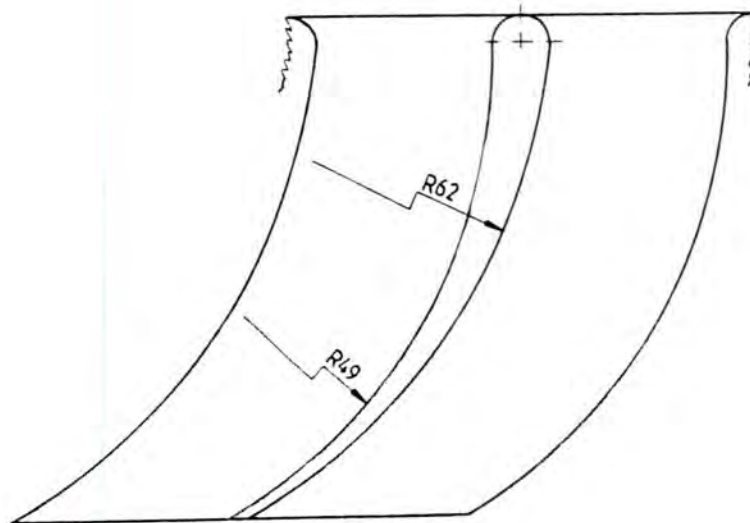
Figure 3.5: Guide Vane for Injection Slot at 30°
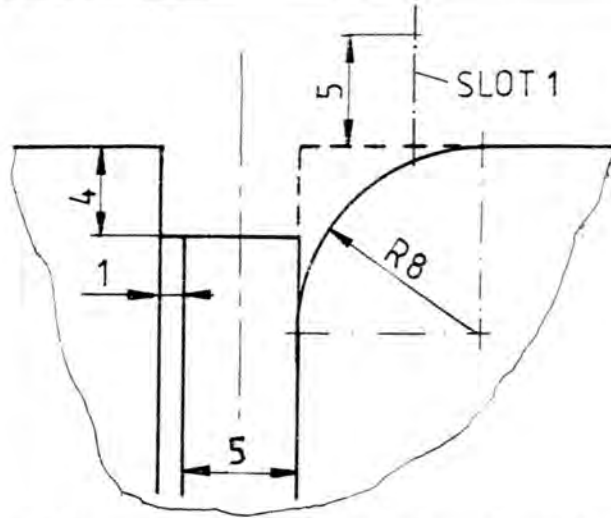
Figure 3.6: Injection Slot (Cross-Section)

subtracting the thicknesses of eight injection vane trailing edges from the injection slot width multiplied by the blade pitch.

$$A_j = t \cdot s - 8 \cdot t \cdot 2\,mm \qquad (3.1)$$

$$= 875\,mm \qquad (3.2)$$

The slot mounted into the cascade is depicted in Figure 3.7.

Supply and Metering of the Injected Air

The injected air was supplied by a variable speed fan (originally used for an organ). Its characteristic was measured for some operation conditions and found to satisfy the overall requirements of giving the desired mass flow for a required total pressure at the point of injection.

An orifice plate with D and D/2 tappings according to BS1042 (see Appendix C) was chosen to meter the injected mass flow with an error of $\pm$ 1.75% and 95% confidence. To guarantee this, the air had to be guided straight in front and after the orifices for specified distances.

A manifold consisting of ten tubes distributed the air to a plenum of the

Figure 3.7: Injection Slot Mounted onto Cascade
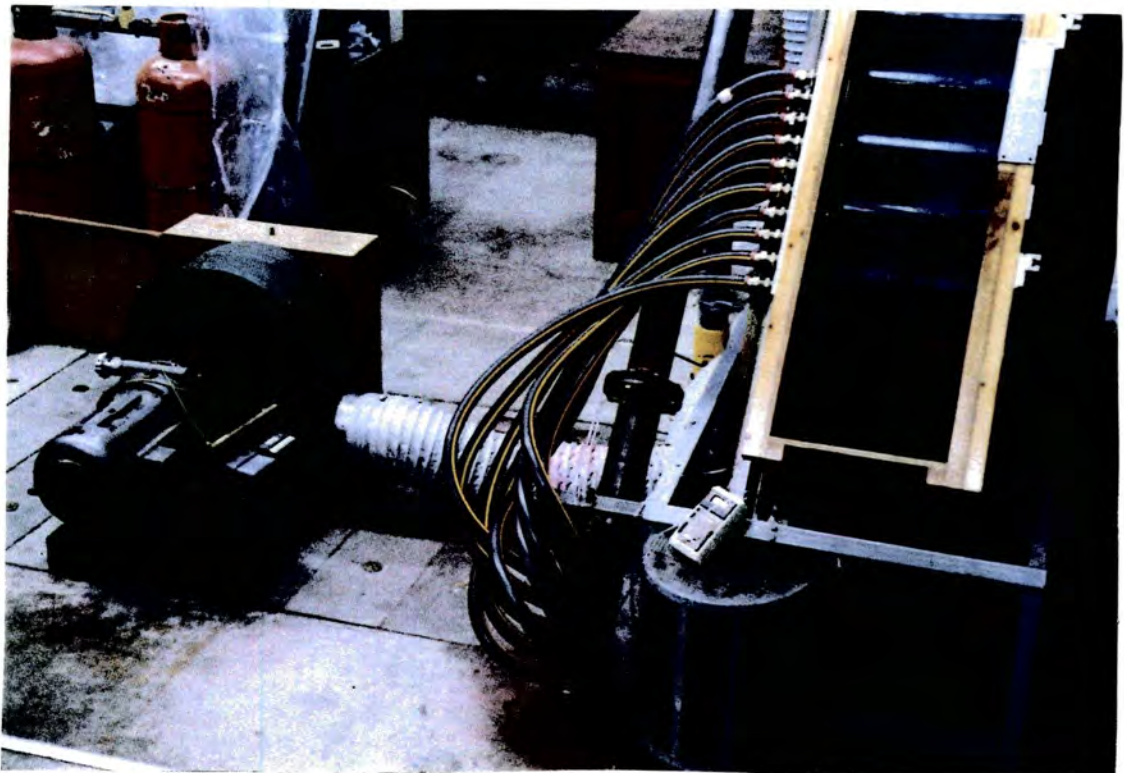
Figure 3.8: Working Area next to Cascade

injecting slot built (see Figure 3.3). From there, it entered the guide vane passage passing struts in front of the vane leading edges.

The working area next to the cascade is shown in Figure 3.8.

3.2 Measurement Technique

A PC-386DX with an AT-bus was used to control both traversing and data recording.

3.2.1 Traverse Equipment

Motors

Low current, bipolar, 4-phase, hybrid stepper motors[2] were fitted onto the existing tangential and radial traverse slides. They were driven by the power supply of the PC via Darlington transistors[3] of high gain connected to the stator. The transistors were switched by an Intel 8255 I/O chip to drag the permanent magnet rotor along the 4 phases of the stator. The step size of the motor was 1.8° resulting in a probe movement of 0.005 mm with a slide lead-screw pitch of 1. The driver's circuitry was implemented by the re-design of an existing PC plug-in card. The language *C* was used as a programming tool.

End/Opto-Switches

Micro-switches[4] and slotted opto-switches[5] mounted onto the slides served to protect the assembly against crashes and to set both tangential and radial reference points easily. The end-switches were connected in series and the opto-switches in

---

[2]McLennan 23HS-202E
[3]TIP121
[4]RS 334-381
[5]RS 304-560

parallel to an input port of the 8255. Their status was polled after each stepping unit, which consisted of four single steps or 0.02 mm of probe movement.

Traverse Time

The overall time of a traverse was reduced from two to three days to about an hour. A traverse could be done fully automatically without interaction of the experimenter. Thus, together with a fast data analysis procedure, it was possible to perform parametric studies.

3.2.2 Five-Hole Pressure Probe

The Cobra type five-hole pressure probe described by Graves [1985] was used to measure the flow field. Wall proximity effects (Dominy & Hodson [1992]) and influences of the turbulence level (Bubeck [1988]) on the measurements were critical for this cascade. They are described below followed by other information.

Wall Interference

Probe-wall interference is negligible when the probe head to wall distance is at least 1.5 times the probe head diameter. For a tip width of 2.28 mm, this corresponds to the first radial traverse position at 5 mm wall distance. The distance of the probe head from the blade surfaces was always greater than that value. A linear extrapolation through a boundary layer to a solid surface is performed when area-averaging the data but this may lead to some inaccuracy as seen with e.g. the cascade mass flow in Section 3.1.1.

Turbulence Correction

The effect of turbulence on 5H-probe measurements is to produce an over-reading of the total pressure

$$\overline{p_{0_{probe}}} = \overline{p_s} + \frac{\rho}{2}(U^2 + \overline{u^2}) \tag{3.3}$$

The error is identical to the local turbulence level neglecting velocity fluctuations normal to the main flow direction (Bubeck [1988])

$$\frac{\overline{p_{0_{probe}}} - (\overline{p_s} + \frac{\rho}{2}U^2)}{\frac{\rho}{2}U_1^2} = \frac{\overline{u^2}}{U_1^2} \tag{3.4}$$

A representative value for the local turbulence level in the downstream loss core may be taken as 16% (Cleak [1989]) which reduces to about 2% when referenced to the square of the upstream velocity. The peak loss coefficient value is about 1.2, so a correction of the data was not carried out.

Pitch Angle Correction

Depending on the axial slot position of the probe a correction for the measured pitch angle had to be introduced to guarantee zero spanwise flow at midspan. Due to difficulties (bending of stem, mountings, slots) in the exact alignment of the probe right angles to the cascade endwall, the correction was accepted but it should tried to be avoided in future work. With an increase in blowing a maximum increase of about 1° in the pitch angle measured at midspan was noticed. The non-symmetry in the blowing is most probably responsible for this effect.

Turret Setting Angle

The probe was supported by a turret that allowed a rotation of the probe around its axis in order to vary the angle relative to the flow. The non-nulled calibration technique allowed for a maximum variation in the flow angle of $\pm$ 30°. To make practical use of the range, the probe was approximately nulled at midspan before measuring a slot and then the setting was maintained until the probe was moved to a different slot. This procedure had the disadvantage of sometimes getting close to the edge of the calibration, where the fitted splines may give an error, but was preferred since it rendered a re-adjustment of the probe during a run unnecessary and therefore assisted a fully automated data acquisition. Some runs were performed at different setting angles were performed to ensure the consistency of the results.

Values for the probe turret angle set during runs are given in Table 3.3.

Slot	1	2	5	8	10
Turret Angle	+135	+135	-138	-128	-114

Table 3.3: Turret Setting Angle at Different Slot Positions

Probe Support

The 5H-probe was mounted onto traverse slides for the radial and tangential direction to move freely within the plane of an axial slot. Plastic strips around the probe stem were guided by brushes to prevent the leakage of air through mid-passage and upstream slots. To minimize probe bending and to ensure centering of the probe stem, a new support was manufactured. The influence on the positional accuracy and calibration of the probe appears to be negligible.

3.2.3 Data Acquisition

Hardware

Pressure Transducers Standard commercial pressure transducers produce an electronic output signal due to the change in capacity of a bending metal diaphragm. The output signal is linearly dependent on the measured pressure. Because of errors in the linearity, the range of the transducer should closely match that to be measured. The accuracy, defined as the root-mean-square of errors in repeatability, hysteresis and non-linearity, together with thermal errors such as shift of offset and drift of sensitivity is important for determining their contribution to the overall experimental accuracy (Appendix D). Built-in amplifiers help to reduce noise by providing a high voltage output signal. The response time would only be of significance in unsteady measurements.

In the experiment, each of the five probe pressure tubes is connected to an individual pressure transducer. The four side hole tubes were linked to less accurate and sensitive transducers[6] than the center tube[7]. The latter records - when nulled - the local total pressure relative to the upstream one and therefore works over a smaller, double range (0-±200 Pa). The range of the side tube transducers (0-500 Pa) is also determined by the upstream total pressure. An additional low sensitivity transducer was connected to the upstream pitot tube.

AD-Converter The output signal of the transducers was recorded by a commercial 12-bit, 16 channel, bipolar A/D-converter with a pacer triggered sample-hold mechanism and a programmable gain to reduce noise. The specified non-linearity was 1 LSB (Appendix D). The maximum conversion time of 30 kHz was set when recording (via DMA) time-dependent data of the wind tunnel in order to detect

---

[6] Furness FCO-40
[7] CMR 200-008

resonance frequencies. The average recording frequency during an area traverse was about 10 kHz for six multiplexed channels. The A/D converter was mounted onto a data acquisition board plugged into one of the AT-bus slots of the PC.

Software

Sampling Time An optimum overall sample time was obtained by taking into account the resonance present in the wind tunnel, the overall time necessary to take a reading, the maximum conversion time of the A/D-converter as well as the available computer memory. The data acquisition program prompts the user to modify or accept a default value of 1.645 s, which gives 25 periods at 15.2 Hz (resonance frequency, see Section 3.1.1) at an overall A/D conversion time of about 10 kHz for six channels, resulting in 100 samples per channel per period. This attempt to minimize the scatter of the data is most effective for low sample numbers but only works if the upstream reference total pressure - relative to which all readings are taken - is in phase, depending on the axial position of the probe. Following the Nyquist criterion, i.e. data sampled at least twice as fast as the highest dominant frequency is sufficient to get reasonable results, the actual sampling time was not too critical.

Confidence Test A confidence test was performed by comparing the number of recorded samples to the one calculated from the variance of the data, typical transducer and A/D-converter tolerances and assuming a confidence level of 99% (Kreyszig [1988], pp. 1249). For a negative test result, the program firstly tried to repeat exactly the same measurement. If the test failed for the second time, the program suggested a new number of samples up to three times the initial sampling time. The confidence allows for a dynamic logging of the data depending on the degree of scatter and therefore minimizes the accumulated logging time of a full

traverse.

3.2.4 Data Analysis

The analysis procedure firstly determines from the measured raw data the flow quantities by means of a program that contains the 5H-probe calibration information. An integration over a lossfree region at midspan/midpitch gives a slot dependent correction value which is subtracted from the data so that the Bernoulli condition (constant total pressure along an ideal streamtube) is satisfied. Average corrections for the total pressure loss coefficient are listed in Table 3.4. They

Slot	1	2	5	8	10
Correction Value	0.066	0.058	0.072	0.0032	0.016
Percentage of c_p	74%	67%	75%	4%	9%

Table 3.4: Midspan/Midpitch Lossfree Correction Values

probably arise from a different location of the 5H-probe and the reference pitot tube during calibration (Cleak [1989]). The corrected and ordered data is fed to a program for calculating the streamwise and tangential vorticity components, the former being obtained by the method of Gregory-Smith *et al.* [1988]. Before plotting the data, redundant information such as flow angles obtainable from the velocity components, is removed from the data file, which contains all the results from a single slot traverse. Instead of plotting the data directly, pitch- and mass-averaging is possible, also producing graphical output (pitch-averaged curves for single or multiple slot traverses). This data analysis procedure has been established in Durham for some years and was made attractive for the present work by transferring the associated software from a slow, out-of-date mainframe computer onto the same modern PC that recorded the data. The replacement of integration and interpolation subroutine-libraries, not available on the PC, by similar one from public domain sources was checked to ensure the consistency of

the programs (Biesinger [1990]). The analysis of slot traverse data including the production of relevant plots was possible within several minutes.

3.2.5 Experimental Accuracy

Errors are categorized into systematic (calibration, non-linearity, shift of offset, drift of sensitivity) and random (repeatability, hysteresis). They propagate, when systematic, depending on the specific algebraic manipulation performed (Bronstein [1981]) and, when random[8], according to Gauss' root-mean-square formula (Busch [1982]). An assessment of the overall error (accuracy) is only possible when all contributions to it are known. A rudimentary error analysis is given in Appendix D. Estimated error bandwidths are given in Table 3.5 of which the error in the total pressure loss coefficient is related to the result obtained in Appendix D ignoring calibration influences.

positional	$< \pm 0.1$ mm
Δp_u	$\pm 0.5\%$
α	$\pm 0.5°$
c_p	± 0.005

Table 3.5: Estimated Accuracy of Measurements

The repeatability of measurements at slots 10 and 1 could be improved when relying on results based on an integration area covering only one blade area rather than parts of the adjacent area.

3.3 Surface Flow Visualization

The most common technique for visualizing limiting streamlines by determining the wall shear stresses is to apply a film of a light oil mixed with dye to both endwall

---

[8]Random errors can be treated as systematic considering their maximum value.

and blade surfaces. The direction of wall limiting streamlines is (Squire [1962])

$$
\left(\frac{dx}{dz}\right)_{oil} = \frac{\left(\frac{\partial v_x}{\partial y}\right)_{y=0}\mu_{air} + \left(\frac{\partial p}{\partial x}\right)\left[\left(\frac{y}{2}\right) - h\right]}{\left(\frac{\partial v_z}{\partial y}\right)_{y=0}\mu_{air} + \left(\frac{\partial p}{\partial z}\right)\left[\left(\frac{y}{2}\right) - h\right]}
\tag{3.5}
$$

whereby x, z lie in the plane of wall and y perpendicular to it; h represents the thickness of the oil film. If the pressure gradient is small and the velocity of the air large, the streamlines indicated by the oil coincide with those of the air. Near separation lines and saddle points, this condition is not always fulfilled and misleading results can be produced (Langston [1989], Merzkirch [1987]). With injection of air, secondary velocities are diminished and may then lead to streamlines dominated by the local pressure gradient. This could affect the flow up the blade surfaces and on the endwall.

In practice, the blades and the endwall were covered with a thin foil. The latter was coated with paraffin thickened by a fluorescent dye until a good adherence to the walls was obtained. Different colours for the endwall and the blade surfaces were used. The start-up of the wind tunnel was done by switching on the main fan after the injection pump to prevent initial disturbance of the coating. The optimum time for interaction between flow and surface was found to lie best between five to eight minutes.

Chapter 4

Experimental Results

$\mathcal{E}$ xperimental results are presented in the form of selected area- and pitch-averaged plots obtained at five axial positions and recorded for various conditions. These, together with an understanding of the effects of injection into the upstream boundary layer, provide an insight into the physics of the complex cascade flow.

4.1 Presentation of Results

4.1.1 Test Conditions

Tests have been performed at blowing rates varying in steps of 50% up to 300% for the high angle and 450% for the low angle. The percentage refers to the design blowing rate, which corresponds at the high angle to the same tangential velocity component and momentum as in the positive skew case of Walsh [1987]. For the low angle, the design blowing rate gives the same near wall velocity with a small difference in tangential momentum. More detail on this is contained in Section 5.1.2.

Five axial planes (Figure 3.1) have been chosen for traversing:

Slot 1 is positioned at 5% axial chord upstream of the blade leading edge and downstream of the injection slot (Figure 3.6), thus providing information on the flow before entering the cascade. It might be affected by separation bubbles on the downstream injection slot radius (cf. Section 4.2.2).

Slot 2 lies 6% behind the blade leading edge and is the first slot position after the flow has entered the blade passage.

Slot 5 (55% axial chord) is situated at mid-passage before the throat and roughly at the position where H_p gets closest to the suction side (SS), if no injection takes places.

Slot 8 is just in front of the blade trailing edge at 97% axial chord. Its pressure side (PS) boundary coincidences with the passage throat.

Slot 10 data, 28% downstream the trailing edge, is already partially mixed-out and wake unsteadiness is reduced.

Results for the high injection angle with a downstream rounded edge of the injection slot (cf. Figure 3.6) are available for traverse slots 1 up to 100% injection, 2 and 10, but not for slots 1 above 100% injection, 5 and 8 where a side tube of the 5H-probe got blocked and therefore rendered the results invalid. Previously, slots 2 and 10 were traversed for the same high angle but sharp downstream edge. Slot 1 was moved after the rounded edge had been introduced. Readings for the low angle (with rounded edge) were taken at all five of traverse positions.

An objective of the present work is to investigate the global effects of injection. Details of the injection are provided, when they are essential for explaining features of the main flow.

4.1.2 Data Structure and Selection

The experimental data was obtained by traversing each slot at different blowing rates. It has been decided to present here area plots of different axial positions together for a single blowing rate. This has the advantage of being able to detect features in the flow by inspection of a nearby traverse slot positions. In the description of an area plot at a particular axial plane, the attempt is made to relate them to different injection conditions. After pitch-averaging the data, localized mechanisms cannot be traced any more and therefore, pitch-averaged curves have been cross-plotted for different blowing rates but the same traverse slot position. Mass-averaged data is presented in Chapter 5.

The low angle of injection has been selected for detailed discussion mainly due to a substantially lower amount of kinetic energy, necessary to re-energize and skew the inlet boundary layer. The results of the high angle are merely summarized, since the intention is to provide an insight and understanding of secondary flow mechanisms rather than a full description of all available data. However, the parameter 'injection angle' is of interest and will be discussed in Chapter 5.

Vorticity contour plots are useful for tracing vortices by indicating a variation in their rotational speed as a different contour height level and the sense of rotation as an either positive or negative value. Example plots are provided for zero and 100% injection at slot 10. Another method for revealing the vortex structure is that of Binder & Romey [1983]. Parallel contour lines in yaw angle plots can indicate a vortex core with solid body rotation whereas concave lines hint at the outer potential boundaries of a vortex. The method is more straightforward but it cannot reveal the rotational sense of a vortex. No examples are provided. A third, less known method is to plot contours of helicity (Levy *et al.* [1990]), which is defined

as the vector product of velocity and vorticity. The technique is very powerful but needed a detailed investigation before it can be used for cascade flows.

4.1.3   Area Traverse Plots

The data is presented on axial planes looking in the upstream direction. Thus, the abscissa represents the tangential and the ordinate the spanwise direction. The lines annotated PS and SS are plotted about 10% of the distance to the closest near wall measurement further towards mid-passage than physically located. This has been found in previous investigations by Cleak [1989] to give quantitatively better results and partially compensate for errors due to linear extrapolations of the pitch- and area-averaging routines.

Upstream and downstream slots span more than one blade area. Downstream plots only contain the wake of a 'left' blade area, looking upstream. This area is referred to in the data analysis of Chapter 5 for its better repeatability. The abbreviations PS and SS, used at a downstream slot, refer to a virtual prolongation of the blade trailing edge.

Secondary velocities are relative to the measured velocity vector direction at midspan where they assume zero values.

Vorticity contours are calculated after a method developed by Gregory-Smith *et al.* [1988]. The streamwise vorticity contribution can be obtained after substitution of its tangential component, which contains a derivative of the velocity in the axial direction, by the incompressible Helmholtz equation. The axial derivatives would be inaccurate from measurements due to the coarse axial spacing of the traverse planes.

Negative and positive contour levels are indicated by full and dashed lines, respectively.

The values plotted are defined in Appendix E.1. The numbering of the contour levels, which unfortunately could only be provided for closed lines by the graphics package, are contained in Appendix G.

4.1.4 Pitch-Averaged Curves

Curves of pitch-averaged data only represent integral values of actually measured data points rather than extrapolating through the blade boundary layer up to the blade surface. It is intended to measure the blade boundary layer in continuation of this project.

The values plotted are defined in Appendix E.2.

4.2 Injection Effects

4.2.1 Non-Uniform Injection

A non-uniform static pressure distribution, which changes with the injection rate, exists along the injection slot and leads to a pitchwise non-uniform injection. There is a lower mass flow near the blade pressure side and the blade nose and a higher one near the suction side and at mid-pitch.

Bindon [1979b] was one of the first to visualize the effects of an upstream static pressure field on an axial gap between an annular nozzle row and a rotating hub by noting a flow from the pressure to the suction side through the gap. In later experiments with injection through the gap, this effect could be prevented but downstream losses were increased.

4.2.2 Separation behind Injection Slot

Lift-off with air injection is dependent on the injection geometry (slot design, jet spacing, angle) and the injection velocity or momentum. In order to reduce the possibility of separation behind the injection slot, a downstream radius curvature was introduced. This was found effective for the high angle and was therefore directly fitted to the low angle injection slot.

Wall fluffs were glued to the endwall behind the radius curvature. The flutter of the fluffs was used as an indicator of a separation of the flow and/or the presence of wakes of the slot vanes. It was found that below a blowing rate of 100%, heavy movement of the fluffs indicated passing slot wakes and separation. For higher values including 100%, a constant flutter of low amplitude could be observed. This may be attributable to the unsteadiness in the injection vane wakes and the internal flow structure of the jets emanating from the injection slot.

The injection slot may be considered as a cascade of very low aspect ratio with strong secondary flows and possibly separation. Moreover, the discharged jets become bent by the main-flow also giving rise to secondary flows (Bario *et al.* [1990]). The resulting internal flow structure of the jets might be very complex and would have to be measured.

Separation bubbles directly on the radius might not have been detected either by the wall fluffs or by measurements at slot 1, which lies in front of the the wall fluffs, but measures only from 5 mm above the endwall outwards (Figure 3.3).

4.2.3 Vorticity

Classical secondary flow theory relates vorticity within the blade passage and downstream to the normal and streamwise components present at the inlet plane. The tangential injection of air both re-energizes and skews the inlet boundary layer

modifying the already existing normal and streamwise vorticity at inlet. The effect on the vorticity components at the exit plane may be assessed by the Came & Marsh [1974] formulæ valid for inviscid flow through many-bladed cascades (cf. Section 2.2.1). Gregory-Smith & Okan [1991] developed a computer program allowing for the convection of 'Bernoulli' surfaces, i.e. surfaces of constant inlet total pressure.

Predictions of flows with a spanwise non-monotonic, pitchwise non-uniform and three-dimensional inlet boundary layer using this code tend to give unsatisfactory answers due to the impact of viscous mixing not only on secondary losses but also on the generation of secondary flows through re-distribution of momentum. There will be some mixing before the leading edge plane, but this is not measured due to the first traverse plane being close to the injection location. The results of classical theory are sensitive to the inlet vorticity distribution and therefore, knowledge of the inlet boundary layer profile at the leading edge is a prerequisite for its use. Inviscid predictions of secondary flows for inlet boundary layers with a steady increase in vorticity towards the endwall are feasible because a little mixing close to the endwall does not influence the production of the passage vortex noticably. With injection, the inlet boundary layer at the leading edge will show substantial re-energization close to the endwall with steep gradients towards midspan and towards the endwall which would mix out within the blade passage while driving the secondary flows. Mixing-out of the re-energized profile in front of the blade passage to obtain a smooth power law profile is not satisfactory although this would reduce the amount of secondary kinetic energy being generated. These shortcomings make assessments based on classical inviscid theory with respect to both experimental and computational data rather inaccurate unless a suitable mixing model were to be included.

However, some information on the effect of injection on the exit streamwise vorticity may be obtained from classical theory. The effect of the inlet normal component of vorticity on the exit streamwise is more significant than the effect of the inlet streamwise component. This comes from the expression (Came & Marsh [1974]) with the inlet and exit flow angles used in this work

$$
\begin{aligned}
\xi_{\sigma_e} &= \xi_{\sigma_i} \frac{\cos \alpha_i}{\cos \alpha_e} + \left(\frac{\xi_{v_i}}{\cos \alpha_i \cdot \cos \alpha_e} \right) \\
&\quad \cdot \left(\frac{1}{2} \left(\sin(2\alpha_e) - \sin(2\alpha_i) \right) + (\alpha_e - \alpha_i) \right) \\
&\simeq \xi_{\sigma_i} \cdot 2.0 - \xi_{v_i} \cdot 10.4
\end{aligned}
\tag{4.1}
$$

indicating a factor of about five. Thus, with injection, the streamwise re-energization of the inlet boundary layer is expected to be most significant in reducing secondary flows and losses and this is found in practice (see below).

4.2.4 Re-Energization of Inlet Boundary Layer

The components of the injected velocity vector relative to the velocity of the
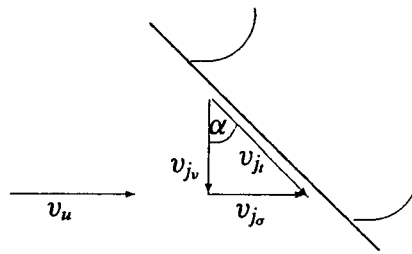
Figure 4.1: Injection Velocity Vector in Pitchwise Plane

mainstream are shown in Figure 4.1 at a pitchwise plane located just above the injection slot. The injection re-energizes the inlet boundary layer with the sine of the inlet angle. Table 4.1 lists the ratio of the streamwise injection velocity

% Design	100%	150%	200%	250%	300%
$\frac{v_{ja}}{v_u}$	0.46	0.69	0.92	1.15	1.38

Table 4.1: Streamwise Injection to Freestream Velocity Ratio - Low Angle

component to the freestream velocity for the low angle. Re-energization of the boundary layer near the endwall takes place from above 200% onward, allowing for some loss at the injection location. A reduction in the downstream secondary flows and losses can be expected. This has been confirmed through experimental work on various endwall film cooling configurations (e.g. Sieverding & Wilputte [1981]) and is also suggested in Chapter 5 of the present work (Figures 5.10, pg. 132, and 5.12, pg. 134).

Injection of air also provides the inlet boundary layer with normal momentum opposing the generation of secondary flows. The flowpath of particles near the endwall are skewed towards PS.

4.3 Area Traverse Plots

4.3.1 No Injection

Figures 4.2 and 4.3 show selected plots of measurements at slots 1, 2, 5, 8 and 10 discussed here.

Slot 1

Secondary Velocities The secondary flow field around (-25,5)[1] is seen to be influenced by H_s. The action of H_p is not clearly discernible.

---

[1] This notation will be adopted in the following to write pairs of coordinates giving the tangential position first and the radial one second.

Total Pressure Loss   Reverse flow is caused by the horseshoe vortex and transports low momentum fluid upstream resulting in a discernible increase in total pressure loss.

Slot 2

Secondary Velocities   A rather compact H_s is visible near SS, whereas the core of the spread-out H_p is hardly visible near PS at about (115,15). The secondary velocities underneath H_p indicate over-turning already existing at slot 2.

Total Pressure Loss H_s gives rise to a distinct loss core, which is as part of the endwall region still covered by 'old' material from the inlet boundary layer (see Figure 2.1). This region roughly extends up to the area influenced by H_p.

Slot 5

Secondary Velocities   A passage vortex, with its centre migrated across the blade passage from PS to SS, has developed out of H_p. The over-turning in the lower part of the vortex has increased.

Total Pressure Loss   Most of the inlet boundary layer is swept into the SS corner. The associated loss core does not coincide with the centre of the passage vortex because of increased turbulence production in the SS corner (cf. Figure 7.2, pg. 171).

Slot 8

Secondary Velocities   The passage vortex is strengthened and has moved towards mid-span while keeping its distance to SS approximately constant. A change in

magnitude of the secondary velocity vectors near SS at about (-150,70), corresponding to the three dimensional suction side separation strip S_4 (Figure 4.33, pg. 99), is discernible. Secondary flows at SS above S_4 are unrealistic. They arise due to the proximity of probe head and stem to SS. Therefore, the vectors of the tangential traverse position closest to SS have to be interpreted with care.

Total Pressure Loss   Two regions of high loss exist: one away from the endwall extending from S_4 towards the mid-passage endwall and another in the SS corner. A shallow loss region exists from PS to SS between the upper double loss core and the endwall.

Slot 10

Secondary Velocities   Downstream mixing results in attenuated secondary flows apart from the former S_4-region, which has merged with accumulated shed vorticity of the same rotational sense. The passage vortex has lifted off the endwall obvious from a disjoined region of over-turning. Very low secondary flows exists at the endwall behind the blade trailing edge, probably due to shed vorticity and the SS corner vortex.

Total Pressure Loss   The passage vortex now covers two distinct loss peaks, which consist mainly of inlet boundary layer material. The upper peak is associated with S_4 and the lower with the passage vortex-centre, both with the same peak values. The endwall corner loss region is augmented and penetrates farther into the wake than into the bulk flow. The shallow PS to SS loss region with an insignificant peak inside the wake is weakened.

Vorticity   The downstream streamwise vorticity distribution consists of three major areas. The first is due to the passage vortex and S_4, showing a negative
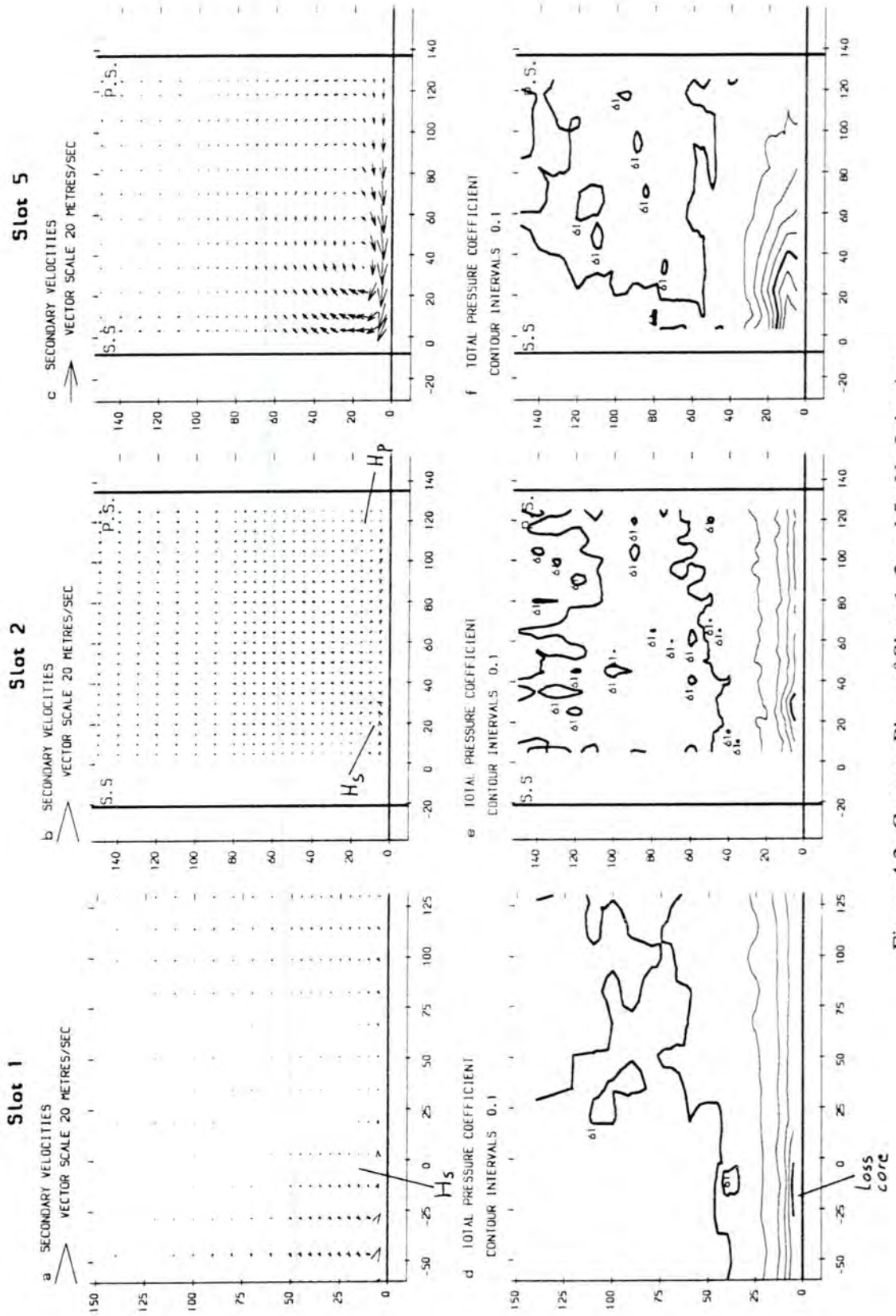
Figure 4.2: Contour Plots of Slots 1, 2 and 5 - No Injection
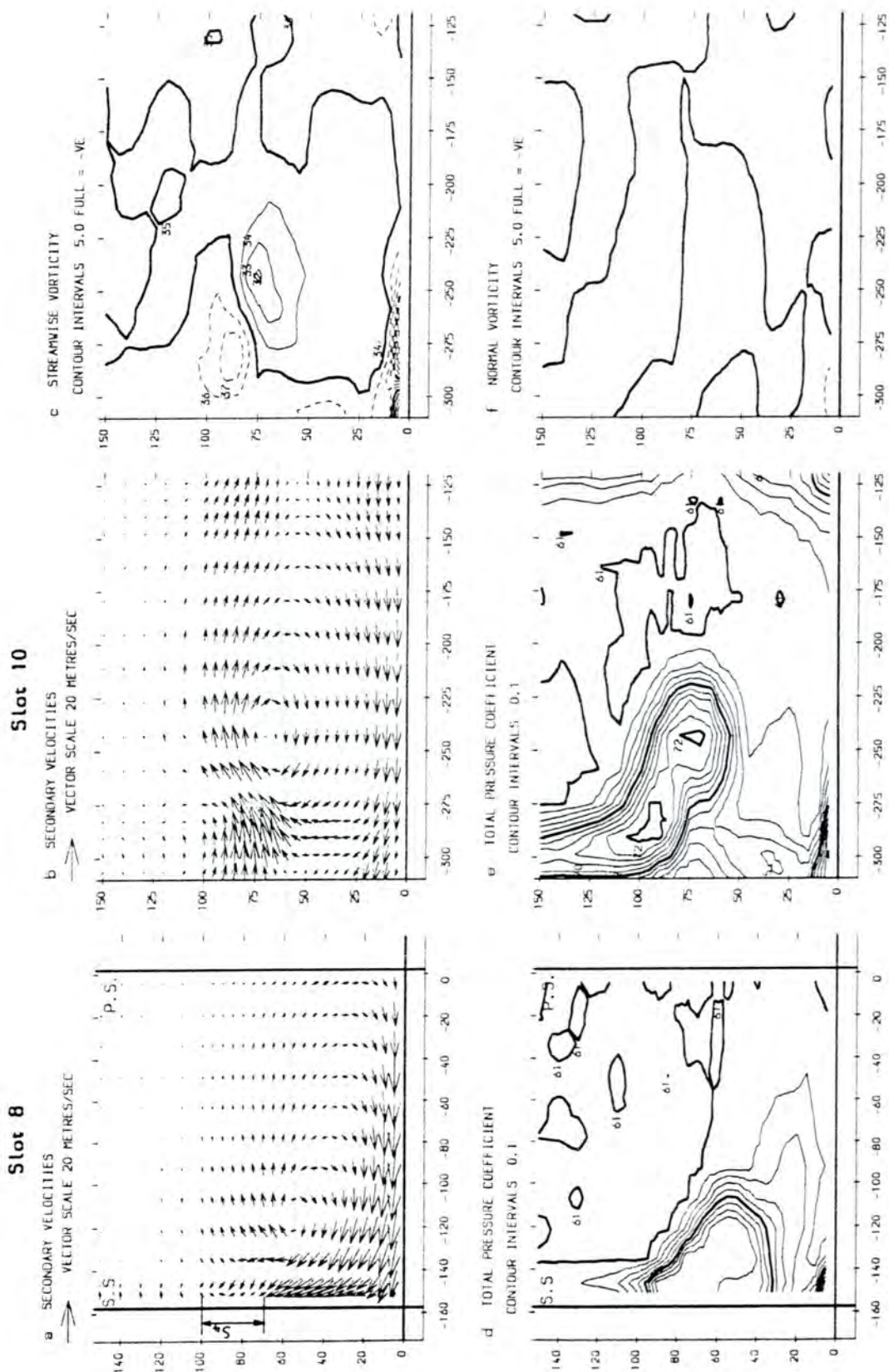
Figure 4.3: Contour Plots of Slots 8 and 10 - No Injection

and positive sense of rotation respectively. The second occurs within the wake, where up- and downward flow of the adjacent SS and PS confront, resulting in an anti-clockwise sense of rotation. The third area underneath near the endwall is difficult to interpret due to the problems with fitting natural splines to boundaries. Contour levels of the normal vorticity component are much lower as expected from classical theory[2].

4.3.2   Low Angle - 100%

Here, the tangential injection velocity corresponds to the velocity of the rotating belt in Walsh's positive skew case (Figure 5.4, pg. 119); the downstream area-averaged total pressure loss coefficient reaches its maximum (Figure 5.12, pg. 134).

Figures 4.4 and 4.5 contain plots of slots 1, 2, 5, 8 and 10.

Slot 1

Secondary Velocities   The plot is almost identical to that of no injection because of the low amount of tangential momentum provided.

Total Pressure   Thickening of the inlet boundary seen by the added contour line is due to a streamwise injection velocity below freestream (Section 4.2.4).

Slot 2

---

[2]An expression for the normal vorticity component at exit obtained by (Came & Marsh [1974]) predicts an approximate halfing of the normal vorticity present at inlet:

$$\xi_{v_e} = \xi_{v_i}\frac{\cos\alpha_e}{\cos\alpha_i} \qquad (4.2)$$

$$\simeq \frac{\xi_{v_i}}{2}$$

In comparison, the exit streamwise vorticity is about thirteen times the inlet normal vorticity (equation (4.2), pg. 44).

Secondary Velocities H_s is stronger and more compact which could be either a result of some of the jets' internal flow structure (cf. pg. 42) or due to the thickened inlet boundary layer. The core of H_p has moved to (100,20) leaving behind stronger secondary flows in the PS corner.

Total Pressure Loss   Six of the eight injection jets are recognized by induced regions of high loss, of which the near SS is largest. A local increase at this position has already been noted for no injection.

Slot 5

Secondary Velocities   Secondary flows are increased due to the thickening of the inlet boundary layer. The vortex centre has not moved discerningly.

Total Pressure Loss   The SS corner loss region is now detached and intensified.

Slot 8

Secondary Velocities   The vortex centre has migrated towards the endwall and the secondary flow field is slightly enhanced. The height of S_4 above the endwall seems to have increased slightly.

Total Pressure Loss   A double loss core is clearly visible, which extends further inside the passage combining the previously weak PS to SS gradient. The SS corner loss core is unchanged. This is mainly due to the unchanged secondary flows directly above the endwall which transport losses from the new endwall boundary layer into the SS corner.

Figure 4.4: Contour Plots of Slots 1, 2 and 5 - 100% Low Angle
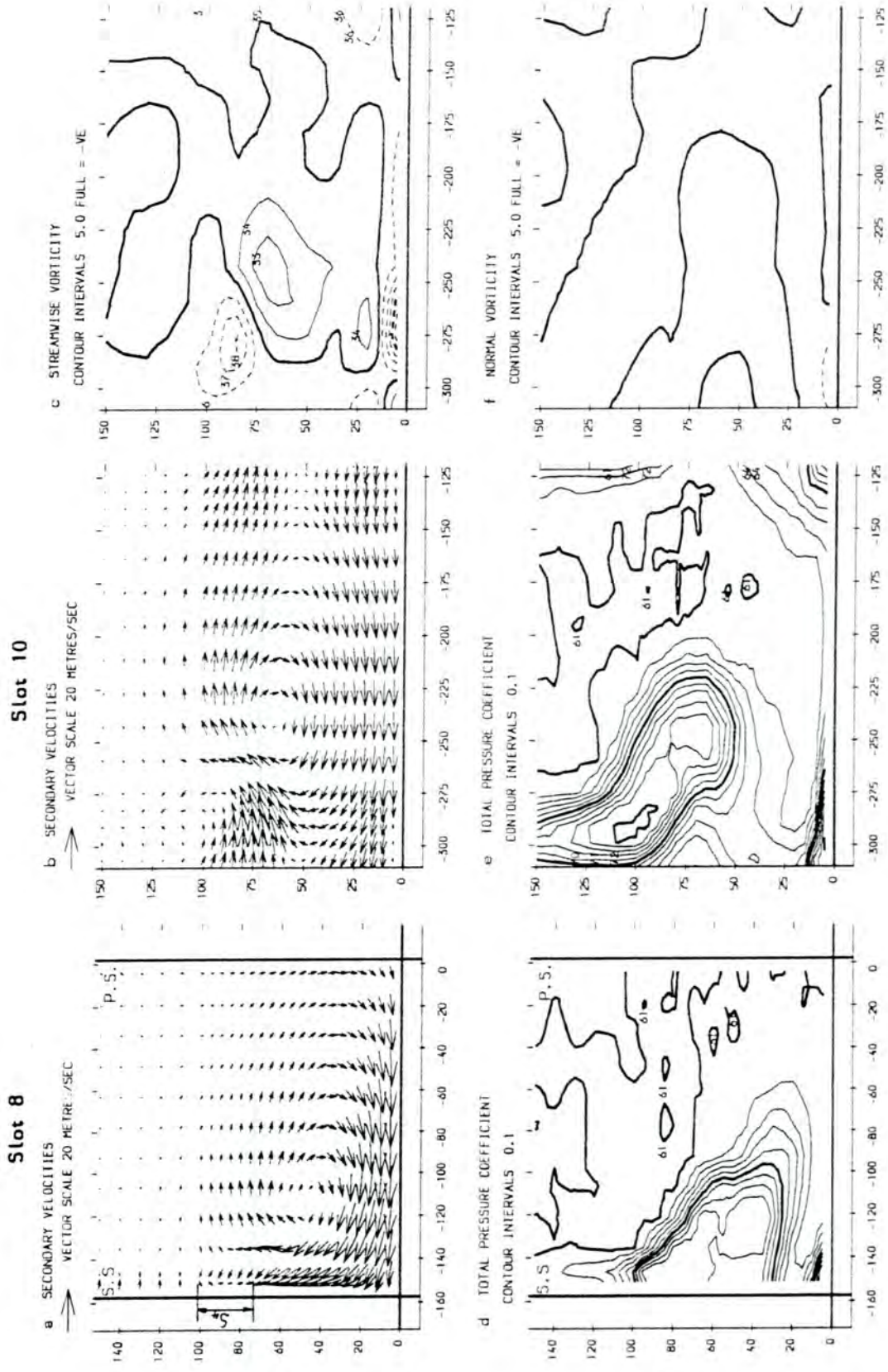
Figure 4.5: Contour Plots of Slots 8 and 10 - 100% Low Angle

Slot 10

Secondary Velocities   Downstream secondary flows are stronger. Almost constant over-turning exist below the un-moved vortex centre up to the endwall.

Total Pressure Loss   The double wake loss core has grown insignificantly at the expense of a contour line in the lower peak. The shallow PS to SS loss region is incorporated, similar to slot 8. The SS corner loss region is seen augmented.

Vorticity   The vorticity field has not changed its basic structure. Most obvious is the growth of an area of negative streamwise vorticity, which belongs to the passage vortex, towards the endwall.

4.3.3   Low Angle - 150%

The tangential momentum and kinetic energy provided at this injection rate is approximately the same as with positive skew (Figure 5.4, pg. 119). The downstream loss coefficient is still higher than without injection but reduced compared to 100% injection (Figure 5.12, pg. 134).

Figures 4.6 and 4.7 contain plots of slots 1, 2, 5, 8 and 10.

Slot 1

Secondary Velocities   The first indication of an influence on the upstream secondary flow field is seen by individually higher velocities distributed on the endwall.

Total Pressure Loss (not shown)   No significant new features are observed.

Pitch Angle[3] The effect of the injection guide vanes is visible by significant pitchwise components of six of the eight jets forming downstream of the injection slot. A zone of zero pitch angle exists around (65,5) in front of the blade nose.

The contour levels indicate the penetration height of the jets, attached to the endwall, into the mainstream. Assuming an height of about 20 mm plus a $\frac{1}{8.4}$ power law profile (average value of measurements TB - 2 to TB - 5 in Table 3.1, pg. 21) an injection to freestream velocity ratio of 0.92 is obtained compared to an actual value of about 0.69 (Table 4.1, pg. 45). The discrepancy mirrors the thickening of the inlet boundary layer at low injection rates.

Slot 2

Secondary Velocities H_s is slightly stronger, whereas H_p is hardly discernible.

Total Pressure Loss (not shown) No qualitative changes are noted; the innermost level of the jet contour lines is missing indicating lower losses.

Pitch Angle Bending and mixing of the jets is almost completed resulting in very low contour levels except in the PS corner. An erroneous reading could have been caused there by reverse flow, despite the 5H-probe not being out of its calibrated range. The peak persists for all higher injection rates at a lower level but could not be associated with any flow feature in particular.

Slot 5

Secondary Velocities The vortex centre does not reach SS, which is promoted by the positive streamwise vorticity supplied at inlet.

---

[3]The pitch angle is defined as the *spanwise* deflection of the flow.
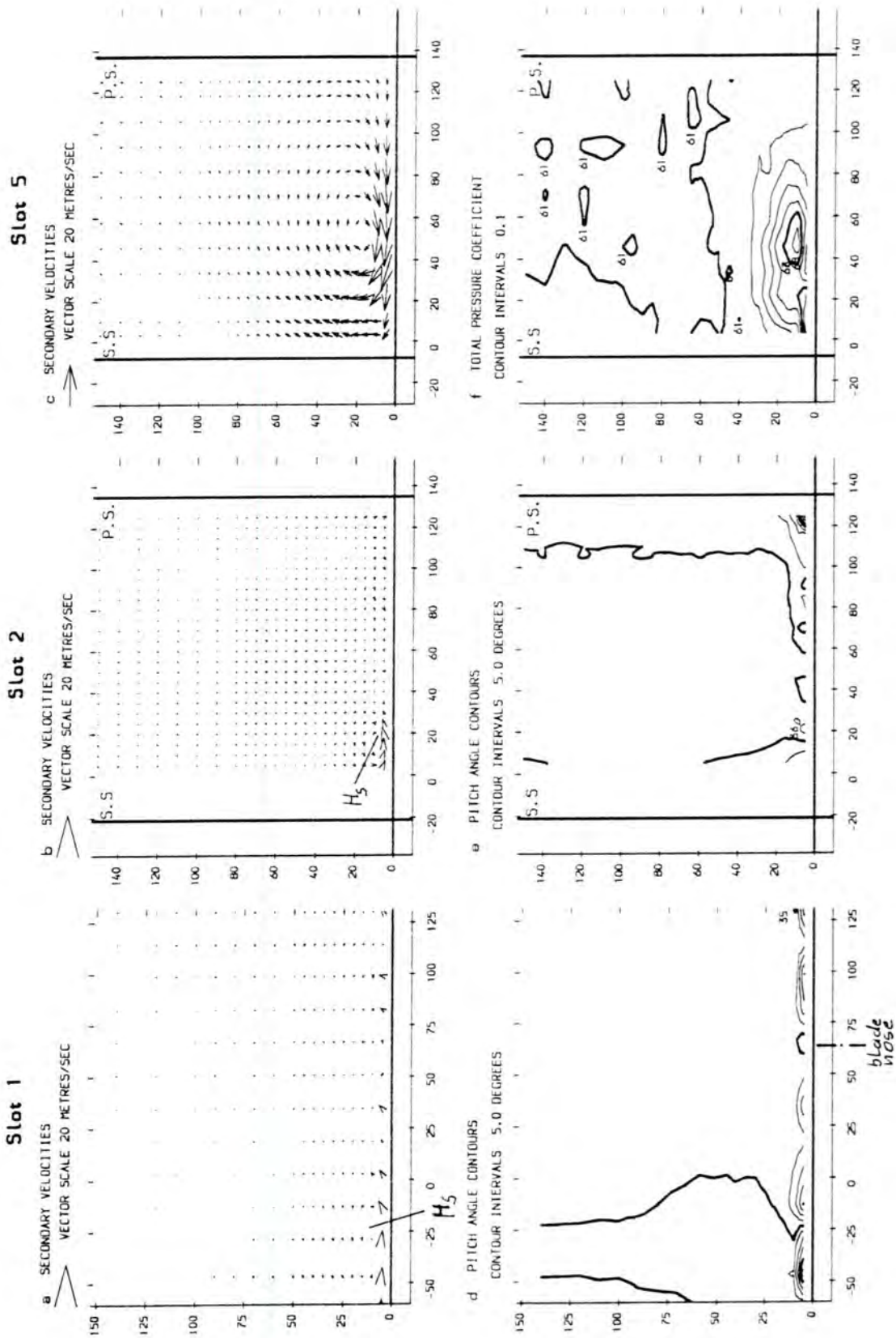
Figure 4.6: Contour Plots of Slots 1, 2 and 5 - 150% Low Angle

Total Pressure Loss   The loss core is found near mid-passage leaving behind a small region of high loss in the SS corner.

Slot 8

Secondary Velocities and Total Pressure Loss   The passage vortex is situated closer to endwall entraining both of its loss peaks. S_4 has dropped back to its height above the endwall with no injection. The SS corner loss remains unchanged.
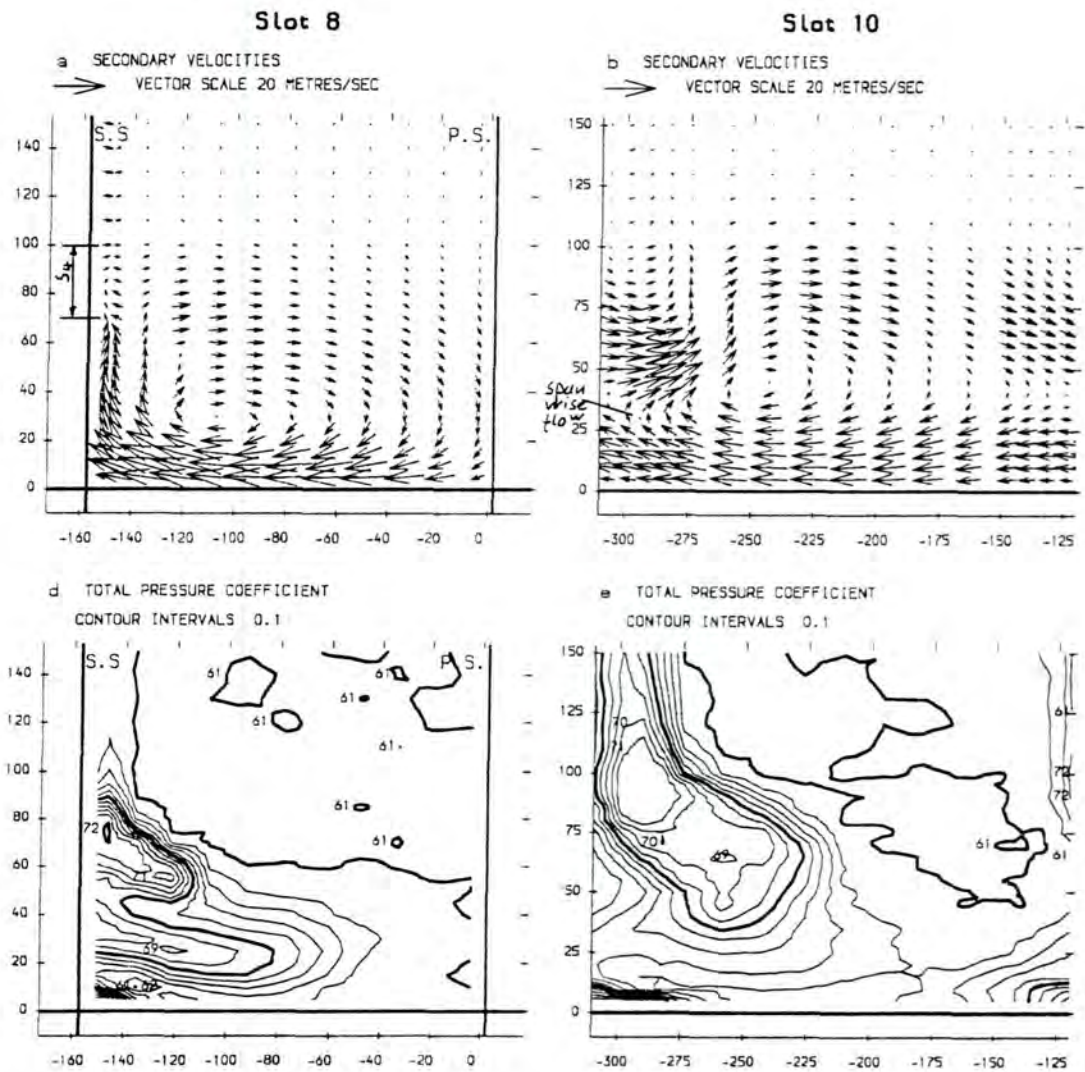
Figure 4.7: Contour Plots of Slots 8 and 10 - 150% Low Angle

Slot 10

Secondary Velocities The passage vortex has approached the endwall. A zone of substantial spanwise flow below S_4 is diminished due to sharp change from over- to under-turning.

Total Pressure Loss The lower loss peak has followed the passage vortex towards the endwall.

4.3.4 Low Angle - 200%

The area-averaged downstream total pressure loss coefficient drops for the first time below the value without injection (Figure 5.12, pg. 134).

Figures 4.8 and 4.9 contain the plots of slots 1, 2, 5, 8 and 10.

Slot 1

Secondary Velocities Increased values due to injection exist along the endwall except in front of the blade nose around (65,5) and most probably inside an injection vane wake at (25,5).

Total Pressure Loss The streamwise injection velocity component has almost reached its freestream value (Table 4.1, pg. 45) resulting in some re-energization of the inlet boundary layer. The re-energization is more obvious from pitch- and area-averaged data (Figure 4.40, pg. 107, and Figure 5.12, pg. 134).

Slot 2

Secondary Velocities and Total Pressure Loss H_s has grown laterally penetrating almost up to mid-passage. Rolling-up of individual jets is anticipated. This might be supported by their internal flow structure (cf. pg. 42) but could also be

due to the re-energization being confined to near the endwall not affecting the inlet boundary above 20 mm (see pitch-averaged curves, pg. 74).

Slot 5

Secondary Velocities The SS corner is dominated by the action of H_s. The passage vortex is forced closer to PS than noted previously.
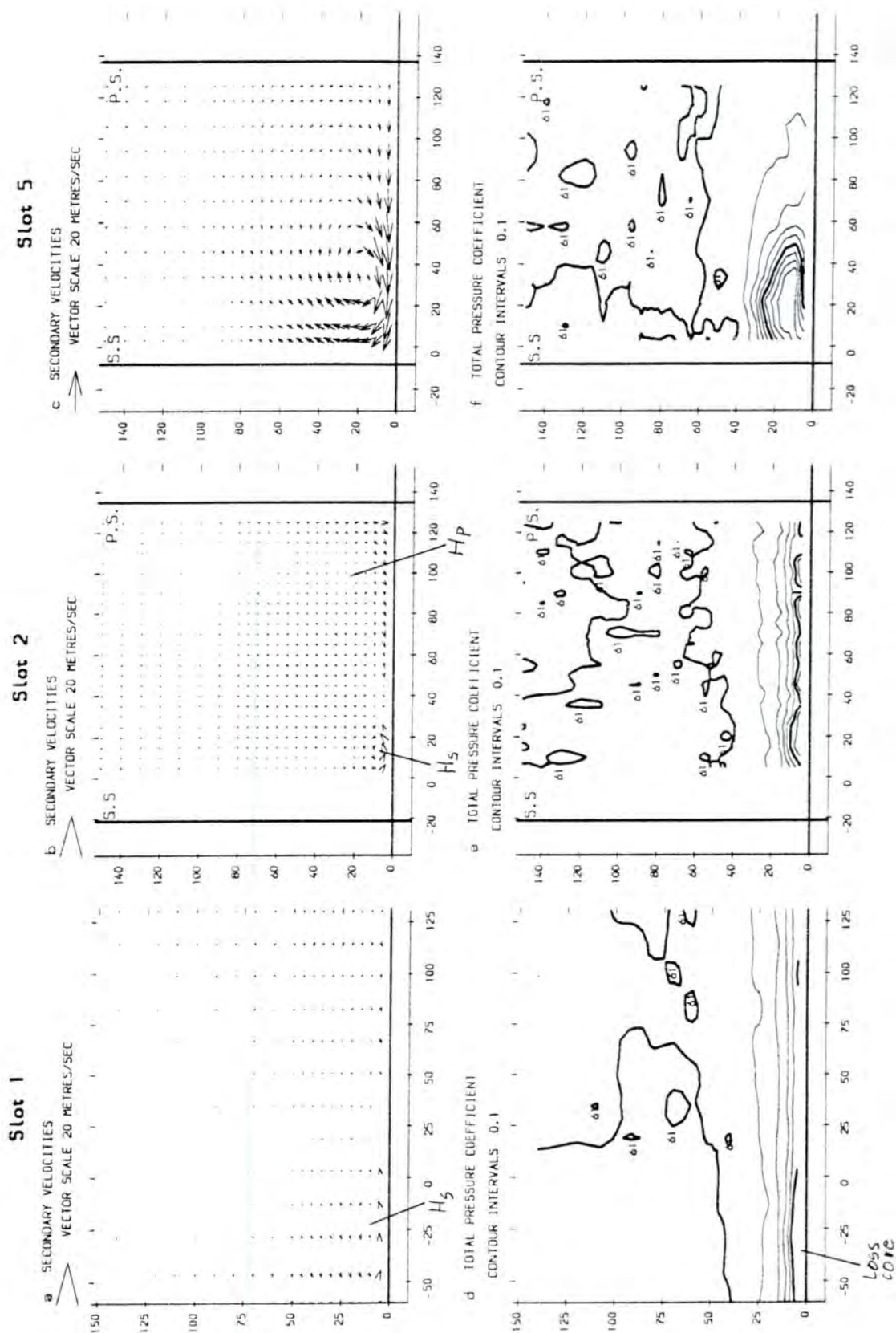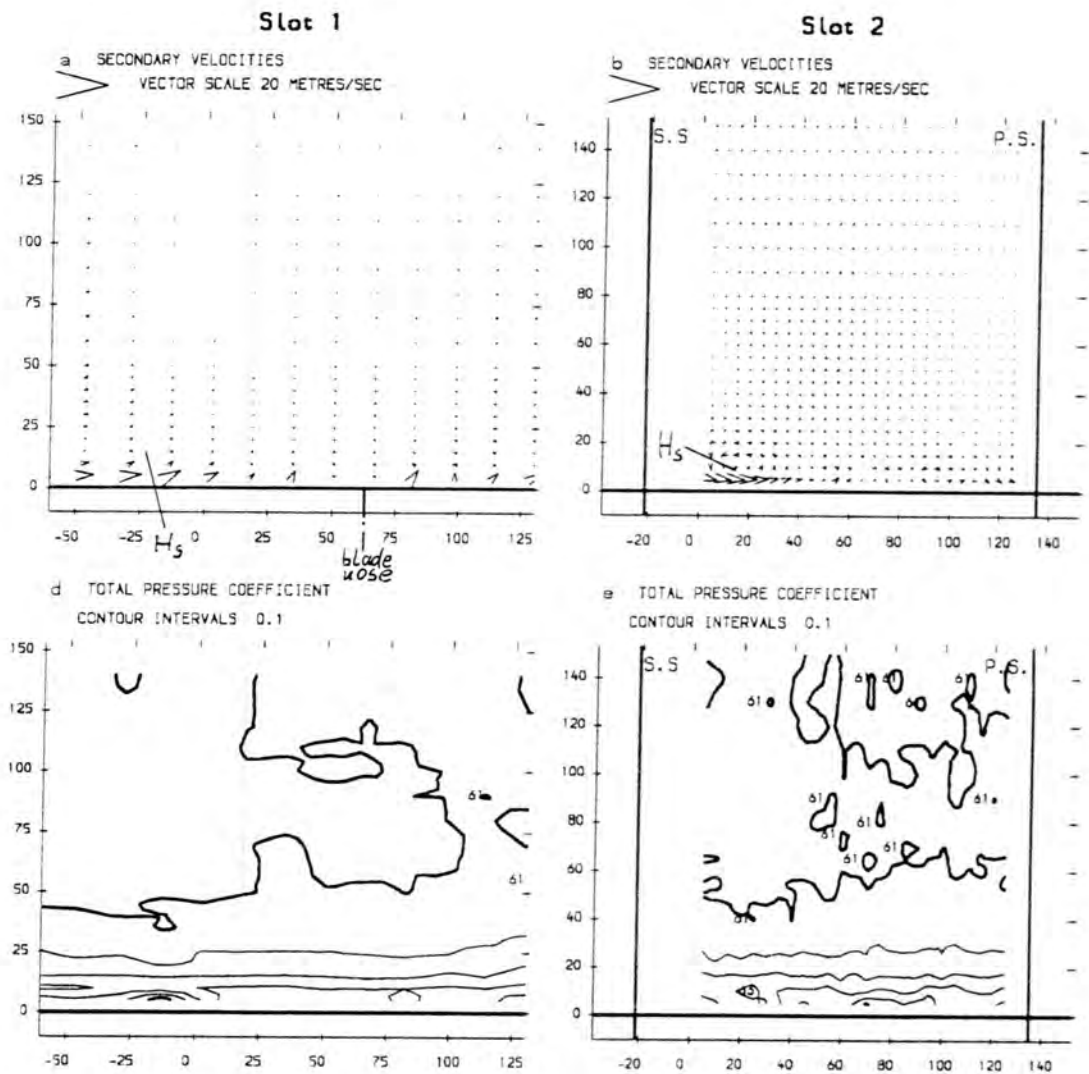

Figure 4.8: Contour Plots of Slots 1 and 2 - 200% Low Angle
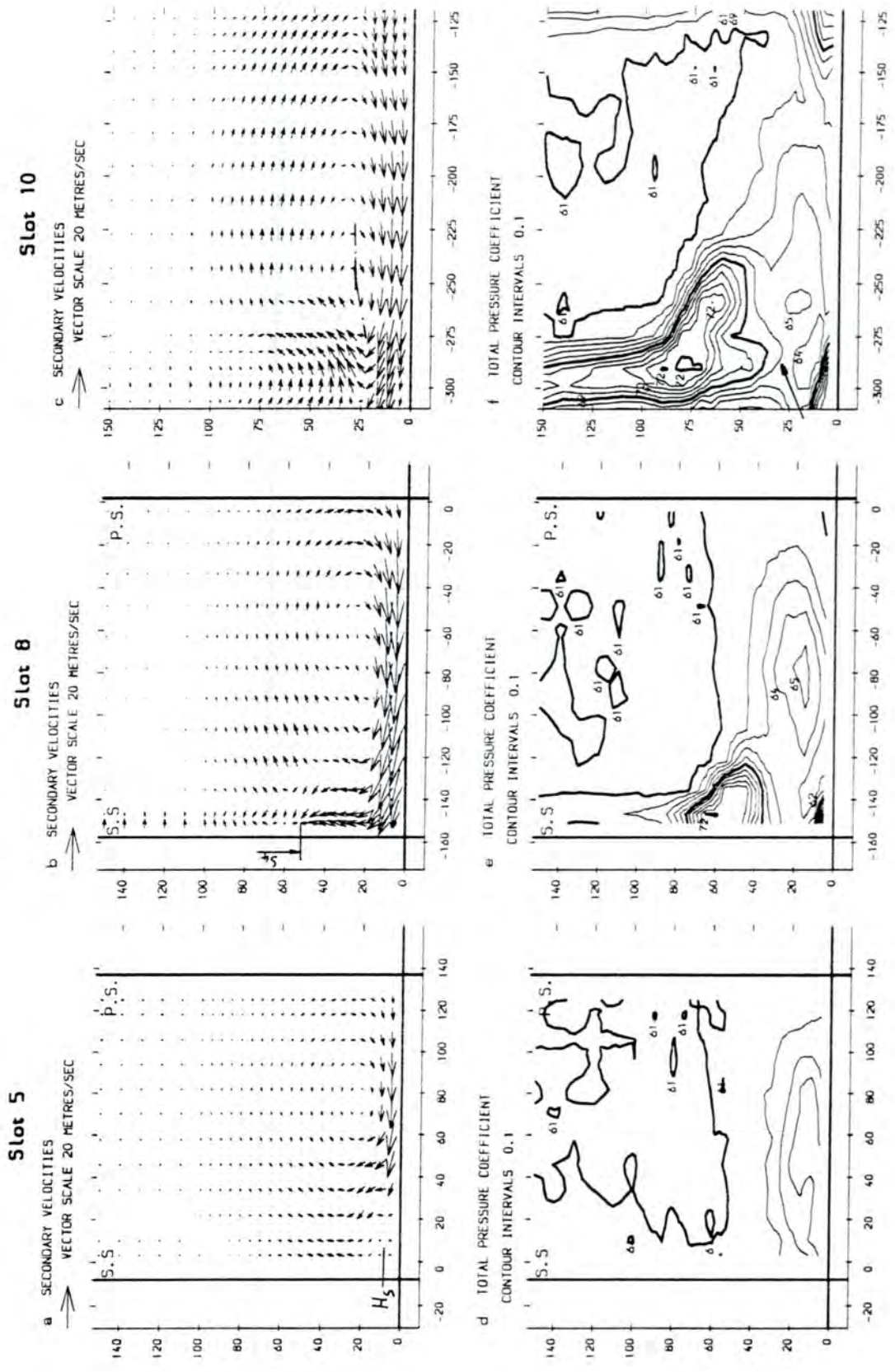
Figure 4.9: Contour Plots of Slots 5, 8 and 10 - 200% Low Angle

Total Pressure Loss   The loss core at mid-pitch is not increased compared to slot 2 manifesting the re-energization and tangential momentum supplied to the main-flow.

Slot 8

Secondary Velocities   The passage vortex lies closer to the endwall with its centre nearer to PS than SS. The location of decay of high SS velocities indicating S_4 has fallen significantly below its original value.

Total Pressure Loss   The lower of the loss peaks has developed into an isolated core at mid-passage close to the centre of the passage vortex. The upper peak has approached the endwall while preserving its peak value. The extent of the SS corner loss region is slightly reduced.

Slot 10

Secondary Velocities   As with slots 5 and 8, the passage vortex is flatter and closer to the endwall. The axis of the vortex core at SS is inclined towards the endwall unlike within the passage.

Total Pressure Loss   The single SS loss core of slot 8 has developed into a double peak, which is supported by the movement of the passage vortex away from the endwall. New is a distinct corner core forming within the blade wake area towards the endwall. The slot 8 mid-pitch loss core has left behind two weak loss regions at (-260,20) and (-280,15).

4.3.5   Low Angle - 250%

Figures 4.10 and 4.11 are compiled of measurements at slots 1, 2, 5, 8 and 10.

Slot 1

Secondary Velocities An influence of the injection is noticeable up to 10 mm span.

Total Pressure Loss An injection velocity greater than unity (Table 4.1, pg. 45) leads to a significant re-energization of the inlet boundary layer close to the endwall indicated by dashed lines. Zero contour lines[4] exist next to the area influenced by the blade nose, where almost no re-energization takes place.

Slot 2

Secondary Velocities The endwall is dominated by the injected flow directed towards PS. H_s and the other rolled-up jets are strengthened and have grown in size.

Total Pressure Loss Mixing on the endwall resulted in a more uniform loss pattern with a significant peak of re-energization at the same location where high loss was generated with no injection.

Slot 5

Secondary Velocities Flow vectors around H_s are clearly visible up to mid-passage. The passage vortex centre is very near to PS supporting over-turning from the endwall to the top of H_s where it ceases.

Total Pressure Loss Further mixing results in an almost uniform loss distribution up to about 30 mm span, which is still below the inlet boundary layer physical thickness of about 40 mm.

---

[4]The data file has to be inspected here, since the level numbering is not complete.
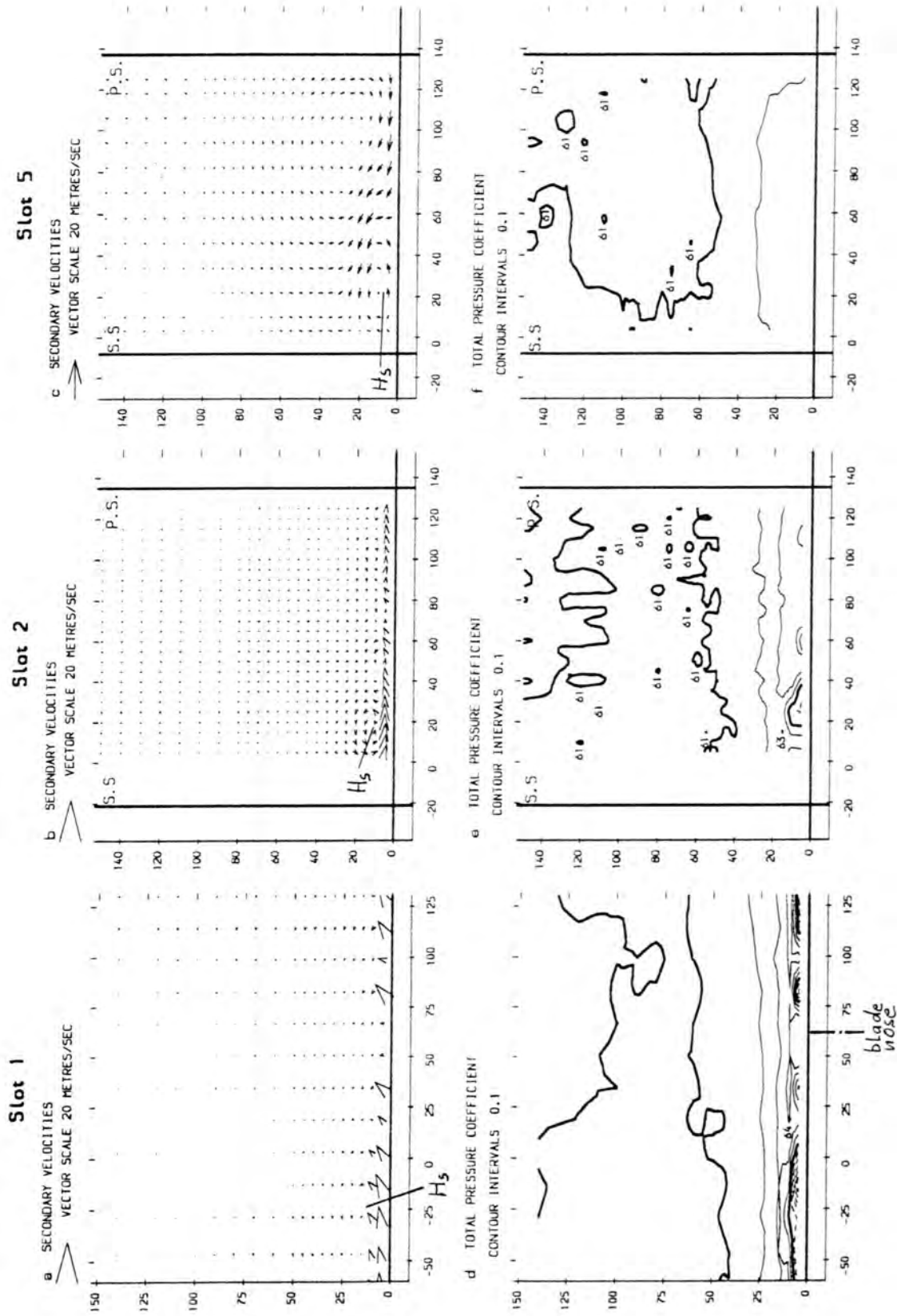
Figure 4.10: Contour Plots of Slots 1, 2 and 5 - 250% Low Angle

Slot 8

Secondary Velocities H_s influences the flow in the near endwall SS half of the passage and over-turning exists all along the endwall. The core of the passage vortex is positioned close to PS and near the endwall at around (-35,20), although significant action over the entire blade passage is seen above 20 mm. There is no indication of S_4 at SS (cf. flow visualization Figure 4.35, pg. 101).
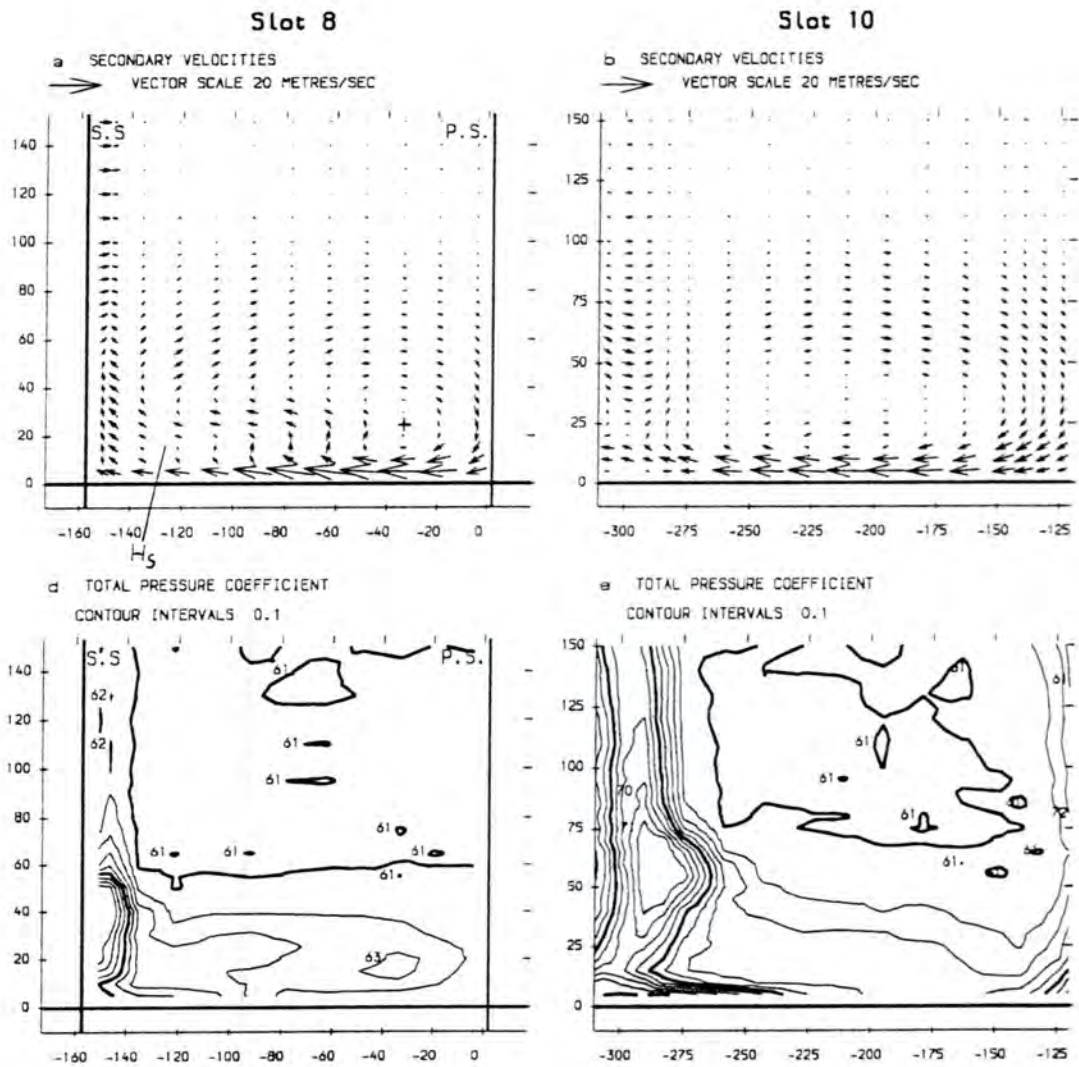
Figure 4.11: Contour Plots of Slots 8 and 10 - 250% Low Angle

Total Pressure Loss A loss core disconnected from the SS corner loss core, not measured fully by the 5H-probe, forms at SS . A third although weak core is associated with the passage vortex centre.

Slot 10

Secondary Velocities Secondary flows are very weak apart from significant over-turning at the endwall of which the blade wake region is excluded. The vortex centre is not clearly distinguishable.

Total Pressure Loss The blade wake loss core, the corner loss core, now penetrating almost up to mid-pitch, and a shallow loss gradient, inside the blade passage and inclined towards the endwall, construct the loss distribution pattern at the exit plane.

4.3.6 Low Angle - 300%

The flow patterns of slots 1 and 2 show increased levels of re-energization and are qualitatively similar to 250% injection but not included here.

Results of slots 5, 8 and 10 are shown in Figure 4.12.

Slot 5

Secondary Velocities The counter-rotating H_s dominates the near endwall flow-field. Over-turning on top of it is only supported by H_s but originates in the higher re-energization of the inlet boundary layer near the endwall. A very weak passage vortex is almost discernible at PS.

Total Pressure Loss A zone of re-energization exists directly at the endwall in the lower part of H_s. The loss contour above about 30 mm span remains
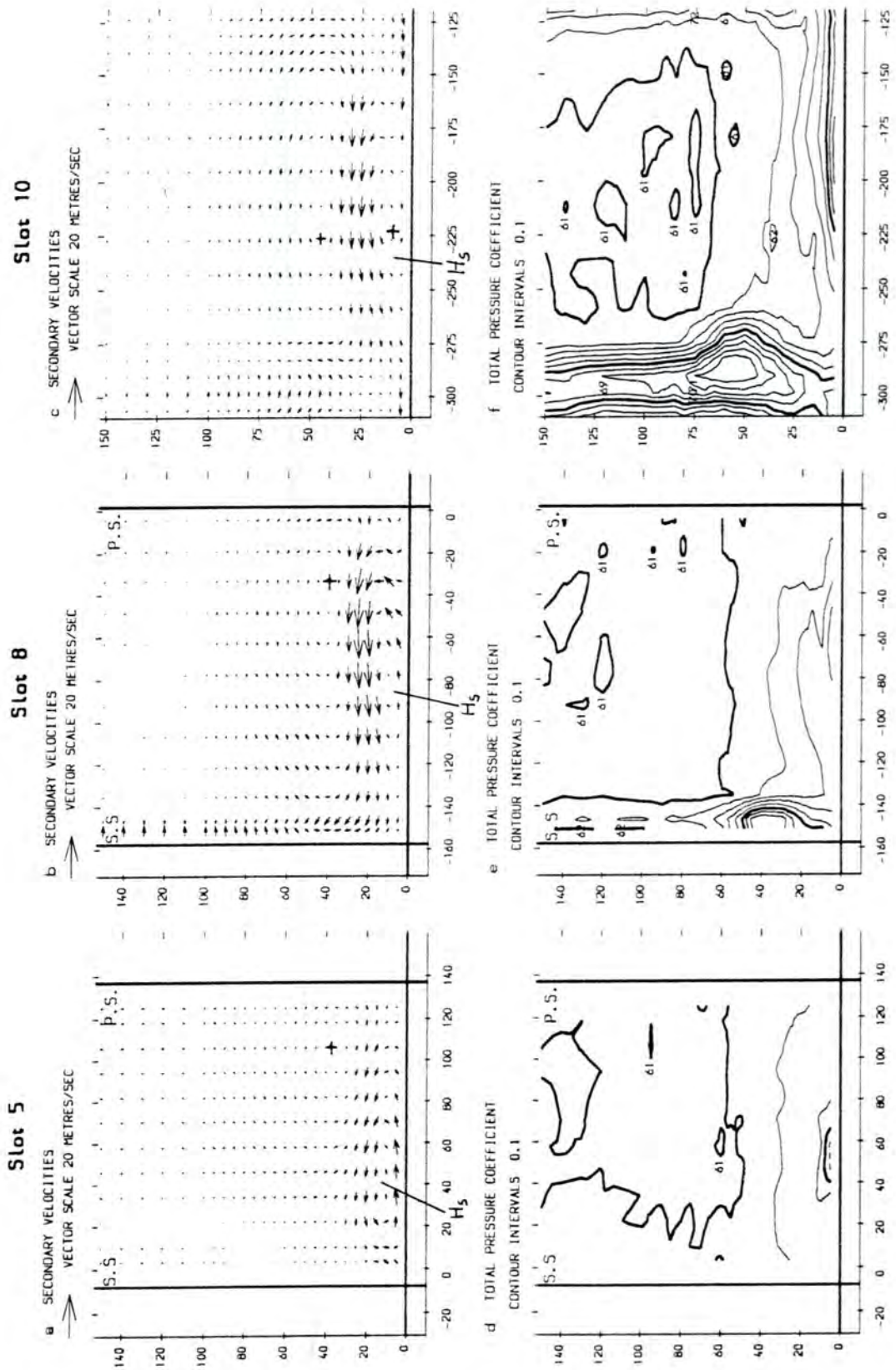
Figure 4.12: Contour Plots of Slots 5, 8 and 10 - 300% Low Angle

unchanged.

Slot 8

Secondary Velocities H_s has moved towards PS causing some under-turning on the endwall, which is in contrast to significant over-turning there with 250%. The over-turning on top of H_s, already seen at slot 5, is enhanced. The passage vortex still remains very weak.

Total Pressure Loss   The SS loss core is positioned as with 250%, despite the different flowfield, but smaller in size. A shallow loss gradient towards the endwall covers most of the passage area.

Slot 10

Secondary Velocities   The removal of high near endwall over-turning but significant amounts away from the endwall yields a flow structure similar to slot 8. H_s and the passage vortex are both centred near mid-pitch.

Total Pressure Losses   A different endwall flow caused the built-up of a loss region with boundary layer character from midpitch towards PS. A SS corner loss region does not exist. The wake loss core has shrunk somewhat compared to 250%.

4.3.7   Low Angle - 350% to 450%

Higher injection rates show the passage vortex rotating in the opposite sense. Results have not been included in this document because the objective of the present work is to remove secondary flows but not to generate new additional ones.

4.3.8 High Angle

Slot 10 results (Figure 4.13) are discussed in the following at injection rates ranging from 150% to 250% and may be compared to those at the low angle (Figure 4.7, pg. 57, Figure 4.9, pg. 60, and Figure 4.11, pg. 64). The high and low angle are related over the same tangential injection velocity but different values for the tangential momentum and kinetic energy (Figure 5.4, pg. 119, and Figure 5.3, pg. 117). Downstream gains are achieved from 150% injection onward (Figure 5.11, pg. 134). The data was obtained with the radius curvature on the injection slot; a comparison to the sharp edge is the objective of Section 4.5.1. Other high angle data is not available due to blockage of the 5H-probe (Section 4.1.1).

The plots span more than one blade wake to facilitate the description of shed vortices, which reduces the size of the vector arrows slightly.

150%

Secondary Velocities The passage vortex is forced closer to the endwall than with the low angle at the same injection rate.

Total Pressure Loss This loss distribution is somewhat similar to 200% injection at the low angle.

200%

Secondary Velocities The flowfield resembles 250% injection at the low angle. The centres of H_s and the passage vortex cannot be identified clearly.

Total Pressure Loss A slightly reduced wake loss and a more compact SS corner loss region characterises the loss field compared to 250% low angle.
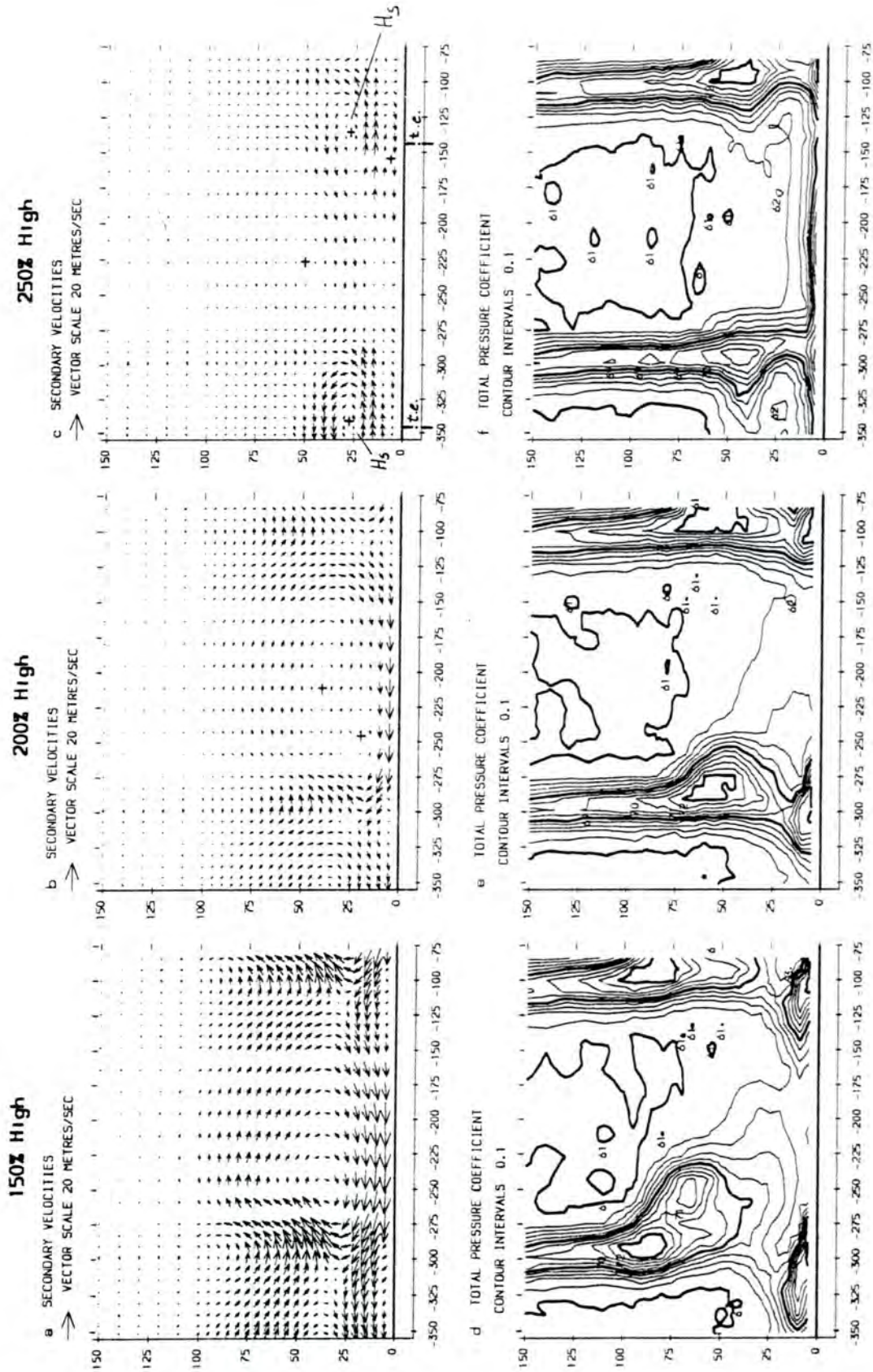
Figure 4.13: Contour Plots of Slot 10 - 150%, 200%, 250% High Angle

250%

Secondary Velocities   Some similarities exists to 300% at the low angle. The centre of H_s lies close to PS above a small vortex at the endwall and below a zone of over-turning influenced by the passage vortex, which is approximately situated at mid-pitch.

Endwall flow visualization (Figure 4.14) directly behind the blade trailing edge

Figure 4.14: Trailing-Edge/Endwall Shed Vortex

shows the action of H_s on the endwall. It lifts off by slot 10 after possibly merging with trailing vorticity of the same rotation.

Total Pressure Loss   The wake loss core forms a corner towards SS, not existing with 300% injection at the low angle and probably caused by the shed vortex. The endwall is covered almost uniformly by the loss profile of a new boundary layer.

4.4   Pitch-Averaged Curves

It is useful to inspect the corresponding area plots of Section 4.3 together with the material discussed here.

4.4.1 Vortex Structure

A Rankine vortex consists of a core with the linear velocity distribution of a rotating solid body and an outer zone with the inverse proportional velocity distribution of a potential vortex. Such an idealized model is helpful in identifying realistic vortices as they are generated by secondary flows. Peak values of the secondary kinetic energy coefficient, for example, can be expected near the outer edge of the vortex core.

4.4.2 Slot 1 - Low Angle

Pitch-averaged curves of slot 1 are cross-plotted in Figure 4.15 for three different injection rates.

Yaw Angle

At zero injection, the flow around the blade nose is responsible for the slight increase near the endwall. As the injection is increased, the incidence becomes significantly positive. A positive incidence angle all along the blade span would result in increased secondary flows. In the present case, the positive incidence at the root helps to prevent the secondary flows by counteracting the generation of secondary vorticity.

The slight increase in yaw seen towards mid-span is within the specified accuracy of angle measurements and probably due to a probe alignment error.

Total Pressure Loss Coefficient

As the injection is increased to 100%, thickening of the inlet boundary is observed. Re-energization at high injection rates only takes place up to about 15 mm span. Above this height, the inlet boundary layer remains virtually unchanged, which is

```
◇ 300% = 0.113 Jet Kinetic Energy Coefficient
⊠ 250% = 0.065 Jet Kinetic Energy Coefficient
✳ 100% = 0.004 Jet Kinetic Energy Coefficient
⊞   0% = 0.000 Jet Kinetic Energy Coefficient
```

a) Yaw Angle (Degrees)

b) Total Pressure Loss Coefficient

c) Secondary Kinetic Energy Coefficient

Spanwise Distance From Endwall (mm)
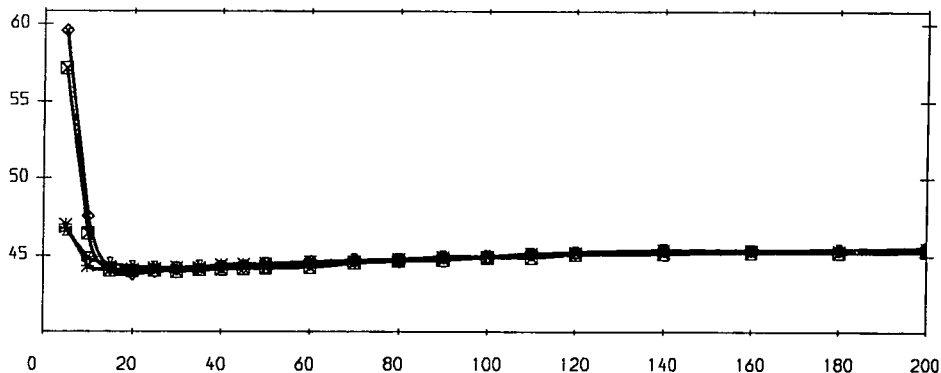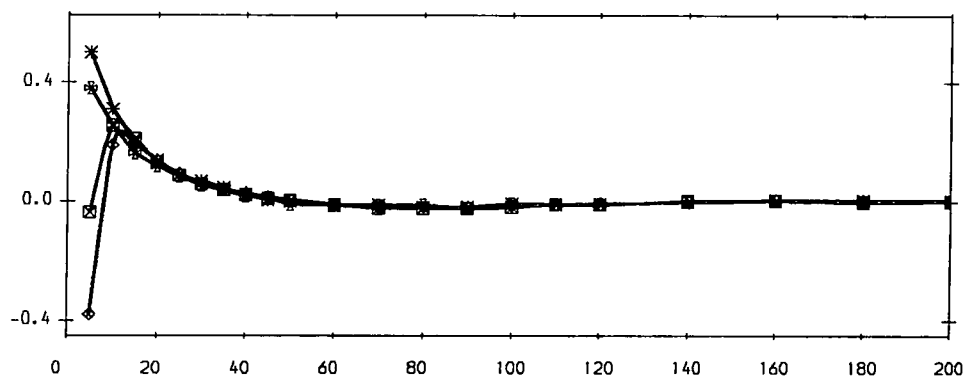
Figure 4.15: Pitch-Averaged Curves at Slot 1 - Low Angle

related the over-turning on top of H_s detectable further downstream (Figure 4.10, pg. 63, and Figure 4.12, pg. 66).

Secondary Kinetic Energy Coefficient

The secondary kinetic energy coefficient at the near wall measurement position increases corresponding to the yaw angle.

4.4.3 Slot 2 - Low Angle

Figure 4.16 contains the pitch-averaged curves of slot 2.

Yaw Angle

As with slot 1, low under-turning near the endwall is observed without injection and with 100%. Higher injection rates show a vortex sheet character (cf. pg. 58). Over-turning reaches its maximum at about 20 mm of span.

Total Pressure Loss Coefficient

The curves are similar in shape to slot 1 showing overall increased losses near the endwall. Mixing of the injected high momentum fluid results in a wider zone of lower re-energization.

Secondary Kinetic Energy Coefficient

An overall lower level may be expected at the endwall as well as increased values near the outer boundary of the injected endwall vortex sheet.

4.4.4 Slot 5 - Low Angle

Plots of pitch-averaged curves at slot 5 are shown in Figure 4.17.

◇ 300% = 0.113 Jet Kinetic Energy Coefficient
⊠ 250% = 0.065 Jet Kinetic Energy Coefficient
✳ 100% = 0.004 Jet Kinetic Energy Coefficient
⊞ 0% = 0.000 Jet Kinetic Energy Coefficient

a) Yaw Angle (Degrees)

b) Total Pressure Loss Coefficient

c) Secondary Kinetic Energy Coefficient

Spanwise Distance From Endwall (mm)
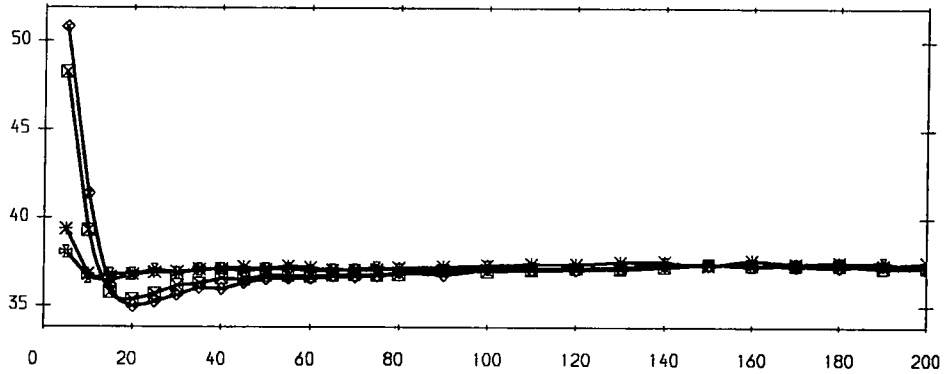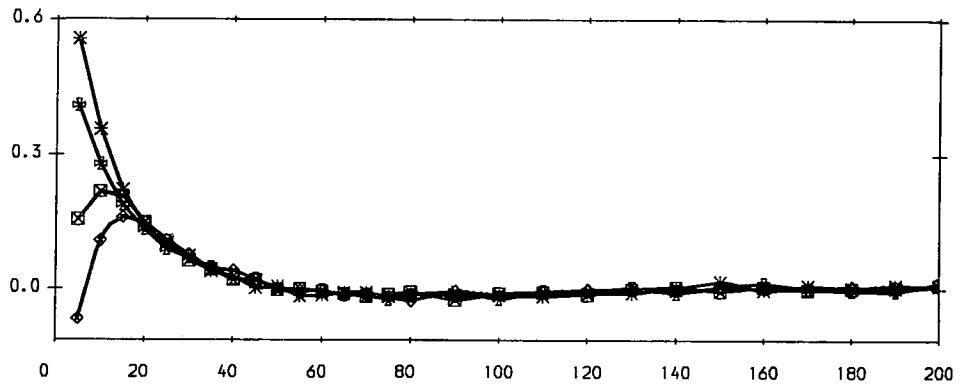
Figure 4.16: Pitch-Averaged Curves at Slot 2 - Low Angle

◈ 300% = 0.113 Jet Kinetic Energy Coefficient
⊠ 250% = 0.065 Jet Kinetic Energy Coefficient
✻ 100% = 0.004 Jet Kinetic Energy Coefficient
⊞ 0% = 0.000 Jet Kinetic Energy Coefficient

a) Yaw Angle (Degrees)

b) Total Pressure Loss Coefficient

c) Secondary Kinetic Energy Coefficient

Spanwise Distance From Endwall (mm)
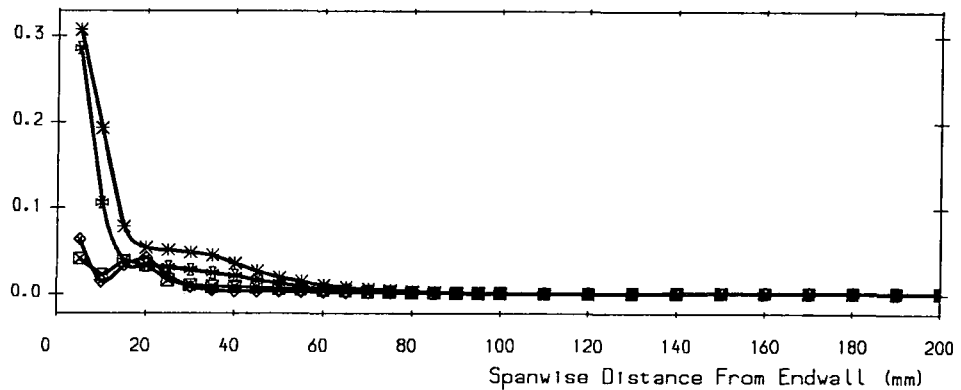
Figure 4.17: Pitch-Averaged Curves at Slot 5 - Low Angle

Yaw Angle

Substantial over-turning near the endwall and weak under-turning above 20 mm span fading towards mid-span exists without and with 100% injection. The two higher injection rates exhibit a reverse behaviour, similar to slot 2, with an overall reduced angle deviation.

Total Pressure Loss Coefficient

Peak loss values may be expected without or with low injection near the centre-line of the already developed passage vortex due to the flow changing direction. Further mixing has reduced the loss peaks compared to slot 2 with the high injection rates.

Secondary Kinetic Energy Coefficient

Substantial over-turning at the endwall causes high values at low injection rates. Increased values with high injection rates is due to a region of overturning away from the endwall between 15 mm and 20 mm span. In general, the high injection rates show a reduced spanwise disturbance of the flow.

4.4.5   Slot 8 - Low Angle

Slot 8 pitch-averaged curves are presented in Figure 4.18.

Yaw Angle

The deflection without and with 100% injection is characteristic of an undisturbed passage vortex. The action of a strengthened H_s at 250% is apparent. No over-turning with 300% injection at the closest near wall measurement position is the result of a strengthened H_s covering almost all of the endwall.

300% = 0.113 Jet Kinetic Energy Coefficient
250% = 0.065 Jet Kinetic Energy Coefficient
100% = 0.004 Jet Kinetic Energy Coefficient
0% = 0.000 Jet Kinetic Energy Coefficient

a) Yaw Angle (Degrees)

b) Total Pressure Loss Coefficient

c) Secondary Kinetic Energy Coefficient

Spanwise Distance From Endwall (mm)
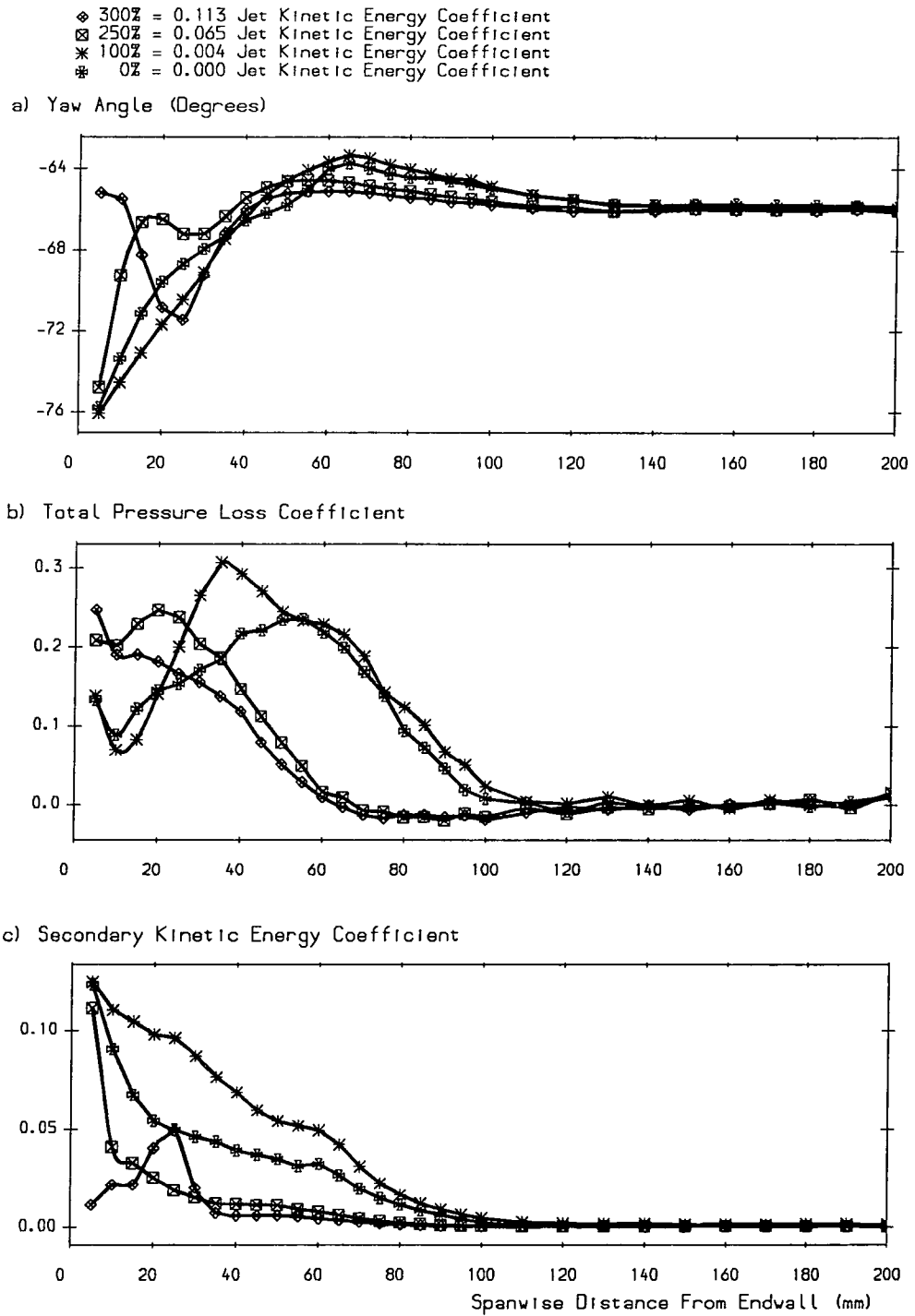
Figure 4.18: Pitch-Averaged Curves at Slot 8 - Low Angle

Total Pressure Loss Coefficient

The curve for zero injection shows an up-turn at the endwall, probably due to the SS corner loss region, and a loss peak at about 55 mm span within the double loss core region known from area plots. With 100% injection, the loss peak has fallen to the lower edge of the double loss core at 35 mm span. There is no SS corner loss region with 250% and the loss peak at 10 mm span is due to a small loss core of the near PS passage vortex (see area plots). A peak value at the endwall with 300% is caused by an endwall loss region in the PS half of the passage.

Secondary Kinetic Energy Coefficient

The steady decrease from the endwall towards midspan is related to the stronger over-turning of the flow inducing the weaker under-turning. The peak at 300% injection is related to a region of over-turning away from the endwall between 15 mm and 30 mm span.

4.4.6   Slot 10 - Low Angle

Figure 4.19 consists of pitch-averaged curves of slot 10 at the low injection angle.

Yaw Angle

Over-turning at the endwall is diminished by the SS corner vortex with low injection rates. A steady increase towards its peak characterizes the 100% injection curve in contrast to a dip with zero injection caused by a passage vortex detached from the endwall. The higher injection rates exhibit an under- and over-turning behaviour similar to slot 8 although reduced. The maximum exit-angle deviation at the highest injection rate of 300% amounts to $\pm 2°$.

◇ 300% = 0.113 Jet Kinetic Energy Coefficient
⊠ 250% = 0.065 Jet Kinetic Energy Coefficient
✳ 100% = 0.004 Jet Kinetic Energy Coefficient
❋ 0% = 0.000 Jet Kinetic Energy Coefficient

a) Yaw Angle (Degrees)

b) Total Pressure Loss Coefficient

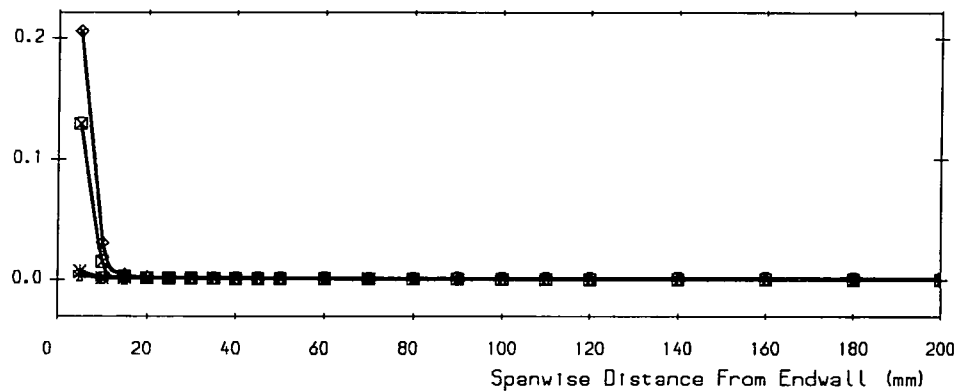c) Secondary Kinetic Energy Coefficient

Spanwise Distance From Endwall (mm)
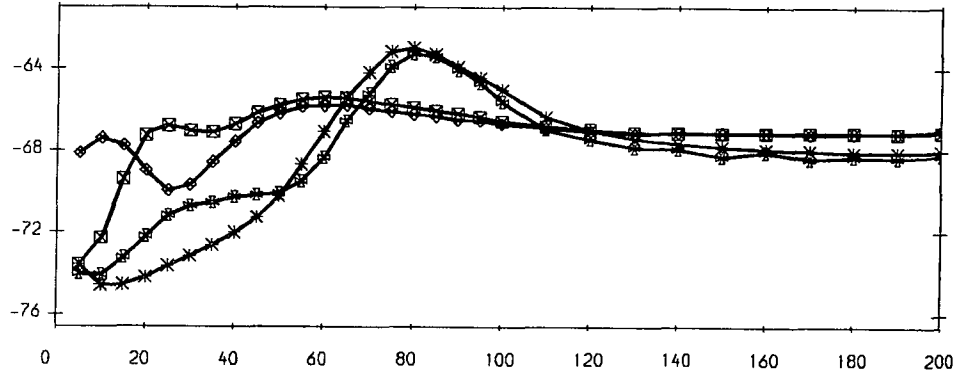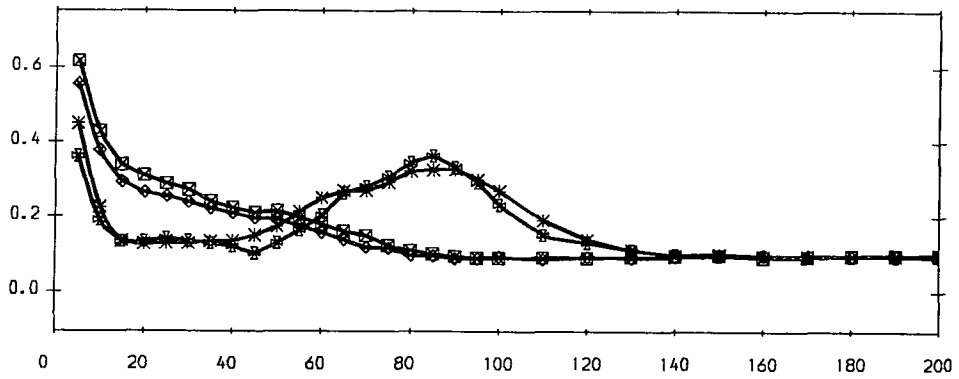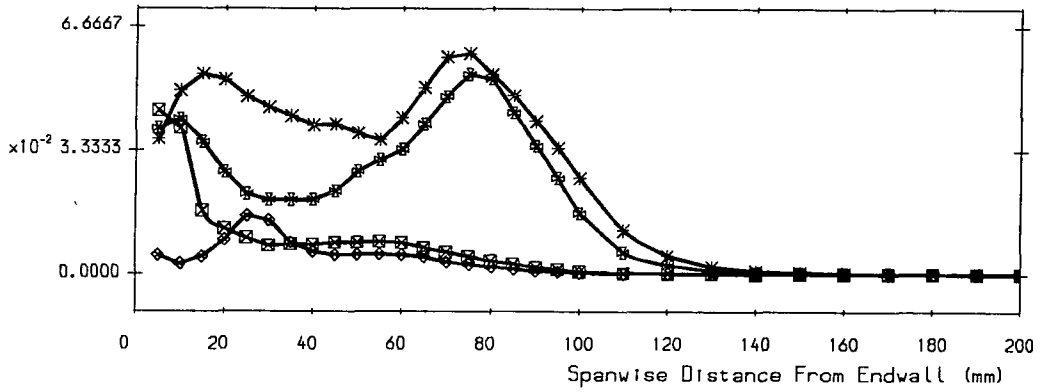
Figure 4.19: Pitch-Averaged Curves at Slot 10 - Low Angle

PITCH-AVERAGED CURVES 4.4

A discrepancy in the midspan exit angle suggests a moderate influence of the blowing on the midspan flow. This could be due to the non-symmetrical injection and requires further investigation. The effect could be neglected in the light of other experimental uncertainties.

Total Pressure Loss Coefficient

The high endwall losses may be attributed to the SS corner loss excluding the 300% injection rate, at which a loss region similar to a boundary layer develops from the trailing edge to downstream (Figure 4.12, pg. 66). At the high injection rates, the loss falls continuously whereas low injection leads to two loss peaks characterizing the upper and lower half of a double loss core. The lower loss peak is hinted at by a dip at about 75 mm span.

Secondary Kinetic Energy Coefficient

Zero and 100% injection show two maxima corresponding to the upper and lower half of the passage vortex. Under-turning leads to higher coefficient values as a result of higher velocities unlike with the blade passage. A continuous decrease is seen with 250% injection. The peak at 300% is again linked to the over-turning strip. A zero value is noted at the endwall.

4.4.7   Slot 10 - High Angle

Curves at the high injection angle are presented in Figure 4.20. The following discussion is confined to the most interesting injection rate of 250%.

◇ 250% = 0.195 Jet Kinetic Energy Coefficient
⊠ 200% = 0.100 Jet Kinetic Energy Coefficient
✳ 150% = 0.042 Jet Kinetic Energy Coefficient
✤   0% = 0.000 Jet Kinetic Energy Coefficient
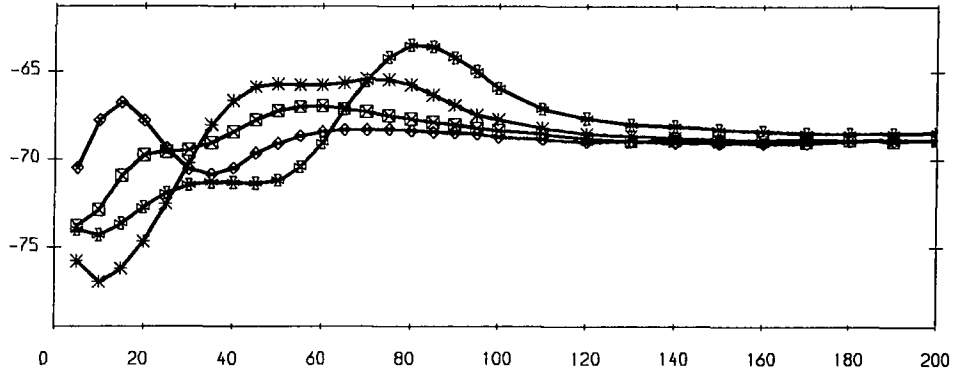
a) Yaw Angle (Degrees)

b) Total Pressure Loss Coefficient

c) Secondary Kinetic Energy Coefficient

Spanwise Distance From Endwall (mm)
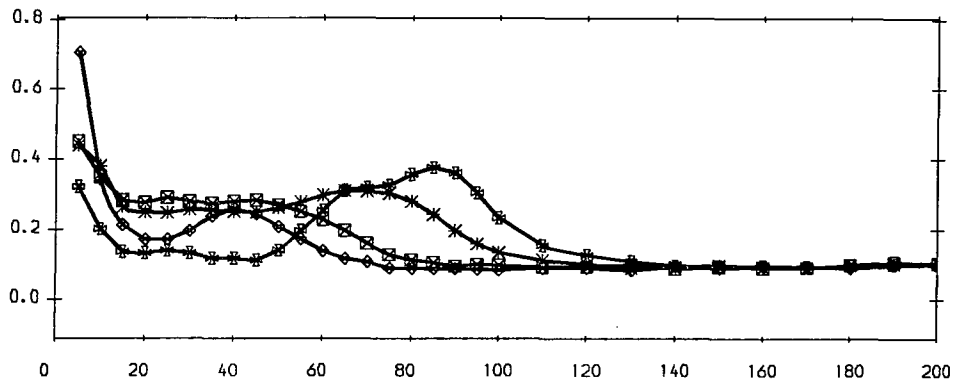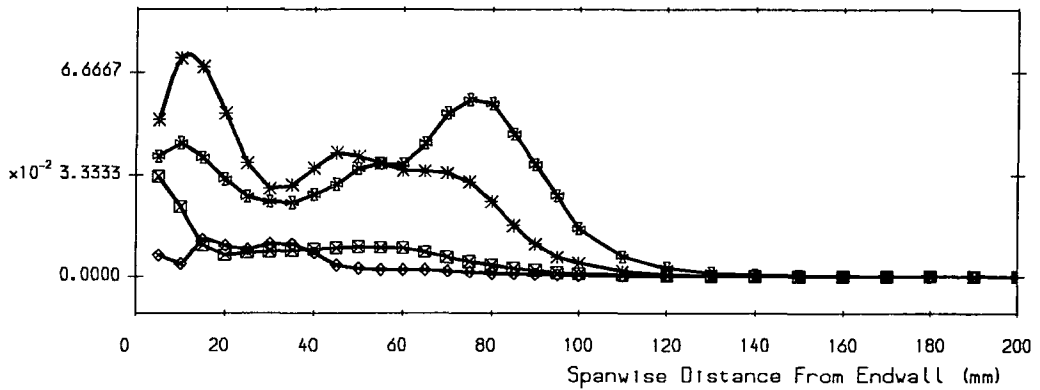
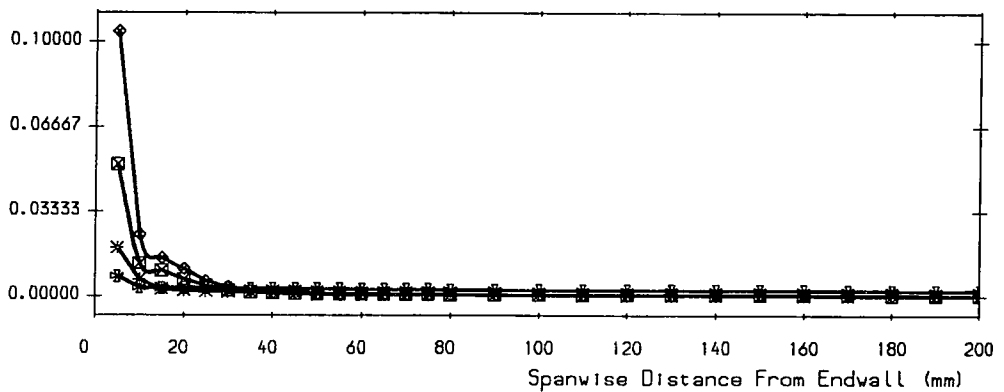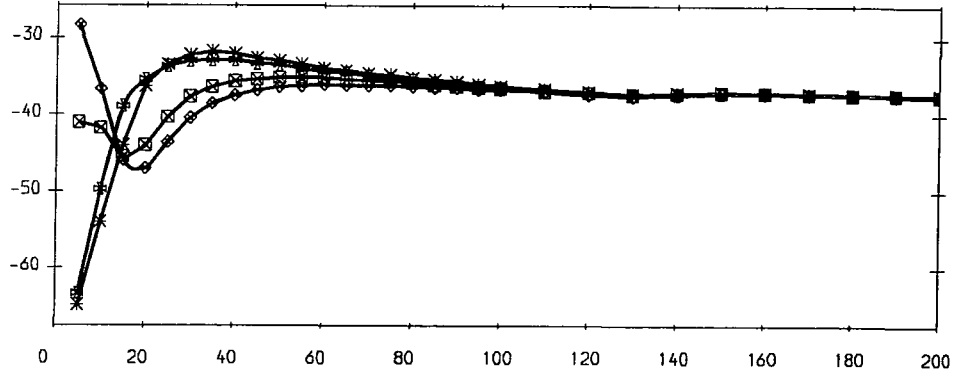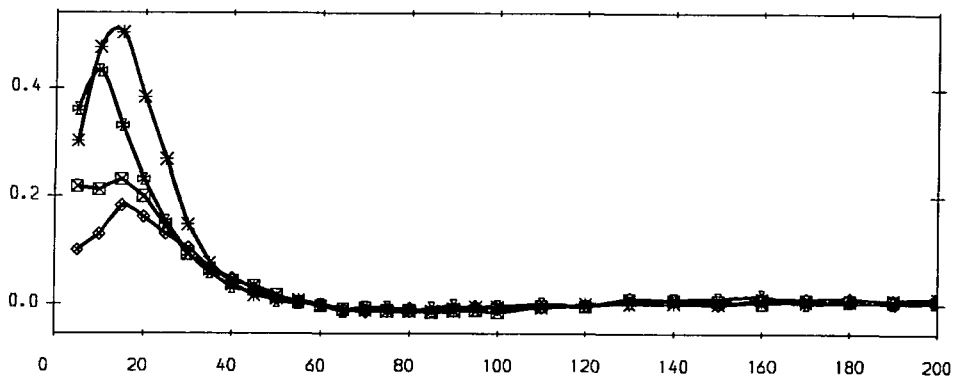Figure 4.20: Pitch-Averaged Curves at Slot 10 - High Angle

Yaw Angle

A maximum exit-angle deviation of ±2° may be compared to 300% injection at the low angle.

Total Pressure Loss Coefficient

The development of a downstream loss covering the endwall similar to 300% at the low angle leads to the peak value at the endwall.

Secondary Kinetic Energy Coefficient

Overall lowest values of secondary kinetic energy are noted for the high angle at the injection rate of 250%.

4.5 Injection Slot with Sharp Edge

Initial investigations at the high injection angle were performed without the downstream radius curvature on the injection slot. Possible separation and re-circulation behind the injection slot result in increased mass-averaged downstream losses (Figure 5.8, pg. 131).

4.5.1 Area Traverse Plots

200% - High Angle

Slot 2 Figure 4.21 compares measurements under equal conditions for the high angle with and without the downstream radius curvature. Numbering of the loss contour level is omitted to enhance the clarity of the plots.

Secondary Velocities A stronger SS to PS flow is noticed with the sharp edge. This could be due to the jets penetrating the main-flow higher above the
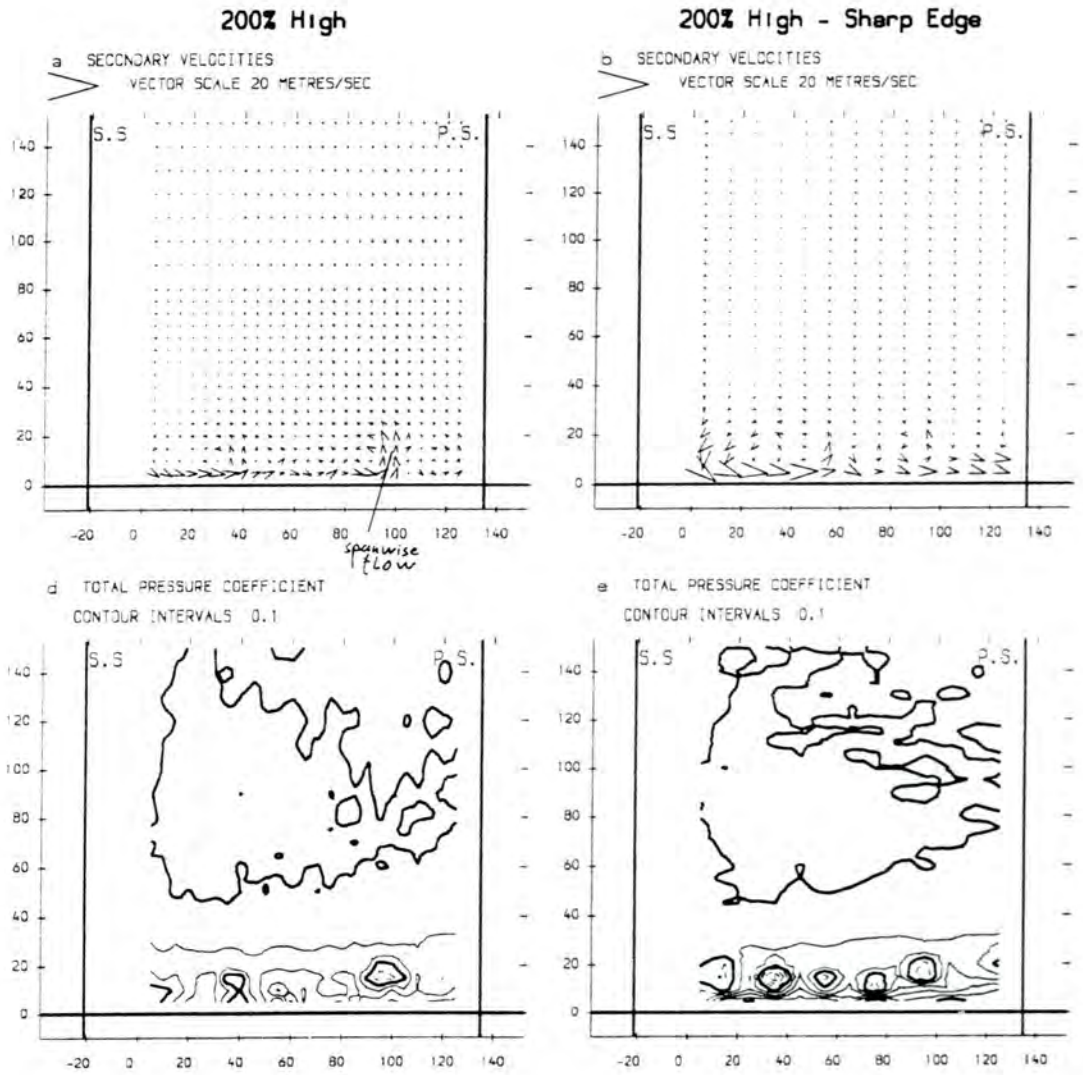
Figure 4.21: Contour Plots of Slot 2 - 200% High Angle - Radius Curvature versus Sharp Edge

endwall. The structure of the injected jet sheet is clearer with the radius as an effect of the finer grid of measurement. A significant spanwise flow is visible at some distance from PS.

Total Pressure Loss Individual lifted-off jets are discernible with the sharp edge. The jet closest to PS coincides with the above noted spanwise flow vectors and is almost identical in size and position to its equivalent with the radius curvature. The remaining jets lie close to the endwall. This is surprising and may partly be explained by the lower injection rate near PS causing separation of the injected air regardless of a downstream radius curvature. The plot demonstrates the necessity of interpreting secondary flow vectors together with total pressure loss contours for relatively coarse grids of measurement.

Slot 10 The left hand plot of Figure 4.22 with the sharp edge may be compared to the corresponding plot in Figure 4.13, pg. 69, with downstream radius curvature at the high angle.

Secondary Velocities The rounded edge seems to be more effective in suppressing secondary flows although a similar degree of over-turning exists close to the endwall.

Total Pressure Loss The wake loss core is larger and higher above the endwall as well as the SS endwall corner loss region is. Thus, the rounded edge is more effective in reducing downstream losses than the sharp edge.

250% - High Angle

Slot 10 The right hand plot of Figure 4.22 with the sharp edge may also be compared to the corresponding plot in Figure 4.13, pg. 69, with downstream radius curvature at the high angle.
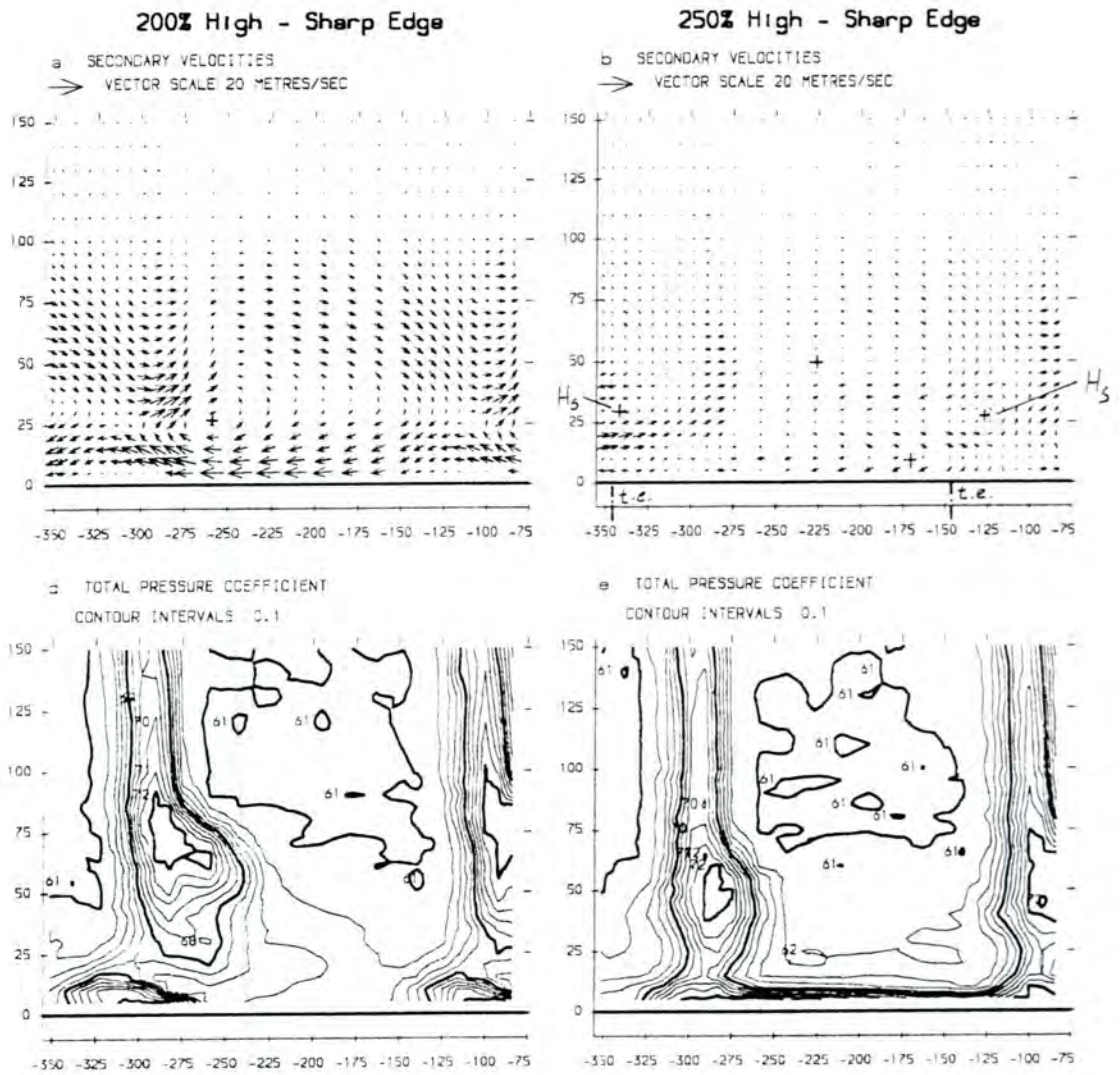
Figure 4.22: Contour Plots of Slot 10 - 200%, 250% High Angle - Sharp Edge

◇   250% (sharp edge) = 0.195 Jet Kinetic Energy Coefficient
⊠   250% (radius)   = 0.195 Jet Kinetic Energy Coefficient
✳   200% (sharp edge) = 0.100 Jet Kinetic Energy Coefficient
⊞   200% (radius)   = 0.100 Jet Kinetic Energy Coefficient
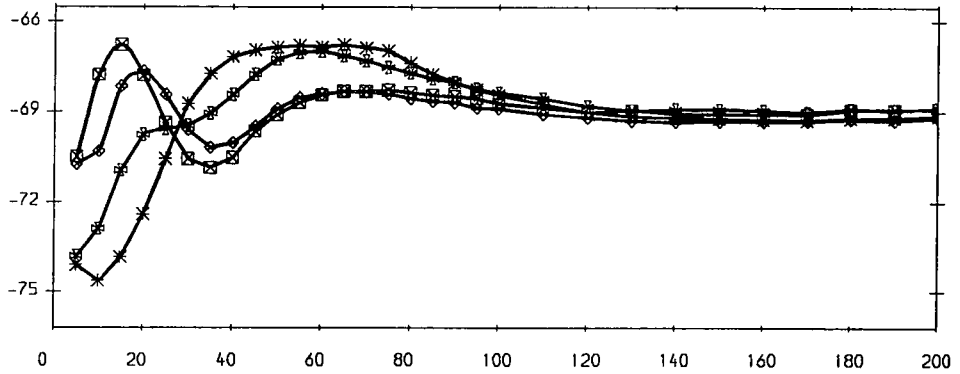
a) Yaw Angle (Degrees)

b) Total Pressure Loss Coefficient

c) Secondary Kinetic Energy Coefficient

Spanwise Distance From Endwall (mm)
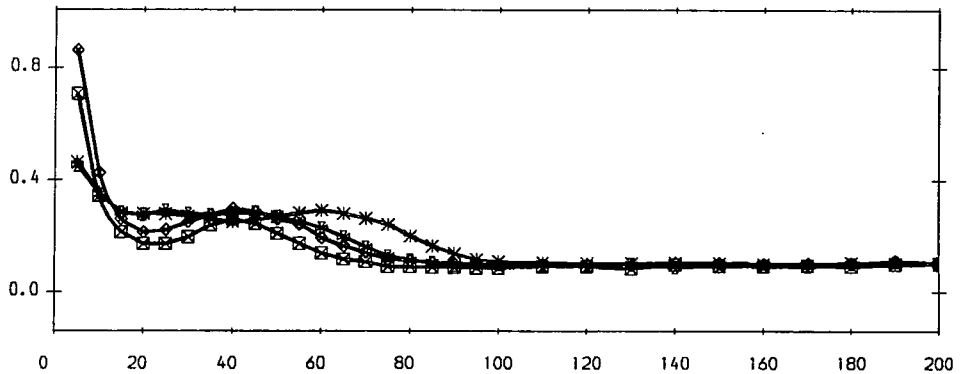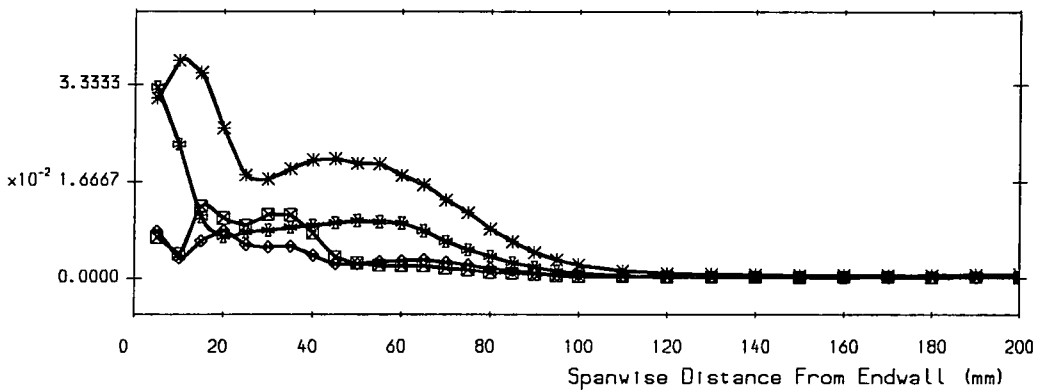
Figure 4.23: Pitch-Averaged Curves at Slot 10 - 200%, 250% High Angle - Radius Curvature versus Sharp Edge

Secondary Velocities The counter-rotating shed vortex which is merged with H_s and a over-turning strip at the same height above the endwall are stronger with the radius curvature. The underlying flow structure is similar in both cases.

Total Pressure Loss The peak of the wake loss core with the sharp edge is higher than the peak with the radius curvature, which exhibits a corner induced by the shed vortex towards the former PS.

4.5.2   Pitch-Averaged Curves

Figure 4.23 compares curves obtained with radius curvature to those obtained with the sharp edge. The curves follow the trends already described with the area-plots. Note the lower total pressure losses with radius curvature.

4.6   Blade Static Pressures

Surface static pressures were measured by Cleak [1989] and are shown in Figure 4.24. Their coefficient value is obtained by subtraction of the local static from the upstream static pressure and non-dimensionalizing with respect to the upstream dynamic head. Surface flow visualization has not revealed a separation bubble on the suction surface due to the high turbulence level present.

Computed static pressures are based on MEFP results (Chapter 6) assuming turbulent blade surface boundary layers throughout. The exact location of the transition on SS is unknown and will be an objective of future work but might be guessed from intermittency predictions at about 80% of axial chord (Cleak [1989]). The blade static pressure distribution without injection for the high inlet turbulence level has not been calculated from computations so far, but Cleak [1989] compared

measurements by Walsh [1987] at a low inlet turbulence level to MEFP results obtained at different inlet angles and with different turbulence models.

4.6.1 Experiment

A fairly 'aft'-loaded balde design is recognized in Figure 4.24.

Suction Side

An adverse pressure gradient dominates the three curves closest to midspan. As the spanwise penetration of the secondary flows increases, the curve at 53.5 mm clearly deviates in the second half of the blade passage.

Reduced loading exists near the endwall up to about 55% of axial chord. The kink at about 25% corresponds to a location just before the blade maximum curvature (where slot 3 is situated, cf. Figure 3.1, pg. 19) and is followed by a modest adverse gradient for a short distance. The increasing action of the passage vortex produces for two of the near endwall curves a favourable pressure gradient until a peak at about 80% of axial chord.

Pressure Side

The curves differ little but show the tendency to a higher pressures as the endwall is approached.

4.6.2 Computation

Results are shown in Figure 4.25. The values close to the blade edges arise from the very fine calculation grid in these areas.

Figure 4.24: Blade Static Pressure Distribution (Experiment)
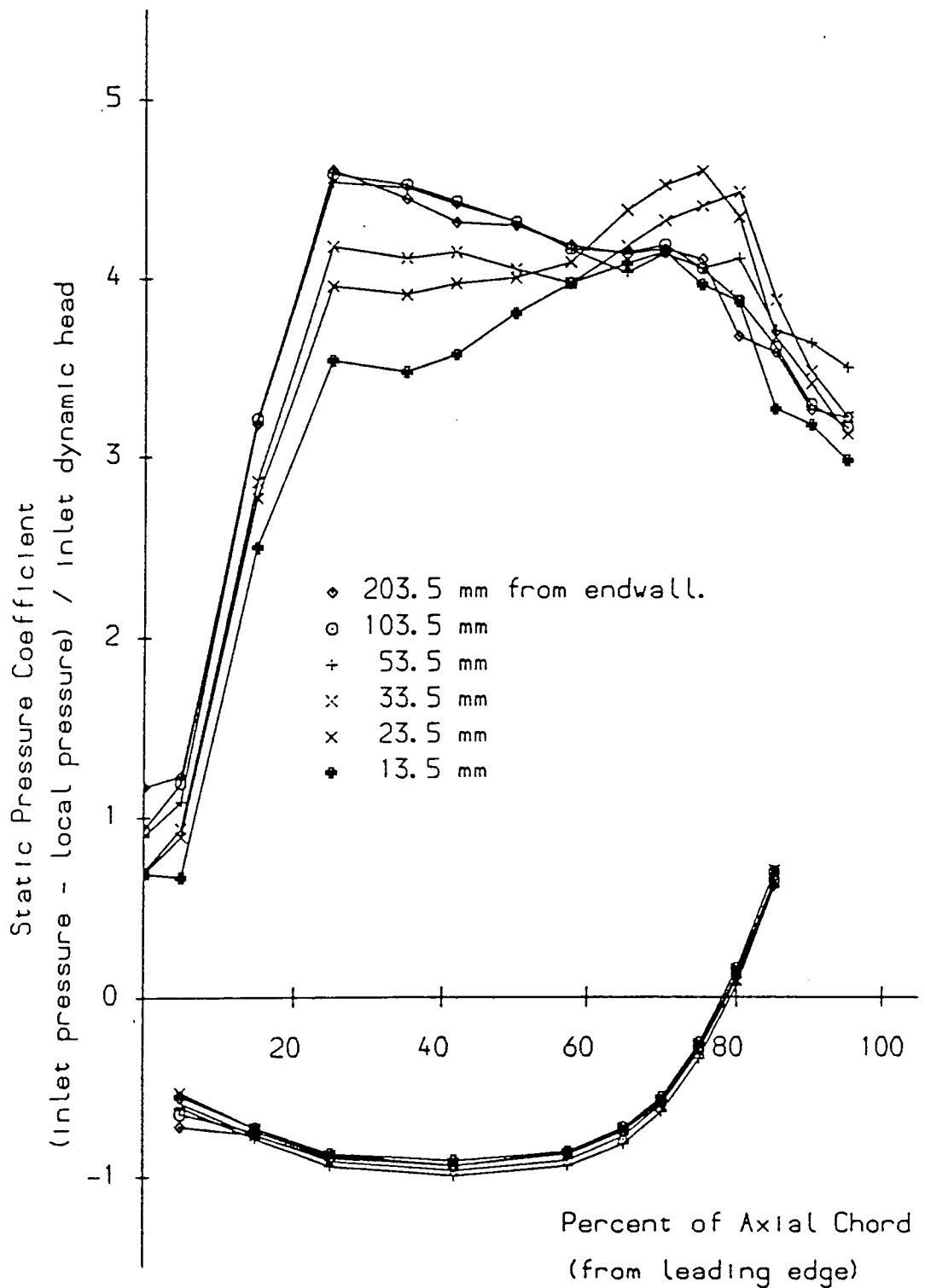
Figure 4.25: Blade Static Pressure Distribution (Computation)

KEY

◇ Distance from Endwall = 13.5
○ Distance from Endwall = 23.5
+ Distance from Endwall = 33.5
⋇ Distance from Endwall = 53.5
× Distance from Endwall = 103.5
⊛ Distance from Endwall = 199.5

Static Pressure Coefficient (inlet pstat – local pstat) / inlet dyn head

Percent of Axial Chor (from leading edge)
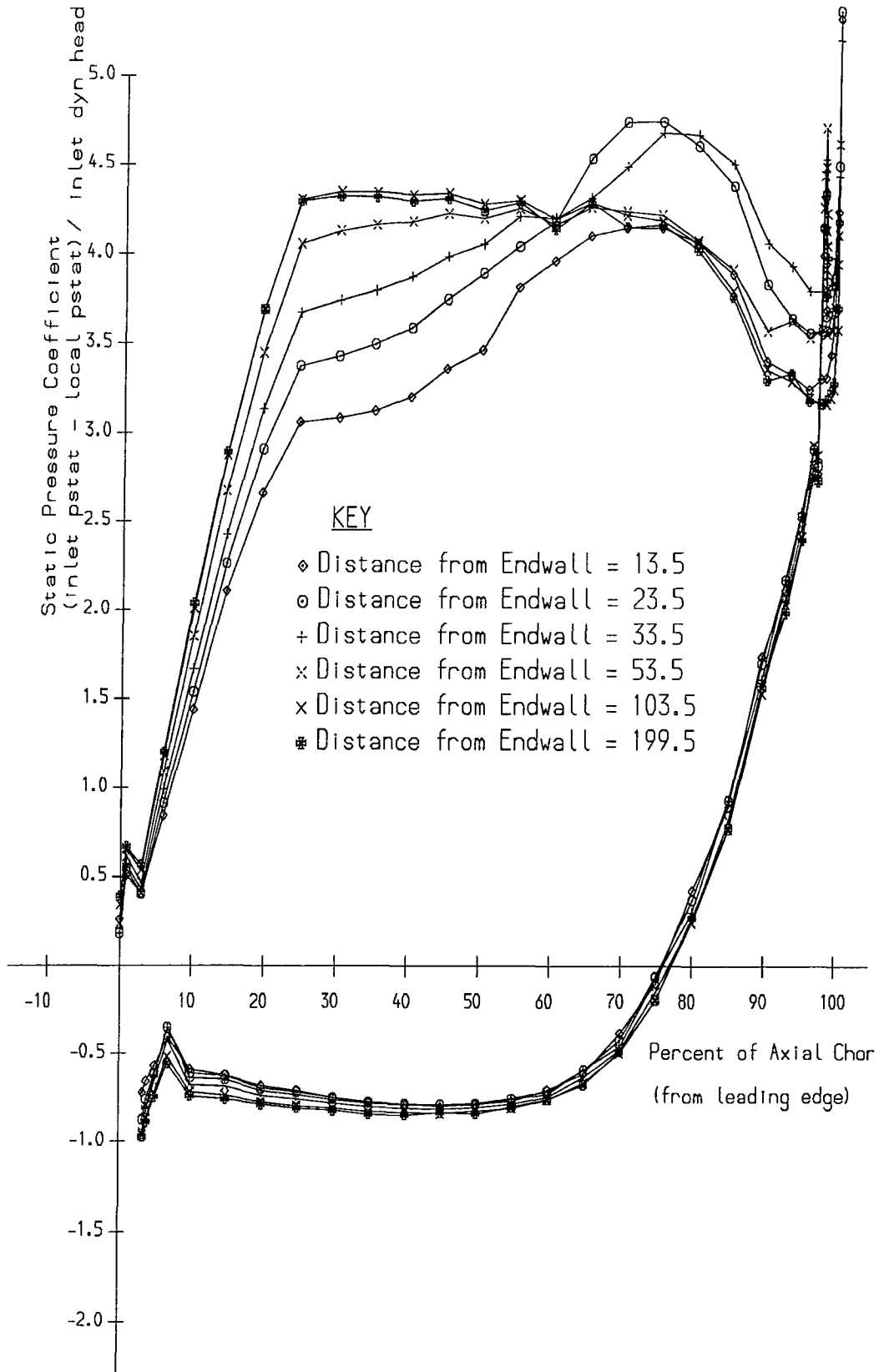
Suction Side

The static coefficients are overall lower in the first half of the blade passage. A similar result was obtained in a 2D prediction carried out by Walsh [1987]. An almost constant pressure distribution follows for the three near midspan curves of which the lowest is seen to deviate somewhat. The near endwall curves show a more favourable gradient and miss the adverse region behind the kink at 25%.

The peak values of the two near wall curves correspond well with those found experimentally although they are predicted too early.

Pressure Side

A slightly reduced loading distribution is anticipated. Increasing pressures towards the endwall are observed similar to the experiment.

4.6.3 Computation with Injection

Figure 4.26 presents results with injection of air at 232% of design blowing. The pressure distribution at midspan could not be calculated from MEFP data due to software problems. It can be assumed to lie very close to the curve of 103.5 mm as expected from the previous plot without injection.

Suction Side

Slightly increased coefficient values, i.e. lower static pressures, are observed near midspan which suggests some influence of the injection up to midspan. Overall, the decrease in loading towards the endwall is significantly reduced and the peaks of the near endwall curves are lost. This is expected because the passage vortex is closer to the endwall and is weakened by the injection (Figure 6.12, pg. 161).

Figure 4.26: Blade Static Pressure Distribution (Computation with Injection)

KEY

⬦ Distance from Endwall = 13.5
⊙ Distance from Endwall = 23.5
+ Distance from Endwall = 33.5
× Distance from Endwall = 53.5
x Distance from Endwall = 103.5
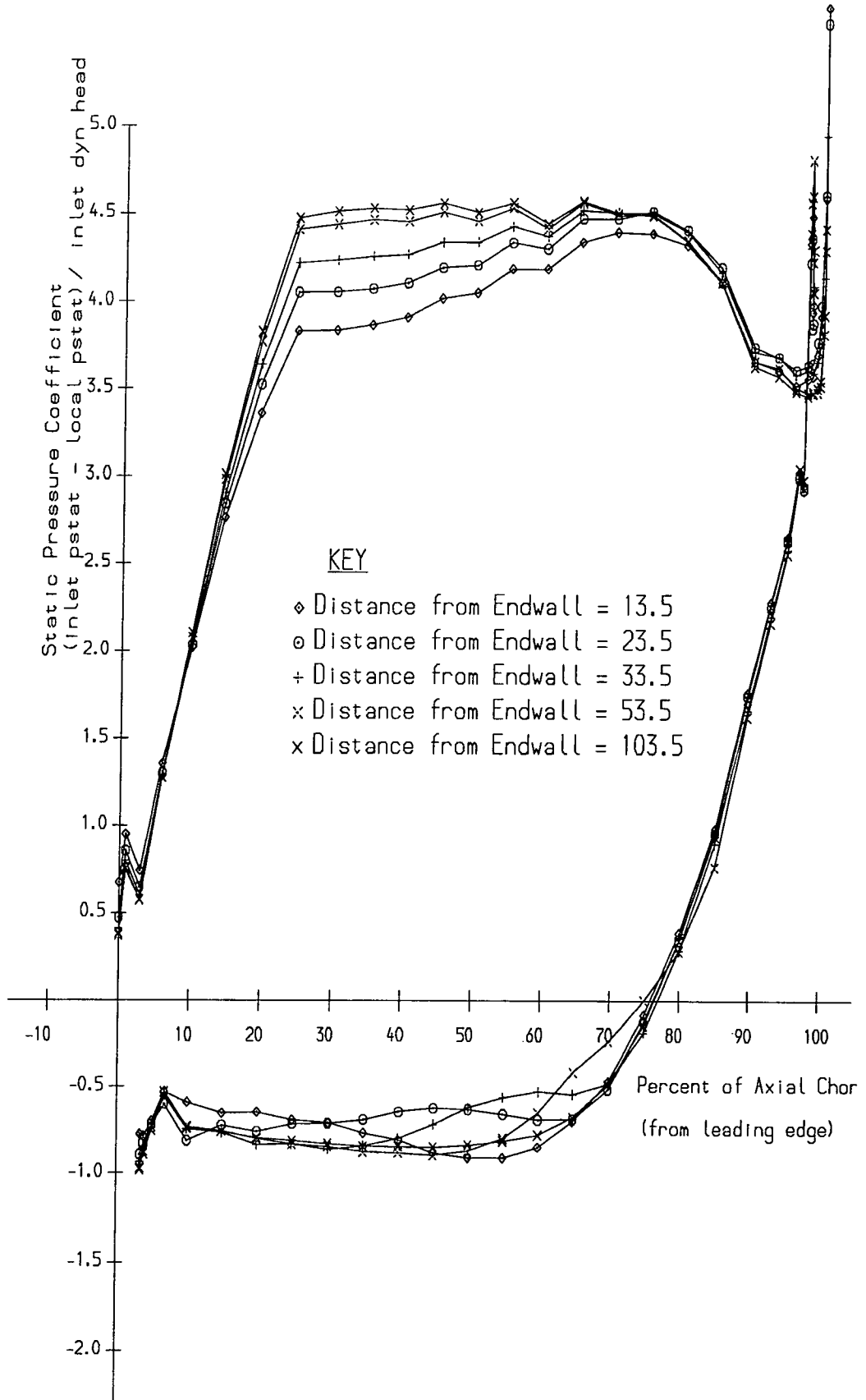
A similar trend was observed in experimental data for positive skew obtained by Walsh [1987].

Although the flow pattern measured by the 5H-probe is different for Walsh's positive skew case and 250% injection (Figure 4.41, pg. 108, and 4.11, pg. 64), the static pressure distribution is very similar (Walsh [1987], Figure 5.21). It appears that the near SS flow field which could not be measured is similar in both cases.

Pressure Side

A confused picture due to the unrealistic prediction of a counter cross-flow resulting in a PS vortex (cf. pg. 156) is given. Positive skew data showed the curves to lie almost on top of each other which supports the inadequacy of predictions by MEFP near PS.

4.7 Surface Flow Visualization

The technique used is described in Section 3.3. The presented pictures are bit-mapped re-productions of scanned photographs. The positions of slots 5 and 8 are marked in Figures 4.29 and 4.33.

4.7.1 Endwall

Limiting Streamlines

Figure 4.27 shows limiting streamlines in the cascade environment as reviewed by Sieverding [1985]. H_p causes a double separation line $(S_{1,p}, S_{2,p})$, of which the first is usually weak in HP (not discernible in this cascade facility) and strong in LP cascades (Hodson & Dominy [1986]). Accordingly, there are two saddle points on a curved stagnation line heading towards the blade nose. The inlet boundary layer material trapped between $S_{1,p}$ and $S_{2,p}$ arrives at SS, and, in a similar way to the formation of a horseshoe vortex, causes a counter-rotating corner vortex, which later develops into the separation line S_3. $S_{2,p}$ comes to lie next to it. The region between the two gets washed free from low momentum fluid (side diagram), which is also seen in photographs of oil films (Figure 4.29).

Figure 4.27: Endwall Flow Characteristics after Sieverding [1985]

No Injection

Ink flow visualizations at low Re-numbers show localized horseshoe vortices with high dissipation rates in their outer regions. A lifted-off H_s, for example, does

not necessarily influence the endwall limiting streamlines below it as shown in Figures 4.28 and 4.29. In a region near SS between the blade leading edge and where $S_{2,p}$ meets SS, the streamlines do not posses the same orientation as the opposing H_s. The fluid particles underneath H_s cause the formation of a counter-rotating corner vortex further downstream.

Figures 4.28 and 4.29 were both obtained under the same conditions. A thinner oil film was used for Figure 4.28 in order to visualize the crossing-over of H_p from PS to SS. Figure 4.29 gives a clearer picture of the rear SS flow. The stagnation saddle point lies outside the perspex endwall and was therefore not visualized.

Low Angle - 100%

An injection rate of 100% causes the inlet boundary to thicken due to streamwise injection velocities which are lower than the main stream boundary layer ones. Stronger secondary flows and higher losses result which should cause $S_{2,p}$ to meet SS further upstream. However, the endwall limiting streamlines (Figure 4.30) show $S_{2,p}$ disjoined from S_3 almost up to the blade trailing edge. This could be caused by the providing skew normal to the inlet boundary layer which does not mix so rapidly with the mainstream.

Low Angle - 250%

Higher injection rates redirect the flow path of boundary layer particles away from SS, which is apparent from the lower curvature of the limiting streamlines (Figure 4.31). S_3 has vanished, which might indicate a SS corner vortex lifting off the endwall and merging with H_s (cf. Figure 4.10 at slot 5, pg. 63, and Figure 4.11 at slot 8, pg. 64). $S_{2,p}$ could be expected at mid-pitch from the area plot at slot 5 but is not discernible. The diminished down-wash capability of the passage vortex is seen by an almost unaffected oil film near PS. The stagnation saddle point is
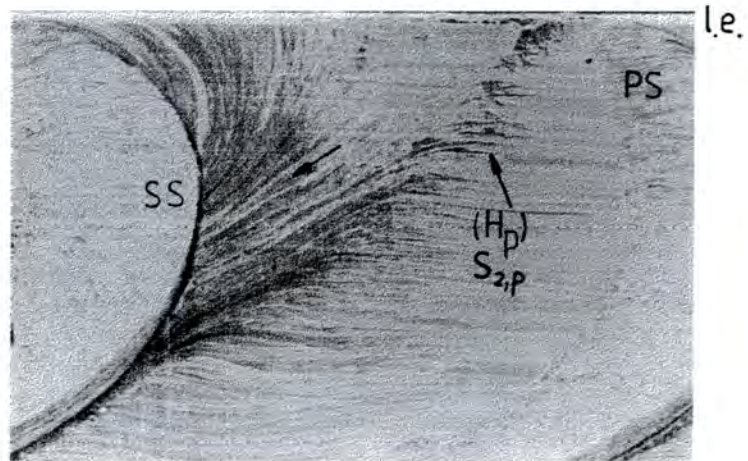
Figure 4.28: Flow Visualization at Endwall: No Injection I
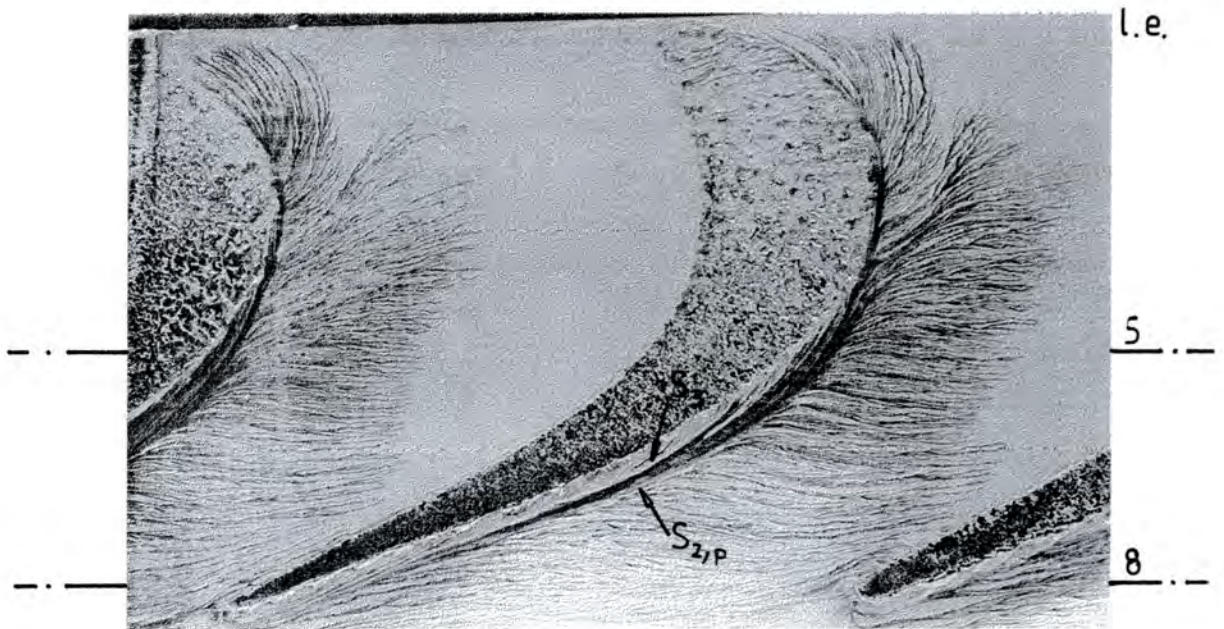
Figure 4.29: Flow Visualization at Endwall: No Injection II
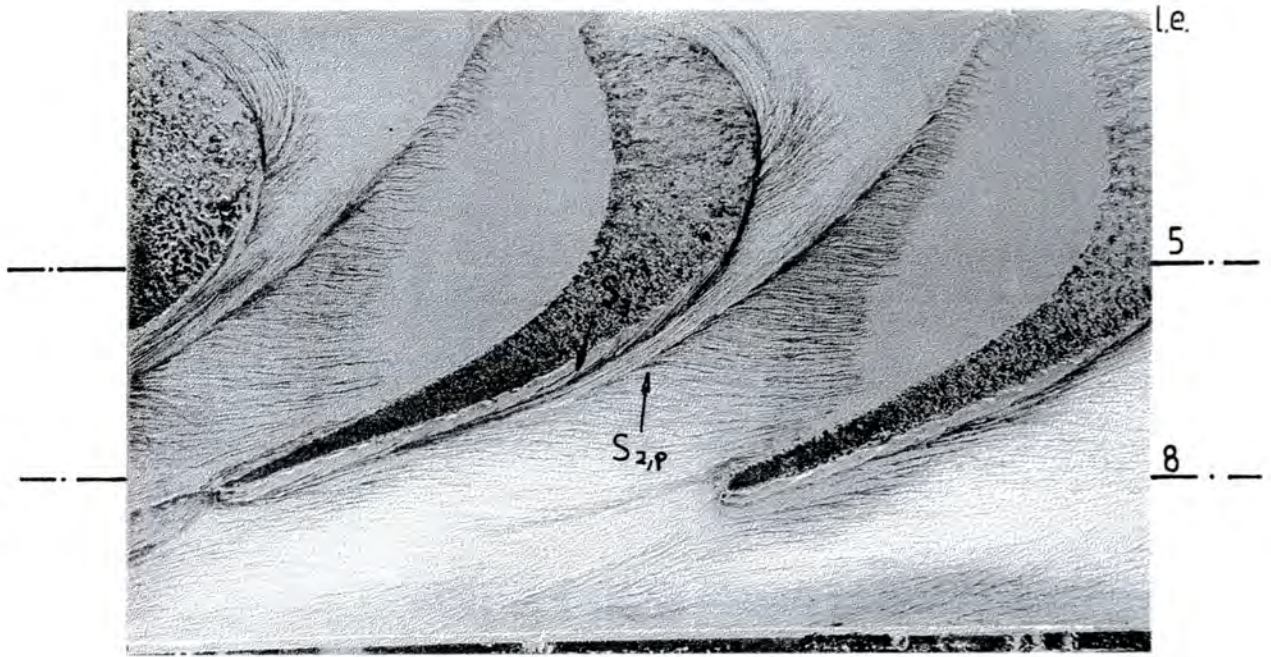
Figure 4.30: Flow Visualization at Endwall: Low Angle - 100%
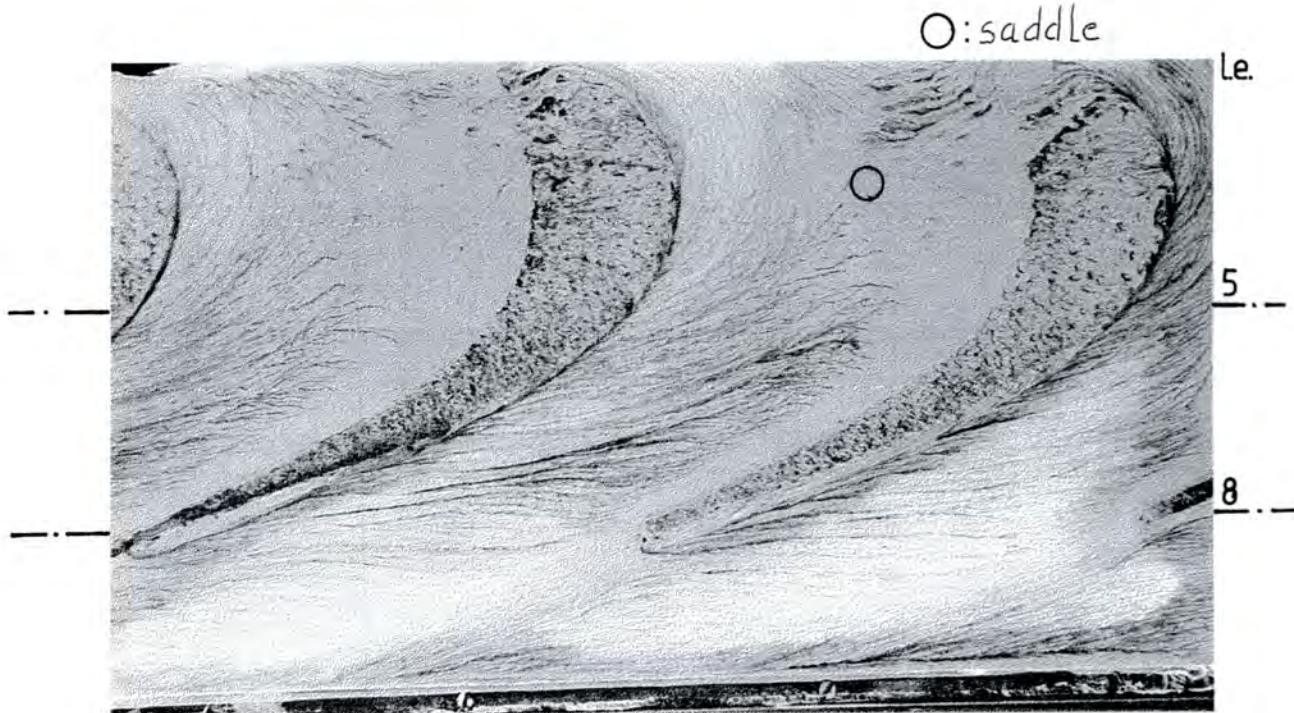
Figure 4.31: Flow Visualization at Endwall: Low Angle - 250%

Figure 4.32: Flow Visualization at Endwall: Low Angle - 300%

seen to lie within the blade passage.

The endwall cross-flow pattern inferred from area plots differs from the flow visualization results. This would mean that a highly skewed endwall boundary layer profile with a very rapid variation in the flow angle close exists on the endwall. It seems that the normal and streamwise re-energization of the inlet boundary almost influence independently the flow pattern directly on the endwall and further away from it. A similar characteristic has been found with 100% injection.

Low Angle - 300%

The streamlines in Figure 4.32 hardly show any over-turning. In contrast, area plots (Figure 4.12, pg. 66) show a spread out counter vortex at a distance from the endwall.
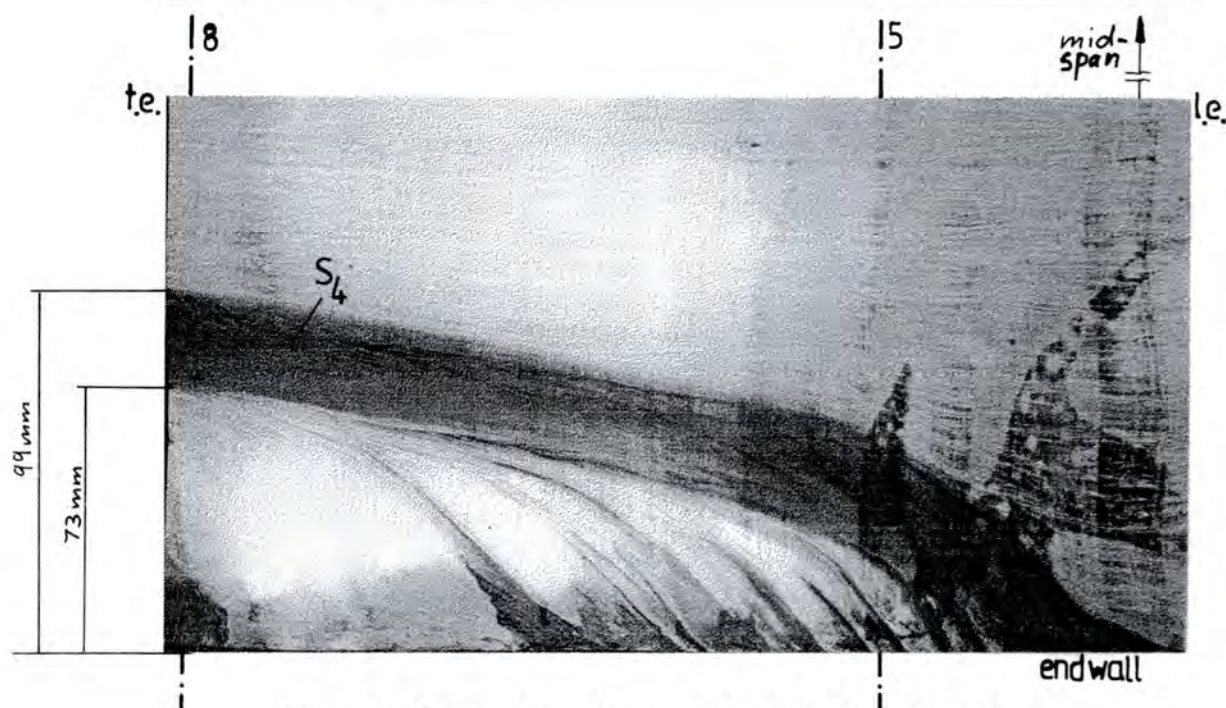
Figure 4.33: Flow Visualization at Suction Side: No Injection

4.7.2   Suction Surface

No Injection

In front of where the SS corner vortex starts to form, particles from the endwall migrate along S_4 up SS (Figure 4.33). Streaks consisting of material which is drawn off from the endwall corner up SS by the secondary flow induced spanwise static pressure gradient (cf. Figure 4.24, pg. 89) join with other limiting streamlines and are observable underneath S_4.

A detailed investigation of the streaks as provided by Bindon [1980] for his annular cascade is not aimed at in this work.

The history of fluid particles trapped in H_s is not obvious from flow visualization results alone. Tracing techniques, such as described by Gaugler & Russel [1980], Sieverding & Van den Bosch [1983] or Moore & Smith [1984] are necessary to determine whether the physical H_s has dissipated, migrated up SS, or wrapped around the passage vortex.

There are no separation bubbles present on SS due to the high free-stream
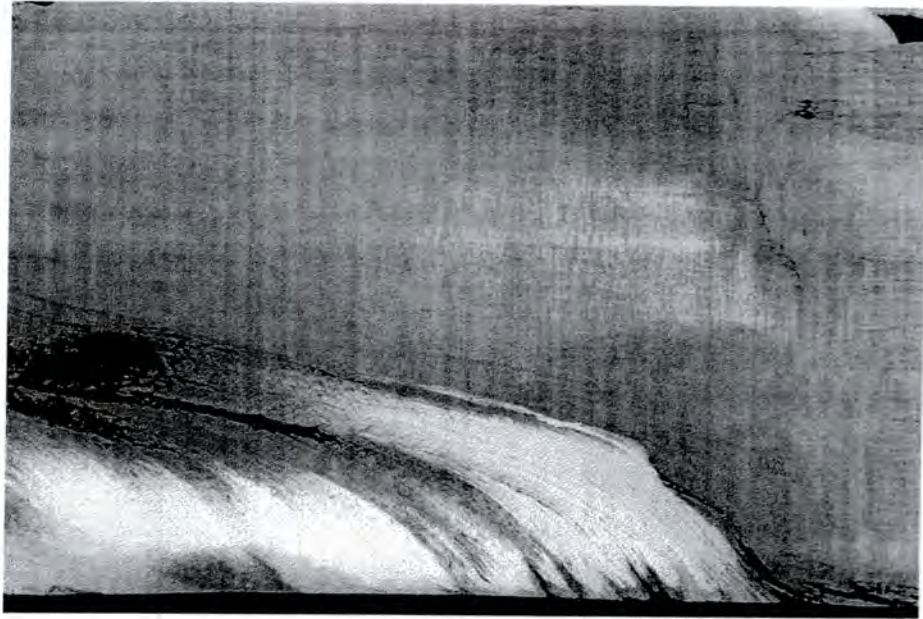
Figure 4.34: Flow Visualization at Suction Side: Low Angle - 100%

turbulence level.

Low Angle - 100%

Figure 4.34 (annotation cf. Figure 4.33) shows flow features very similar to no injection.

Low Angle - 250%

The flow pattern (Figure 4.35) has changed significantly with increased injection. S_4 has disappeared, as with positive skew (Walsh [1987], Figure 5.20), and the streaks have straightened. The enhanced H_s seems to be successful in preventing the interaction between the passage vortex and SS causing S_4.

Low Angle - 300%

Substantial migration of endwall material up SS is still existing. The streaks are further flattened. They are weaker due to a reduced spanwise static pressure

Figure 4.35: Flow Visualization at Suction Side: Low Angle - 250%
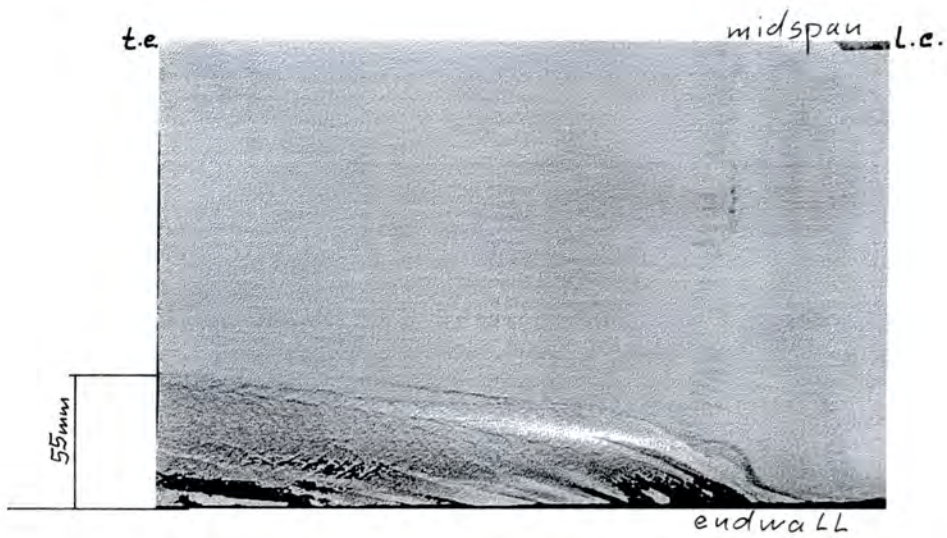
Figure 4.36: Flow Visualization at Suction Side: Low Angle - 300%
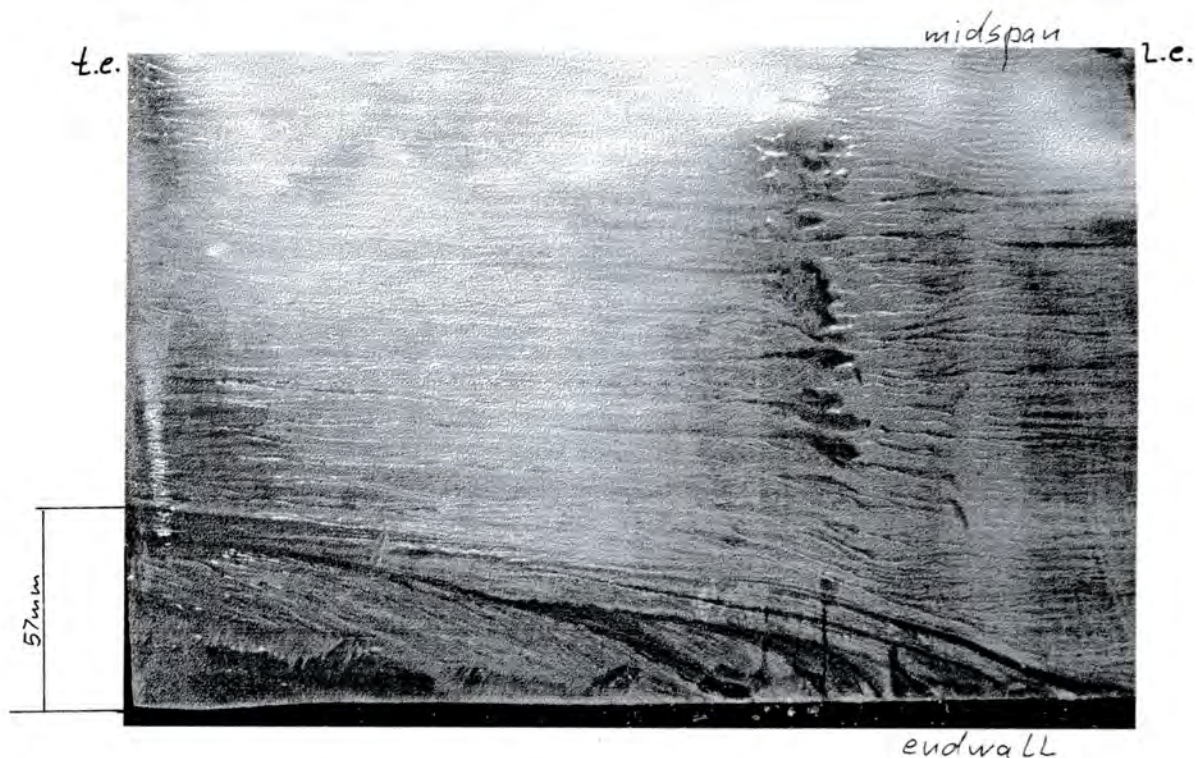
Figure 4.37: Flow Visualization at Suction Side: High Angle - 250%

gradient as anticiapted computationally (cf. Figure 4.26, pg. 92) and more clearly discernible in the original photograph.

High Angle - 250%

The interpretation of flow visualization results shown in Figure 4.37 lacks area plots of slots 5 and 8, which have been measured, but were invalidated by one of the 5H-probe side tubes having been blocked as found later. The different flow visualization technique (low viscosity oil instead of paraffin) used poses an additional difficulty. However, the overall flow pattern looks similar to 300% injection at the low angle (Figure 4.35).
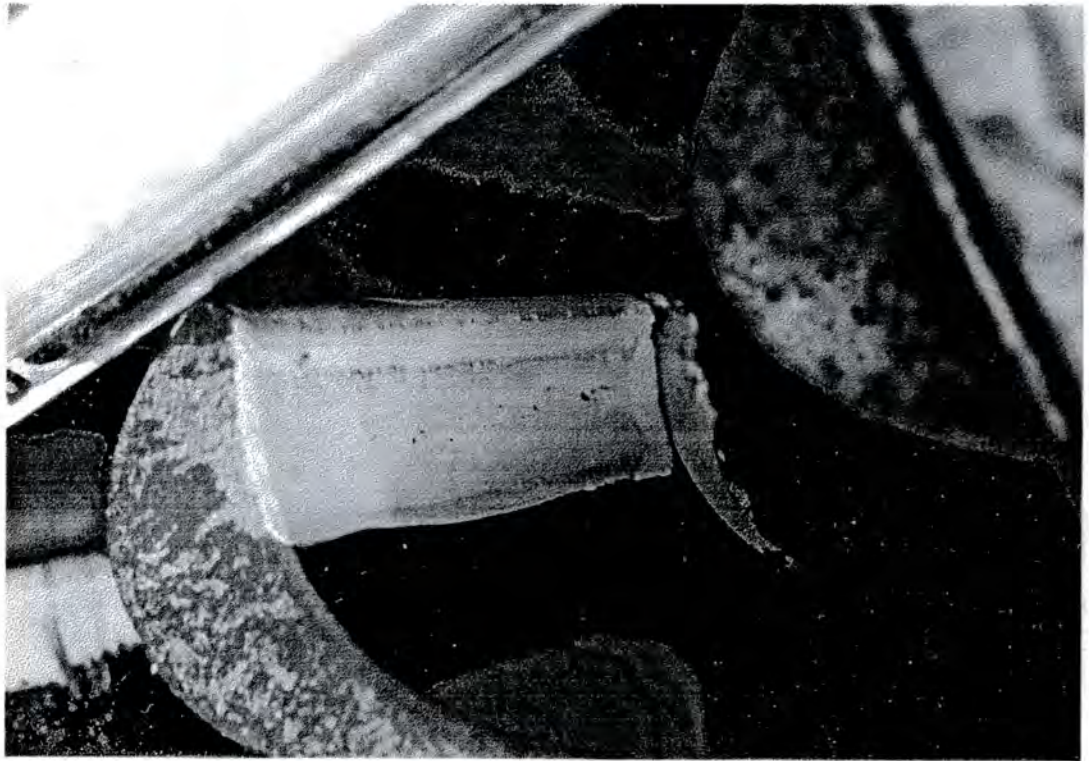
Figure 4.38: Flow Visualization at Pressure Side: No Injection

4.7.3   Pressure Surface

No Injection

A laminar separation bubble was detected at PS near the blade leading edge (Figure 4.38). After acceleration past the leading edge radius, the bubble forms under the presence of an adverse streamwise static pressure gradient.

Low Angle - 100% to 300%

Streamlines pointing away from the endwall which do not exist with no injection are observable at PS (Figure 4.39). Their divergence is increased with increasing injection. Area plots (e.g. Figure 4.10, pg. 63) show the flow close to PS being directed towards the endwall. The normal momentum provided to the flow by the
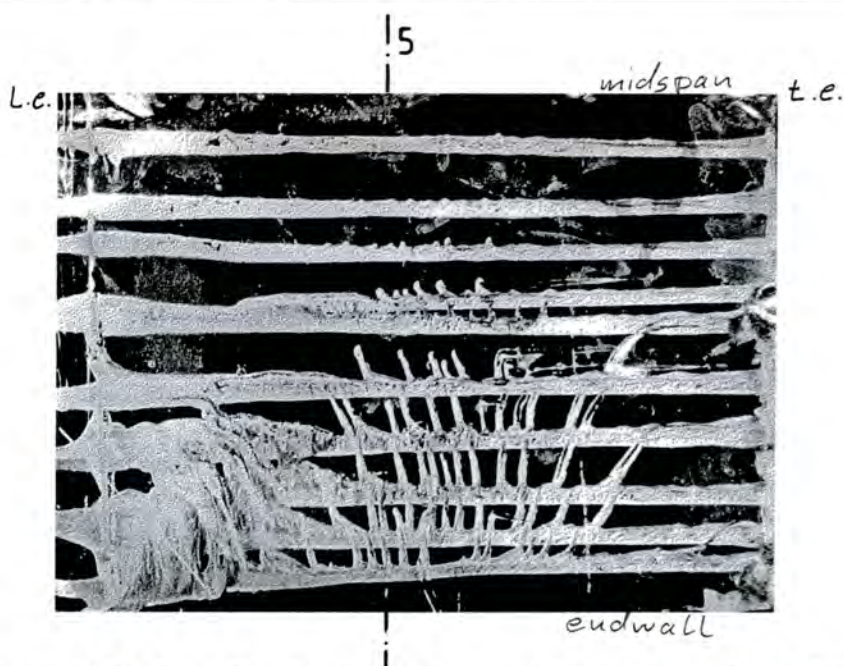
Figure 4.39: Flow Visualization at Pressure Side: Low Angle - 250%

injection could be responsible for its reaching PS and the subsequent spanwise upward migration. Measurements on the blade surface and close to it would have to be performed to obtain a better understanding since the computational results are not satisfactory (Section 4.6.3).

Another possibilty is that the streamwise velocities near PS are so low that the static pressure field may dominate the limiting streamlines (see Section 3.3). This would have to be verified by an order of magnitude analysis of equation (3.5).

4.7.4 Traces of Air Injection

Dye powder was fed at the downstream tapping of the orifice plate into the injected air flow and the blade surfaces was covered with a thick oil. Particles of the added dye adhered to the oil indicating the end of their flowpath. Results obtained for the high angle indicated terminating flow paths almost everywhere in the passage except the endwall region underneath the passage vortex. This gives some indication of the mixing within the blade passage but did not contribute much to an understanding of the flowfield, and so the technique was not used with the low

angle.

4.8 Comparison with Positive Skew

The following comparison is based on results obtained by Walsh [1987]. They will be referred in the following as 'positive skew case'.

4.8.1 Similarities and Differences

Similarities to Walsh's positive skew case with the upstream rotating belt exist for an injection rate of 200% at the low angle, despite different values for the near wall velocity, momentum and energy coefficients (Figure 5.3, pg. 117) and a different inlet boundary layer loss ($c_{p_{pos.skew}} = 0.041$ versus $c_{p_{injection}} = 0.023$) as well as a lower free-stream turbulence level ($Tu_{pos.skew} \sim 1\%$ versus $Tu_{injection} \sim 5\%$). The effect of a different shape of the inlet boundary layer profile ($n_{12_{pos.skew}} \approx 6.8$ versus $n_{12_{injection}} \approx 8.4$) on the flowfield and the generated losses is difficult to assess (cf. pg. 136) and hinders a direct comparison of the two cases.

In terms of momentum and energy, the positive skew case corresponds to 150% injection at the low angle and 100% at the high angle. Loss reductions achieved with the injection are not as great as with the belt (Section 5.3.6) due to increased mixing of primarily the spanwise component. Higher than estimated near wall velocity, momentum and energy have to be provided to achieve comparable flow features to positive skew. At 200% injection, these values are about twice as high as with positive skew (Figure 5.3).

4.8.2 Slot 1

Pitch-Averaged Curves

The yaw angle plot in Figure 4.40 shows considerably higher deflection closest to the endwall with positive skew than with injection. This is despite a theoretical injection velocity of twice the belt speed at 200%. The kink in the positive skew curve may be attributed to problems with the curve-fitting.

The total pressure loss curves show a re-energization of the inlet boundary layer near the endwall with 200% but not with 150% and positive skew. The measured re-energization depends on the distance of the first point of measurement from the endwall and is therefore more obvious at high injection rates.

A similar argument as for the yaw angle curve is valid for the the secondary kinetic energy coefficient.

4.8.3 Slot 5

Area Traverse Plots

The area plots for positive skew (Figure 4.41) may be compared to both 200% (Figure 4.9, pg. 60) and 150% (Figure 4.6, pg. 56) injection. A loss core in the SS corner is visible with 150%, which does not exist with 200% injection and with positive skew.

4.8.4 Slot 8

Area Traverse Plots

The flow field near the trailing edge resembles 200% injection apart from the near SS flow and the flatter passage vortex with reduced secondary flows in the upper half. Overall lower secondary flows and lower levels of total pressure loss may be

◈   Positive Skew = 0.017 Jet Kinetic Energy Coefficient
⊠   200% = 0.033 Jet Kinetic Energy Coefficient
✳   150% = 0.014 Jet Kinetic Energy Coefficient
✛   0% = 0.000 Jet Kinetic Energy Coefficient

a) Yaw Angle (Degrees)

b) Total Pressure Loss Coefficient

c) Secondary Kinetic Energy Coefficient

Spanwise Distance From Endwall (mm)
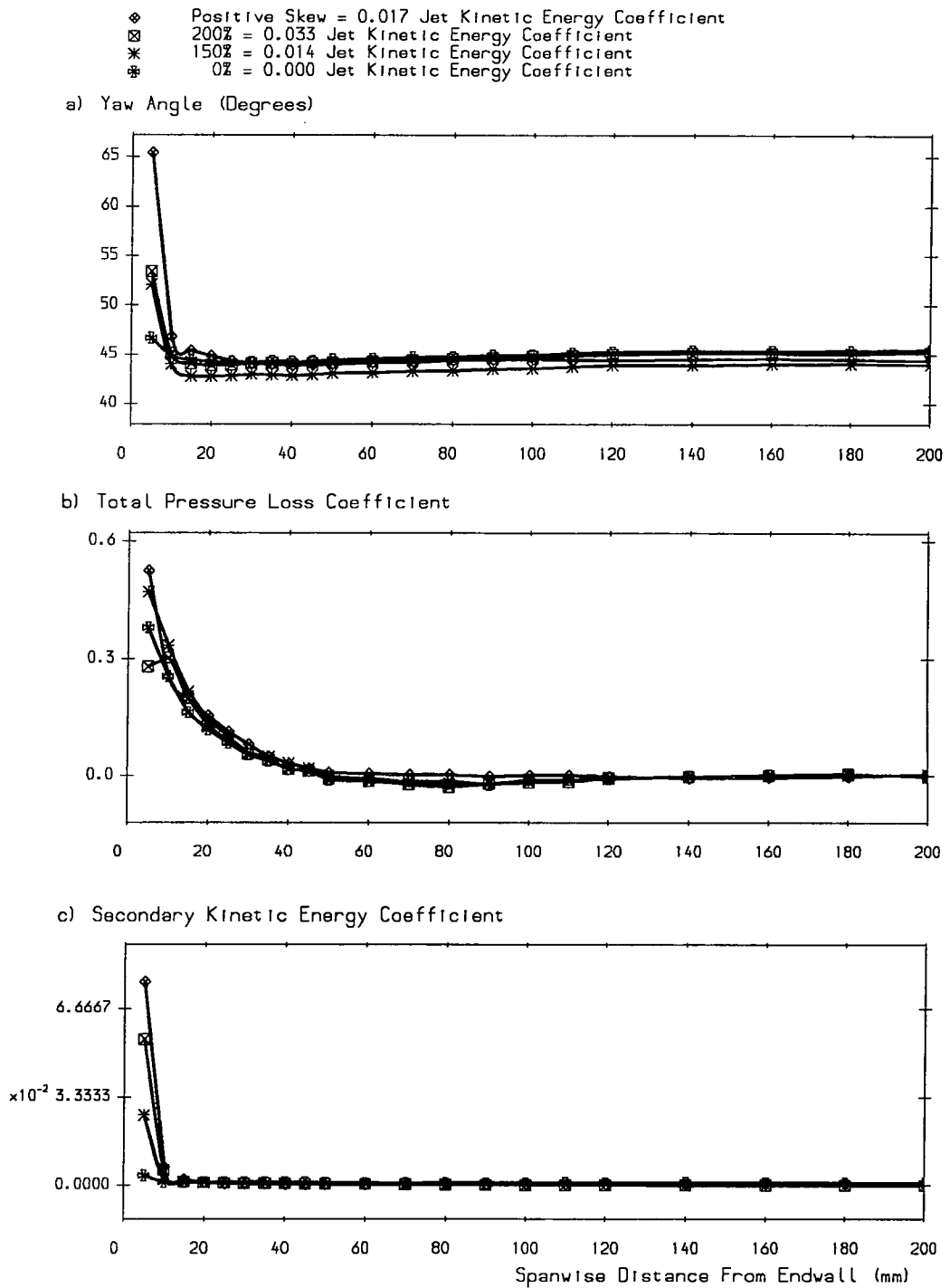
Figure 4.40: Comparison of Pitch-Averaged Curves at Slot 1 - No Injection, 150%, 200%, Positive Skew
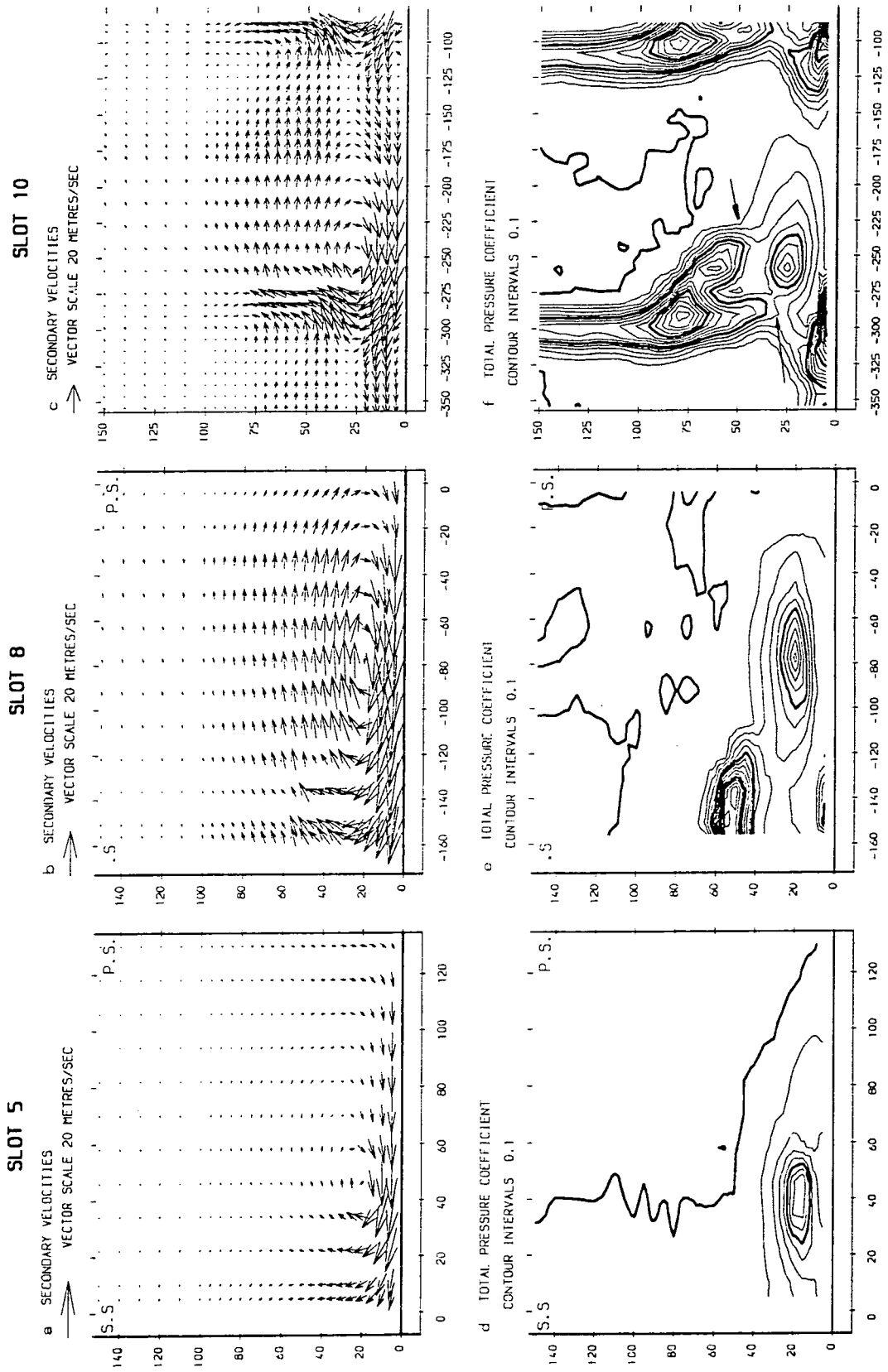
Figure 4.41: Contour Plots at Slots 5, 8 and 10 - Positive Skew

attributed to the lower inlet loss and higher free-stream turbulence with injection compared to the positive skew case.

4.8.5 Slot 10

Area Traverse Plots

There are differences in the secondary flow field to 200%, but the overall flow structure is similar. The shape of the double loss core with two corners pointing towards the endwall, a nearby isolated loss core and the SS corner loss core agree fairly well.

Pitch-Averaged Curves

The positive skew spanwise exit angle variation resembles most 200% injection. The spanwise total pressure loss distribution for positive skew is again overall similar to 200%; a hump at 25 mm span corresponds to a more pronounced isolated loss core (see area plot). Overall higher values are due to a different inlet boundary layer. The overall level of secondary kinetic energy is higher with positive skew as expected from the thicker inlet boundary layer.

◈   Positive Skew = 0.017 Jet Kinetic Energy Coefficient
⊠   200% = 0.033 Jet Kinetic Energy Coefficient
✳   150% = 0.014 Jet Kinetic Energy Coefficient
✠   0% = 0.000 Jet Kinetic Energy Coefficient

a) Yaw Angle (Degrees)

b) Total Pressure Loss Coefficient

c) Secondary Kinetic Energy Coefficient

Spanwise Distance From Endwall (mm)
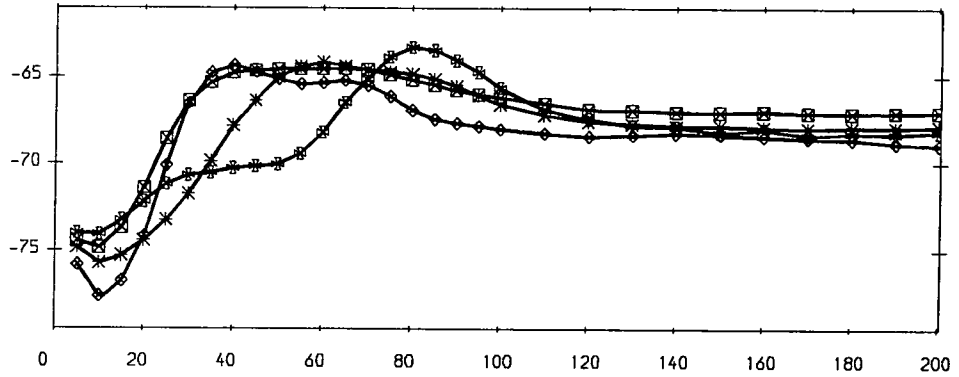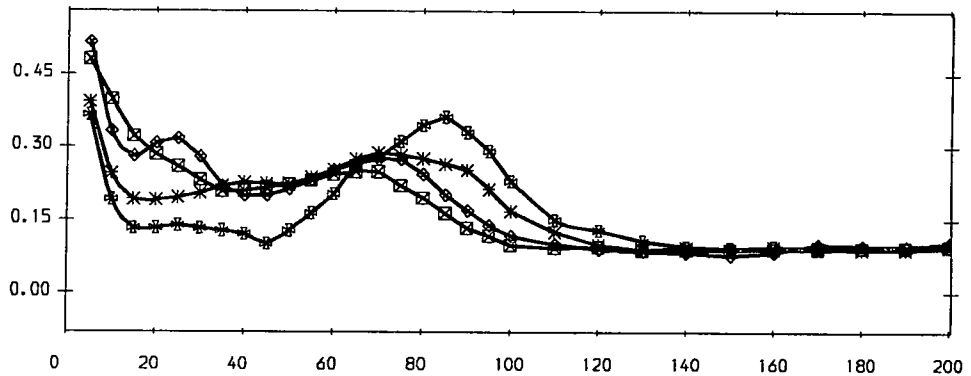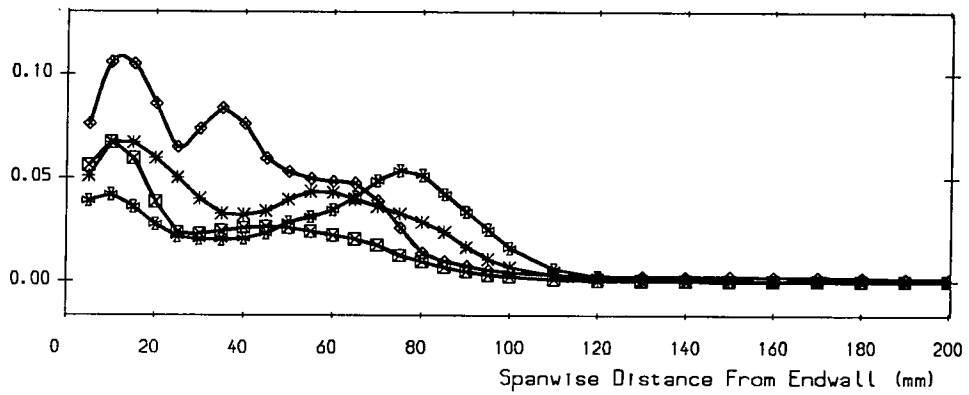
Figure 4.42: Comparison of Pitch-Averaged Curves at Slot 10 - No Injection, 150%, 200%, Positive Skew

Chapter 5

Data Analysis

$\mathcal{D}$ ata from the experiment is analysed on the basis of availability considerations for incompressible flows. It is shown that a reduction in secondary flows does not necessarily lead to an overall energy saving when the kinetic energy of the injection is taken into account. However, subtraction of the mixing-out loss of the blown layer shows significant overall gains for the low injection angle.

5.1 Design

5.1.1 Inlet Boundary Layer

The inlet angle to a turbine rotor cascade is determined for the freestream according to its fictitious rotational speed and the fictitious discharge angle of an upstream nozzle guide vane. The inlet boundary layer is skewed when changing the frame of reference. If an upstream rotating belt is used for simulation, it rotates in the negative direction, i.e. towards SS, for a turbine and in the positive direction, i.e. towards PS, for a compressor rotor cascade. Negative skew enhances and positive skew counteracts secondary flows. The positive skew case investigated by

Walsh [1987] is designed to simulate the first row of an axial compressor rotor with axial inlet flow. The corresponding velocity triangle is shown in Figure 5.1 where
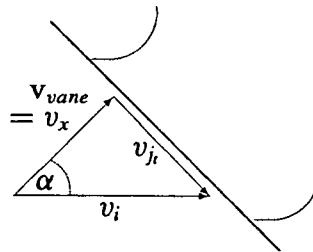
Figure 5.1: Positive Skew with Axial Inflow

$\mathbf{V}_{vane}$ denotes the absolute inlet velocity, which coincides with the cascade axial flow direction v_x, and v_{belt} the corresponding rotating belt speed. The simulation of a compressor inlet was not complete because of cascade blade profiles following the design of an HP turbine.

5.1.2 Preliminary Design

The requirement of a tangential injection velocity and momentum identical to the positive skew together with a fixed injection area forms the basis of the following considerations. The required injection angle is calculated first, the injection mass flow per pitch follows and an effectiveness of the injection, relative to the loss reduction previously obtained with the belt, is assessed.

High Angle

An integral value of the additional tangential momentum supplied to the cascade inlet boundary layer by the rotating belt (Figure 5.2) is calculated in order to quantify the associated skew. This value is used as a basis to determine the design injection conditions for the high angle. Using the identity $\frac{v_y''}{v_i - v_i'} = \frac{v_{belt}}{v_i}$ gives for
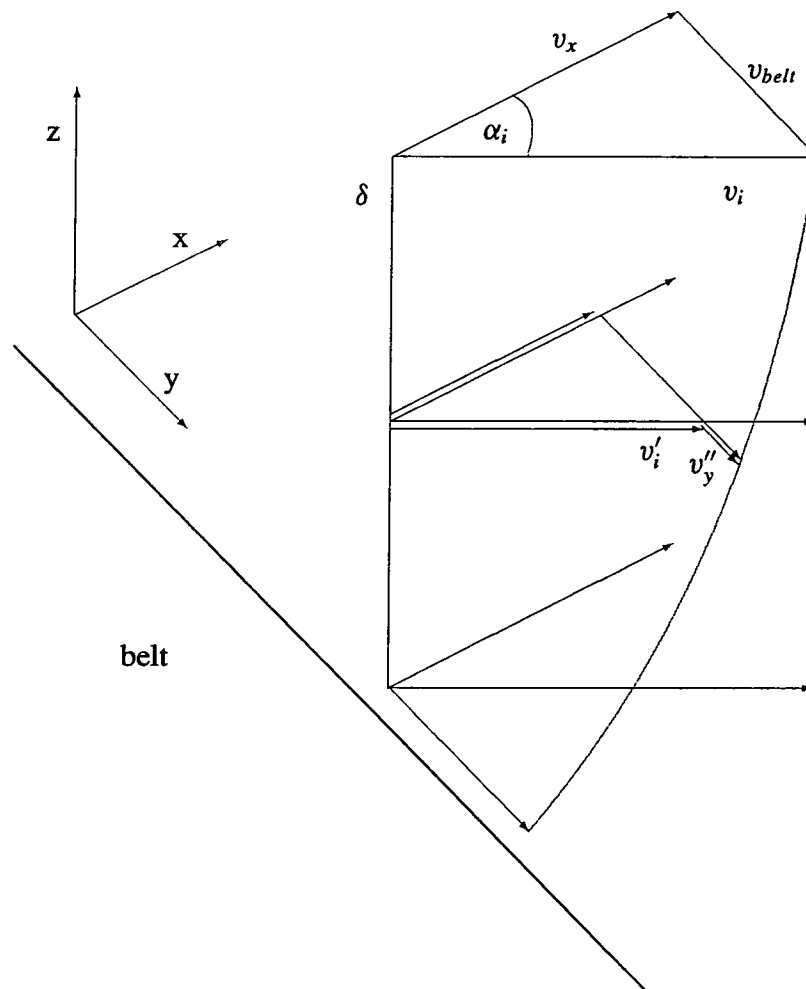
Figure 5.2: Inlet Boundary Layer for Positive Skew with Axial Inflow

the additional momentum provided by the belt

$$\dot{M}_{belt} = \int_0^{\delta} v_y'' \, d\dot{m} \tag{5.1}$$

$$= \int_0^{\delta} v_y'' \rho s v_x \, dz \tag{5.2}$$

$$= \int_0^{\delta} \frac{v_{belt}}{v_i} (v_i - v_i') \rho s v_x \, dz \tag{5.3}$$

$$= \rho s \cos(\alpha_i) \frac{v_{belt}}{v_i} \int_0^{\delta} (v_i - v_i') v_i' \, dz \tag{5.4}$$

The integral is solved by substitution of the 'undisturbed' momentum thickness

$$\delta_2 = \frac{1}{v_i^2} \int_0^{\delta} (v_i - v_i') v_i' \, dz$$

together with the geometric relation[1] $\sin(\alpha) = \frac{v_{belt}}{v_i}$

$$\dot{M}_{belt} = \rho s \delta_2 v_i^2 \cos(\alpha) \sin(\alpha) \tag{5.5}$$

The momentum of air injected tangentially at an angle θ is

$$\dot{M}_{j_t} = \dot{m}_j v_{j_t} \tag{5.6}$$

$$= \rho A_j v_{j_t}^2 \tan(\theta) \tag{5.7}$$

With the same tangential injection velocity as the belt speed

$$v_{j_t} = v_{belt} = v_i \cdot \sin(\alpha) = 13.3 \frac{m}{s}$$

a geometrical fixed injection area of $A_j = 875$ mm^2 (pg. 26) and a momentum

thickness of $\delta_2 = 3.1$ mm (Table 3.1, pg. 21) yields after equating (5.5) and (5.7)

---

[1] α denotes the inlet flow angle α_i in the following.

a required injection angle of

$$\theta = \arctan\left(\frac{s\delta_2 \cot(\alpha)}{A_j}\right) \qquad (5.8)$$

$$\simeq 36° \qquad (5.9)$$

This is close to an assumed[2] value of 35° for the actual discharge angle from the injection slot.

The jet to mainstream mass flow ratio neglecting the displacement by the boundary layer amounts to

$$r = \frac{\dot{m}_j}{\dot{m}_u} \qquad (5.10)$$

$$= \frac{\rho A_j v_{j_i} \tan(\theta)}{\rho \hbar s v_i \cos(\alpha)} \qquad (5.11)$$

$$= \frac{A_j \tan(\alpha) \tan(\theta)}{\hbar s} \qquad (5.12)$$

$$\simeq 0.0154 \qquad (5.13)$$

The kinetic energy of the injected air

$$\dot{E}_j = \frac{1}{2}\dot{m}_j \left(\frac{v_{j_i}}{\cos(\theta)}\right)^2 \qquad (5.14)$$

$$= \frac{1}{2}\rho A_j v_{j_i}^3 \frac{\tan(\theta)}{\cos^2(\theta)} \qquad (5.15)$$

is related to an energy gain associated with a loss reduction of $c_{P_s} = 0.043$ in Walsh's positive skew case

$$\dot{E}_g = \frac{\dot{m}_u}{\rho}\frac{1}{2}\rho v_i^2 c_{P_s} \qquad (5.16)$$

$$= \frac{1}{2}\rho s \hbar v_i^3 c_{P_s} \cos(\alpha) \qquad (5.17)$$

---

[2]The actual value is uncertain to some extent (Section 3.1.2).

The ratio may be approximated to

$$\frac{E_g}{E_j} = \frac{s\hbar c_{p_g} \cos^2(\theta)}{A_j \sin^2(\alpha) \tan(\alpha) \tan(\theta)} \tag{5.18}$$

$$\approx 4 \tag{5.19}$$

indicating a gain four times larger than the investment. This is an over-estimation of the realistically achievable gains as explained in Section 5.3.6 on pg. 138.

Low Angle

The design conditions for the low angle ensure a tangential injection velocity identical to the belt speed but not an identical tangential momentum amounting to about half $\left(\frac{\tan(36°)}{\tan(20°)} \simeq 2\right)$ of that of the high angle.

Optimum Angle

The injection angle for a maximum momentum is obtained by substitution of equation (5.15) into equation (5.7) and finding a local maximum for constant energy. After some manipulation, a theoretical optimum of the injection angle is obtained to

$$\frac{d(\cos(\theta) \sin^{\frac{1}{3}}(\theta))}{d\theta} = 0 \tag{5.20}$$

$$\theta = 30° \tag{5.21}$$

5.1.3 Injection Conditions

For a constant injection angle, a *percentage of the design injection conditions* refers to the tangential velocity component and the injected mass flow per pitch. A characterization of the injection can be accomplished by determination of either

the jet to mainstream total pressure ratio or the kinetic energy ratio. The latter has the advantage of not depending on the static conditions at the injection location, which are not necessarily known. Moreover, a variation in mass flow produces a significant change of the kinetic energy whereas the dynamic head is small compared to the static pressure for near incompressible flow. A jet kinetic energy coefficient can be defined relative to the upstream kinetic energy of the mainflow

$$\dot{E}_u = \frac{1}{2}\dot{m}_u v_u^2 \tag{5.22}$$

$$= \frac{1}{2}\rho s \hbar v_u^3 \cos(\alpha) \tag{5.23}$$

as (see equation (5.14)) for kinetic energy of injection

$$c_j = \frac{\dot{E}_j}{\dot{E}_u} \tag{5.24}$$

$$= r\left(\frac{v_j}{v_u}\right)^2 \tag{5.25}$$

$$= \frac{\rho A_j v_j^3 \sin^2(\theta)}{\rho s \hbar v_u^2} \tag{5.26}$$

The coefficient is proportional to the cube of percentage injection. Figure 5.3 gives a graphic representation of c_j and Table 5.1 contains the numeric values,
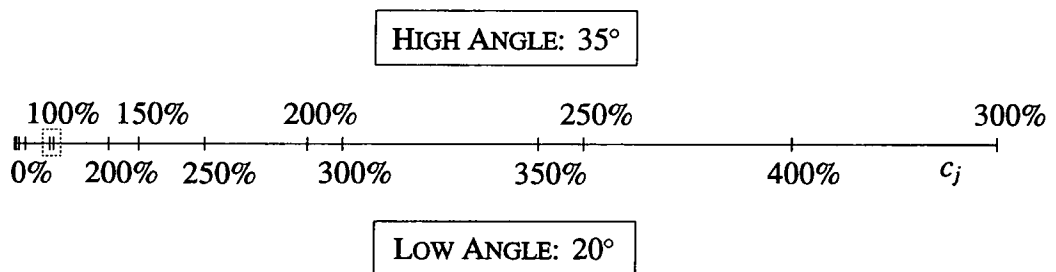
Figure 5.3: Relation of Design Injection Rate in % to Jet Kinetic Energy

relative to design injection conditions. The kinetic energy of the injection for the low angle is less than for the high angle in the ratio of $\left(\frac{\cos(35°)}{\cos(20°)}\right)^3$.

	100%	150%	200%	250%	300%
High Angle	0.01256	0.04231	0.09980	0.1950	0.3377
Low Angle	0.004167	0.01414	0.03340	0.06520	0.1126

Table 5.1: Relation of Design Injection Rate in % to Jet Kinetic Energy (Numerical Values)

For the moving belt case with the skewed inlet boundary layer, the product of the tangential momentum component and the belt speed divided by the upstream[3] kinetic energy gives a coefficient of

$$c_{j_{belt}} = \frac{\dot{M}_{belt} \cdot v_{belt}}{\dot{E}_u} \tag{5.27}$$
$$= 0.017$$

compared to a value of about 0.007 for the design injection using equation (5.25). The value for the belt is surrounded in Figure 5.3 by a dashed box.

The injected tangential momentum is plotted in Figure 5.4 together with the streamwise tangential injection to freestream velocity ratio (cf. Table 4.1, pg. 45) for the high and low angle as well as for the belt. Both the injected tangential momentum and kinetic energy correspond on this scale to 100% and 150% of the high and low angle respectively.

Table 5.2 summarizes the measured conditions for 100% injection per blade pitch. As a consequence of a difference in the actually set to the desired tangential injection velocity, the values for the high angle are slightly increased. This was accepted since the set values were measured correctly.

The injected mass flow as percentage of the cascade mass flow is given in Table 5.3. The values are typical for film cooling investigations (Goldman & McLallin [1977], Sieverding & Wilputte [1981]). They are an order of magnitude

---

[3]The difference between 'upstream' and 'inlet' planes is specified at the begin of Section 5.2.

□	Vjs/Vu (high)	+	Vjs/Vu (low)	◇	Mjt/Mu * 10 (high)	△	Mjt/Mu * 10 (low)
		×	Vs/Vu (belt)	▽	Ms/Mu * 10 (belt)		
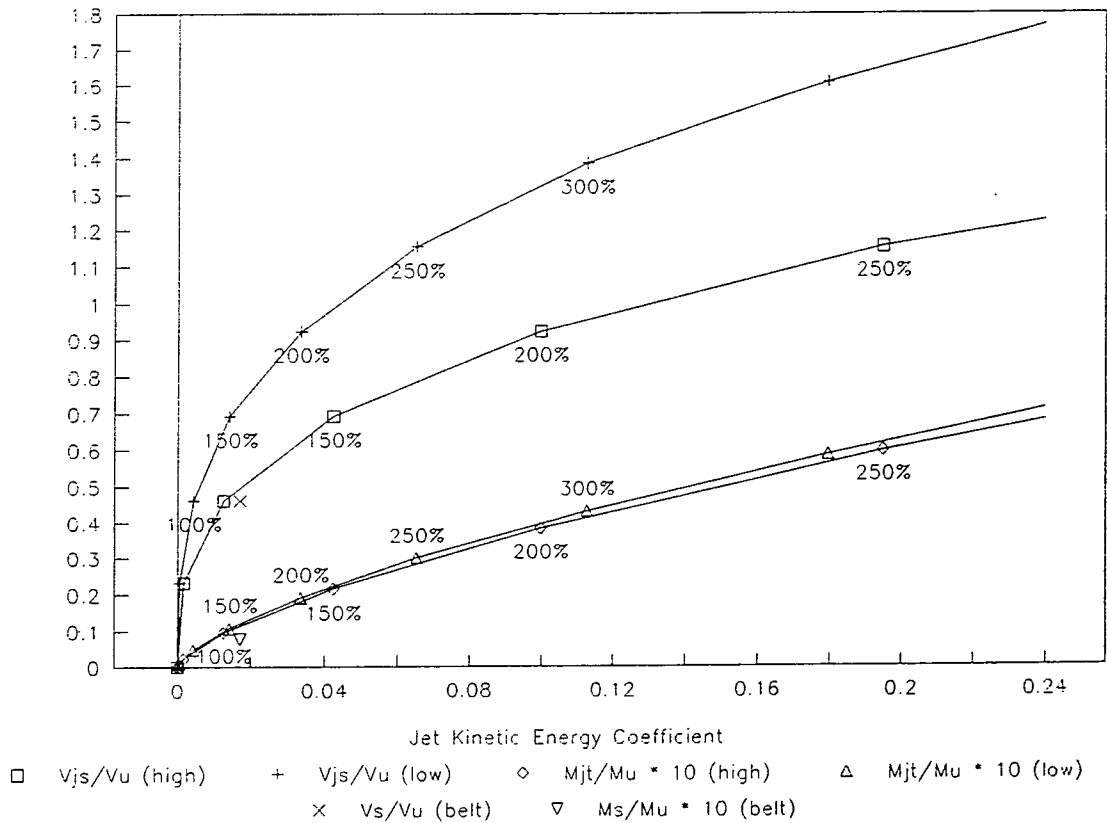
Figure 5.4: Tangential Momentum Ratio $\frac{\dot{M}_{j_t}}{\dot{M}_u}$ and Streamwise Tangential Injection to Freestream Velocity Ratio $\frac{v_{j_a}}{v_u}$ of Injection

	High Angle	Low Angle	Positive Skew
$\dot{m}_j$	9.7 $\frac{g}{s}$	4.8 $\frac{g}{s}$	–
v_{j_t}	14.1 $\frac{m}{s}$	13.3 $\frac{m}{s}$	13.3 $\frac{m}{s}$
M_{j_t}	0.136 N	0.063 N	0.127 N
c_j	0.0126	0.0042	0.017

Table 5.2: Reference 100% Set Injection Conditions compared to Positive Skew (per Blade Pitch)

Design Injection	High Angle	Low Angle
100%	1.62	0.80
150%	2.42	1.21
200%	3.22	1.60
250%	4.02	1.80
300%	4.83	2.40

Table 5.3: Injected Air to Cascade Mass Flow Ratio r in Percent [%]

higher than common root leakage air fluxes.

5.2 Injection Model

The comparison of losses for the cascade flow with upstream injection compared to the unblown case is not straightforward, since some account has to be taken of the energy of the injected air. The problem is similar to that with air injection for turbine blade cooling. An idealized model is shown in Figure 5.5.
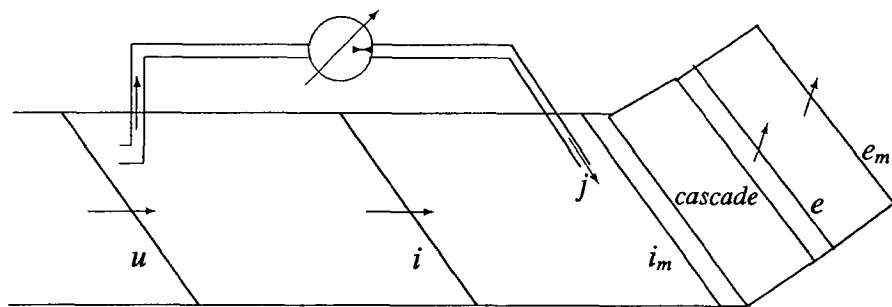
Figure 5.5: Idealized Model for Injection

The mass flow through the cascade is kept constant and the injected air may be thought of as being taken after the upstream plane u, so the mass flow past the inlet i and the injected air j equal the cascade flow $\dot{m}_u = \dot{m}_e = \dot{m}_i + \dot{m}_j$. There are two planes used for the mixed-out analysis, one at inlet i_m and the other at exit e_m. There is a pump which provides the energy for the injected air.

5.2.1 Availability

The concept of availability is helpful in this situation where the availability function for steady flow in open systems may be defined (Hahne [1992], pg. 213) as

$$\varepsilon \doteq h_0 - T_{amb}\sigma \qquad (5.28)$$

Availability is also called *exergy*, hence the symbol ε.

For an infinitesimal change

$$d\varepsilon \;=\; dh_0 - T_{amb}d\sigma \tag{5.29}$$

and for incompressible flow at ambient temperature

$$d\varepsilon \;=\; dh_0 - T_0 d\sigma \tag{5.30}$$

$$=\; \frac{1}{\rho}dp_0 \tag{5.31}$$

or for a finite change, the change in availability is

$$\Delta\varepsilon \;=\; \frac{1}{\rho}\Delta p_0 \tag{5.32}$$

Here, availability or exergy can be thought of in terms of total pressure loss.[4] The

analysis becomes more complex in compressible flow.

The stagnation pressure p_0 is constant between planes u and i, so that

$$p_{0_u} \;=\; p_u + \frac{1}{2}\rho v_u^2 \tag{5.33}$$

$$=\; p_i + \frac{1}{2}\rho v_i^2 \tag{5.34}$$

$$=\; p_{0_i} \tag{5.35}$$

The change in availability flux between the exit plane and the inlet and injected

air (per cascade unit mass flow) is

$$\Delta\varepsilon \;=\; \varepsilon_e - ((1 - r)\varepsilon_i + r\varepsilon_j) \tag{5.36}$$

---

[4]A loss in exergy is also identical to the irreversible production of entropy (Hahne [1992], pg. 216), thus confirming the result of Moore [1983] on pg. 5.

where $r = \frac{\dot{m}_j}{\dot{m}_u}$ denotes the mass injection ratio. It follows

$$\Delta\varepsilon \;=\; p_{0_e} - p_{0_i} - r(p_{0_j} - p_{0_i}) \tag{5.37}$$

For this model it is convenient to assume that the static pressure at the injection plane p_j is the same as the upstream pressure p_u, although the flow will have some contraction from the inlet plane i to allow for the injected mass flow. Thus $p_{0_j} - p_{0_i} = p_{0_j} - p_{0_u} = \frac{1}{2}\rho(v_j^2 - v_u^2)$. Non-dimensionalising the availability change with respect to the upstream kinetic energy per unit mass flow gives

$$\begin{aligned}
c_{\varepsilon_b} &= \frac{\Delta\varepsilon}{\frac{1}{2}v_u^2} \tag{5.38} \\[2mm]
&= \frac{p_{0_e} - p_{0_u}}{\frac{1}{2}\rho v_u^2} - r\left(\left(\frac{v_j}{v_u}\right)^2 - 1\right) \\[2mm]
&= -c_{p_e} - c_j + r \tag{5.39}
\end{aligned}$$

where c_{p_e} is the total pressure *loss* coefficient from upstream to exit. c_{ε_b} is a gross coefficient in that it includes the inlet boundary layer loss, which is assumed to occur downstream of plane i.

Comparing the blown and unblown cases, an availability gain coefficient can be derived

$$\begin{aligned}
c_{\varepsilon_g} &= [c_{p_e}]_{ub} - [c_{p_e}]_b - c_j + r \tag{5.40} \\[2mm]
&= \big([c_{p_e}]_{ub} - [c_{p_e}]_b\big) - r\left(\left(\frac{v_j}{v_u}\right)^2 - 1\right) \tag{5.41}
\end{aligned}$$

The first term in equation (5.41) is the change in loss coefficient for the unblown and blown cases. The second is the excess kinetic energy of the injected air over the inlet air. Thus, in Figure 5.5, the air is shown as being extracted by a pitot tube, i.e. at the stagnation pressure p_{0_u}, and the pump has to supply only this

excess kinetic energy. In fact, if $v_j < v_u$, the pump would produce work, which is unrealistic. An alternative assumption is that the injected air is available at upstream static pressure p_u, so that the pump has to supply all the kinetic energy of the injected air. This gives a modified availability gain coefficient

$$c_{\varepsilon_g^*} = \left([c_{p_e}]_{ub} - [c_{p_e}]_b\right) - r\left(\frac{v_j}{v_u}\right)^2 \tag{5.42}$$

$$= [c_{p_e}]_{ub} - [c_{p_e}]_b - c_j \tag{5.43}$$

In reality there will be extra losses due to the internal friction in the injection system. These are excluded here.

It would be possible to derive both equations (5.40) and (5.43) from a simple consideration of the energy fluxes occurring in a cascade with injection. The above analysis is more general and may be extended to compressible or heated flows in which case the concept of availability would be essential.

5.2.2 Mixed-Out Analysis[5]

To remove to some extent the effect of a downstream traverse plane's distance from the trailing edge, losses are often expressed in terms of mixed-out values, i.e. those at a fictitious mixed-out plane e_m (Figure 5.5). With the disparity between the injected and inlet air vectors, a potential mixing loss can be evaluated by considering an inlet mixed-out plane i_m. Of course, the real flow does not mix out before the cascade inlet, the plane i_m being a mathematical fiction.

The continuity equation is

$$\dot{m}_i + \dot{m}_j = \dot{m}_{i_m} \tag{5.44}$$

[5]Private Communication, Gregory-Smith [1991].

$$= \dot{m}_u \qquad (5.45)$$

and per blade pitch s

$$\rho h s v_i \cos\alpha_i + \rho t s v_j \sin\theta = \rho h s v_{i_m} \cos\alpha_{i_m} \qquad (5.46)$$

The *axial* momentum equation is

$$\dot{m}_{i_m} v_{i_m} \cos\alpha_{i_m} - \dot{m}_i v_i \cos\alpha_i = (p_i - p_{i_m})\hbar s \qquad (5.47)$$

(The injected air has no axial component of momentum.)

With continuity this can be expressed as

$$p_i - p_{i_m} = \frac{\dot{m}_u^2}{\rho\hbar^2 s^2}\left(1 - (1-r)^2\right) \qquad (5.48)$$

Using equations (5.46) and (5.48), the total pressure change ('loss') between planes i and im is given by

$$p_{0_i} - p_{0_{i_m}} = p_i - p_{i_m} + \frac{1}{2}\rho(v_i^2 - v_{i_m}^2) \qquad (5.49)$$

$$= \frac{\dot{m}_u}{\rho\hbar^2 s^2} \cdot$$

$$\left(1 - (1-r)^2 + \frac{1}{2}\left((1-r)^2 \sec^2\alpha_i - \sec^2\alpha_{i_m}\right)\right) \qquad (5.50)$$

or in terms of a loss coefficient

$$c_{p_{i_m}} = \frac{p_{0_i} - p_{0_{i_m}}}{\frac{1}{2}\rho v_u^2} \qquad (5.51)$$

with $\alpha_u = \alpha_i$ it follows

$$c_{p_{i_m}} = 2\left(1 - (1-r)^2\right)\cos^2\alpha_i + (1-r)^2 - \cos^2\alpha_i\sec^2\alpha_{i_m} \quad (5.52)$$

The mixed-out flow angle α_{i_m} is obtained from the *tangential* momentum equation

$$\tan\alpha_{i_m} = (1-r)^2\tan\alpha_i + \frac{r^2}{\frac{t}{h}}\cot\theta_j \quad (5.53)$$

Together with the continuity equation (5.46), this gives

$$\tan\alpha_{i_m} = (1-r)^2\tan\alpha_i + \frac{r^2}{\frac{t}{h}}\cot\theta_j \quad (5.54)$$

Substitution into equation (5.52) yields with some manipulation

$$c_{p_{i_m}} = (1-r)^2 - \cos^2\alpha_i \cdot$$
$$\left(2(1-r)^2 - 1 + \left((1-r)^2\tan\alpha_i\left(\frac{r^2}{\frac{t}{h}}\right)\cot\theta_j\right)^2\right) \quad (5.55)$$

Following the availability analysis on pg. 122, the change of availability from the inlet plus jet to the mixed-out inlet plane i_m is

$$\frac{\Delta\varepsilon_{i_m}}{\frac{1}{2}v_u^2} = -c_{p_{i_m}} - c_j + r \quad (5.56)$$

A similar expression can be written for the mixed-out exit plane, so that on subtraction to get the change from the mixed-out planes i_m to e_m, the jet kinetic energy term cancels to give

$$\frac{\Delta\varepsilon_{e_m}}{\frac{1}{2}v_u^2} = c_{p_{i_m}} - c_{p_{e_m}} \quad (5.57)$$

whereby $c_{p_{e_m}}$ is the mixed-out exit loss coefficient $\frac{p_{0_{e_m}} - p_{0_u}}{\frac{1}{2}\rho v_u^2}$ obtained by measurement.

Thus comparing blown and unblown cases, the availability gain coefficient between the mixed-out planes is

$$c_{\varepsilon_{g_m}} = \left[c_{p_{i_m}} - c_{p_{e_m}} \right]_b + \left[c_{p_{e_m}} \right]_{ub} \tag{5.58}$$

It could be said that $c_{\varepsilon_{g_m}}$, the mixed-out gain coefficient, is an indication of the aerodynamic gain of blowing excluding the mixing loss effect of the injection.

The mixing loss coefficient $c_{p_{i_m}}$ can be evaluated from equation (5.55) for some typical conditions at the low angle. An injection rate of 1% corresponding to about 75% of design gives $c_{p_{i_m}} = 8.9 \cdot 10^{-3}$ (Figure 5.12) and 2% corresponding to exactly 250% gives $c_{p_{i_m}} = -4.35 \cdot 10^{-3}$, i.e. a rise in total pressure. It happens that within the range of these injection rates $c_{p_{i_m}}$ is approximately zero and so all the excess kinetic energy in equation (5.56) is lost on mixing and the mixed-out gain coefficient $c_{\varepsilon_{g_m}}$ (equation (5.58)) is approximately $c_{\varepsilon_{g_m}} \approx \left[c_{p_{e_m}} \right]_{ub} - \left[c_{p_{e_m}} \right]_b$. With higher blowing ratios, $c_{p_{i_m}}$ becomes more significant.

The mixed-out analysis assumes that the jet is mixing with a uniform flow, whereas in fact there is a boundary layer on the end wall into which the jet is injected. Unfortunately this boundary layer will be altered by the upstream effects of the jet injection, so its details are not known exactly, and, if it were known, a complete mixing analysis would have to be done by numerical integration. One way of simplifying the problem is to assume that the inlet boundary layer mixes out to a uniform flow before the injection process and its subsequent mixing out. Thus the value of $c_{p_{i_m}}$ excludes the inlet boundary loss, which cancels by subtraction of the unblown from the blown mixed-out exit coefficients. It can be shown that for a boundary layer, the loss coefficient can be expressed as $c_p = \frac{\delta_2}{h - \delta_1}$ and the

mixed-out loss coefficient as $c_{P_m} = \frac{2\delta_2}{h} + \left(\frac{\delta_1}{h}\right)^2$. For the end wall boundary layer

with $h \gg \delta_1$, the ratio of mixed-out to unmixed loss is $\frac{c_{P_m}}{c_P} \simeq \frac{2\delta_2}{\delta_3} = \frac{1+3n}{1+2n}$ for a

power law profile with the inverse exponent n. The unblown boundary layer has

an average value of 0.119 (Table 3.1, pg. 21), so that the ratio is 1.10, indicating

only a small increase in loss on mixing out.

The mixing out of individual jets rather than a uniform injected flow would

result in an higher mixing loss. This effect is not be accounted for in the above

analysis.

5.2.3 Skew Correlation Parameter

Wegel [1969] suggests a 'subflow' parameter defined as tangential velocity times

tangential massflow to correlate the effect of (negative) skew, provided by either a

rotating belt or by upstream boundary layer blowing, on loss. The more physical

tangential momentum, which is defined as tangential velocity times the *axial* mass-

flow, together with the kinetic energy of the injection should yield a more robust

correlation. Combination of equations (5.7) and (5.15) gives for the tangential

momentum

$$\dot{M}_{j_t} = (4\rho A_j)^{\frac{1}{3}} \cdot \cos(\theta) \sin^{\frac{1}{3}}(\theta) \cdot \dot{E}_j^{\frac{2}{3}} \qquad (5.59)$$

The first term is a constant, the second is approximately constant (0.67 ± 0.01 for

typical angles between 20° and 35°) and the kinetic energy becomes fairly linear at

high values. The relation between kinetic energy and tangential momentum seems

to be rather independent of the injection angle within a certain range and shows an

almost proportional relationship to the injected kinetic energy at higher injection

rates (Figure 5.4, pg. 119). However, this might not be true for a different pitchwise

injection angle and would have to be investigated together with the indifference to

the injection angle for that case.

The non-dimensionalised loss reduction is plotted against the ratio of tangentially injected to mainstream momentum (Figure 5.6). The similar shape of the curves for the downstream non-mixed and mixed-out loss coefficients and the high and low angle could justify a general loss correlation based on momentum. The loss reduction is lower for the low angle but occurs at a lower tangential momentum. The performance of the belt is superior to injection.

A plot of non-dimensionalised loss reductions against the jet kinetic energy in Figure 5.7 is qualitatively similar to the previous Figure 5.6 with the tangential momentum as abscissa. This may be expected from their almost linear relation at higher injection rates and the independence from the injection angle. Although the tangentially injected momentum is a more physical correlation parameter, plots against the jet kinetic also provide information on the necessary investment in energy to achieve a reduction.
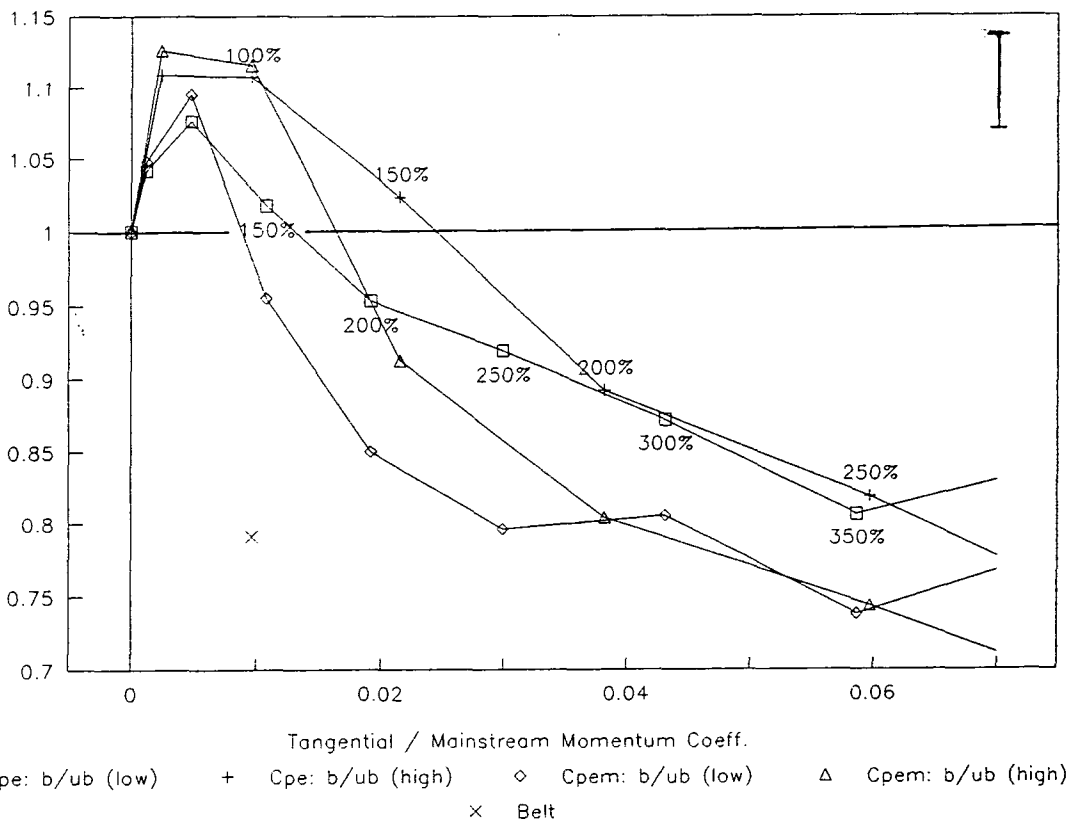
Figure 5.6: Total Pressure Loss Reduction $\frac{[c_{p_e}]_b}{[c_{p_e}]_{ub}}$ over Tan. Momentum Ratio $\frac{\dot{M}_{jt}}{\dot{M}_u}$
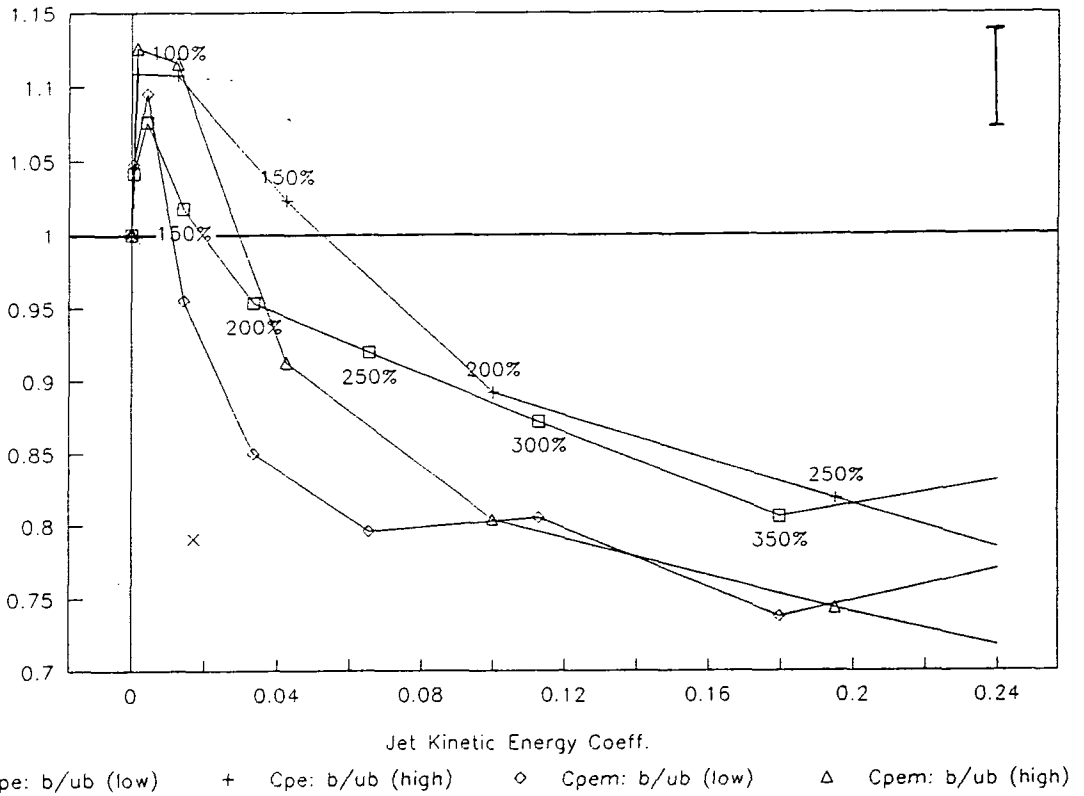
Figure 5.7: Total Pressure Loss Reduction $\frac{[c_{p_e}]_b}{[c_{p_e}]_{ub}}$ over Jet Kinetic Energy c_j

INJECTION MODEL 5.2

5.3 Area-Averaged Results

Mass-averaged data is plotted over a given traverse plane area against the jet kinetic energy coefficient c_j in the following. The distance of the 5H-probe not only from the endwall but also from the blade surface introduces an uncertainty in the mass-averaged data.

Error bars drawn in Figures 5.6 to 5.17 are based on assessments in Section 3.2.5 and follow the propagation rules for systematic and maximum random contributions. The error in the jet kinetic energy is not represented in the error bandwidth due to difficulties with the exact injection conditions (Section 3.1.2). The error of the secondary kinetic energy coefficient is not given because of its indirect calculation from pressure calibration data.

Numerical values for zero and 250% at the high and low angle are listed in Appendix A.2.

5.3.1 Injection Slot Downstream Radius

The first slot geometry for the high angle had a sharp downstream edge, which was later rounded, in an attempt to avoid separation and recirculation behind the jet sheet (Section 3.1.2). The resulting different flow structure could be seen in area plots (Section 4.5). The effect on the mass averaged loss coefficient c_p over the area of slots 2 and 10 is shown in Figure 5.8. It can be seen that there is a definite improvement with the rounded edge, particularly at the exit slot 10. All subsequent results are for the rounded downstream edge.

5.3.2 Secondary Kinetic Energy

The effect of the injection on the secondary kinetic energy for the high angle is seen in Figure 5.9 at slots 2 and 10 and for the low angle in Figure 5.10 at slots 1,
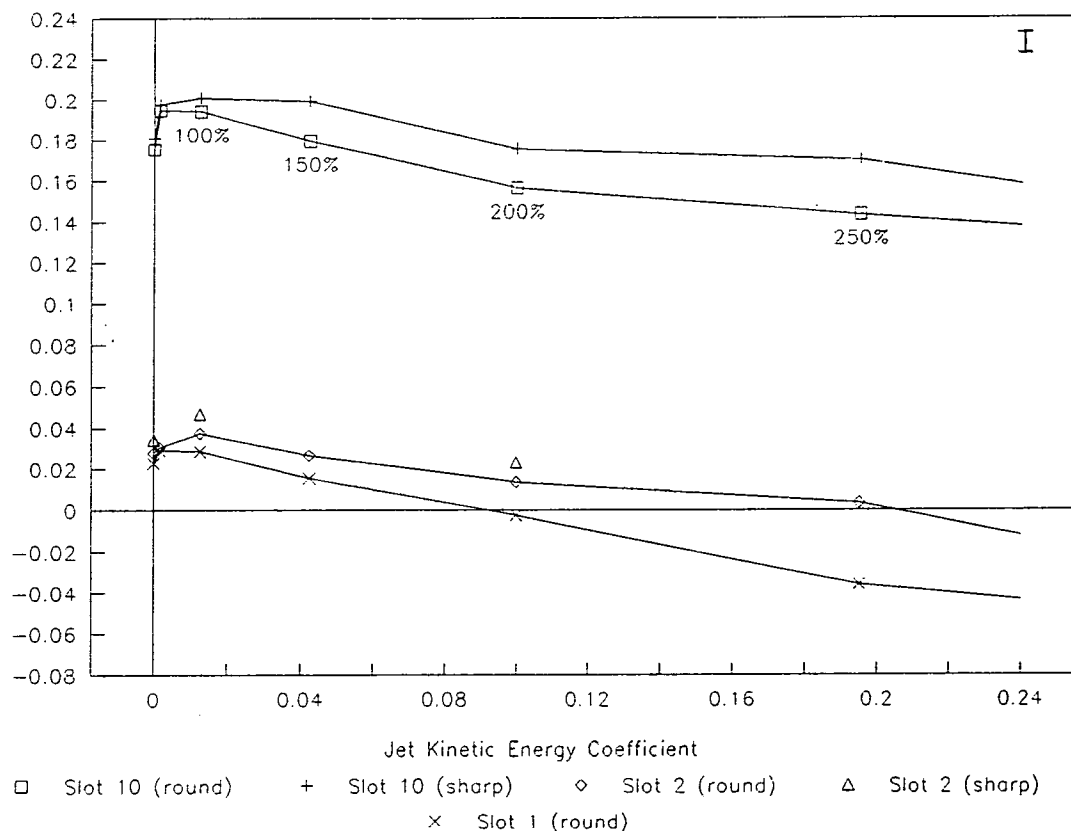
Figure 5.8: Comparison of Total Pressure Loss Coefficients c_p for the Sharp and Round Edge - High Angle

2, 5, 8 and 10. The values increase almost steadily for both the high and low angle at slot 2 and also for low angle at slot 1. Data for the high angle at slot 1 is not plotted due erroneous readings by 5H-probe (Section 4.1.1, pg. 38). The slot 10 kinetic energy at the high angle rises initially before falling to a minimum at 250% injection. With the low angle, similar behaviour is noted for slots 5, 8 and 10 with a minimum at 300% for the latter two. The jet kinetic energy coefficient at 300% injection amounts to 0.195 and 0.113 for the high and low angle. The trend has already been seen in the area plots with an initial increase and then a decrease at higher injection rate due to enhancement and re-energization of the inlet boundary layer. The rise in secondary kinetic energy beyond the minimum point is attributed to the injection being so strong that the exit flow starts to contain a vortex counter to the original secondary vortex. With higher injection (300% high and 400% low angle data are not shown but have been measured) there is no significant further
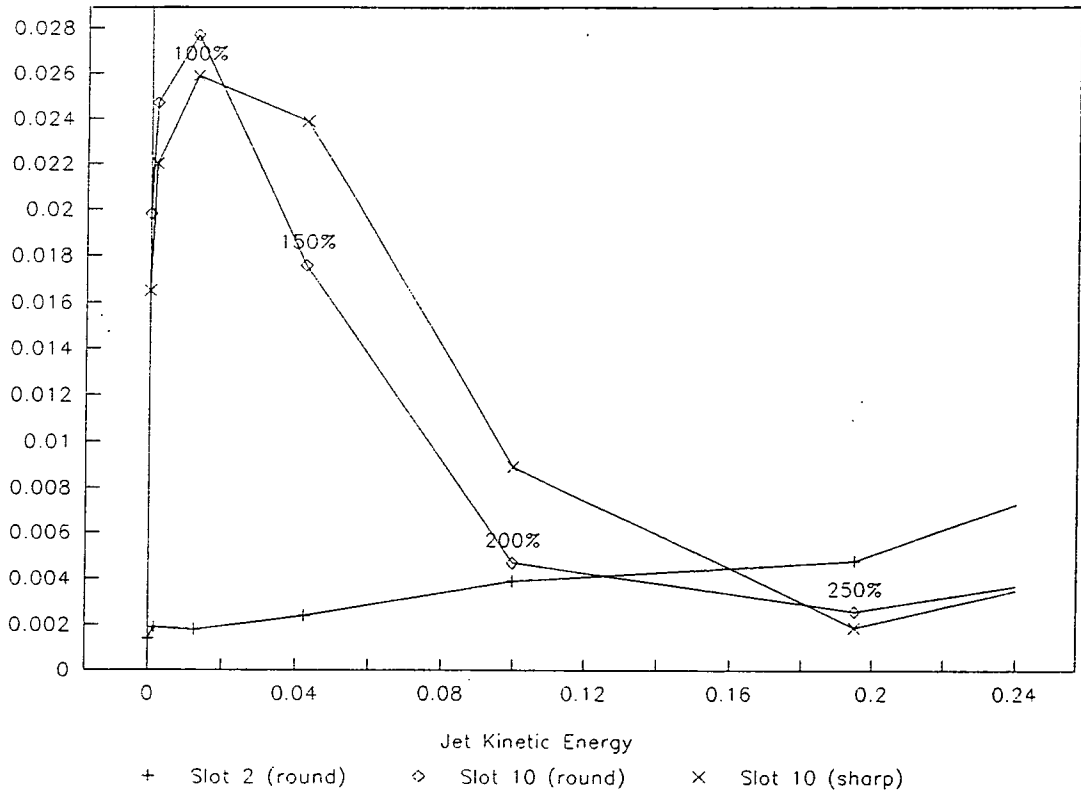
Figure 5.9: Variation of the Secondary Kinetic Energy Coefficient c_{ske} over Jet Kinetic Energy Coefficient c_j - High Angle
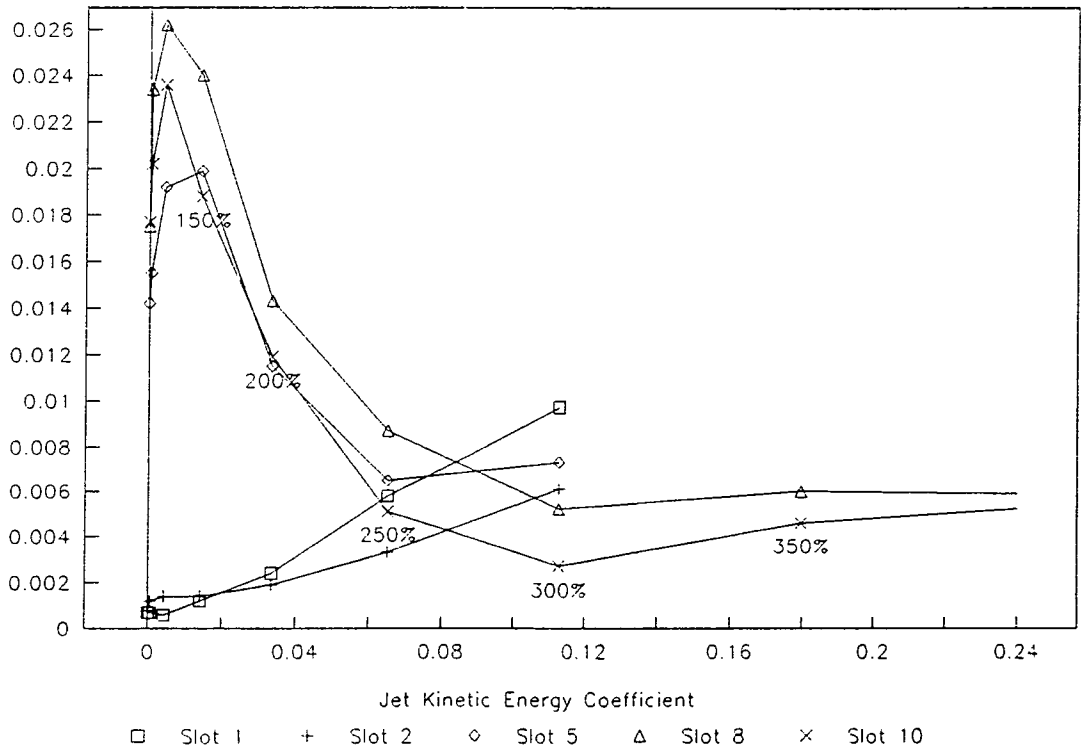
Figure 5.10: Variation of the Secondary Kinetic Energy Coefficient c_{ske} over Jet Kinetic Energy Coefficient c_j - Low Angle

rise which is partly due to the scaling of the plots.

In Walsh's positive skew case, a halving in c_{ske} at slot 10 from 0.043 to 0.022 was achieved. The much higher values for the secondary kinetic energy coefficient is due to a thicker inlet boundary layer (0.041 compared to 0.023 here) and so the comparison is not exact. For the same momentum and kinetic energy as with the belt, the high and low angle injection rates are 100% and 150% respectively (Figure 5.4), corresponding to a peak in c_{ske} at slot 10 for the high angle and a near peak value for the low angle.

5.3.3 Overall Total Pressure Loss

Loss coefficients for the high injection angle are shown in Figure 5.11. There is an initial rise in loss for all the coefficients, those for slot 10 being particularly marked. The value of $c_{p_{i_m}}$ (equation (5.55)) gives an indication that the low energy fluid added at low injection rates causes a rise in loss initially, which is magnified by the time slot 10 is reached. The difference between the mixed-out and non mixed-out coefficients at slot 10 is largely due to the secondary kinetic energy as noted by e.g. Moore & Adhye [1985]. As the secondary kinetic energy is suppressed by the injection, the two values become closer. It follows that the improvement caused by injection for the mixed-out loss is greater than for the non-mixed out loss. Similar trends may be seen in Figure 5.12 for the low angle. The loss reduction from the maximum value is more rapid for slot 10 than for slots 1 and 2 indicating a longer actual mixing-out path from the injection location to within the blade passage. Low values of $c_{p_{i_m}}$ up to 250% are associated with a low hypothetical mixed-out loss but also indicate low levels of realistic mixing from the injection slot up to the blade leading edge.

A larger reduction in the loss coefficient c_{p_e} of 0.043 (from 0.206 to 0.163)
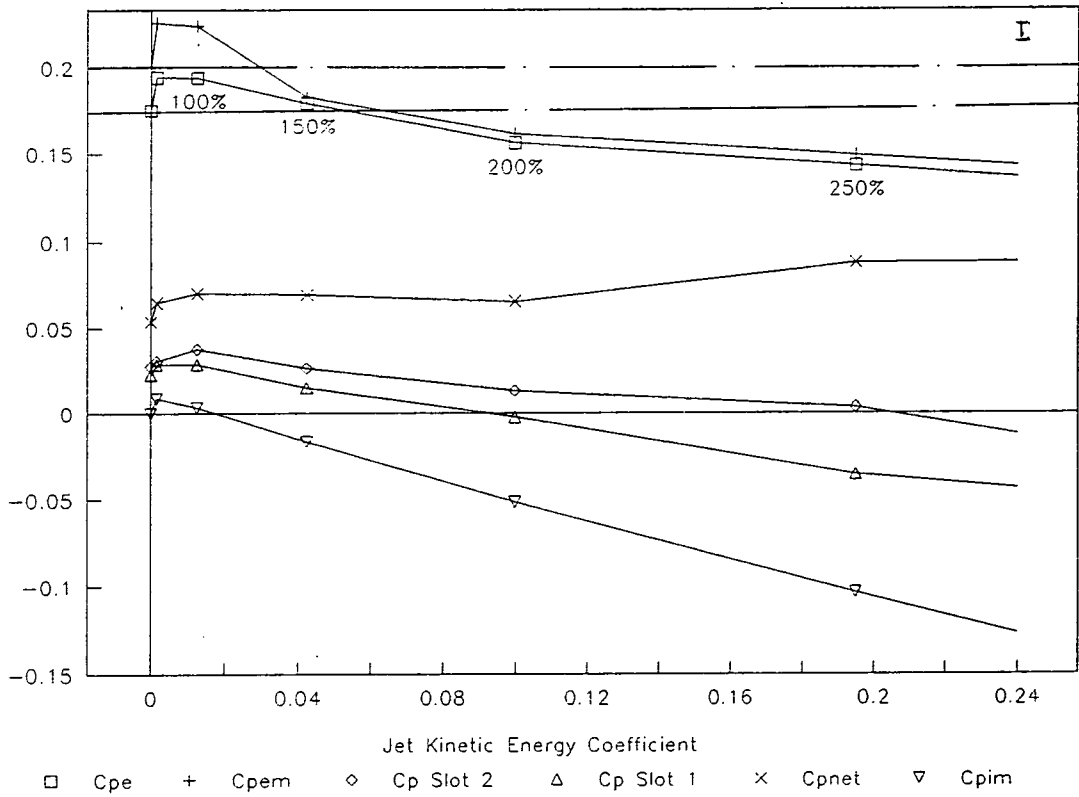
Figure 5.11: Variation of Loss Coefficients c_{p_e}, $c_{p_{e_m}}$, c_p, $c_{p_{net}}$, $c_{p_{i_m}}$ over Jet Kinetic Energy Coefficient c_j - High Angle
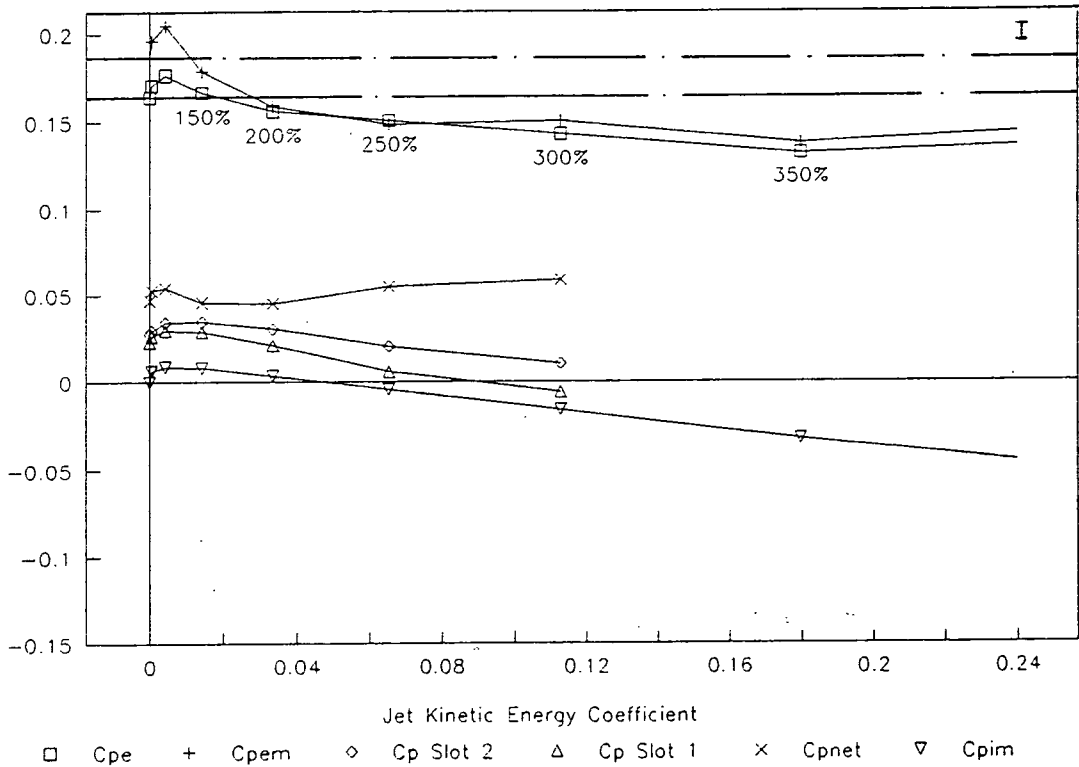
Figure 5.12: Variation of Loss Coefficients c_{p_e}, $c_{p_{e_m}}$, c_p, $c_{p_{net}}$, $c_{p_{i_m}}$ over Jet Kinetic Energy Coefficient c_j - Low Angle

was measured by Walsh in his positive skew case.

5.3.4 Axial Growth of Loss

Figure 5.13 shows the growth of total pressure losses along the cascade. The values start to rise from mid-passage to the trailing edge around the blade throat and downstream. A significant proportion of the loss generated within the blade passage is close to the walls and thus not detectable by 5H-probe measurements. This could explain the lower value at slot 5 compared to slot 2 for the no injection curve, if not attributable to experimental error. Higher injection rates reduce the amount of loss produced between mid-passage with increased and the trailing edge with lower values.
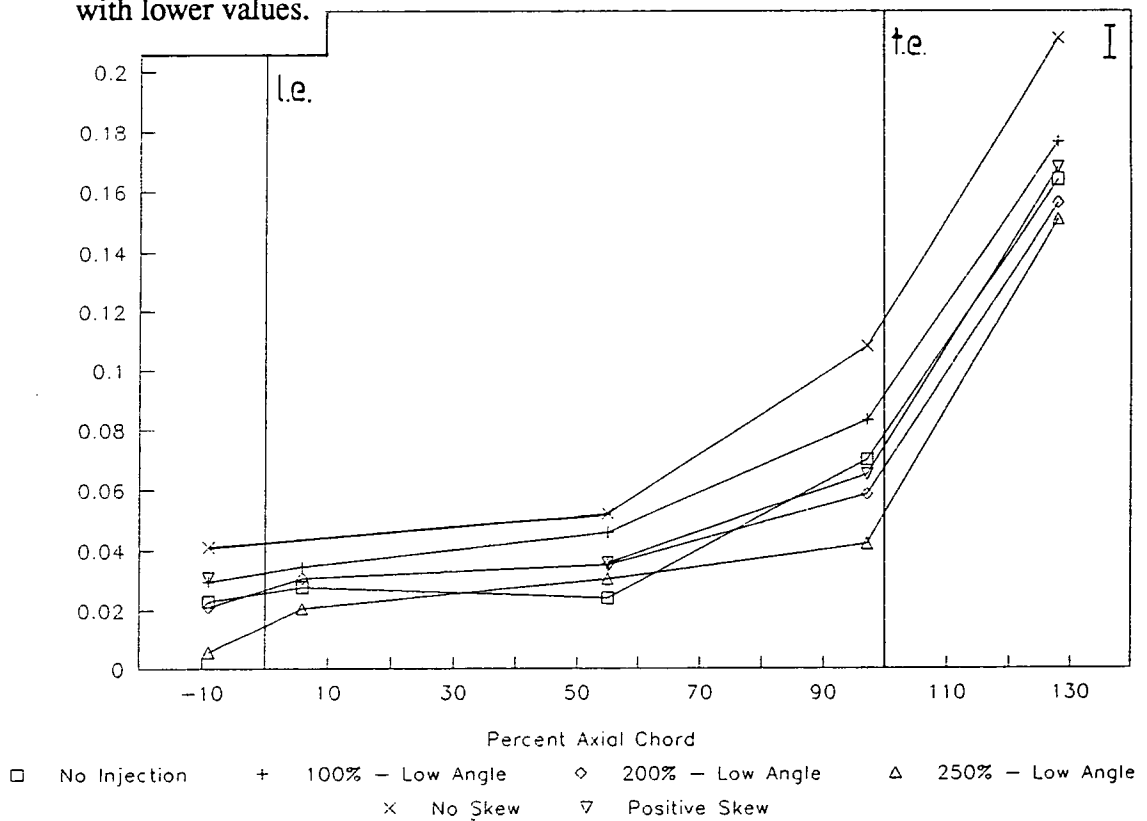
Figure 5.13: Growth of Total Pressure Loss along Axial Chord

Walsh's positive skew shows overall reduced values compared to no skew and a reduced gradient in the second half of the blade passage. A quantitative

comparison between positive skew and injection is seen to be difficult due to different values for the inlet loss (cf. Section 4.8.1) and a different loss growth but not invalid since the correct trends are oberservable. The positive skew curve is similar to 200% injection at the low angle following the discussion in Section 4.8.

5.3.5 Net Secondary Loss

The loss assessment has been based so far on constant upstream conditions being important for the transfer of the results to a real engine. A further investigation of loss generation mechanisms deals with the loss changes relative to the inlet conditions modified by the injection. A net secondary loss coefficient may be defined as the inlet loss coefficient downstream of the injection plane and the mixed-out profile loss coefficient subtracted from the downstream total pressure loss coefficient (cf. Section A.2):

$$c_{p_{net}} = c_{p_e} - c_{p_{slot\,1}} - c_{p_{midspan_{e_m}}}$$

The non mixed-out loss at inlet is used here since the mixing of the inlet boundary layer up to the blade leading edge is incomplete and insignificant with the blade passage.

Numerous investigators, e.g. Klein [1966], Marchal & Sieverding [1977], have shown the cascade net secondary loss to be independent of the non-skewed inlet boundary layer thickness, which is mainly due to an only small variation in the 'extra' loss associated with the secondary kinetic energy (Gregory-Smith & Graves [1983]). More generally, the influence of changes in the inlet vorticity components and shape parameters have to be considered (e.g. Belik [1968]).

The net secondary loss coefficient at the high angle is plotted in Figure 5.11, pg. 134. An almost constant increase is seen up to 200%. A further rise is noted

when the inlet loss coefficient becomes negative. The curve for the low angle in Figure 5.12, pg. 134, shows no increase for 150% and 200% injection. It starts to rise again when the inlet loss coefficient approaches zero. There is much uncertainty in these results because of the proximity of the injection slot to the measuring plane and the distance of the first 5H-probe measurement point above the endwall.

In Walsh's positive skew case, a substantial reduction in the net secondary loss coefficient of 0.027 is obtained (not shown).

5.3.6 Energy Gain

Figure 5.14 shows the two gain coefficients, which include accounting for the inlet kinetic energy, the availability gain coefficient c_{ε_g} from equation (5.40) and the
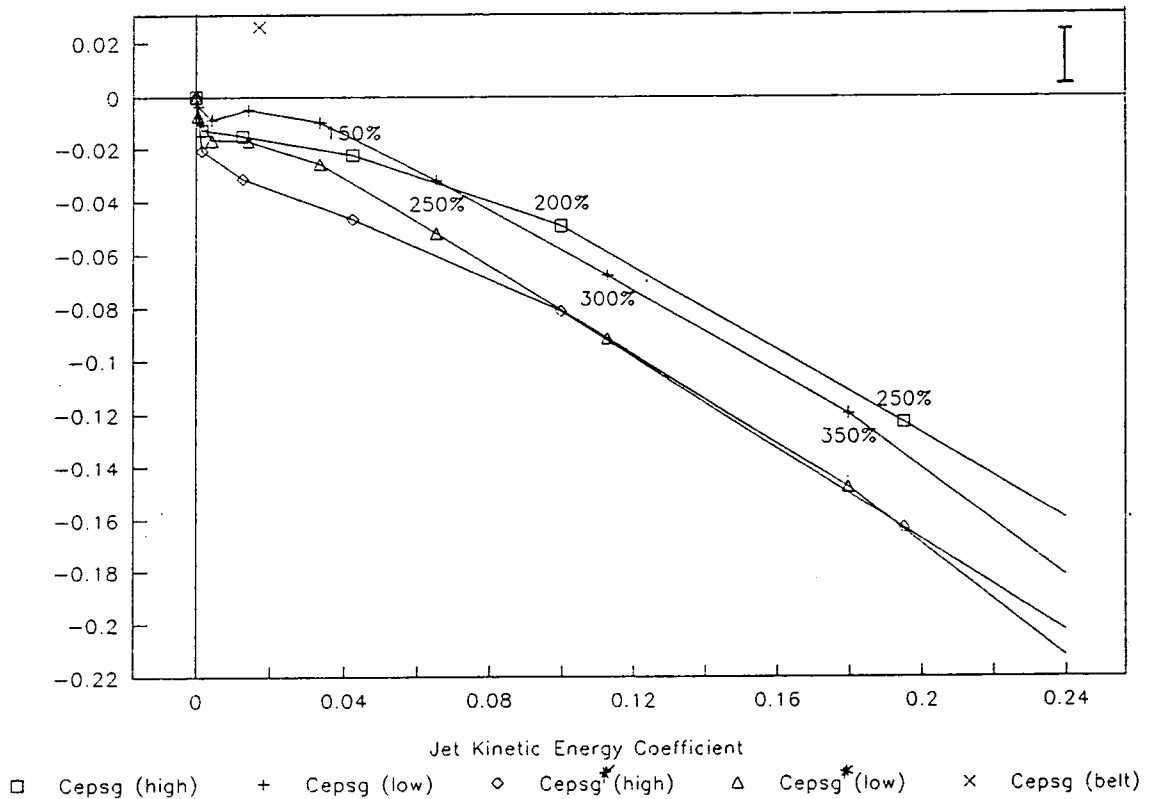
Figure 5.14: Variation of Gain Coefficients $c_{\varepsilon_g^*}$, c_{ε_g} over Jet Kinetic Energy Coefficient c_j

modified availability gain coefficient $c_{\varepsilon_g^*}$ from equation (5.43). The difference in the coefficients is r, the jet mass flow ratio, so for a given injection angle the two curves diverge slowly. The values of $c_{\varepsilon_g^*}$ for the high angle drop rapidly at very low injection and then level off with the low injection angle at 0.10 jet kinetic energy coefficient. The gain coefficient c_{ε_g} shows a slight rise for the low angle after an initial drop, before falling below the high angle curve due to the lower mass flow ratio of the former. However, neither of the curves give a positive gain, which indicates that there is no net improvement.

Walsh's positive skew case shows a positive gain of $c_{\varepsilon_g} = +0.026$.

An expression for the ratio of pay-back by loss reduction to investment by required power could be defined to:

$$\eta = \frac{\text{gain}}{\text{investment}}$$

$$= \frac{[c_{p_e}]_{ub} - [c_{p_e}]_b}{c_j}$$

Calculated values are shown in Figure 5.15. The pay-back ratio η is identical to the slope of the availability coefficient $c_{\varepsilon_g^*}$ of Section 5.2.1 for a constant gain. The value of about 2.5 for positive skew is much higher compared to about 0.3 with injection at the low angle and a negative value for the original design condition of 100% injection, which is due to a measured increase in loss (negative gain).

A comparison to equation (5.18), pg. 116, is possible: a four times larger gain than investment was obtained, if the integral value of the tangential momentum is provided by injection rather than by a rotating belt. The injection may provide the tangential momentum at a lower level of kinetic energy (equation (5.21)) but not with an optimum spanwise distribution, resulting in an over-estimation of the
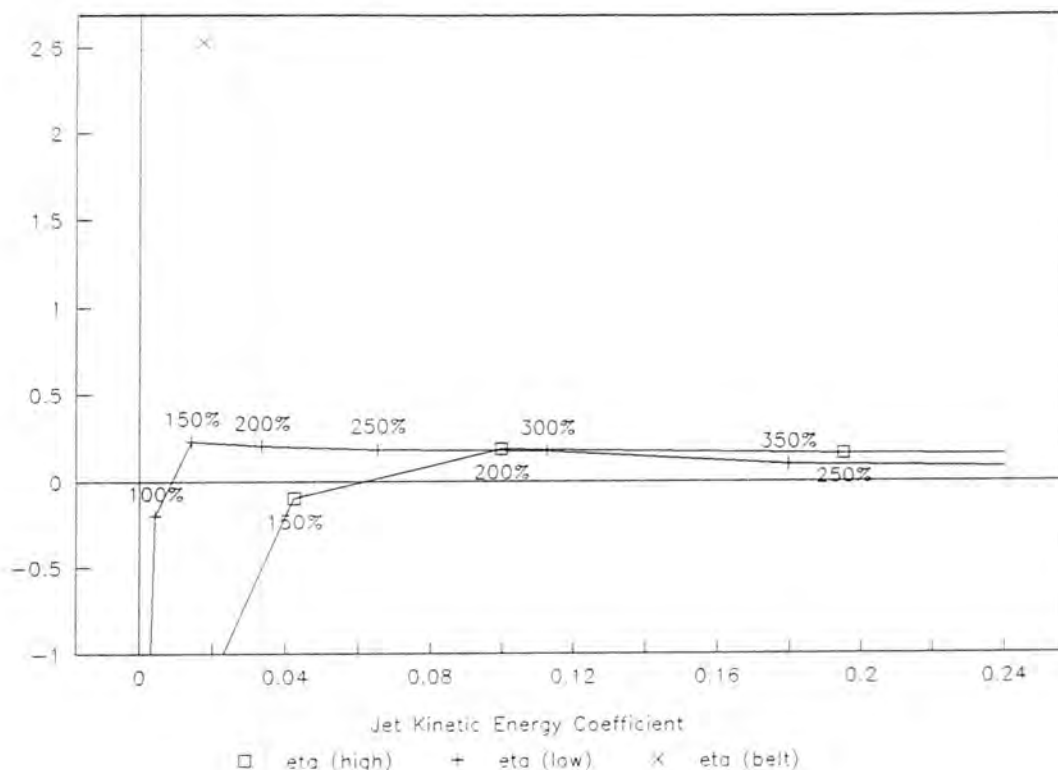
Figure 5.15: Efficiency of Injection

blowing benefits. A different inlet boundary with positive skew and with injection might also influence the comparison as well as injection losses and experimental uncertainties.

5.3.7 Mixed-Out Gain

Accounting for the injection mixing-out loss resulted in the mixed-out availability gain coefficient $c_{\varepsilon_{gm}}$ (equation (5.58)) plotted in Figure 5.16. A considerable region of positive gain exists for the low angle, with a peak in the region 200% to 250%, falling off beyond that as the increased energy of injection is not matched by a corresponding decrease in the exit mixed-out loss shown in Figure 5.12, pg. 134. The much poorer performance of the high angle indicates less significant, although high, mixing-out of the injected air at high injection rates due to lower loss reductions.
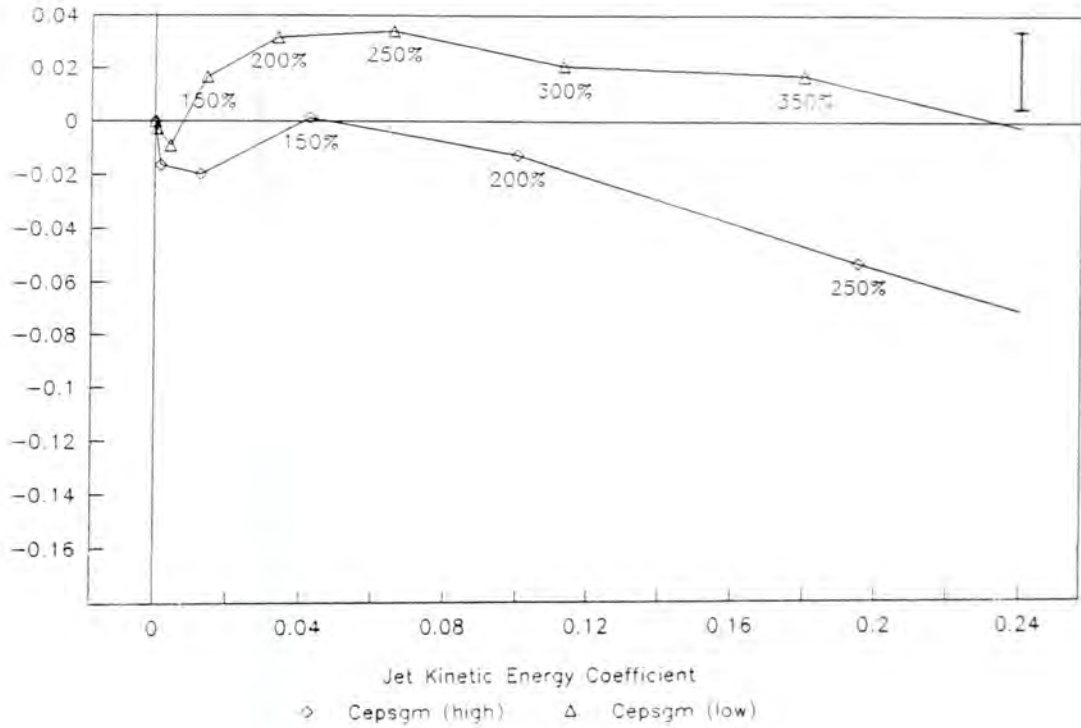
Figure 5.16: Variation of the Mixed-Out Gain Coefficient $c_{\varepsilon_{gm}}$ over Jet Kinetic Energy Coefficient c_j

A determination of the value for positive skew may require the numerical calculation of a 2D boundary layer mixing loss and will probably give a more positive coefficient than with injection.

5.3.8   Variation of Injection Angle

A study was carried out to see the effect of changing the assumed injection angle on the results presented above. An example is shown in Figure 5.17, where the modified availability gain coefficient $c_{\varepsilon_a^*}$, probably the most important parameter in terms of practical assessment, is shown for a variation from 30° to 40°. Although the actual points for a given injection condition (250% is marked) move, the overall curves fall within a narrow band, and so the results are essentially similar.

Uncertainties due to the distance of the 5H-probe from solid walls, an undeter-
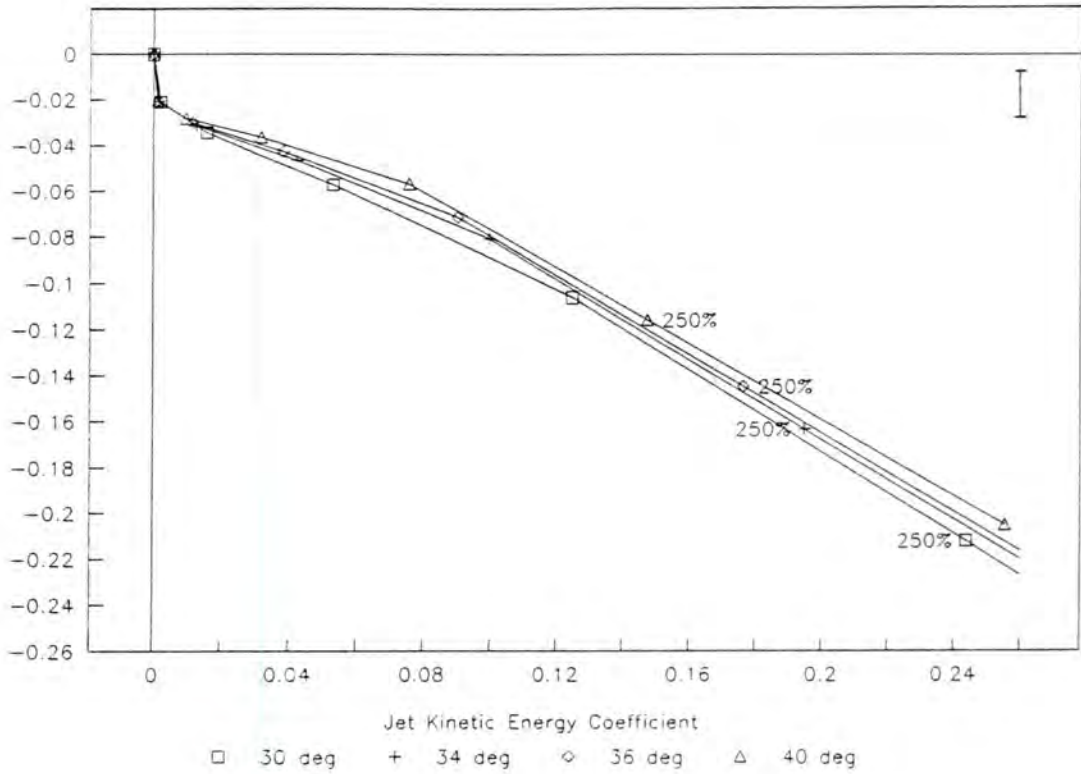
Figure 5.17: Effect of the Assumed Injection Angle Modified Availability Gain Coefficient $c_{E_g^*}$ - High Angle

mined injection slot exit area (Section 3.1.2) as well as the pitchwise non-uniform injection (Section 4.2.1) are thought not to affect the results qualitatively but might alter the curves in a similar manner as shown above.

Chapter 6

Computation

Computer simulation of air injection poses a severe test case for both the computational code (Section 6.1.1) and the turbulence modelling (Sections 7.4, 6.1.2) due to the injection details and complexity of the simulated flow. The calculated results are in only partial agreement with the experiment but have given valuable guidelines for the experiment and could help future attempts in injection modelling.

6.1 Numerical Methods

6.1.1 Navier-Stokes Solver[1]

Conventional Methods

Lakshminarayana [1991] provides a comprehensive review of Finite Volume and Finite Difference solution techniques for turbomachinery fluid dynamics concluding that the Moore Elliptic Flow Program (MEFP) gives one of the best performances due to low numerical mixing. Convergence of partial differential equations

---

[1]The main emphasis in this discussion is on steady, incompressible, single-passage flows as they are applicable to flow conditions found in the Durham Linear Cascade.

such as the Navier-Stokes equations requires the consistency (finite-difference equation approaches the partial differential one for an infinitesimal small grid) and stability (attenuation of truncation errors) of the differential operators.[2] Convective terms of the steady state equations are stabilized in MEFP by integration of linear interpolated central differences over upwinded control volumes (Moore [1985a]) leading to second order accuracy without numerical mixing (viscosity) and thus maximizing their consistency. The resulting set of equations is solved by means of a modified pressure correction method (Moore [1985b]). Low amounts of numerical viscosity are important, particularly when the control volumes are skewed relative to the main flow direction (Carey *et al.* [1992]). The effect of the turbulence model on the flow may be swamped by numerical mixing. MEFP had been chosen for simulating the cascade flow with injection despite the substantial cost of running the code.

An alternative method to the above described is the addition of (adaptive) artificial viscosity terms to control the stability of convective central differences from the governing equations' conservative form together with a time-marching solution algorithm (e.g. Dawes [1991]). The accuracy of these schemes is significantly less than second order.

Another method of stabilizing the discretized equations is to upwind convective terms and to perform a power law [3] interpolation (Spalding [1972]). No additional smoothing is necessary but numerical viscosity is being generated, which depends on the ratio of convection to diffusion terms (grid Péclet number). Commercial CFD packages such as PHOENICS and FLUENT use modified versions of this approach mostly combined with pressure correction solution techniques on staggered

---

[2]The theorem of Lax is strictly only valid for linear problems but frequently applied to non-linear problems such as the Navier-Stokes equations (Roache [1976]).

[3]The analytical solution of the convection/diffusion equation is an exponential.

grids. The former code had been applied to the cascade flow without injection; the performed study had to be abandoned due to the prediction of a total pressure loss gradient in the lossfree mid-span/mid-pitch region.

Hah [1984] uses a quadratic upwinding pressure correction scheme providing almost second order accuracy. In terms of accuracy, this code should be able to compete with MEFP. Comparing the mass-averaged growth of loss through Langston's cascade predicted by both codes, Hah's code is seen to over-predict the loss generation (Moore & Moore [1985]). However, results of this and previous work by Cleak *et al.* [1992] have shown a similar over-prediction of mass-averaged losses.

. Alternatively, viscous effects in adiabatic flows may be represented by a body force calculated from loss correlations (Hirsch [1988], pg. 81). The method is superior to Euler solvers and has given good results both for single blade rows (Denton [1986]) and for the multi-stage environment (Denton [1990]).

Alternative Techniques

Method of Weighted Residuals (MWR)   The governing equations may be represented by variational principles as a functional to be minimized (Finlayson [1972]). Various methods such as the Finite Element (Zienkiewicz [1971]) or the Spectral Method (Canuto *et al.* [1987]) evolve depending on the choice of weighting and trial functions. The Finite Volume method may also be considered as a specialized MWR (Fletcher [1988]). Advantages of these methods, such as accuracy, computing efficiency and geometrical flexibility should lead to a more widespread use in turbomachinery (e.g. Combes [1992]).

Lagrangian Methods   Convective terms in the governing equations may be avoided by maintaining the substantial derivative. The freely moving grid cells represent fluid control volumes causing no numerical mixing (Boris [1989]). The method is still impracticable for complex geometries.

Cellular Automata   Highly parallel structures derived from gas dynamics are able to model (compressible) fluid flows by definition of collision rules for a lattice gas - a 'silicon wind tunnel' is conceivable (Despain [1990]). Turbulence modelling is intrinsic. Solution of the Boltzmann equations with Monte Carlo methods has recently gained on interest (Chen *et al.* [1992]). Use of these approaches is still limited.

6.1.2 Turbulence Modelling

A mixing length model (Prandtl [1925]) with the mixing length depending on the shear layer thickness determined by the total pressure gradient (Cleak *et al.* [1991]) together with a 'Laminar Block', extending across the blade pitch up to 80% axial chord and up to 10% span from the end wall, has shown a superior performance in terms of passage vortex mobility and midspan loss production to a one-equation and k-ε/mixing-length hybrid model (Cleak & Gregory-Smith [1992]). Since the basic flow features in a linear turbine cascade are inviscid and with the complexity of the turbulent flow field (Chapter 7), this might even be expected.

The mixing length model had to be chosen also for the present investigation, for no other model had been implemented with the latest version of MEFP. The flow field was specified as turbulent throughout (no laminar regions) except from inside the injection slot (Section 6.2.2).

6.2   Computational Setup

6.2.1 Grid Geometry

The computational grid described in Cleak [1989] was refined to allow for upstream slot injection. The first plane above the endwall is displayed in Figure 6.1, where the area spanned by the injection slot and the downstream radius is indicated. The
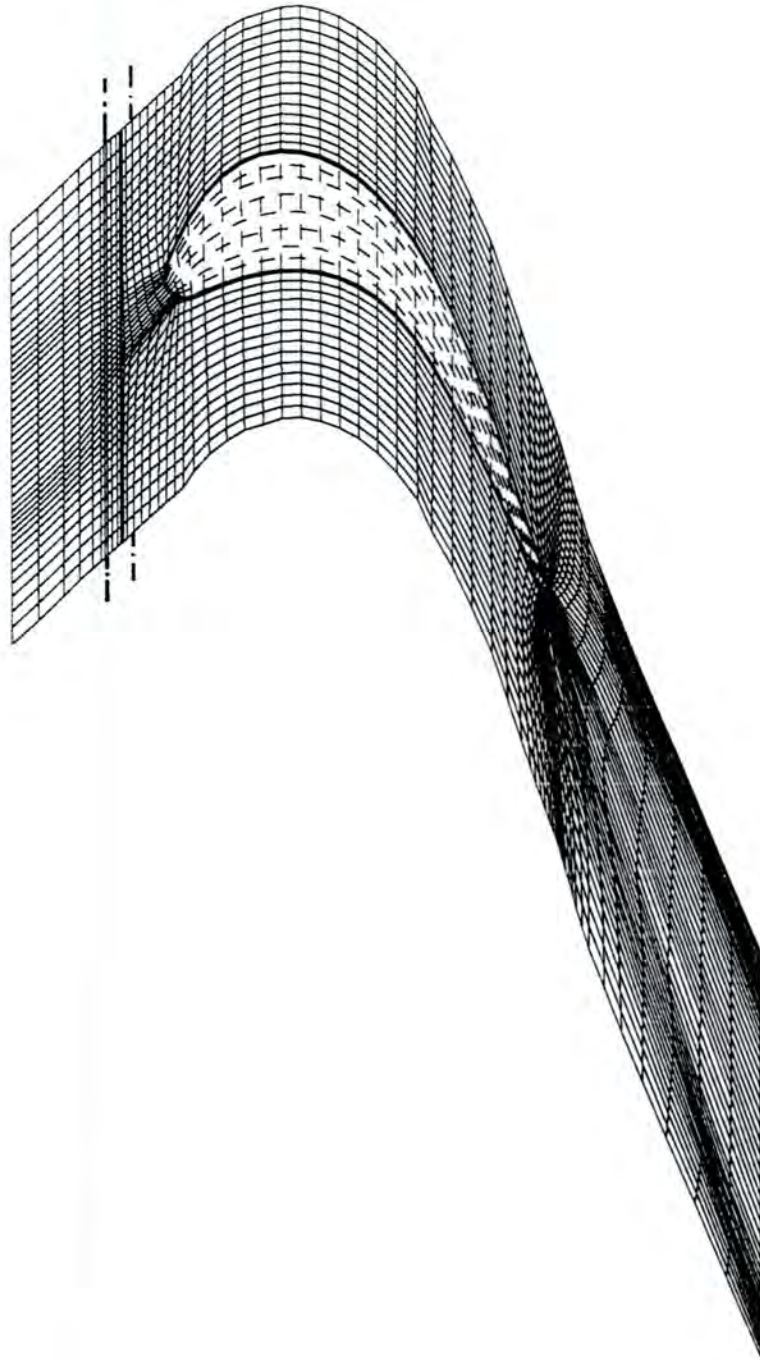
Figure 6.1: Blade-to-Blade View of Mesh at First Plane above Endwall
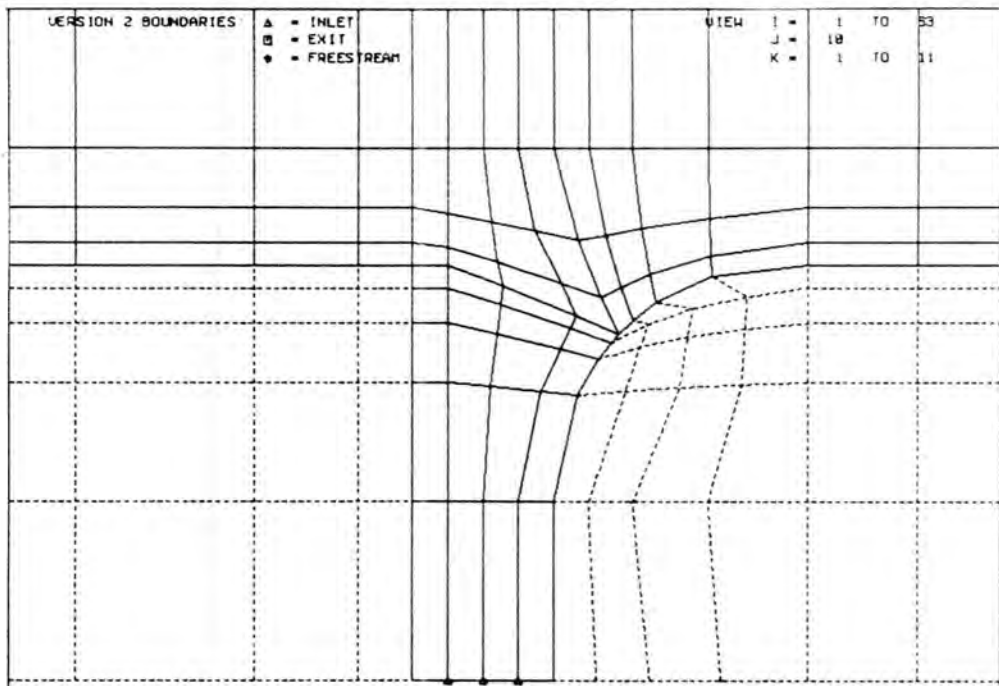
Figure 6.2: Cross-Section of Mesh at Injection Slot

structured grid extends into the injection slot and models the downstream radius (Figure 6.2).

The grid dimensions are 63 axial, 43 tangential and 25 radial plus 4, 43 and 5 lines within the injection slot giving a total of 68,585 points. Although a coarser grid of 49,622, which showed no substantial discrepancy to the finer grid, was used initially, the former was employed to ensure maximum flow resolution.

6.2.2 Injection Modelling

Injection Conditions

Addition of mass and momentum in MEFP is accomplished by specification of the total pressure. An experimental value was not available and so the total pressure of the injection was calculated by using the continuity of the mass flow measured at the orifice plate and the upstream measured free-stream static pressure. This gives rise to an error in the injected mass flow and velocities due to the loss produced between the two stations and the pitchwise non-uniform static pressure.

Injection Slot Geometry

The guide vanes of the injection slot were tried to be modelled by a sinusoidal total pressure variation with a period based on the eight injection vanes per pitch used in the experiment. This affects the injected kinetic energy causing a slight increase. The injected mass flow fell from its original value to give an injection rate of 232% instead of 250% at the low angle. In order to prevent early mixing out, the injected mass flow was kept laminar until it reached the endwall plane.

Initial runs without modelling the wakes of the injection vanes suggested inadequate mixing of individual jets with each other and with the mainstream. Introduction of a sine-wave superimposed on the injection did not change the situation significantly. An exact modelling of the injection slot geometry including its guide vanes and the emanating jets, was restricted by the effort associated with the generation of a suitable, structured grid. Solution-adaptive unstructured mesh geometries (Dawes [1992]) could be a remedy, but cost more CPU time and require more input data.

6.2.3 Inlet Boundary Layer

Experimental values (Table 3.1, pg. 21) suggested an approximate power law coefficient of 0.1 except for points closest to the endwall where the power law gives too low loss values. Measured 3H-probe data obtained by Walsh [1987] had to be substituted. Sole use of the power law results in an indistinct horseshoe pressure side leg on the endwall, which is out of position.

6.3 Computational Results

6.3.1 Data Selection

After initial modifications of both the injection rate and angle, the runs were confined to a representative case of nominal 250% injection (the actually achieved value is 232%, see Section 6.2.2) at the low angle. Total pressure loss and secondary flow vectors, plotted with the same post-processor as the experimental data although over different ranges at slots 1 and 10, may be compared for zero and 232% injection with measurements of slots 1, 2, 5, 8 and 10 at the low angle. Thus, a complete data set providing a starting point for future modelling purposes is available. Pitch- and area-averaged values were evaluated showing an increase in loss with the injection. A thorough comparison between computation and experiment, however, would require the knowledge of the near surface flow, which is not yet available.

The results for no injection may be compared to those of Cleak *et al.* [1991] comprising a version change of MEFP and modified mesh. The results are qualitatively very similar but show quantitative discrepancies (Section 6.3.3).

6.3.2 Area Plots

Predicted results (Figures 6.3, pg. 151, to 6.7, pg. 155) may be compared to experimental results (Figures 4.2, pg. 48, and 4.3, pg. 49) for no injection. Computations at nominal 250% injection (Figures 6.9, pg. 158, to 6.13, pg. 162) may be compared to the experiment at 200% (Figures 4.8, pg. 59, and 4.9, pg. 60). and 250% (Figures 4.10, pg. 63, and 4.11, pg. 64) injection. The different contour numbering should be noted (Appendix G.2).

A full comparison of computed to experimental data requires knowledge of the

5H-probe's minimum distance from the blade surfaces and the endwall (Table 6.1);

flow features close to walls revealed by computation cannot always be verified by

experiment. The distances are indicated in the area plots by point-dashed lines.

	SS	PS	Endwall
Slot 2	$\sim 23\ mm$	$\sim 12\ mm$	$5\ mm$
Slot 5	$\sim 11\ mm$	$\sim 12\ mm$	$5\ mm$
Slot 8	$\sim 21\ mm$	$\sim 9\ mm$	$5\ mm$

Table 6.1: Distance of Measurement from SS, PS and Endwall

No Injection

Slot 1   A higher total pressure loss than specified at inlet is calculated by slot 1

due to wall friction. Contour lines are plotted close to the endwall in contrast to

experimental data.

Slot 2 H_s is found slightly closer to the SS corner and H_p closer to midpitch

than in the experiment. The endwall loss is too high.

Slot 5   The total pressure loss core in the SS corner is qualitatively well predicted.

The centre of the passage vortex is situated too far away from SS and too high

above the endwall.

Slot 8   The lower of the double total pressure loss cores is displaced towards

the endwall and midpitch.   It is followed by a passage vortex, which lies at

approximately the same as measured distance from SS but closer to the endwall.

Slot 10   The predicted loss is overall too high with a distribution somewhat

similar to the experiment.   A counter-rotating vortex not measured is computed

behind the trailing edge at the former endwall corner.

a   SECONDARY VELOCITIES

———▶   VECTOR SCALE 20 METRES/SEC

d   TOTAL PRESSURE COEFFICIENT

CONTOUR INTERVALS 0.1
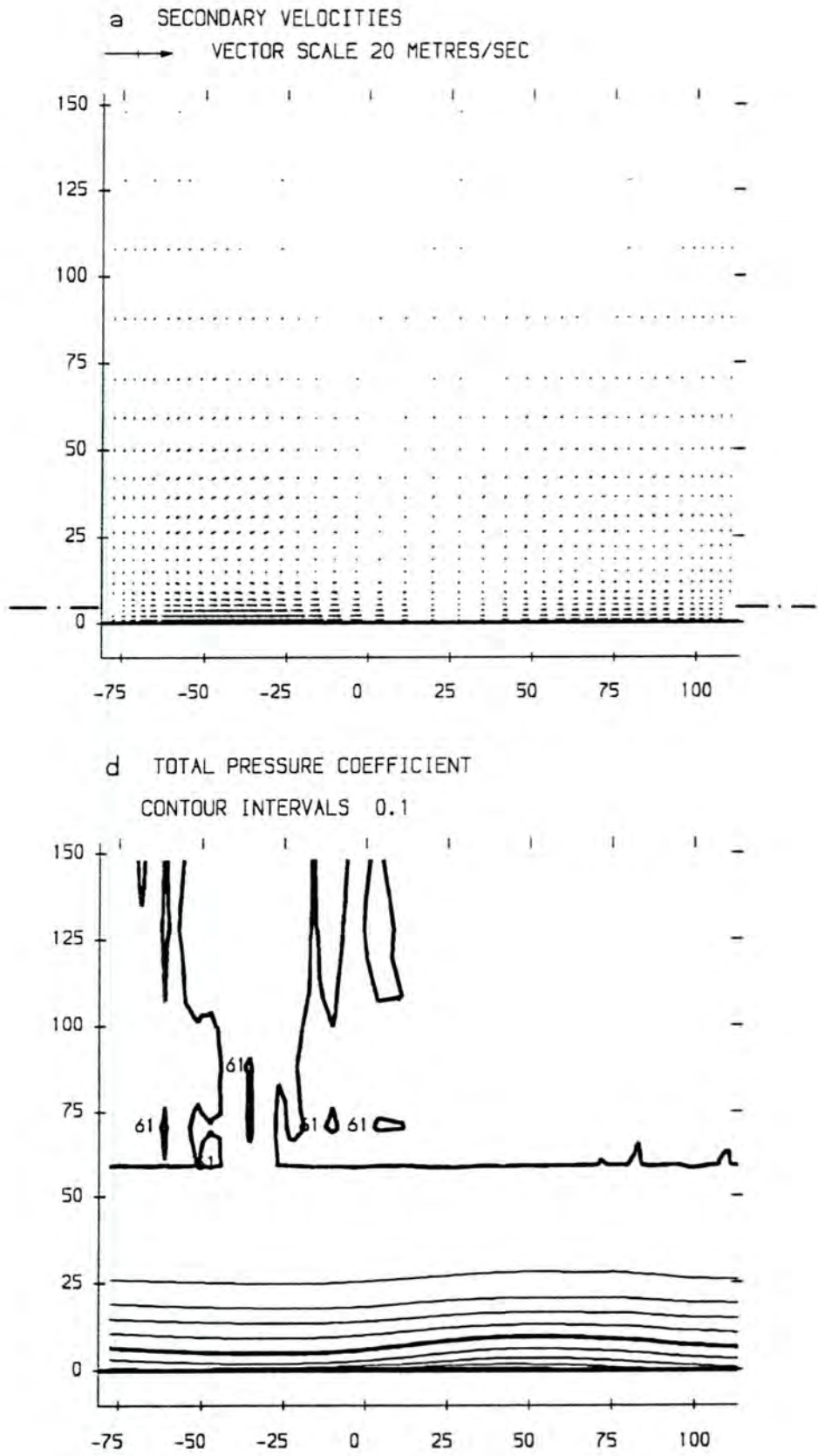
Figure 6.3: Contour Plot (Computation) of Slot 1 - No Injection

a   SECONDARY VELOCITIES

→   VECTOR SCALE 20 METRES/SEC

d   TOTAL PRESSURE COEFFICIENT

CONTOUR INTERVALS 0.1
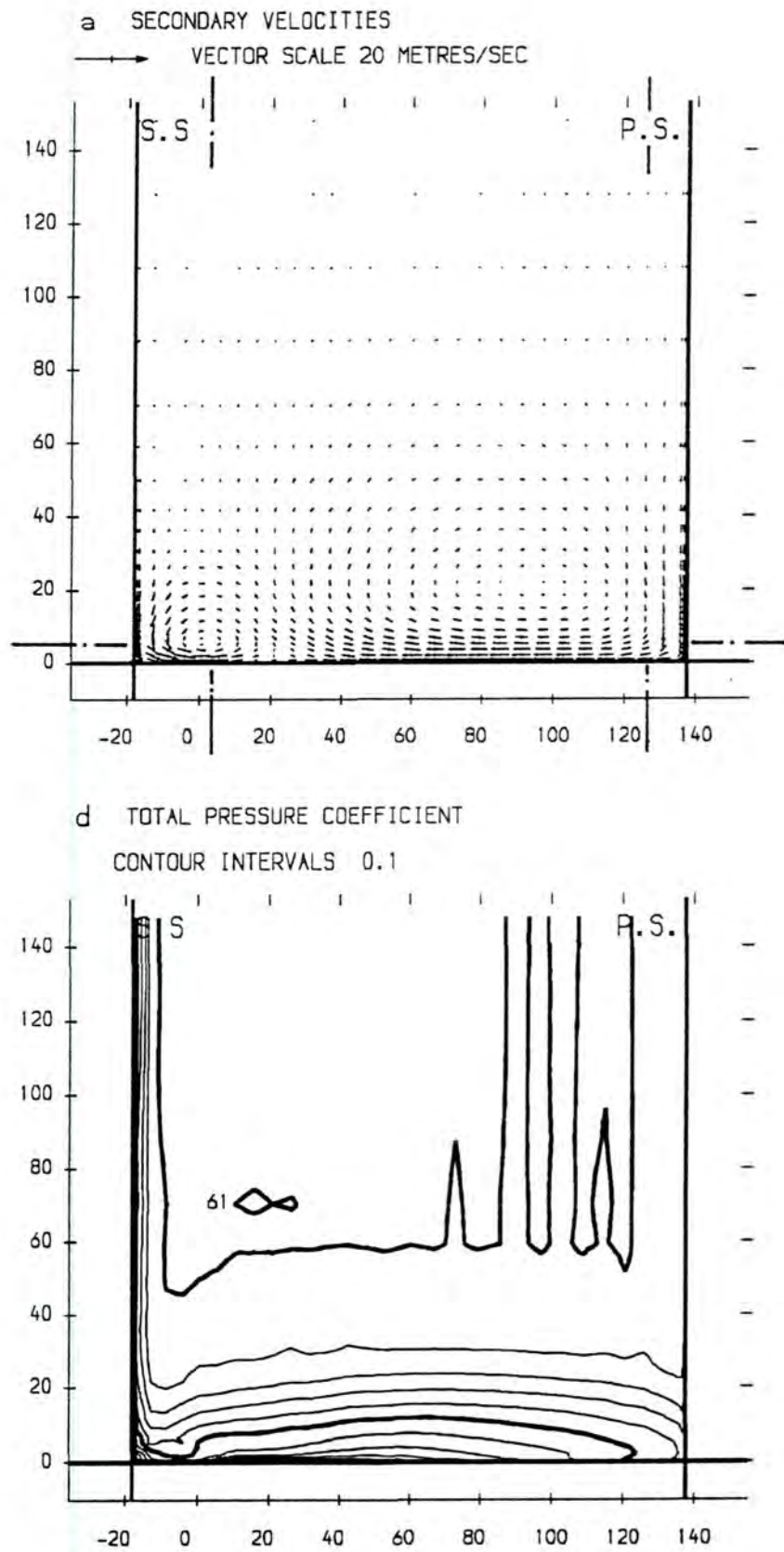
Figure 6.4: Contour Plot (Computation) of Slot 2 - No Injection

a SECONDARY VELOCITIES
VECTOR SCALE 20 METRES/SEC

d TOTAL PRESSURE COEFFICIENT
CONTOUR INTERVALS 0.1
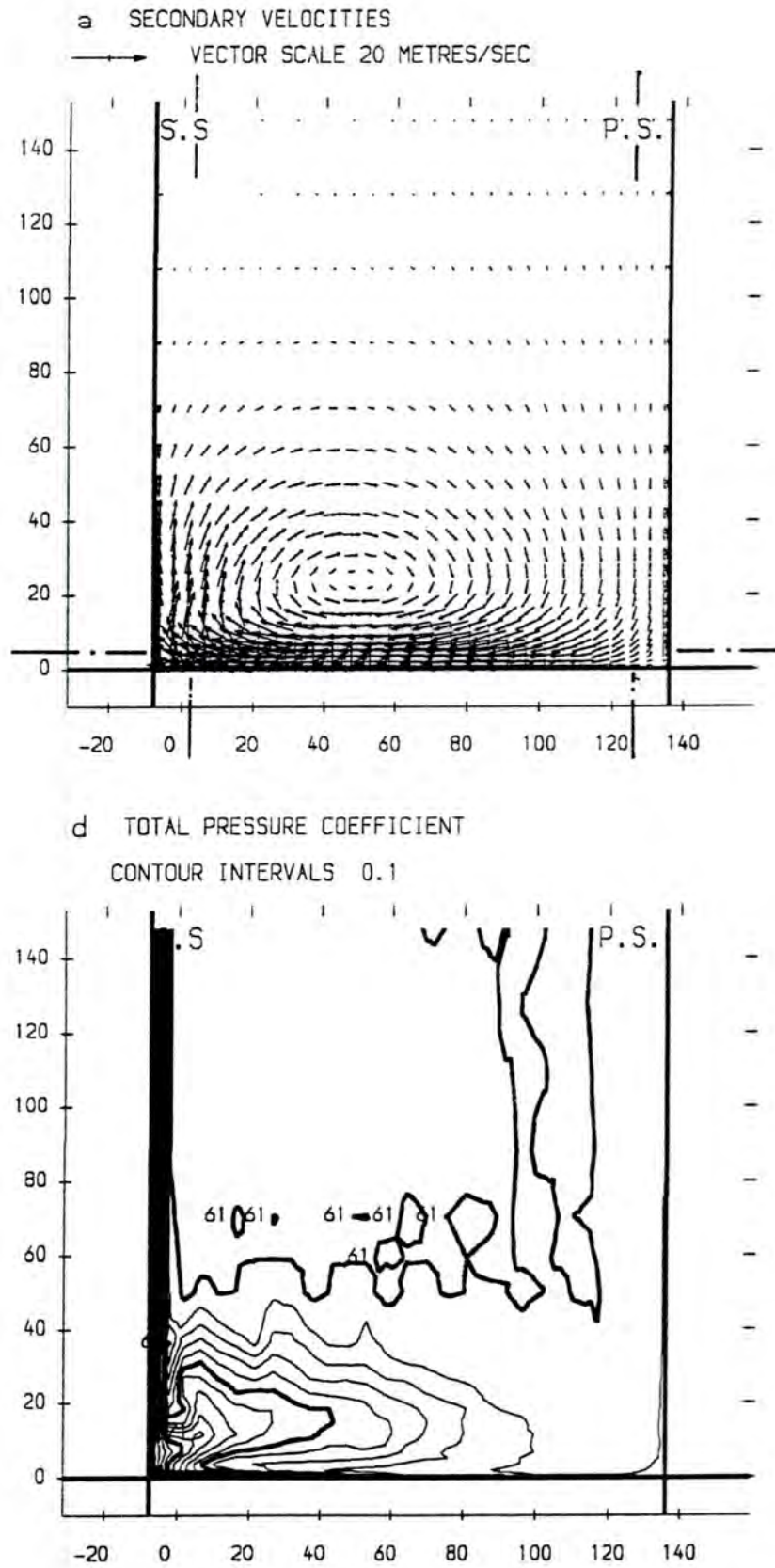
Figure 6.5: Contour Plot (Computation) of Slot 5 - No Injection

a   SECONDARY VELOCITIES
    ⟶   VECTOR SCALE 20 METRES/SEC

d   TOTAL PRESSURE COEFFICIENT
    CONTOUR INTERVALS 0.1
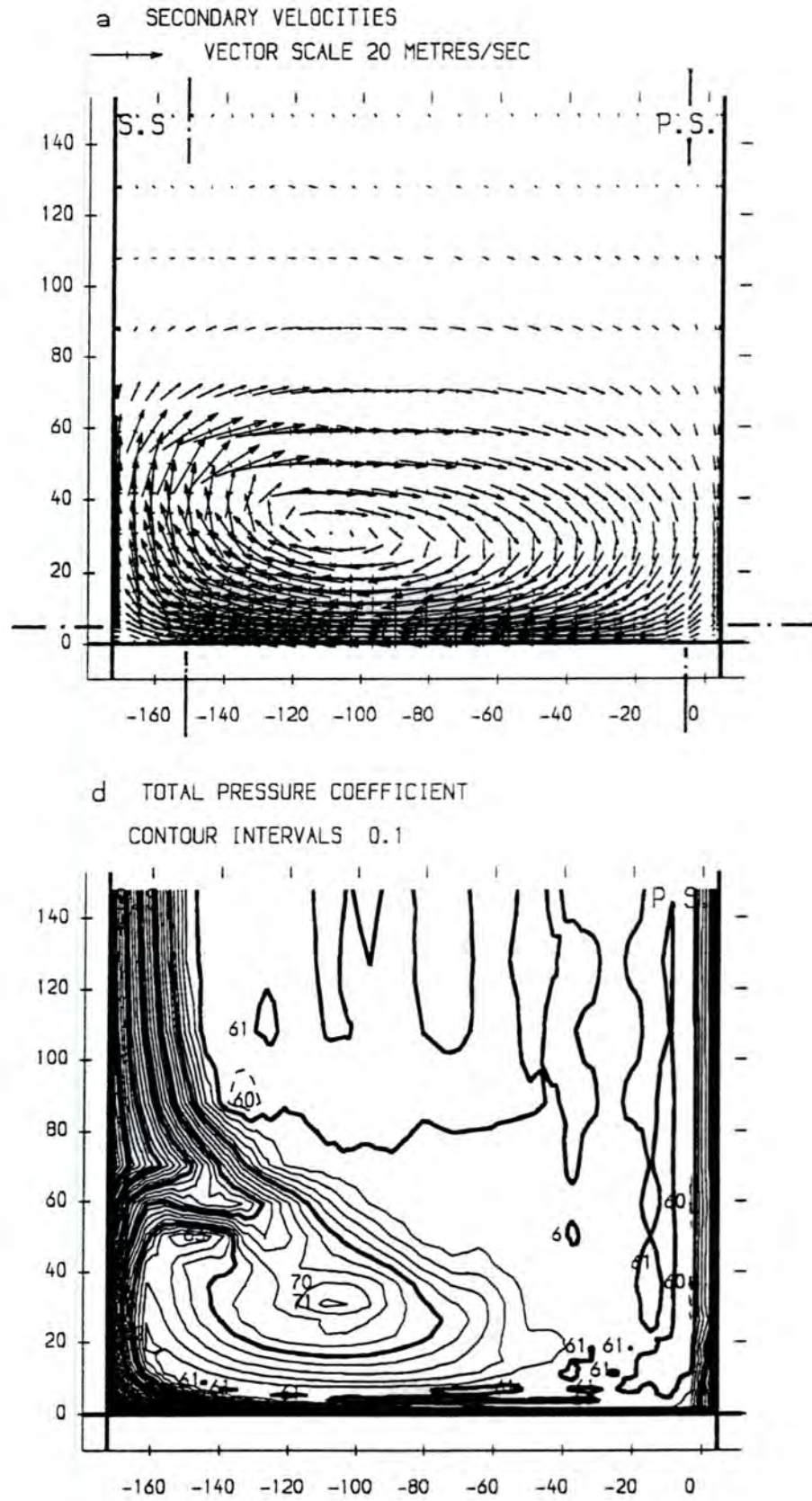
Figure 6.6: Contour Plot (Computation) of Slot 8 - No Injection

a   SECONDARY VELOCITIES
→   VECTOR SCALE 20 METRES/SEC

d   TOTAL PRESSURE COEFFICIENT
CONTOUR INTERVALS 0.1
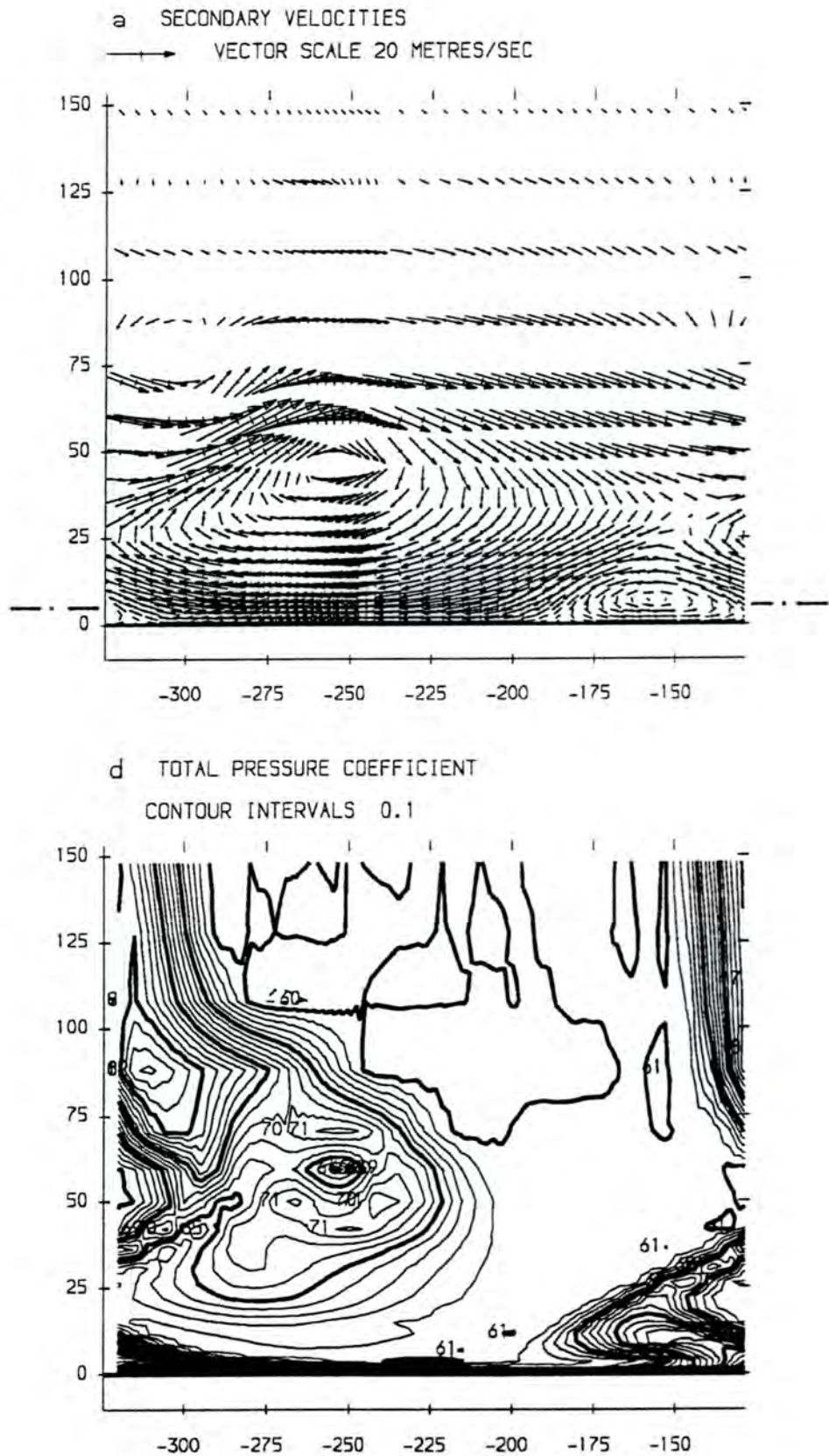
Figure 6.7: Contour Plot (Computation) of Slot 10 - No Injection

Low Angle - 232%

Slot 1 Re-energization and high secondary velocities, i.e. tangential injection velocities, are discernible close to the endwall.

Slot 2 A single flattened vortex is spread over the endwall in contrast to discrete vortices found experimentally.

Slot 5 A counter cross-flow towards PS at the endwall ends in a vortex at PS, which has not been measured. Flow visualization results (Figure 4.39, pg. 104) using an 'ink stripe' (Section 4.7.3) technique, motivated by the computational results, indicated a flow up PS. The existence of the associated vortex is not clear since there is no evidence from area plots and the flow up PS could also be a result of the blade surface static pressure field (see explanation on pg. 104). The endwall counter-cross-flow in the simulation also seems to be unrealistic and may arise due to inadequate mixing out of the injected air. Experimental endwall flow visualization results indicate a PS to SS cross-flow (Figure 4.31, pg. 97); even at 300% injection (Figure 4.32, pg. 98), no counter-cross flow exists. Computed endwall flow vectors (Figure 6.8) are directed towards PS. The computed PS-vortex is associated with a zone of re-energization indicating the injected fluid going across the endwall up PS with little mixing. This could not be seen experimentally.

Slot 8 The flow structure of slot 5 is basically repeated except the PS-vortex is split, one part in the PS corner and the other high up PS. A significant loss is generated close the endwall due the depressed vortex, which is related to the counter-cross flow.
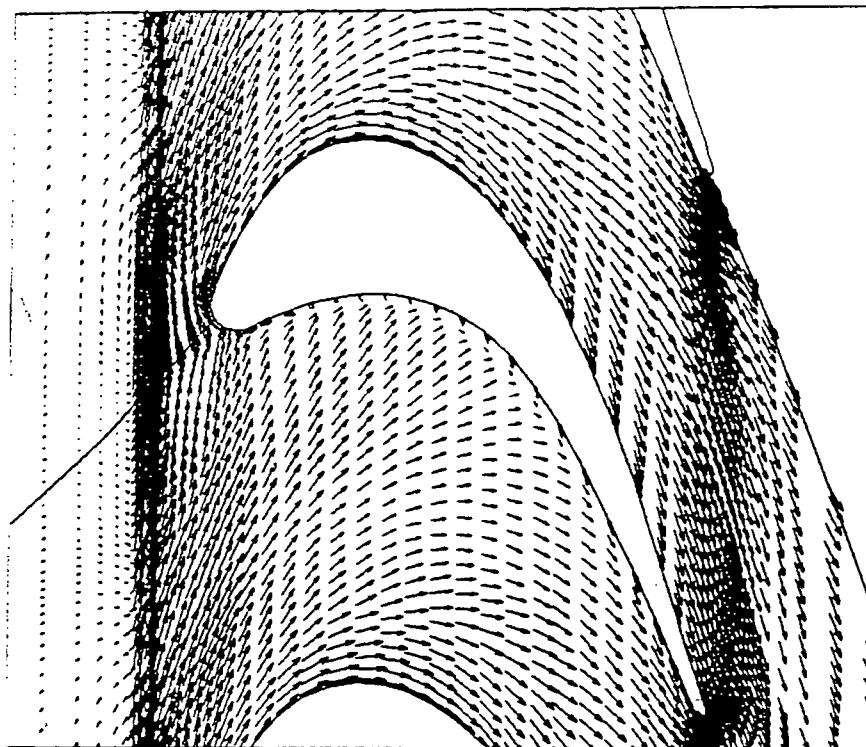
Figure 6.8: Computed Endwall Flow Vectors - 232% Low Angle

Slot 10 The flow field at the exit plane shows a lowered passage vortex as with

200% injection in the experiment but differs in general. The computed trailing edge

counter vortex, although larger, could not detected by 5H-probe measurements but

could be seen in the endwall flow visualization directly behind the trailing edge

(Figure 4.14, pg. 70). High losses on the endwall could not be observed in the

experiment.

a   SECONDARY VELOCITIES

→   VECTOR SCALE 20 METRES/SEC

d   TOTAL PRESSURE COEFFICIENT

CONTOUR INTERVALS   0.1
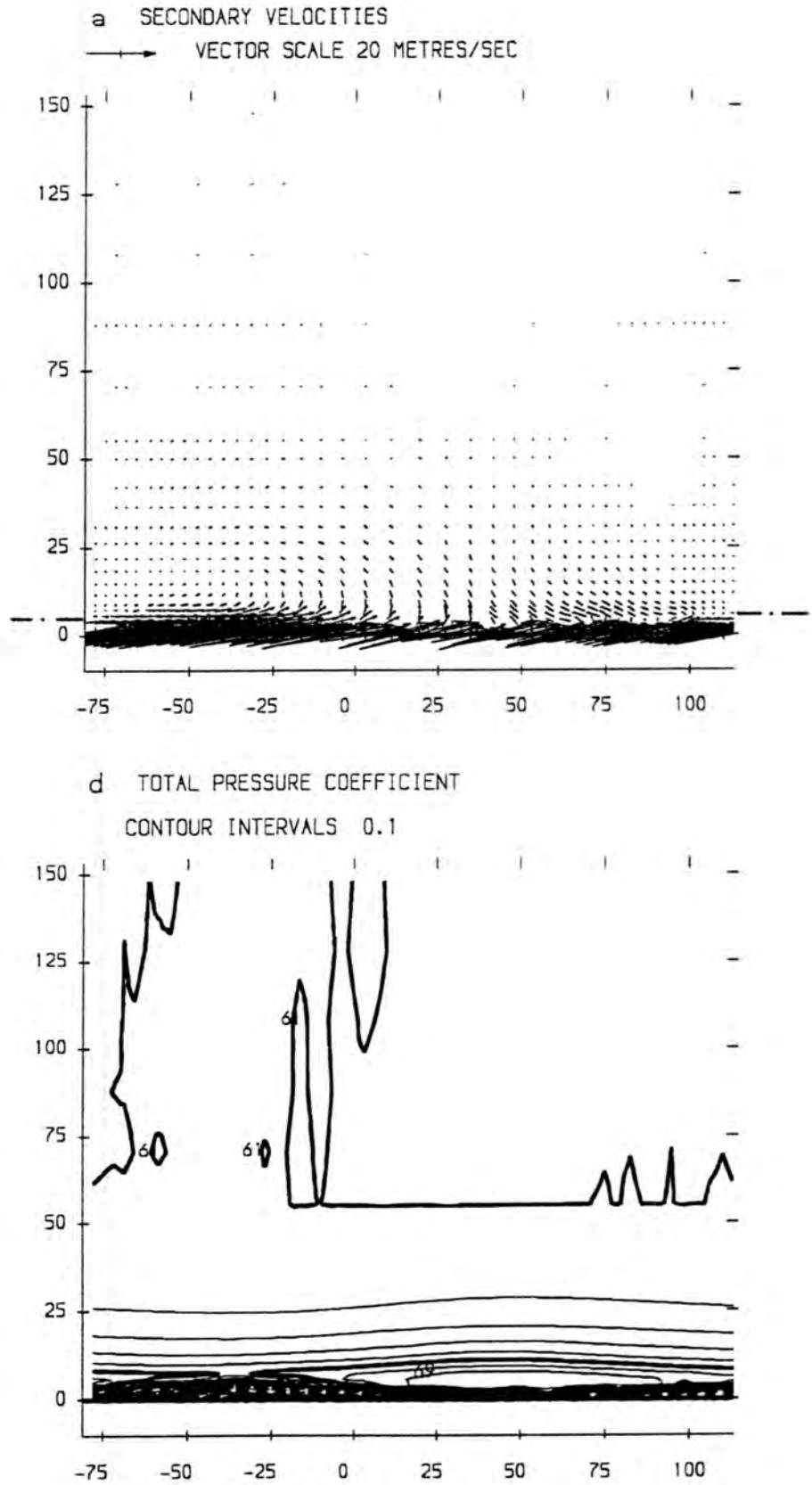
Figure 6.9: Contour Plot (Computation) of Slot 1 - 232% Low Angle
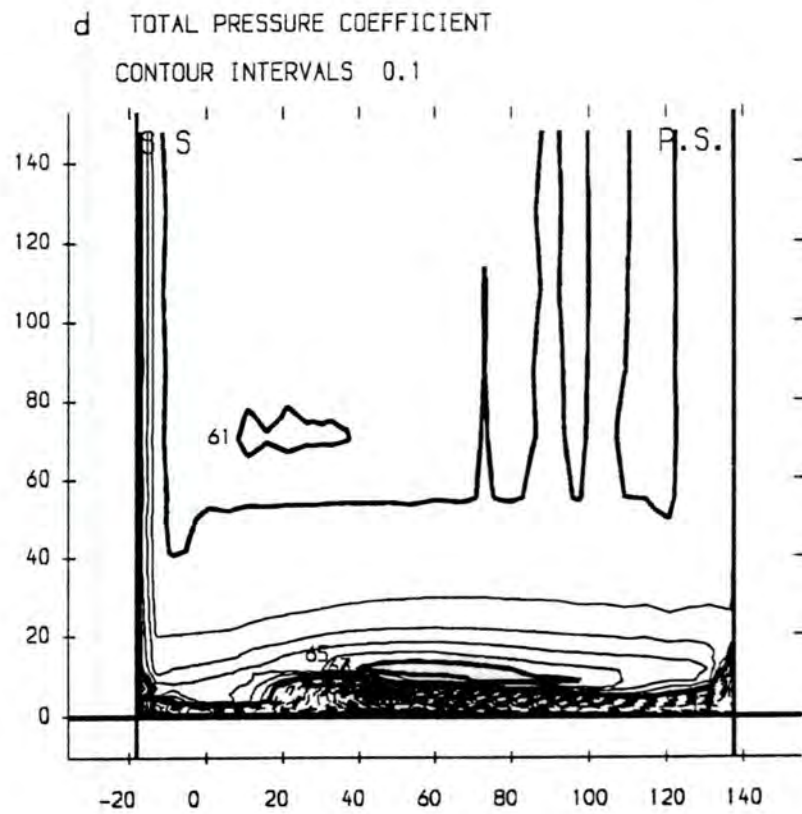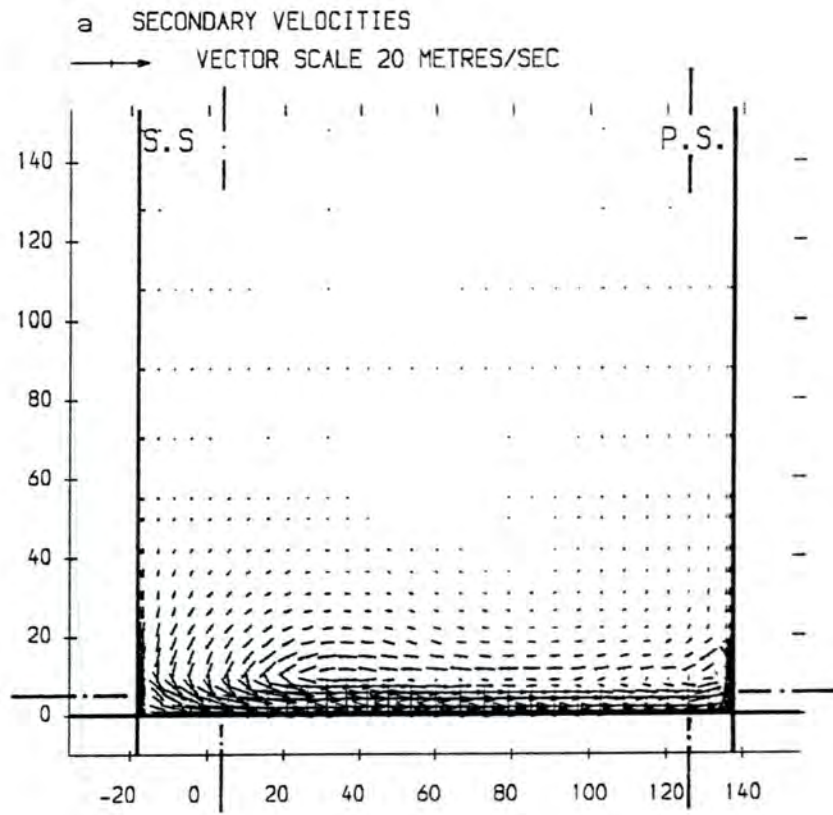
Figure 6.10: Contour Plot (Computation) of Slot 2 - 232% Low Angle

a   SECONDARY VELOCITIES

⟶   VECTOR SCALE 20 METRES/SEC

d   TOTAL PRESSURE COEFFICIENT

CONTOUR INTERVALS 0.1
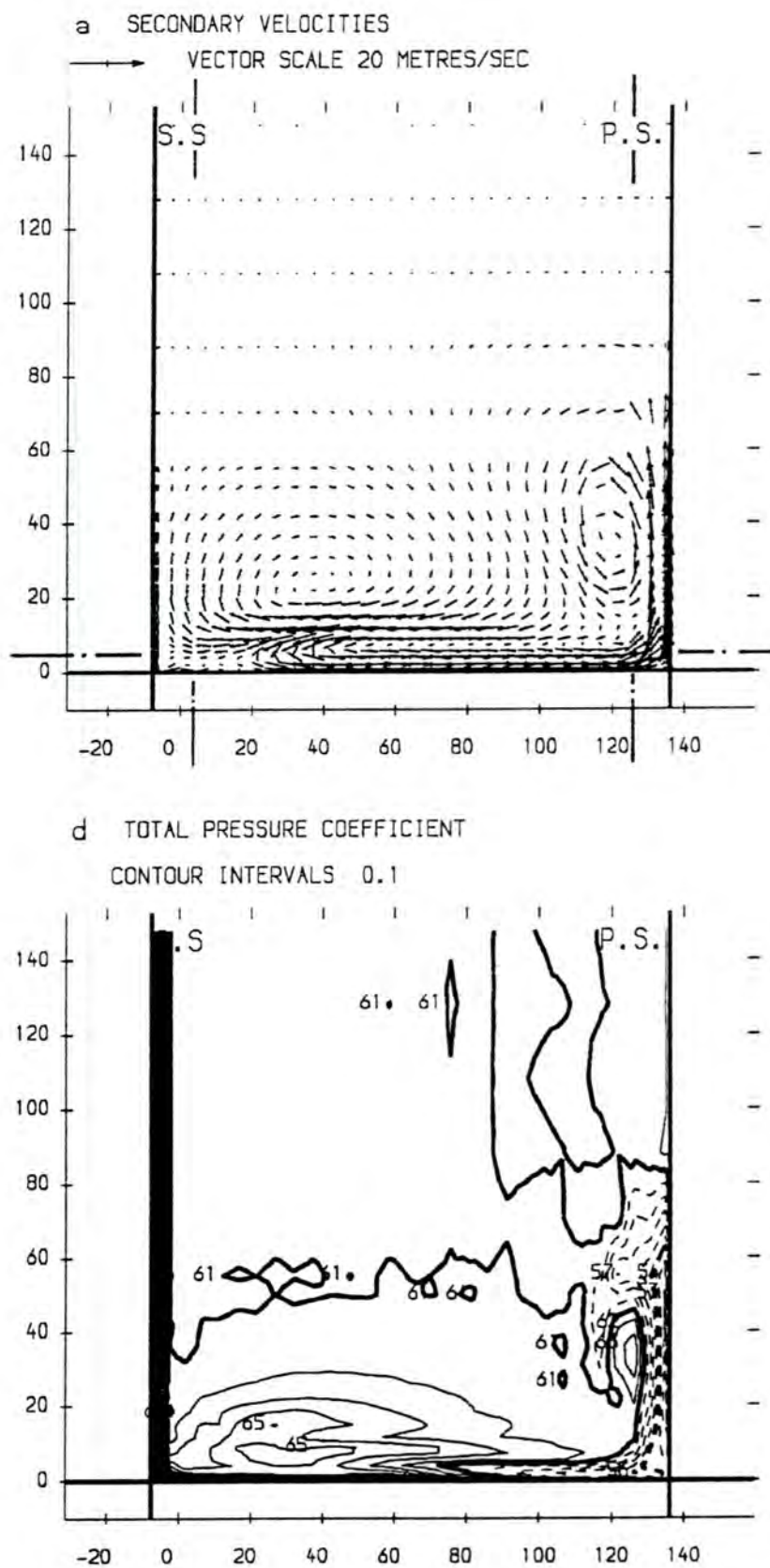
Figure 6.11: Contour Plot (Computation) of Slot 5 - 232% Low Angle

a   SECONDARY VELOCITIES

VECTOR SCALE 20 METRES/SEC

d   TOTAL PRESSURE COEFFICIENT

CONTOUR INTERVALS 0.1
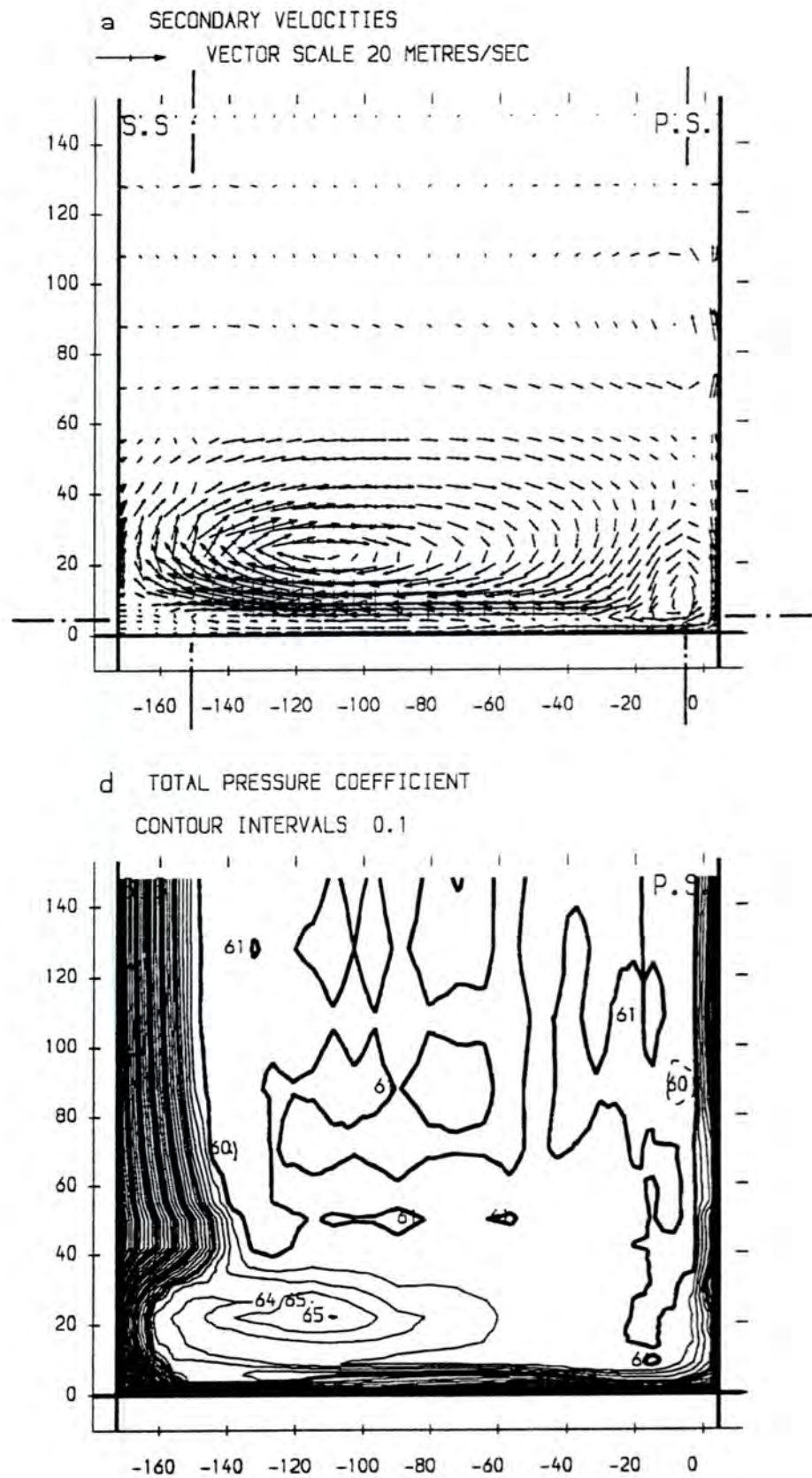
Figure 6.12: Contour Plot (Computation) of Slot 8 - 232% Low Angle

COMPUTATIONAL RESULTS   6.3

a SECONDARY VELOCITIES

⟶ VECTOR SCALE 20 METRES/SEC

d TOTAL PRESSURE COEFFICIENT

CONTOUR INTERVALS 0.1
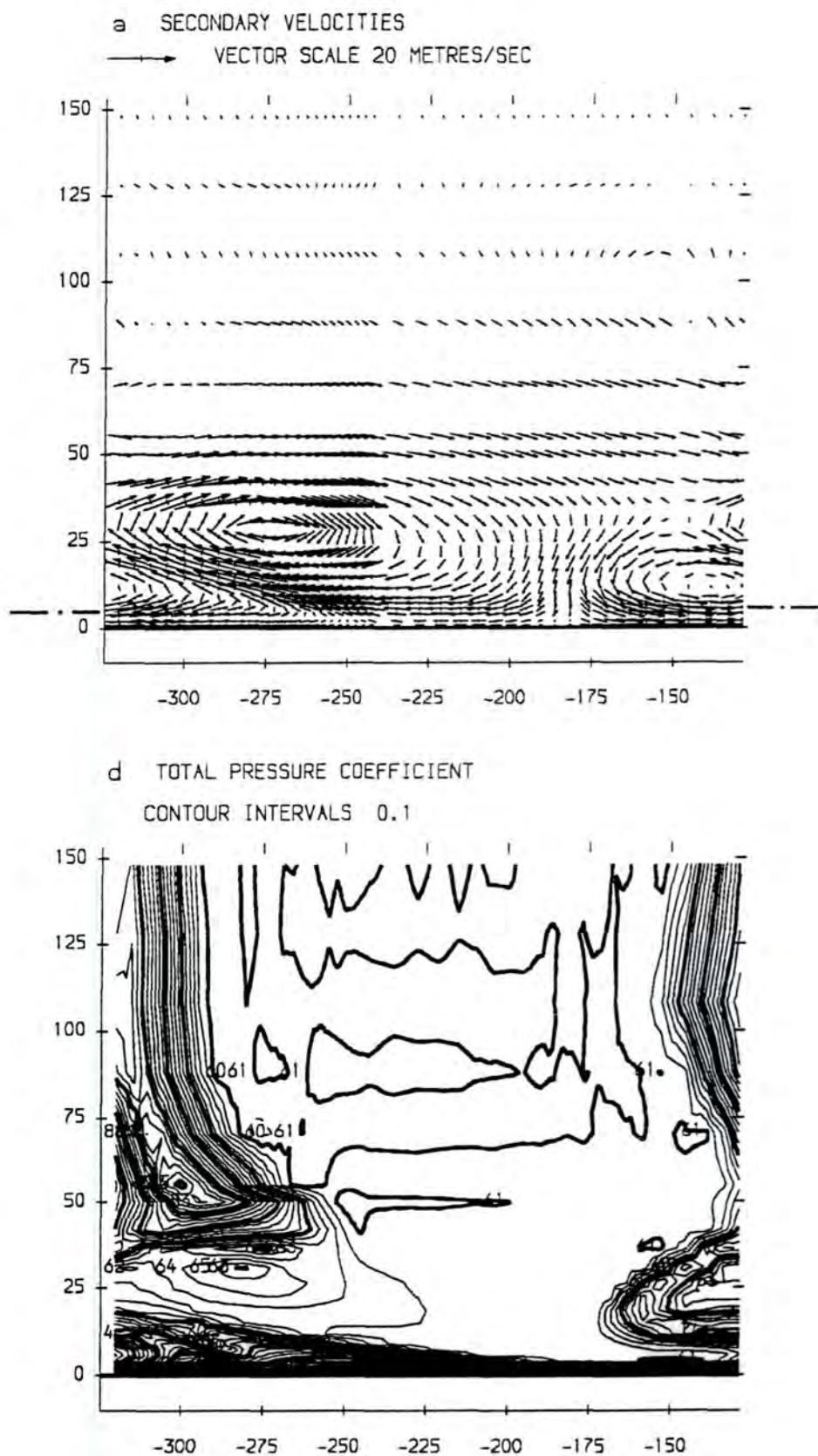
Figure 6.13: Contour Plot (Computation) of Slot 10 - 232% Low Angle

6.3.3 Mass-Averaged Results

Computational and experimental results at 232% and 250% injection (Section 6.3.1) are compared quantitatively. A further evaluation (e.g. gain coefficients) is not attempted because of significant discrepancies in their absolute values.

Secondary Kinetic Energy

Area-plots (Section 6.3.2) have shown differences in the computed and measured flow fields particularly with injection. Therefore, a quantitative comparison of the secondary kinetic energy coefficients can be misleading since the directional information of the secondary flow vectors is lost. However, it is interesting to compare the percentage reduction in the experiment and computation (Table 6.2).

Slot	5	8	10
$\frac{[C_{ske}]_b}{[C_{ske}]_{ub}} (Exp.)$	-54 %	-50%	-71%
$\frac{[C_{ske}]_b}{[C_{ske}]_{ub}} (Comp.)$	-47 %	-71%	-72%

Table 6.2: Reduction in Secondary Kinetic Energy (Experiment and Computation)

Reasonable agreement is found from mid-passage to the downstream plane. The comparison is limited to this area since the injected air did not mix sufficiently in the first half of the passage.

Total Pressure Loss

The loss growth along the blade passage predicted by MEFP compared to the measurements is shown in Figure 6.14. The experimental data analysis uses a linear extrapolation to the walls and this may lead to lower than the real losses within the blade passage. The jump across the trailing edge is caused by the high losses from the trailing edge and is also due to the decay of secondary kinetic energy. With the computations, a steeper gradient exists within the blade passage
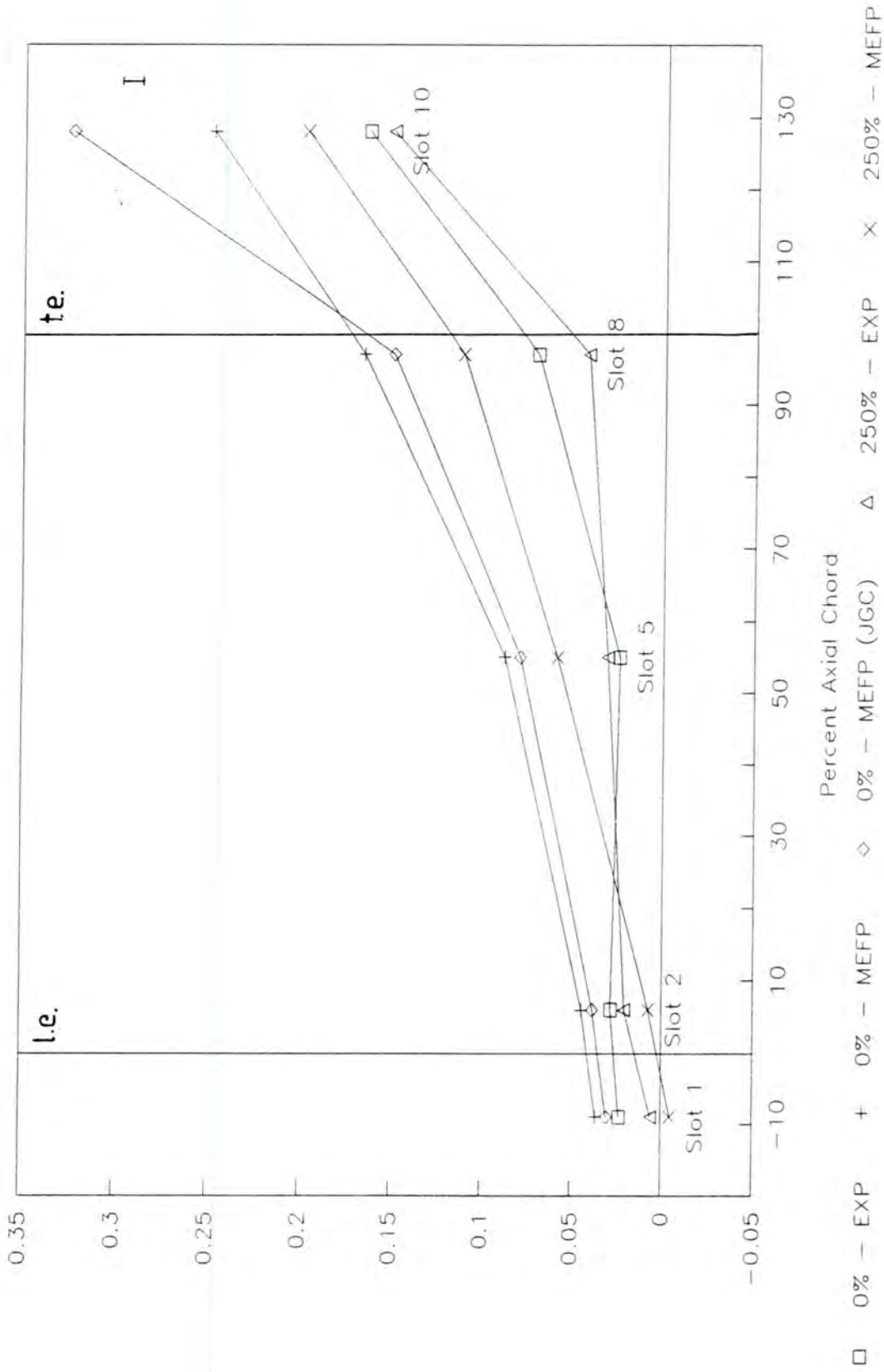
Figure 6.14: Growth of Total Pressure Loss c_p along Axial Chord (Experiment and Computation)

for no injection. The height of the jump across the trailing edge is of the same order of magnitude as measured but much less than predicted in simulation runs ('JGC') by Cleak [1989]. The higher value for the inlet loss in the simulation is due to data from 3H-probe measurements by Walsh [1987] which has been used for the near wall grid points below 5 mm span.

The magnitude of the reduction in total pressure loss with blowing is predicted reasonably well for the trailing edge and the downstream planes (Table 6.3). This is due to the loss production within the passage occurring close to solid walls from which region the turbulence model has been derived and therefore gives satisfactory answers. In the experiment, the new endwall boundary layer is thin and laminar over a significant proportion whereas MEFP predicts a thicker turbulent boundary layer. However, the overall loss prediction may be fairly similar to the experiment. Discrepancies in loss values within the passage indicate different loss production distributions in experiment and computation.

Slot	5	8	10
$\frac{[c_p]_b}{[c_p]_{ub}}(Exp.)$	+28%	-40%	-8%
$\frac{[c_p]_b}{[c_p]_{ub}}(Comp.)$	-33%	-33%	-20%

Table 6.3: Reduction in Total Pressure Loss (Experiment and Computation)

6.4   Improvements

Some improvements to help future modelling attempts are suggested.

Validation: Discrepancies in the prediction of mass-averaged values by Cleak [1989] to results presented in this work have to be resolved. At the same time, the predicted blade profile loss which amounts to twice the measured loss should be brought into better agreement with the experiment

by e.g. introducing laminar blocks (transition occurs roughly at about 50% axial chord), better near wall turbulence modelling and improvement in the grid around the blades.

Measurement: Knowledge of the total pressure distribution above the injection slot as well as other injection details are required for an exact modelling as well as loss measurements close to the endwall and the blade surfaces are essential.

Injection Slot: More detailed modelling of the injection slot would lead to a representation of the internal jet flow structure as well as the vane wakes. It might not be necessary to have exact knowledge of the injection details, e.g. the total pressure could be specified in the plenum in front of the injection guide vanes. Improvements to the injection modelling should be carried out in a stepwise manner.

Turbulence Model: A non-isotropic turbulent shear stress tensor of the main-flow requires sophisticated turbulence modelling (Section 7.4). The same argument is valid for the internal jet flow structure (Bario et al. [1990]). The mixing-length model with near-wall assumptions (Moore & Moore [1985]) used in the present investigation generated too high values of loss in the main-stream and apparently did not mix out the jets adequately resulting in an unrealistic cross-flow on the endwall.

Chapter 7

Turbulence Evaluation

$\mathcal{T}$urbulence structures of secondary flows are investigated through evaluation of five of the six Reynolds-stresses presented by Cleak [1989]. The therefore necessary strain rates, i.e. mean velocity gradients, are derived from previously not available 5H-probe data at slots 5 and 8 presented in this work (Chapter 4) and redundant data for slot 10 was used for a consistency check. The results are also put into perspective for computational turbulence modelling. Turbulent shear stresses, mean laminar dissipation, turbulence production and eddy viscosities have been discussed by Gregory-Smith & Cleak [1992]. The material provided here supplements and completes that of Gregory-Smith & Biesinger [1992].

The data of this chapter provides an insight into loss production mechanisms (cf. Appendix F.2) and completes the description of the flowfield without air injection. Measurements of the turbulence structure with injection are not available.

7.1 Loss Generation

The 'energy cascade' (Bradshaw [1978]) describes the decay of mean kinetic energy to mean laminar dissipation and turbulence production (equation (F.1),

Appendix F). The generated turbulence, several magnitudes larger than laminar dissipation, is dissipated in turn by viscous action (equation (F.2)). It is possible to approximate the losses from the rate of turbulence production (Moore [1985]).

The data presented below is evaluated following the procedure described in Appendix F. The corresponding mean flow fields were presented in Figures 4.2, pg. 48, and Figure 4.3, pg. 49.

7.1.1 Mean Laminar Dissipation

Slot 5

The top right diagram in Figure 7.1 shows most of the mean laminar kinetic energy being dissipated in the suction side corner. A shallow gradient exists in the bulk of the flow. The strain rates are significant at slot 5 due to a strong transverse pressure gradient resulting in accelerated flow near SS.

Slot 8

The bottom right diagram in Figure 7.1 shows increased viscous action compared to slot 5, still being relatively low in relation to turbulence production rates. High values near midspan at the suction side are due to the natural spline fit, which may be in error near the boundaries.

7.1.2 Turbulence Production

Figure 7.2 and Figure 7.3 show five of six turbulence production rates including their sum.

Slot 5

Turbulence action is confined to the suction side corner.
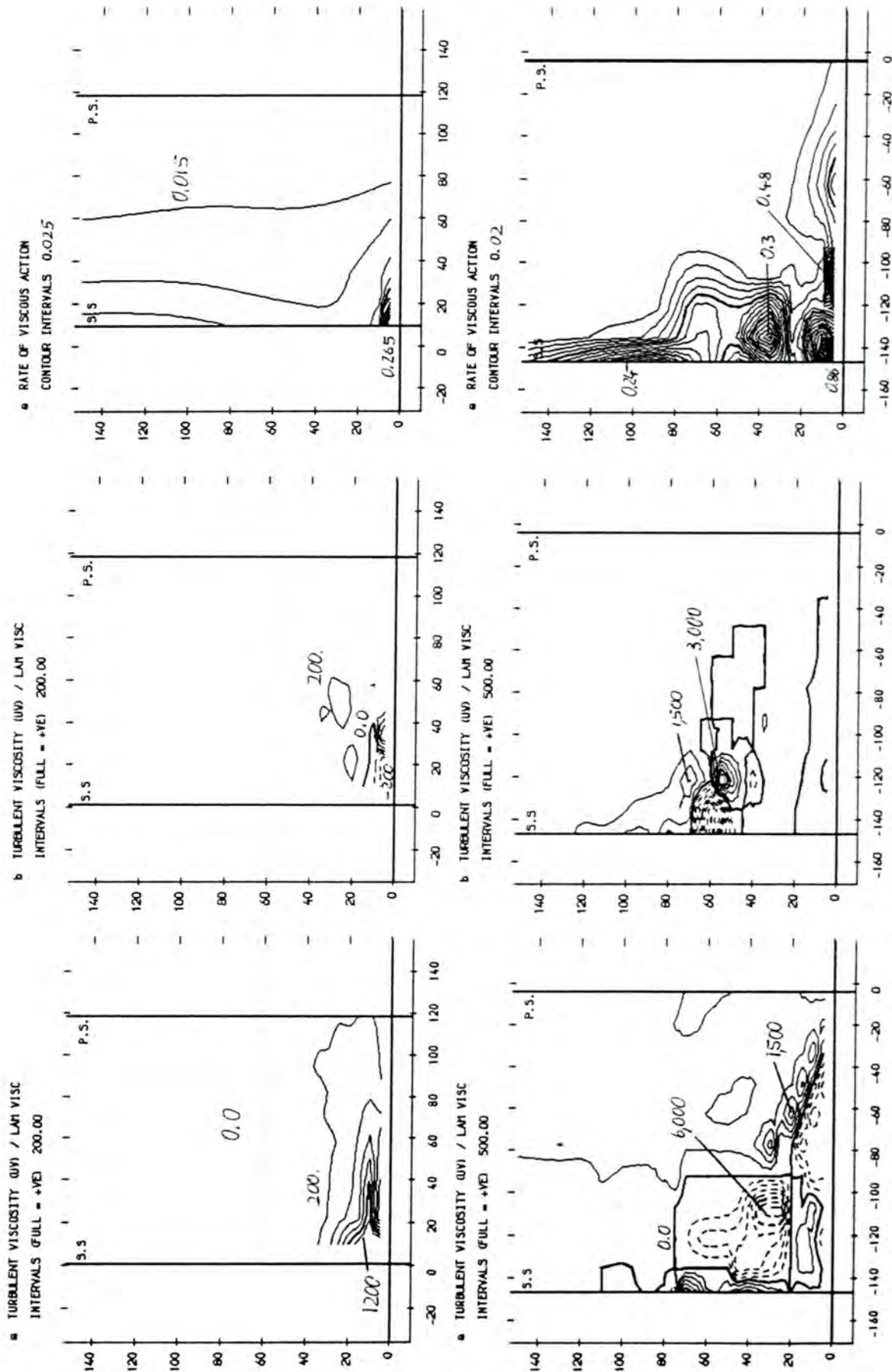
Figure 7.1: Turbulent Viscosities and Mean Laminar Dissipation at Slot 5 (top) and Slot 8 (bottom)

Slot 8

The action of significant normal stresses, which are neglected in Reynolds-averaged Navier-Stokes equations using eddy viscosity assumptions, are noted. The positive and negative signs arise from zones of deceleration or diffusion of the mean flow. They are associated with sinks and sources for mean flow kinetic energy.

7.2 Turbulent Viscosity

An experimental value for the eddy viscosity may be obtained from equation (F.8) given in Appendix F.3.

$$\nu_T = \frac{-\overline{\rho u_i u_j}}{\left(\frac{\partial U_i}{\partial x_j} + \frac{\partial U_j}{\partial x_i}\right)} \tag{7.1}$$

This fraction possesses poles, which have to be excluded to obtain a continuous function. A zero value is set, when the mean strain (denominator) falls below a cut-off value and the turbulent shear stress (nominator) is low, too. In the same case but for significant turbulent shear stress values, a weighted bi-cubic spline technique was used to smoothen the calculated values.

Calculated experimental eddy viscosities can also be negative in contrast to computations, which only render positive values (compare equation (F.9) in Appendix F.3).

7.2.1 Slot 5

The two left hand pictures of Figure 7.1 give the $\overline{u_x u_y}$ and $\overline{u_x u_z}$ (UV and UW in plots) related eddy viscosities non-dimensionalised by a reference laminar viscosity. A
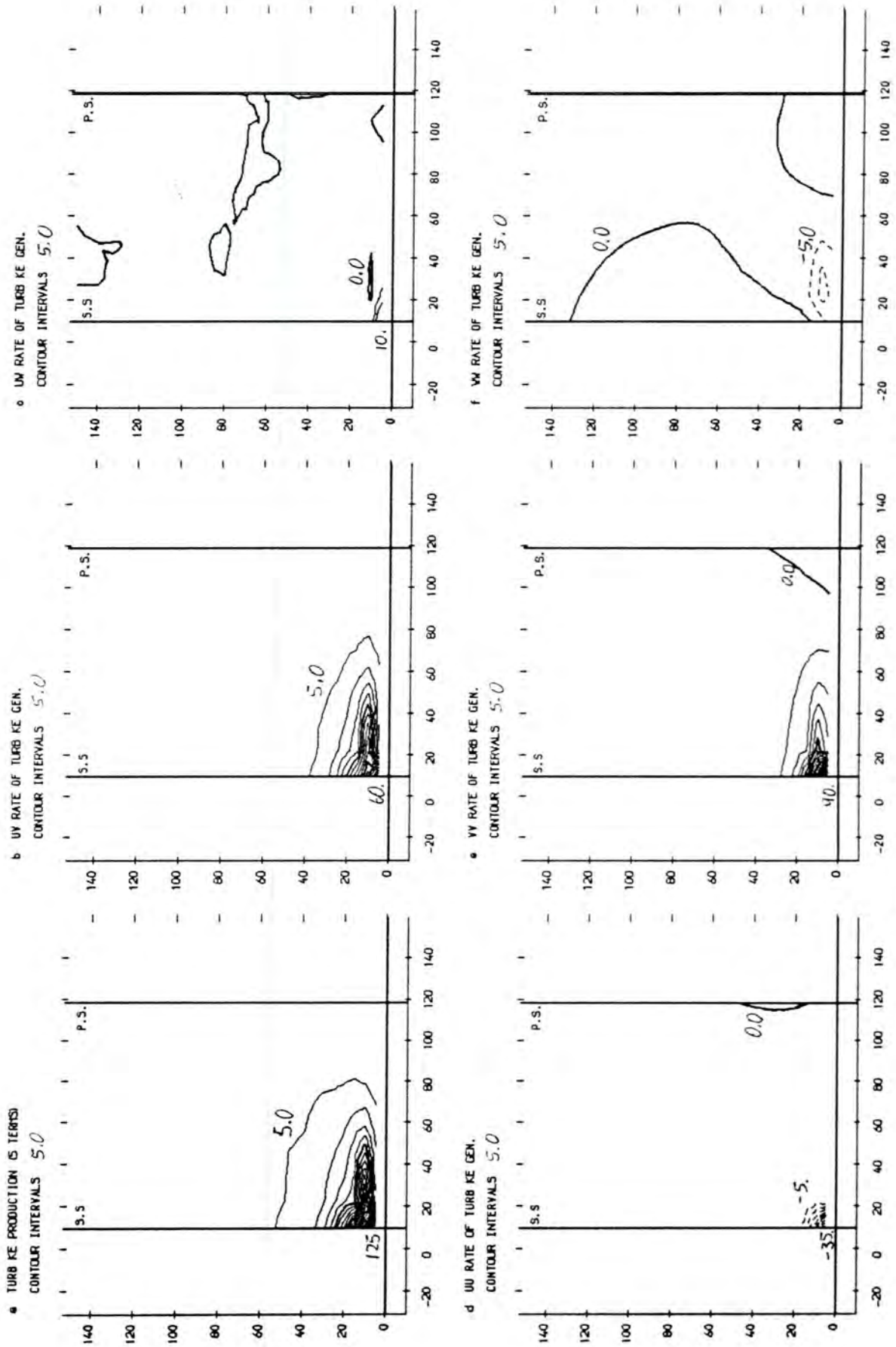
Figure 7.2: Turbulence Production Rates at Slot 5
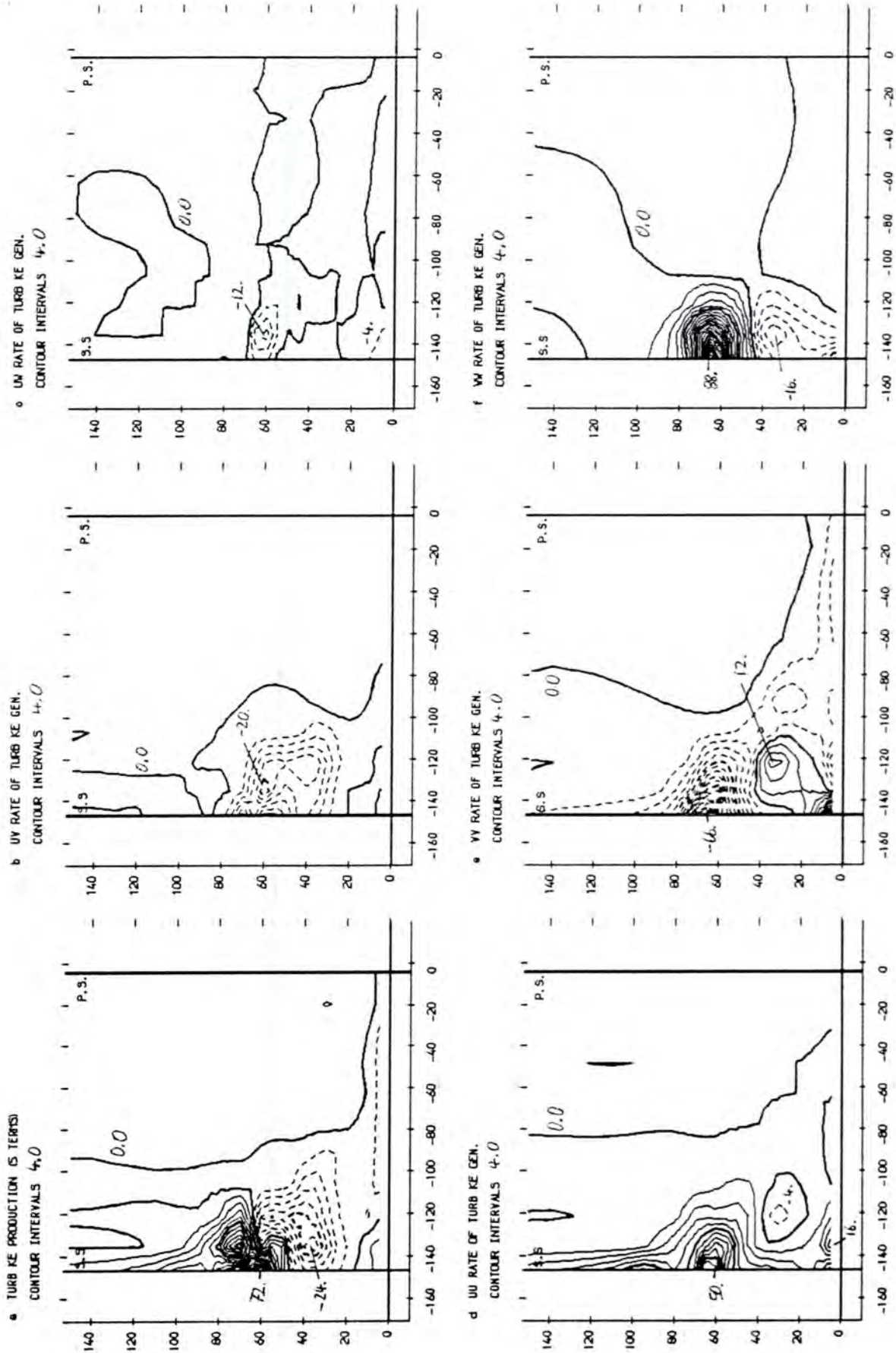
Figure 7.3: Turbulence Production Rates at Slot 8

heterogeneous flow-field is observed.

Eddy viscosities are proportional to the turbulence production rates for constant strain and possess the same sign. Since turbulence production rates are not smoothed by splines, the different sign of the UW-component (Figure 7.1) indicates an error in the spline fit near the suction side corner.

7.2.2 Slot 8

The left hand diagrams of Figure 7.1 show considerably negative values for the UV-component in the lower part of the vortex. The UW-component exhibits a sign change across the vortex centre, which is associated with up- and downward directed secondary flows.

7.3 Turbulence Characteristics

This streamwise/cross-passage turbulent velocity correlation $-\overline{u_x u_y}$ (UV in plot) is seen to change sign from slot 8 to downstream slot 10 due to the formation of a wake behind the blade trailing edge. The corresponding rate of strain changes sign from slot 5 to slot 8, where the blockage due to the passage vortex slows down the flow. This is summarized in Table 7.1. The turbulent shear stress seems to lag behind the corresponding change in strain of the mean flow.

7.4 Turbulence Modelling

7.4.1 Conventional Approaches

An algebraic eddy viscosity concept as used with mixing-length, one-equation or k-ε turbulence models (Appendix F.3) is strictly valid for isotropic turbulence

Slot	5	8	10
Turbulent Shear Stress $\tau_{xy} = -\overline{\rho u_x u_y}$	−	−	+
Mean Strain $\left(\frac{\partial U_x}{\partial y}\left(+\frac{\partial U_y}{\partial x} \ll\right)\right)$	−	+	++
Turbulence Production $\Psi_T = -\overline{u_x u_y}\frac{\partial U_x}{\partial y}$	+	−	+
Eddy Viscosity $\nu_T = \frac{-\overline{u_x u_y}}{\left(\frac{\partial U_x}{\partial y}+\frac{\partial U_y}{\partial x}\right)}$	+	−	+

Table 7.1: Streamwise/Cross-Passage Turbulence Components of Passage Vortex Loss Core

only. Experimental results revealed a locally non-isotropic turbulent shear stress tensor as well as a spatially inhomogenous three-dimensional turbulent flow field. A comparison of the therefore limited prediction capability of the three models is given by Cleak *et al.* [1991] and Gregory-Smith & Cleak [1992]. Algebraic or full (second-order) Reynolds-stress modelling is more suited to capture accurately the physics of high turning, complex flows. Special features such as secondary flow of the second kind may be modelled in addition (Lai *et al.* [1991]). The underlying numerical code should produce only low amounts of numerical viscosity (Section 6.1).

Modelling of the blade boundary layer laminar to turbulent transition is of equal importance to the flow prediction. Mayle [1991] provides a comprehensive review of transition phenomena. Low-Reynolds-Number k-ε models are developed to replace the cruder turbulence wall functions by taking the viscous and semi-viscous sublayers into account (Launder & Spalding [1974]). The models may be used to predict transition (Schmidt & Patankar [1991]).

7.4.2 Novel Techniques

Direct Numerical Simulation (DNS) of the non-averaged Navier-Stokes equations on

grids fine enough to resolve all of the turbulent scales are still limited to low Reynolds

number flows in relatively simple geometries. Large Eddy Simulations (LES) do not

model smallest eddies but may already be used at higher Reynolds numbers, if sufficient

computing resources are available (Schwab [1992]). These approaches should be feasible

to turbomachinery applications in the future.

Chapter 8

Overview and Discussion

*S*econdary flows are generated by influence of the freestream blade-to-blade pressure gradient on low momentum fluid near the endwall resulting in over-turning, which in turn leads to the formation of a passage vortex. These flows and the associated losses may be reduced by provision of counter skew to the inlet boundary layer by injection of air or by an upstream rotating belt. The tangential momentum counteracts the over-turning near the endwall and reduces secondary flows and losses. In this project, the injected tangential momentum is set initially identical (on an integral basis) to the tangential momentum provided by the belt in Walsh's positive skew case, which showed a substantial loss reduction. The spanwise injected momentum is less effective in preventing secondary flows. Its value depends on the injection angle calculated from the additional constraint of a near wall velocity identical to the belt and a fixed injection area. The calculated injection angle was halved, approximately, to reduce the required blowing power (see below). The set injection conditions are termed as 100% of design. A variation of this percentage is always proportional to the tangential component of the injection velocity vector as well as mass flow. The tangential momentum and kinetic energy are related to the square and cube of the tangential injection velocity

respectively.

The tangentially injected momentum may be further divided into streamwise and normal components relative to the main-stream (Figure 4.1, pg. 44). The streamwise component might be lower than that of the inlet boundary at low injection rates around 100%, which leads to thickening of it and that results in an overall increase in loss and stronger secondary flows. At higher injection rates, the inlet boundary layer becomes re-energized, mostly at some distance from the endwall depending on the injection angle. This results in a counter-rotating vortex. On the endwall and above the zone of re-energization, over-turning persits (Figure 4.31, pg. 97 and Figure 4.12, pg. 66) due to boundary layer profiles influenced by skin frictional forces and undisturbed by the injection. The normal component of momentum, although roughly equal to the streamwise, is not equally effective in countering the secondary flow. This is expected from classical theory.

The guide vanes inside the injection slot cause a blown sheet of eight individual jets per pitch. At the optimum injection (see below), they are found to roll up by slot 2 and merge with H_s into a single counter-rotating vortex by reaching slot 5. This vortex, based in the SS corner, interacts with the passage vortex and confines its centre to the PS half of the passage. At the downstream slot 10 position, a substantially weakened passage vortex spans the area between the blade wakes despite enhancement of the counter-rotating vortex by vorticity shed from the blade trailing edge. Spanwise migration of the passage vortex as it is observed without injection is prevented.

One of the benefits of reducing secondary flows is a more uniform downstream flow field. At optimum injection, the exit angle deviation is reduced to about one third of the original. The wake loss core is almost confined to the trailing edge region not penetrating far into the mainflow. A new loss region develops on the downstream cascade endwall.

An optimum injection rate in terms of secondary flow control has been found for *both* the high and low angles to occur at 250% of the design injection rate design. This shows that the tangential near wall velocity (Figure 5.4, pg. 119) plays an important role in identifying the injection. Increased downstream losses below 150% and counter-rotating flow beyond 300% constitute the limits of the injection.

★

A calculation of the obtained net energy gain is performed to account for the required blowing power. It is shown that the generalized concept of availability simplifies to an assessment of energy fluxes in the cascade for the incompressible flow situation. The assumption of an upstream tapping is not realized in the experiment but would be adequate in an real engine environment. Reference is made to the downstream loss as measured at the exit plane thus separating the effect of mixing out the downstream secondary kinetic energy. The achievable gains might be higher in a real engine, depending on the distance of the following blade row, due to a higher reduction in the downstream mixed-out losses (Figure 5.7, pg. 129). The latter includes the losses associated with the exit secondary kinetic energy which decreases as the exit loss decreases. In general, it is found that the investment in terms of injection kinetic energy is higher than the achieved gains. The skew provided by the belt seems to be more effective and actually achieves a positive gain considering a 'tangential component' of kinetic energy inherent in the skewed inlet boundary layer. The reason might be that only tangential but no spanwise momentum is provided to the flow with a monotonic variation starting from the endwall where the over-turning is strongest.

Mixing-out of the injected air with the main-stream at a fictitious plane provides further information on the potential effectiveness of the high and low injection

angles. The calculated mixed-out losses are found to be low for the low angle and high for the high angle at a representative rate of 250%. Overall energy gains are obtained relative to a downstream mixed-out plane with significant gains for the low but not high angle. The difference between the high and low angle is the spanwise injection component which is not very effective in reducing the secondary loss if the injected air is mixed out. The low angle is more effective on an energy basis (Figure 5.14, pg. 137) although the loss reductions are not as high as with the high angle at a given injection rate (Figure 5.7, pg. 129). The mixing-out analysis also indicates the superior performance of the low angle, if mixing was enhanced e.g. by a bigger distance between injection location and blade leading edge.

<div align="center">★</div>

The generation of losses with and without injection is determined by the production of turbulence; rates of laminar viscous dissipation are comparatively small. Most of the loss is produced close to solid walls where turbulence models tend to work well although the use of the positive definite, scalar eddy-viscosity concept sometimes leads to an over-prediction of the loss. Experimental values of eddy-viscosity may be negative and posses vector characteristics within the secondary vortex. The mixing-length turbulence model used to calculate the cascade flow with injection caused together with other difficulties, such as exact specification of the injection conditions as well as the slot geometry, the qualitative inaccuracy of the computation. However, predictions of the relative reduction in secondary kinetic energy and losses agree fairly well. The computational work is also able to suggest flow features not obvious from the experiment such as the flow very close to the walls.

<div align="center">★</div>

Summarizing the above discussion, the following points are made. Compared to other secondary flow and loss reduction methods, the upstream injection of air is shown to be an effective means with variable control of the secondary flow reduction. The expense of blowing power is accounted for by an availability analysis providing a legitimate estimate of the overall achievable gain. The accounting procedure is recommended for incorporation into other investigations of injection of air and is summarized in Biesinger & Gregory-Smith [1992]. A mixing-out analysis shows the optimum injection angle to be low - limited in practice by fabrication. Not many of the other secondary loss reduction methods being discussed in the open literature may be integrated into the engine environment to combine an effective control of secondary flows with endwall and possibly disk cooling.

Chapter 9

Conclusions and Future Work

$\mathcal{R}$ ealistic secondary flow and loss reduction techniques as applicable to the hot engine environment are the objective of the present work. A particular method, the tangential injection of air through an upstream slot opposing the secondary flow direction, has been selected after a thorough investigation of the pertinent literature. The Durham Linear Cascade was used as test vehicle providing fundamental insights into the generation of secondary flows and losses. An accounting procedure for the blowing power necessary for the injection is established. The flow field was traversed at various slot positions by a 5H-probe at constant Reynolds number for a wide range of injection conditions and two injection angles.

The following specific conclusion may be drawn:

- The spanwise distribution of vorticity in the inlet boundary layer provided by upstream boundary layer blowing shows a more significant impact on secondary flows and losses than could be expected from the integral value of tangential skew supplied by an upstream rotating belt.

- The dynamic control of the secondary flows by injection through an up-stream slot enables their reduction to a minimum resulting in low exit angle variations and a loss re-distribution on the endwall. The reduction mecha-nism consists of the provision of inlet positive streamwise vorticity and the more significant streamwise re-energization of the inlet boundary layer. A counter-rotating vortex on the blade suction side is supported by individual jets emanating from the injection slot. This vortex mixes with the near pressure side passage vortex to dissipate the rest of the secondary kinetic energy within and downstream of the blade passage.

- The injection of air does not result in an overall loss reduction when ac-counting for the injected kinetic energy. An equivalent kinetic energy is derived for the positive skew case giving substantial positive gains. An initial guess at the design stage using the optimum angle of 30° gave an even higher estimate. This could not be achieved because of the different spanwise momentum distribution of the jet compared to the skew produced by the belt and the injection losses.

- Mixing-out of the injected air at the low angle produces only little loss due to the relatively small spanwise component. With respect to an overall mixing-out analysis from the inlet mixed-out to the exit mixed-out plane, however, the achievable gains are higher than for the high angle. Thus, injection at the low rather than high angle would be more effective, if the jet mixed out with the mainstream. The low angle already performs much better with respect to the investment in the required blowing power.

★

Improvements to the existing experiment are suggested as follows:

- The experimental accuracy could be increased by the calibration of a new 5H-probe, which has already been manufactured.

- A re-design of the existing injection slot and measurement of the injection conditions with a specialized probe could help to avoid the uncertainties in the blowing discharge such as the exit area, exit angle and pitchwise non-uniformities. In a re-design, the following details might be considered:

  - A variable spanwise and/or pitchwise injection angle would be important in an attempt to optimize the existing design. The use of an expert-system would have to be re-considered (Section 2.3.3).

  - The discrete jets caused by the injection vanes give rise to additional losses and would increase the heat transfer from the hot mainstream to the endwall. A possible design of the injection slot discarding the guide vanes was produced by a final year undergraduate project and could be manufactured.

  - The downstream radius on the injection slot seemed to be successful in confining the injected jets closer to the endwall and preventing separation directly behind the slot. Overall losses are reduced. The influence of different radii could be examined.

  - A miniaturized 5H-probe has been designed in a companion project; a replica could be used to measure injection details above the injection slot.

- 3H-probe traverses close to the walls would lead to quantitatively more accurate area/mass-averaged results and reveal partially the flow structure there.

- Measurement of the static pressures on the blade surfaces and endwall would

support the flow visualization. They are required to complete the information of the flowfield inside the cascade.

- Knowledge of turbulence quantities of the injection jets and the main flow could help to obtain a deeper insight into loss production mechanisms. The streamwise/spanwise turbulent shear stresses are not available with the current data set but will be of interest with injection. A high level of automation is required to enable the logging of large amounts of data and to allow for a fast analysis.

- Information on the state of the endwall boundary layer is obtainable by intermittency measurements using hot-films (Harrison [1989], Pucher & Göhl [1987]) or the laser-density-gradient technique (Broichhausen [1983]).

- The situation in a real engine could be approached by rotating the cascade belt to provide negative skew and, at the same time, supplying the injected air with excess momentum counteracting the belt negative streamwise vorticity.

★

Computer simulation of the complex flowfield with and without injection poses a severe test case for state-of-the-art Navier-Stokes solver. A consideration of the guidelines given below might lead to better future agreement between computation and experiment:

- A code with very low artificial diffusion such as MEFP should be further used to enable correct predictions and to provide a basis for turbulence modelling.

- The measured non-isotropic Reynolds-stresses should be accounted for in the turbulence model other than by an algebraic eddy-viscosity assumption.

Laminar to turbulent transition plays an important role in predicting the profile loss and should be incorporated.

- Flexibility with the computational mesh is important. The representation of geometric details such as injection guide vanes might be crucial to the flows as well as facilitate the specification of the injection conditions. A correct modelling of the blade trailing edge is essential to the downstream flowfield.

- A comparison with experimental data should encompass the mean and turbulent flow fields in the mainstream and close to solid walls.

- Aspects of software design and management have become of importance to mechanical engineers because of the complexity of the computer programs used in simulation runs and the need of to process and visualize large amounts of computational output. Object-oriented rather than conventional views in programming should be favoured. They group data objects and the functions defined on them together and also introduce a hierarchical class structure into the code. Advantages are an easily understood program with easy maintenance and mending; a disadvantage is the effort required in writing an application.

★

The material discussed in this thesis is of relevance to endwall film cooling. Figure 9.1 shows a schematic of cooling and secondary flow control requirements as they are met by streamwise and tangential injection of cooling air. A uniform flow above the endwall is desirable to avoid the accumulation of cooling air, e.g. in the suction side corner, causing 'cold spots'. An advantage of tangential injection is apparent: the coolant provided is ideally distributed on the endwall whilst possibly reducing secondary flows and losses. In a real engine environment, disk
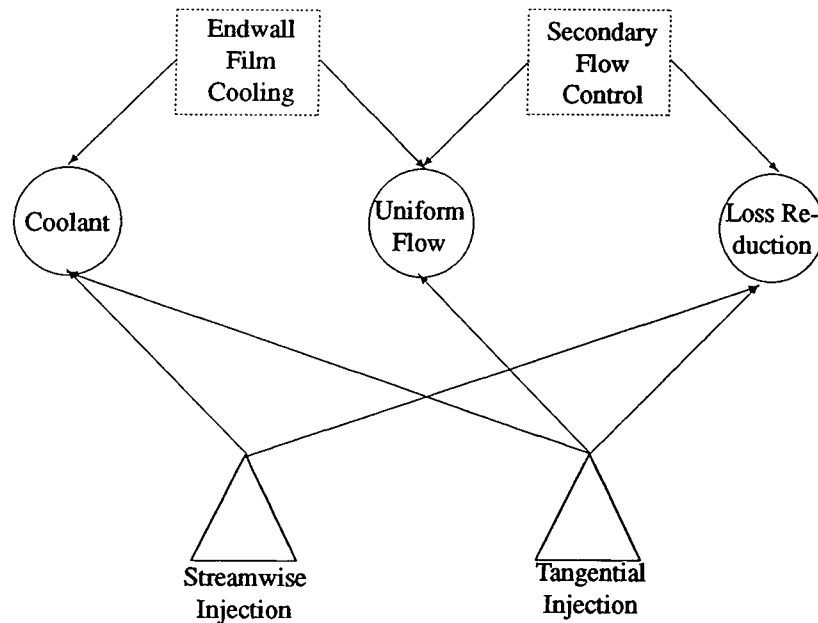
Figure 9.1: Secondary Flow Control and Endwall Film Cooling

cooling air with sufficient remaining heat capacity could be used to supply the injectant.

An extension to film cooling applications would have to account on the aerodynamics side for similarity constraints such as Mach number (Sieverding [1981]) and total temperature ratio (Colladay [1974], Hanus [1976]). Considering the thermodynamics, an increased number of non-dimensional parameters would have to be modelled (Schlichting [1979], pp. 271, Harasgama & Burton [1992]). Major changes in the experimental setup are required to meet these constraints and some of them are outlined below:

- An annular or full-stage, transonic test facility with provision of a disk cavity and cooling air could lead to a better aerodynamical representation of the injection. Vanes, attached to the either rotor or stator disk, could guide the cooling air emanating from the cavity in a similar way to the injection slot.

- Measurement of heat transfer rates and coefficients (Jones [1991]) employs the injection of a foreign gas (Karni & Goldstein [1990]) using the

heat/mass transfer analogy (Shadid & Eckert [1991]), fully calibrated hot films (Hodson [1984]) and transient or steady liquid-crystals methods (Harvey *et al.* [1989], Boyle & Russel [1989]).

- Heat transfer rates obtained from computations are dependent on the specified boundary conditions, assumptions in the governing equations (Dibelius *et al.* [1990]) and the near wall turbulence structure (Moore & Moore [1989]).

- The increased number of parameters to be controlled in order to find optimum injection conditions also makes the use of an expert-system attractive (Section 2.3.3).

★

The verification of a loss correlation based on the tangentially injected momentum (Section 5.2.3) could make an inclusion into existing through-flow codes possible. Alternatively, more sophisticated methods such as the inviscid method developed by Okan & Gregory-Smith [1992] could be used to calculate the effect of additional inlet vorticity on the exit flow. Preliminary tests have suggested promising results.

Appendix A

Durham Linear Cascade

A.1 Design Data

The flow at slot 1 is already influenced by the flow around the blade nose. The value for the measured inlet flow angle therefore depends on the pitchwise extent of the integration region. An angle of 42.8° has been used conventionally in the data analysis. The integration is carried out over a midspan-midpitch region. A different value of 45.5°, seen in the pitch-averaged curves (Figure 4.15, pg. 72), is obtained by integration over a full pitch. The specified accuracy measured angles is about ±0.5° (Section 3.2.5).

Blade Inlet Angle	47.6°
Flow Inlet Angle	42.8°
Blade Exit Angle	−68.0°
Flow Exit Angle	−68.8°
Stagger Angle	−36.1°
Blade Chord	224 mm
Axial Chord	181 mm
Blade Pitch	191 mm
Blade Span	400 mm
Reynolds Number (axial chord and exit velocity)	$4.3 \cdot 10^5$
Exit Mach Number	0.11
Zweifel Loading Coefficient	0.97
Inlet Turbulence Level	$\sim 4.5\%$

Table A.1: Cascade Design Data

A.2 Loss Characteristics

The data given in Table A.2 is valid for the modified blade described by Walsh [1987] and was measured with the turbulence grid in position.

The discrepancy of results without injection to previous measurements by Cleak [1989] indicate the necessity of a re-calibration of the 5H-probe. There is also an influence of taping down the rim of the mounted belt (Section 3.1.1) and the fact that the integration is carried out over the 'second' blade wake (Section 3.2.5) compared to the average of the traversed two.

With injection, the two important results with optimum injection at 250% design for both the low and high angles are listed. The percentages are relative to the measured exit loss at slot 10. The inlet loss is obtained at slot 1.

	No Injection	250% - Low	250% - High
Exit Loss (Slot 10) c_{p_e}	0.164 (100 %)	0.151 (100 %)	0.132 (100 %)
Exit Sec. Kin. Energy c_{ske_e}	0.018 (11 %)	0.005 (3 %)	0.003 (2 %)
Exit Mixed-Out Loss $c_{p_{em}}$	0.187 (114 %)	0.149 (99 %)[a]	0.138 (105 %)
Inlet Loss (Slot 1) c_{p_i}	0.023 (14 %)	0.006 (4 %)	-0.036 (-27 %)
Profile Loss $c_{p_{midspan_{em}}}$	0.094 (57 %)	0.090 (60 %)	0.088 (66 %)
Gross Secondary Loss $c_{p_{gross}}$ $= c_{p_e} - c_{p_{midspan_{em}}}$	0.070 (43 %)	0.061 (40 %)	0.044 (33 %)
Net Secondary Loss $c_{p_{net}}$ $= c_{p_{em}} - c_{p_i} - c_{p_{midspan_{em}}}$	0.047 (29 %)	0.055 (36 %)	0.080 (60 %)

[a]A lower mixed-out value is unrealistic and may be attributed to numerical errors in the calculation.

Table A.2: Mass-Averaged Total Pressure Loss Characteristics

Appendix B

Operation at Constant Reynolds Number with Injection

The existing correction method (Graves [1985]) makes comparisons between data taken under different atmospheric conditions possible. It was extended to account for the addition of mass by injection of air.

A reference day is chosen (Table B.1). The viscosity is calculated by a

Barometric Pressure (mmHg)	Atmospheric Temperature (deg K)	Dyn. Viscosity of Air ($\frac{Ns}{m^2}$)	Density of Air ($\frac{kg}{m^3}$)	Dynamic Head (mmWg)	Upstream Velocity $\frac{m}{s}$
741.45	292.15	$1.814 \cdot 10^{-5}$	1.1785	21.92	19.10

Table B.1: Reference Standard Day Conditions

polynomial function and the density is obtained from the ideal gas law. The Reynolds number for standard day conditions

$$Re = \frac{\rho v_e l}{\nu} \approx 4.3 \cdot 10^5$$

is based on the axial chord as reference length and the exit velocity.

Comparing two days (index 1 and 2, where the former denotes standard day conditions) and employing Bernoulli's formula and the ideal gas law, a correction factor for the required upstream dynamic head on an arbitrary day

$$k_{pitot} = \frac{\Delta p_{pitot_2}}{\Delta p_{pitot_1}} \tag{B.1}$$

$$= \frac{p_{at_1}}{p_{at_2}} \left(\frac{\nu_1}{\nu_2}\right)^2 \frac{T_1}{T_2} \tag{B.2}$$

is obtained. Δp denotes the dynamic head, which is measured by a far upstream pitot tube (see Figure B.1).
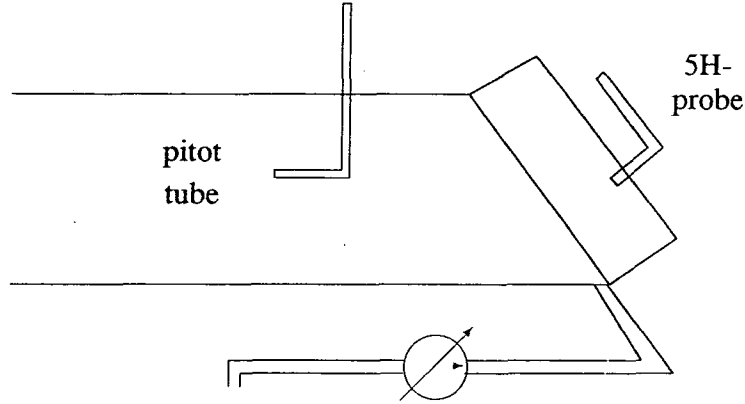
Figure B.1: Reynolds Number Correction with Injection

A similar factor k_{probe} is used to correct the measurements by the five-hole probe after the upstream dynamic head has been set to its required value as close as possible. The factor is the ratio of the actual set upstream dynamic head to the standard day dynamic head.

$$k_{probe} = \frac{\Delta p_{pitot_2}}{\Delta p_{pitot_1}} \tag{B.3}$$

In the blown case (superscript ' $'$ '), the upstream pitot tube is exposed to only a percentage of the total mass flow.

$$\dot{m}'_{pitot_2} = (1 - \frac{m_{jet}}{m_{cas}})\dot{m}_{cas} \tag{B.4}$$

$$= (1 - r)\dot{m}_{cas} \tag{B.5}$$

Therefore an adjustment of the reference standard day dynamic head according to the jet to cascade mass flow ratio $r = \frac{m_{jet}}{m_{cas}}$ is necessary.

Due to similarity

$$\frac{\Delta p_{pitot_2}}{\Delta p_{pitot_1}} = \frac{\Delta p'_{pitot_2}}{\Delta p'_{pitot_1}} \tag{B.6}$$

$$k_{pitot} = k'_{pitot} \tag{B.7}$$

Rearrangement and substitution yields

$$\frac{\Delta p'_{pitot_1}}{\Delta p_{pitot_1}} = \frac{\Delta p'_{pitot_2}}{\Delta p_{pitot_2}} \tag{B.8}$$

$$= \frac{\frac{1}{2}\rho v'^2_{pitot_2}}{\frac{1}{2}\rho v^2_{pitot_2}} \tag{B.9}$$

$$= (1 - r)^2 \tag{B.10}$$

Using equations (B.6), (B.7) and (B.10), the correction factor for the pitot tube becomes

$$\Delta p'_{pitot_2} = k'_{pitot} \cdot \Delta p'_{pitot_1} \tag{B.11}$$

$$= k_{pitot} \cdot (1-r)^2 \cdot \Delta p_{pitot_1} \tag{B.12}$$

$$= \frac{p_{at_1}}{p_{at_2}} \left(\frac{v_1}{v_2}\right)^2 \frac{T_1}{T_2} \cdot (1-r)^2 \cdot \Delta p_{pitot_1} \tag{B.13}$$

The correction to the pressures measured by the 5H-probe can be derived from the similarity

$$\frac{\Delta p_{pitot_2}}{\Delta p_{pitot_1}} = \frac{\Delta p'_{probe_2}}{\Delta p'_{pitot_1}} \tag{B.14}$$

$$= \frac{\Delta p'_{probe_2}}{\Delta p_{pitot_1}} \tag{B.15}$$

$$k_{probe} = k'_{probe} \tag{B.16}$$

Substituting equation (B.6) into equation (B.15) gives for the probe correction factor

$$k'_{probe} = \frac{\Delta p'_{probe_2}}{\Delta p_{pitot_1}} \tag{B.17}$$

$$= \frac{\Delta p'_{pitot_2}}{\Delta p_{pitot_1}(1-r)^2} \tag{B.18}$$

The mass flow of the injected air has to be adjusted to a change in the atmospheric conditions it has to be corrected in the same way as the cascade mass flow. The mass flow ratio for an arbitrary day to a standard day is

$$\frac{\frac{\dot{m}_2 \cdot l}{A}}{v_2} = \frac{\frac{\dot{m}_1 \cdot l}{A}}{v_1} \tag{B.19}$$

$$\frac{\dot{m}_2}{\dot{m}_1} = \frac{v_2}{v_1} \tag{B.20}$$

Since the injected air is a fraction 'r' of the cascade mass flow, equation (B.20) can be written as

$$\frac{\dot{m}'_{jet_2}}{\dot{m}'_{jet_1}} = \frac{v_2}{v_1} \tag{B.21}$$

The data acquisition program suggests in the first place a mass flow of injected air for a standard day. This value is corrected to the present day conditions and tried to be set on the orifice as closely as possible . The actually set value of the

injected air mass flow is then also corrected and subsequently used to calculate the necessary upstream dynamic head for the cascade mass flow as well as to correct all sampled data to standard day conditions.

Appendix C

Orifice Plate

On the basis of a theoretical necessary mass flow for the injected air, the design data for the orifice plate given in Table C.1 was obtained. The corresponding mass

Orifice Plate Diameter D	Inner Pipe Diameter d	Diameter Ratio $\frac{d}{D}$	Area Ratio $m = \frac{d^2}{D^2}$
102.5 mm	50.0 mm	0.4878	0.238

Table C.1: Design Data of Orifice Plate

flow can be calculated using the formula

$$\dot{m}_j = 0.01252 \cdot C \cdot Z \cdot \varepsilon \cdot E \cdot d^2 \cdot \sqrt{\Delta p \cdot \rho}$$

where C denotes a basic coefficient, Z a correction factors, ε an expandibility factor, E the velocity-of-approach factor, d the diameter of the orifice plate, Δp the measured pressure drop and ρ the density of air. Evaluation of the individual parameters results in

$$\dot{m}_j = 1.7563 \cdot \sqrt{\Delta p \cdot \rho}$$

The sum tolerance of the measured mass flow is determined in the following. Errors are of systematic and random origin. The former are considered first.

The following systematic errors X are contained in the equation for the mass flow

X_C: The given value for the basic coefficient C has to be increased by 0.5% twice to account for shorter upstream and downstream pipe lengths.

$$X_C = 0.7\% + 0.5\% + 0.5\%$$
$$= 1.7\%$$

$X_{Z_{(R)}}$: The error of the Reynolds number correction factor amounts to

$$X_{Z_{(R)}} = 0.3795\%$$

$X_{Z_{(D)}}$: The Pipe size correction factor is zero.

$$X_{Z_{(D)}} \simeq 0.0\%$$

The systematic errors in the fluid density X_ρ and the pressure measurements $X_{\Delta p}$ are unknown. Instead their random errors were estimated to 0.05 and 0.3 respectively.

The overall error is calculated by substituting into the formula of the root-mean-square method of combining tolerances (eq. (45), pg. 73, BS1042).

$$
\begin{aligned}
X_{Sum} &= \sqrt{X_C^2 + X_{Z_{(R)}}^2 + X_{Z_{(D)}}^2 + X_\rho^2 + X_{\Delta p}^2} \\
&= 1.75\%
\end{aligned}
$$

This value has a confidence interval of 95% for the normal distribution. It has further been assumed that errors due to thermal expansion as well as expandibility are negligible. The error is thought to be acceptable in the light of the errors associated with the main flow.

Appendix D

Error Analysis

D.1 Systematic Errors

A typical systematic error is the one inferred by an inaccurate probe calibration. Another example is the over-reading of total pressure by the probe depending on the turbulence level present. Misalignment of the probe head relative the flow due to bending of the probe stem, imperfect support and slide mountings are of systematic geometrical nature. An error, which appears as random but is genuinely systematic is due to the linearity of the transducers and A/D-converter for which maximum errors are given in Table D.1. Shifts of offset and drifts of sensitivity are mostly thermal errors and are so low that they are not included in the investigation.

Systematic				Random	
Transducer		A/D-converter		Transducer	
Furness	CMR	Furness	CMR	Furness	CMR
0.10 mmWg $(0.5 \% p_{d_u})$	0.51 mmWg $(2.3 \% p_{d_u})$	0.019 mmWg $(0.1 \% p_{d_u})$	0.049 mmWg $(0.2 \% p_{d_u})$	0.10 mmWg $(0.5 \% p_{d_u})$	0.051 mmWg $(0.2 \% p_{d_u})$

Table D.1: Errors of Transducer and A/D-converter

D.2 Random Errors

Typical random errors are those due to repeatability and hysteresis in transducers and are also listed in Table D.1. The value for the Furness transducer is identical to the systematic one since only an 'accuracy of reading' was given in the specifications. Another source are inaccurate readings of the atmospheric conditions, which influence the pressure correction to ensure constant Reynolds number operation and may result in an error of as much as 2 mmWg (Biesinger [1991]). The upstream pitot tube relative to which all other pressures are recorded also contributes a random error. Finally, a 'probe' error can be determined by subtraction of transducer and A/D-converter random and systematic errors from the measured variance of the data.

0.51 + 0.051

ref. - CMR

ref. - FUR

0.0 + 0.12

probe - CMR

Flow

probe - FUR

0.081 + 0.02

0.1

A/D - CMR

0.049

A/D - FUR

Conf. Test

dyn. head

0.019

0.041
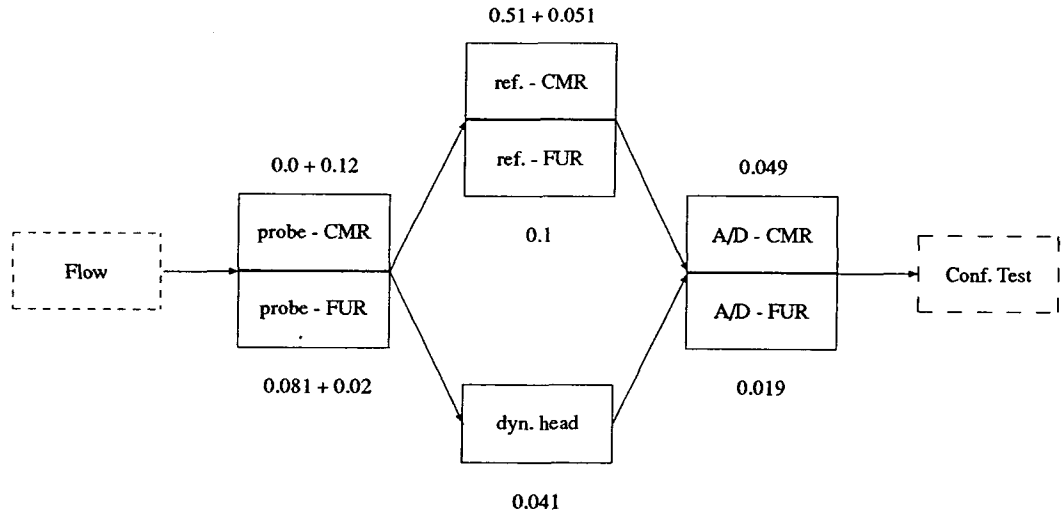
Figure D.1: Map of Overall Error Contributions (in mmWg)

D.3 Overall Error

Figure D.1 shows different measuring components and their maximum possible errors linked together. The flow is measured by transducers connected to the 5H-probe and is referenced to the upstream total pressure, which depends on the set dynamic head. The voltage output is processed by an A/D converter and finally undergoes a confidence test to limit the scatter of the data (Section 3.2.3). An estimate of the overall error is obtained by adding the corresponding relative[1] maximum random errors to the systematic ones. Values of 0.77 mmWg for the CMR transducer and 0.26 mmWg for the Furness transducer are obtained.

Although these values represent the *maximum* overall error, they might provide an estimate of the *actual* (statistical) overall error by compensating for 5H-probe calibration errors not accounted for. Referencing the value of the Furness transducer, which is connected to the central tube of the 5H-probe, to a standard inlet dynamic head of 21.92 mmWg (Table B.1, pg. 190) yields a tolerance for the total pressure loss coefficient of ±0.006. This is close to a slightly better estimate of ±0.005 listed in Table 3.5, Section 3.2.5).

---

[1]The relative error is the absolute error divided by an absolute value.

Appendix E

Definitions

E.1 Area Traverse Plots

E.1.1 Total Pressure Loss Coefficient

$$c_{p_l} \doteq \frac{p_{0_u} - p_{0_l}}{\frac{1}{2}\rho v_u^2} \tag{E.1}$$

E.1.2 Vorticity Components

$$c_{\xi_\sigma} \doteq \frac{(\xi_x \cos\alpha_y + \xi_y \sin\alpha_y) \cdot s}{v_u} \tag{E.2}$$

$$c_{\xi_v} \doteq \frac{(\xi_x \sin\alpha_y - \xi_y \cos\alpha_z) \cdot s}{v_u} \tag{E.3}$$

E.2 Pitch/Mass-Averaged Curves

E.2.1 Total Pressure Loss Coefficient

$$\overline{c_{p_l}} \doteq \frac{\int v_x c_{p_l}\, dy}{\int v_x\, dy} \tag{E.4}$$

E.2.2 Secondary Kinetic Energy

$$\overline{c_{ske_l}} \doteq \frac{\int v_x (v_y^2 + v_z^2)\, dy}{\int v_x\, dy \cdot v_u^2} \tag{E.5}$$

E.2.3 Yaw Angle

$$\overline{\alpha_y} \doteq \arctan \frac{\int v_x v_y \, dy \cdot s}{\left(\int v_x \, dy\right)^2} \tag{E.6}$$

$$= \arctan \frac{\overline{v_y}}{\overline{v_x}}$$

E.3 Area/Mass-Averaged Values

E.3.1 Total Pressure Loss Coefficient

$$c_p \doteq \frac{\iint v_x c_{p_l} \, dydz \cdot \rho}{\dot{m}_{cas}} \tag{E.7}$$

$$= \overline{\overline{c_{p_l}}}$$

E.3.2 Secondary Kinetic Energy

$$c_{ske} \doteq \frac{\iint v_x (v_y^2 + v_z^2) \, dydz \cdot \rho}{\dot{m}_{cas} \cdot v_u^2} \tag{E.8}$$

$$= \overline{\overline{c_{ske_l}}}$$

E.3.3 Exit Angle

$$\alpha_e \doteq \arctan \frac{\iint v_x v_y \, dydz \cdot \rho^2 \cdot \hbar \cdot s}{\dot{m}_{cas}^2} \tag{E.9}$$

$$= \frac{\arctan \frac{\iint v_x v_y \, dydz \cdot \rho}{\dot{m}_{cas}}}{\frac{\dot{m}_{cas}}{\rho \hbar s}} \tag{E.10}$$

$$= \arctan \frac{\overline{\overline{v_y}}}{\overline{\overline{v_x}}}$$

$$= \overline{\overline{\alpha_y}}$$

$\overline{\overline{v_x}}$ denotes here an area- but not mass-averaged value. This is required for calculating correct area/mass-averaged momentum fluxes.

Appendix F

Turbulent Flow Formulæ

F.1 Kinetic Energy Balance Equations

Manipulation of the Navier-Stokes equations yields for the kinetic energy of the mean flow (Tennekes & Lumley [1972], pg. 63)

$$U_j \frac{\partial}{\partial x_j}(\frac{1}{2}\overline{U_i U_i}) = \frac{\partial}{\partial x_j}\left(-\frac{1}{\rho}PU_j + 2\nu U_i S_{ij} - \overline{u_i u_j}U_i\right)$$

$$\underset{pg}{} \qquad \underset{transport}{}$$

$$-2\nu S_{ij}S_{ij} + \overline{u_i u_j}S_{ij} \qquad \text{(F.1)}$$

$$\underset{dissipation}{} \quad \underset{production}{}$$

and for the mean kinetic energy of the turbulent velocity fluctuations (turbulent energy budget)

$$U_j \frac{\partial}{\partial x_j}(\frac{1}{2}\overline{u_i u_i}) = -\frac{\partial}{\partial x_j}\left(\frac{1}{\rho}\overline{pu_j} + \frac{1}{2}\overline{u_i u_i u_j} - 2\nu\overline{u_i s_{ij}}\right)$$

$$\underset{pg}{} \qquad \underset{transport}{}$$

$$-2\nu\overline{s_{ij}s_{ij}} - \overline{u_i u_j}S_{ij} \qquad \text{(F.2)}$$

$$\underset{dissipation}{} \quad \underset{production}{}$$

with the mean and fluctuating strains

$$S_{ij} \equiv \frac{1}{2}\left(\frac{\partial U_i}{\partial x_j} + \frac{\partial U_j}{\partial x_i}\right) \qquad \text{(F.3)}$$

$$s_{ij} \equiv \frac{1}{2}\left(\frac{\partial u_i}{\partial x_j} + \frac{\partial u_j}{\partial x_i}\right) \qquad \text{(F.4)}$$

The above equations are in Eulerian form and denote the contributions due to the pressure gradient *pg*, *transport* and *dissipation* and *production* terms.

F.2 Mean Laminar Dissipation and Turbulence Production

Re-grouping equations (F.1) and (F.2) for the mean laminar dissipation Ψ_L and the turbulence production Ψ_T of a particular strain (Hinze [1975]) yields

$$\Psi_L = -\nu \left(\frac{\partial U_i}{\partial x_j} + \frac{\partial U_i}{\partial x_j}\right) \frac{\partial U_i}{\partial x_j} \tag{F.5}$$

$$\Psi_T = -\overline{u_i u_j} \frac{\partial U_i}{\partial x_j} \tag{F.6}$$

Relating these energies per unit of mass and of time to the upstream dynamic head yields rates in $\frac{1}{s}$. This may be further non-dimensionalized by division with the local axial velocity and multiplication with the blade axial chord before integration and mass-averaging. The obtained values represent a percentage of the energy dissipated by an imaginary fluid particle travelling with axial velocity along the axial chord and may be related to the total pressure loss growth (Moore *et al.* [1985]).

F.3 k-ε Turbulence Model

Reynolds-averaged Navier-Stokes equations contain turbulent shear stresses

$$\tau_{ij} = -\overline{\rho u_i u_j} \tag{F.7}$$

that require modelling. One possibility, derived from two-dimensional boundary layers, is the eddy-viscosity concept in which the turbulent stresses are related to mean flow quantities similar to laminar flows:

$$\overline{u_i u_j} = -\nu_T \left(\frac{\partial U_i}{\partial x_j} + \frac{\partial U_j}{\partial x_i}\right) \tag{F.8}$$

The eddy viscosity itself is made a function of the square of the turbulent kinetic energy $k = \frac{1}{2}\overline{u_i u_i}$ and the turbulent dissipation $\varepsilon = -\mu\left(\frac{\partial u_i}{\partial x_j} + \frac{\partial u_i}{\partial x_j}\right)\frac{\partial u_j}{\partial x_i}$:

$$\nu_T = -const \cdot \frac{k^2}{\varepsilon} \tag{F.9}$$

k and ε are determined by transport equations, the constant is empirical. Since spatial derivatives of fluctuating velocities are very difficult to measure, only the turbulent kinetic energy can be compared to experimental data.

Appendix G

Legend to Contour Plots

Table G.1 shows the relation between the contour level numbering and actual plotted values for the **experimental** work (Chapter 4):

Contour Level	61	62	63	64	65	66/7	68	69	70	71	72
c_{p_l}	0.0	0.1	0.2	0.3	0.4	0.5	0.6	0.7	0.8	0.9	1.0

Contour Level	32	33	34	35	36	37	38
$c_{\xi_{\sigma,\nu}}$	-15.0	-10.0	-5.0	0.0	5.0	10.0	15.0

Table G.1: Relation of Contour Interval Numbering to Coefficients (Experiment)

Table G.2 shows the relation between the contour level numbering and actual plotted values for the **computations** (Chapter 6):

Contour Level	53	54	57	60	61	62	64	65	66	70	71
c_{p_l}	-0.7	-0.6	-0.4	-0.1	0.0	0.1	0.3	0.4	0.5	0.8	0.9

Table G.2: Relation of Contour Interval Numbering to Coefficient (Computation)

Bibliography

Abelson H, Eisenberg M, Halfant M, Katzenelson J, Sacks E, Sussman G J, Wisdom J, Kenneth Y, 1989. *Intelligence in Scientific Computing*. Communications of the ACM 32:546-.

Ainley D G, Mathieson G C R, 1951. *A Method of Performance Estimation for Axial Flow Turbines*. ARCR and M 2974.

Atkins M J, 1987. *Secondary-Losses and Endwall Profiling in a Turbine Cascade*. IMechE C255/87 29-42.

Bario F, Leboeuf F, Onvani A, Seddine A, 1990. *Aerodynamics of Cooling Jets Introduced in the Secondary Flow of a Low-Speed Turbine Cascade*. Journal of Turbomachinery, ASME 112:539-.

Belik L, 1968. *An Approximate Solution for Kinetic Energy of Secondary Flow in Blade Cascades*. International Journal of Mechanical Science 10:765-782.

Bergmann-Schäfer, 1974. *Lehrbuch der Experimentalphysik*. Walter de Gruyter 1:522.

Biesinger T E, 1990. *Experimental and Numerical Investigation of Secondary Loss Reduction Techniques in Linear Turbine Cascades*. First Year Report, University of Durham.

Biesinger T E, 1991. *Errors on Five-Hole Probe Measurements*. Internal Report, University of Durham.

Biesinger T E, Gregory-Smith D G, 1992. *Reduction in Secondary Flows and Losses in a Turbine Cascade by Upstream Boundary Layer Blowing*. ASME paper GT-92.

Binder A, Romey R, 1983. *Secondary Flow Effects and Mixing of the Wake behind a Turbine Stator*. Journal of Engineering for Power 102:40-.

Bindon J P, 1979a. *The Effect of Hub Inlet Boundary Layer Skewing on the Endwall Shear Flow in an Annular Turbine Cascade*. ASME paper 79-GT-13.

Bindon J P, 1979b. *Comparison of Transverse Injection Effects in Annular and in Straight Turbine Cascades.* ASME paper 79-GT-17.

Bindon J P, 1980. *Exit Plane and Suction Surface Flows in an Annular Turbine Cascade with a Skewed Inlet Boundary Layer.* International Journal of Heat and Fluid Flow 2:57.

Bischoff H, 1982. *Passage Step.* Patent by MTU.

Bischoff H, 1983. *Suction Side Corner Fillet.* Patent by MTU.

Boletis E, 1985. *Effects of Tip Endwall Contouring on the Three-Dimensional Flow Field in an Annular Turbine Nozzle Guide Vane: Part 1 - Experimental Investigation.* ASME, Journal of Engineering for Gas Turbines and Power 107:983-990.

Boletis E, Sieverding C H, Van Hove W, 1983. *Effects of a Skewed Inlet End-wall Boundary Layer on the 3-D Flow Field in an Annular Turbine Cascade.* AGARD CP 351 'Viscous Effects in Turbomachines' paper 5.

Boris J P, 1989. *New Directions in Computational Fluid Dynamics.* Annual Review Fluid Mechanics 21:345-385.

Boyle M T, Simonds M, Poon K, 1989. *A Comparison of Secondary Flow in a Vane Cascade and a Curved Duct.* Journal of Turbomachinery, ASME 111:530-536.

Bradshaw P (editor), 1978. *Turbulence.* Springer Verlag.

Breugelmans F A H, Carels Y, Demuth M, 1984. *Influence of Dihedral on the Secondary Flow in a Two-Dimensional Compressor Cascade.* ASME, Journal of Engineering for Gas Turbines and Power 106:578-584.

Broichhausen K D, Henne J M, Gallus H E, 1983. *Development of a Laser-Density-Gradient Technique for the Measurement of Unsteady Flow Phenomena.* Proceedings of the 7th Symposium on Measuring Techniques for Transonic and Supersonic Flow in Cascades and Turbomachines, Aachen.

Bronstein I N, Semendjajew K A, 1981. *Taschenbuch der Mathematik.* Thun, Frankfurt/Main.

Bubeck H, 1988. *Fehlerkorrekturen bei Strömungsmessungen mit pneumatischen Mehrlochsonden.* Institut für Thermische Strömungsmaschinen und Maschinenlaboratorium, Aktenzeichen Wa 303/33-1.

Busch M, 1982. *Messtechnik I.* Vorlesungsmanuscript, Lehrstuhl und Institut für Thermische Strömungsmaschinen, Maschinenlaboratorium, Universität Stuttgart.

Carey C, Scanlon T J, Fraser S M, 1992. *The Reduction of False Diffusion in the Simulation of Vortex Shedding.* IMechE, Part C.

Chen S, Wang Z, Shan X, Doolen G D, 1992. *Lattice Boltzmann Computational Fluid Dynamics in Three Dimensions.* Journal of Statistical Physics Vol. 68 No 3/4.

Came P M, Marsh H, 1974. *Secondary Flow in Cascades: Two Simple Derivations for the Components of Vorticity.* Journal Mechanical Engineering Science 16:391-401.

Canuto C, Hussaini M Y, Quarteroni A, Zang T A, 1987. *Spectral Methods in Fluid Dynamics.* Springer Verlag.

Cleak J G E, 1989. *Validation of Viscous Three-Dimensional Flow Calculations in an Axial Turbine Cascade.* PhD thesis, University of Durham.

Cleak J G E, Gregory-Smith D G, 1992. *Turbulence Modelling for Secondary Flow Prediction in a Turbine Cascade.* Journal of Turbomachinery, ASME 114(3):590-598.

Cleak J G E, Gregory-Smith D G, Birch N T, 1991. *Experimental Verification of a 3D Turbulent Flow Calculation in an Axial Turbine Cascade.* Presented at AGARD PEP Symposium on Computational Fluid Dynamics in Propulsion, AGARD-CP-510, paper no 8.

Combes J F, 1992. *Calcul par Elements Finis de L'écoulement 3D Turbulent dans une Pompe Centrifuge.* AGARD-CP-510.

Colladay R S, Stepka F S, 1974. *Similarity Constraints in Testing of Cooled Engine Parts.* NASA TN D-7707, June 1974.

Dadkhah S, Turner A B, Chew J W, 1992. *Performance of Radial Clearance Rim Seals in Upstream and Downstream Rotor-Stator Wheelspaces.* Journal of Turbomachinery 114:439-.

Dawes W N, 1991. *The Simulation of Three-Dimensional Viscous Flow in Turbomachinery Geometries using a Solution-Adaptive Unstructured Mesh Methodology.* to be published in 'Journal of Turbomachinery', ASME paper 91-GT-124.

Dawes W N, 1992. *The Extension of a Solution-Adaptive 3D Navier-Stokes Solver towards Geometries of Arbitrary Complexity.* ASME paper 92-GT-363.

Dejc M E, Trojansowskij B M, 1973. *Aerodynamische Charakteristiken Gerader Gitter bei Unterschallgeschwindigkeiten.* Untersuchung und Berechnung axialer Turbinenstufen 37-51.

Denton J D, 1986. *The Use of a Distributed Body Force to Simulate Viscous Effects in 3D Flow Calculations.* ASME paper 86-GT-144.

Denton J D, 1990. *The Calculation of Three Dimensional Viscous Flow Through Multistage Turbomachines.* ASME paper 90-GT-19.

Denton J D, Cumpsty N A, 1987. *Loss Mechanisms in Turbomachines.* IMechE, C260/87.

Despain A, 1990. *Prospects for a Lattice-Gas Computer in Lattice-Gas Methods for Partial Differential Equations.* In Doolen G D (editor): *Lattice Gas Methods for Partial Differential Equations.* ISBN 020113232X.

Dibelius G H, Pitt R, Wen B, 1990. *Numerical Prediction of Film Cooling Effectiveness an the Associated Aerodynamic Losses with a Three-Dimensional Calculation Procedure.* ASME paper 90-GT-226.

Dominy R G, Hodson H P, 1991. *An Investigation of Factors Influencing the Calibration of 5-Hole Probes for 3-D Flow Measurements.*

Dunham J, 1970. *A Review of Cascade Data on Secondary Losses in Turbines.* Journal of Mechanical Engineering Science 12:48-59.

Finlayson B A, 1972. *The Method of Weighted Residuals and Variational Principles.* Academic Press.

Fletcher C A J, 1988. *Computational Techniques for Fluid Dynamics.* Springer Verlag, Volumes I and II.

Gaugler R E, Russel L M, 1980. *Streakline Flow Visualization Study of a Horseshoe Vortex in a Large-Scale, Two-Dimensional Turbine Stator Cascade.* ASME, 80-GT-4.

Glynn D R, 1982. *Calculation of Secondary Flow in Cascades including Effects of Bernoulli Surface Distortion.* International Journal of Heat and Fluid Flow 3 no 2:73-.

Glynn D R, Marsh H, 1980. *Secondary Flow in Annular Cascades*. International Journal of Heat and Fluid Flow 2:29-33.

Goldman L J, McLallin K L, 1977. *Effect of Endwall Cooling on Secondary Flows in Turbine Stator Vanes*. AGARD-CP-124.

Graves C P, 1985. *Secondary Flows and Losses in Gas Turbines*. PhD thesis, University of Durham.

Gregory-Smith D G, 1982. *Secondary Flows and Losses in Axial Flow Turbines*. ASME, 82-GT-19.

Gregory-Smith D G, Biesinger T E, 1992. *Turbulence Evaluation within the Secondary Flow Region of a Turbine Cascade*. ASME paper 92-GT-60.

Gregory-Smith D G, Graves C P, 1983. *Secondary Flows and Losses in a Turbine Cascade*. unknown.

Gregory-Smith D G, Graves C P, Walsh J A, 1988. *Growth of Secondary Losses and Vorticity in an Axial Turbine Cascade*. Journal of Turbomachinery, ASME 110(1):1-8.

Gregory-Smith D G, Cleak J G E, 1992. *Secondary Flow Measurements in a Turbine Cascade with High Inlet Turbulence*. Journal of Turbomachinery, ASME 114(1):173-183.

Gregory-Smith D G, Okan M B, 1992. *A Simple Method for the Calculation of Secondary Flows in Annular Cascades*. IMechE C423/008.

Hah C, 1984. *A Navier-Stokes Analysis of Three-Dimensional Turbulent Flows inside Turbine Blade Rows at Design and Off-Design Conditions*. ASME, Journal of Engineering for Gas Turbines and Power 106:421-429.

Hahne E, 1992. *Technische Thermodynamik*. Addison-Wesley, Bonn.

Hanus G J, 1976. *Gas Film Cooling of a Modeled High-Pressure, High-Temperature Turbine Vane with Injection in the Leading Edge Region from a Single Row of Spanwise-Angled Coolant Holes*. PhD thesis, Mechanical Engineering Department, Purdue University, West Lafayette, Indiana.

Harasgama S P, Burton C D, 1992. *Film Cooling Research on the Endwall of a Turbine Nozzle Guide Vane in a Short Duration Annular Cascade: Part 1 - Experimental Technique and Results*. Journal of Turbomachinery 114:734-.

Harrison S, 1989. *Secondary Loss Generation in a Linear Cascade of High-Turning Turbine Blades*. ASME 89-GT-47 1-7.

Harrison S, 1990. *The Influence of Blade Lean on Turbine Losses*. ASME paper 90-GT-55.

Harvey N W, Wang Z, Ireland P T, Jones T V, 1989. *Detailed Heat Transfer Measurements in Nozzle Guide Vane Passages in Linear and Annular Cascades in the Presence of Secondary Flows*. AGARD CP 469.

Hawthorne W R, 1955. *Rotational Flow Through Cascades Part I, The Components of Vorticity*. Journal of Mech Appl Math 8:266-279.

Hinze J, 1975. *Turbulence*. McGraw-Hill.

Hirsch C, 1988. *Numerical Computation of Internal and External Flows*. Volumes I and II, Wiley.

Hodson H P, 1984. *Boundary Layer and Loss Measurements on the Rotor of an Axial-Flow Turbine*. ASME, Journal of Engineering for Gas Turbines and Power 106:391-399.

Hodson H P, Dominy R G, 1986. *Three-Dimensional Flow in a Low-Pressure Turbine Cascade at its Design Condition*. ASME paper 86-GT-106.

Horton G C, 1984. *The Effects of Profiled Endwalls on the Secondary Flows within a Turbine Nozzle Guide Vane Row, Part I - A Theoretical Investigation*. Technical Memo P1027, Ministry of Defense, Farnborough.

Jones T V, 1991. *Definition of Heat Transfer Coefficients in the Turbine Situation*. IMechE paper C423/046.

Karni J, Goldstein R J, 1990. *Surface Injection Effect on Mass Transfer from a Cylinder in Crossflow: A Simulation of Film Cooling in the Leading Edge Region of a Turbine Blade*. ASME, Journal of Turbomachinery 112:418-.

Kawai T, Adachi T, Shinoki S, 1988a. *Secondary Flow and Losses in a Turbine Cascade Equipped with Endwall Boundary Layer Fences (Influence of Fence Position)*. Nippon Kikai Gakkai Ronbunshu B Hen 54, n 505:2492-2498.

Kawai T, Shinoki S, Adachi T, 1988b. *Optimization of Endwall Boundary Layer Fences in Controlling Secondary Flow in a Turbine Cascade*. Nippon Kikai Gakkai Ronbunshu B Hen 54 N508:3432-3439.

Klein A, 1966. *Untersuchung über den Einfluss der Zuströmgrenzschicht auf die Sekundärströmungen in den Beschaufelungen von Axialturbinen.* Forschung Ingenieur Wesen 32 6:175-188.

Kopper F C, Milano R, Vanco M, 1980. *An Experimental Investigation of Endwall Profiling in a Turbine Vane Cascade.* AIAA paper.

Kreyszig E, 1962. *Advanced Engineering Mathematics.* Wiley International.

Lai Y G, So R M C, Anwer M, Hwang B C, 1991. *Calculations of a Curved-pipe Flow using Reynolds Stress Closure.* Proceedings IMechE 205:231-.

Lakshminarayana B, 1991. *An Assessment of Computational Fluid Dynamic Techniques in the Analysis and Design of Turbomachinery - The Freeman Scholar Lecture.* Journal of Turbomachinery 113:315-.

Lakshminarayana B, Horlock J H, 1973. *Generalized Expressions for Secondary Vorticity Using Intrinsic Coordinates.* Journal of Fluid Mechanics 59:97-115.

Langston L S, 1970. *Crossflows in a Turbine Cascade Passage.* Journal of Engineering for Power 102:866-.

Langston L S, 1989. *Research on Cascade Secondary and Tip-Leakage Flows - Periodicity and Surface Flow Visualization.* AGARD-CP-469, September 1989.

Langston L S, Nice M L, Hooper R M, 1977. *Three Dimensional Flow within a Turbine Cascade Passage.* ASME Journal Engineering and Power 99:21-28.

Launder B E, Spalding D B, 1974. *The Numerical Computation of Turbulent Flows.* Computer Methods in Applied Mechanics and Engineering 3:269-289.

Levy Y, Degani D, Seginer A, 1990. *Graphical Visualization of Vortical Flows by Means of Helicity.* AIAA Journal 28:1347-.

Lewis R I, Hill J M, 1971. *The Influence of Sweep and Dihedral in Turbomachinery Blade Rows.* Journal of Mechanical Engineering Science, Volume 3, Number 4.

Marchal Ph, Sieverding C H, 1977. *Secondary Flows within Turbomachinery Bladings.* AGARD-CP-214, 'Secondary Flows in Turbomachines' paper 11.

Mayhew Y R, 1991. *Does the Methodology of Teaching Thermodynamics to Engineers Need Changing in the 1990s?* Proceedings IMechE 205:283-.

Merzkirch W, 1987. *Flow Visualization*. Academic Press.

Moore J, 1983. *Flow Trajectories, Mixing and Entropy Fluxes in a Turbine Cascade*. AGARD CP 351 'Viscous Effects in Turbomachines' paper 5.

Moore J G, 1985a. *Calculation of 3D Flow without Numerical Mixing*. AGARD-LS-140, paper no 8.

Moore J G, 1985b. *An Elliptic Calculation Procedure for 3D Viscous Flow*. AGARD-LS-140, paper no 4.

Moore J, Adhye R Y, 1985. *Secondary Flows and Losses Downstream of a Turbine Cascade*. ASME paper no 85-GT-64.

Moore J, Moore J G, 1985. *Performance Evaluation of Flow in Turbomachinery Blade Rows*. Journal of Engineering for Gas Turbines and Power, 107:969-975.

Moore J, Moore J G, 1989. *Effects of Secondary Flow on Heat Transfer in Rotating Passages*. AGARD-CP-469.

Moore J G, Moore H, Shaffer D M, 1985. *Reynolds Stresses and Dissipation Mechanisms Downstream of a Turbine Cascade*. Turbomachinery Research Group Report Number JM/85-9 (also ASME 86 paper).

Moore J, Smith B L, 1984. *Flow in a Turbine Cascade: Part 2 - Measurement of Flow Trajectories by Ethylene Detection*. Journal of Engineering for Gas Turbines and Power 106:409-.

Moore R W, Richardson D L, 1957. *Skewed Boundary Layer Flow near the Endwalls of a Compressor Cascade*. Transaction of ASME 79:1789-.

Morris A W H, Hoare R G , 1975. *Secondary Loss Measurements in a Cascade of Turbine Blaes with Meridional Wall Profiling*. ASME paper in 75 WA/GT 13 for meeting 30-12-75.

Moustapha S H, Paron G J, Wade J H T, 1985. *Secondary Flows in Cascades of Highly Loaded Turbine Blades*. ASME, Journal of Engineering for Gas Turbines and Power 107:1031-1038.

Okan M B, Gregory-Smith D G, 1992. *A Simple Method for Estimating Secondary Losses in Turbines at the Preliminary Design Stage*. ASME paper 92-GT-294.

Prandtl L, 1925. *Über die ausgebildete Turbulenz.* ZAMM 5:136-139.

Press W H, Flannery B P, Teykolsky S A, Vetterling W T, 1988. *Numerical Recipes in C.* Cambridge University Press.

Prümper H, 1975. *Verbesserung des Wirkungsgrades Axialer Turbinenstufen durch Reduzierung der Sekundärverluste.* PhD thesis, RWTH Aachen.

Pucher P, Göhl R, 1987. *Experimental Investigation of Boundary Layer Separation with Heated Thin-Film Sensors.* Journal of Turbomachinery 109:303-.

Rechenberg I, 1973. *Evolutionsstrategie.* Problemata, Frommann-Holzboog.

Roache P J, 1976. *Computational Fluid Dynamics.* Hermosa, Albuquerque.

Sharma O P, Butler T L, 1986. *Predictions of Endwall Losses and Secondary Flows in Axial Flow Turbine Cascades.* ASME, 86-GT-228 1-10.

Scheurlen M, Noll B, Wittig S, 1991. *Application of Monte-Carlo Simulation for Three-Dimensional Flows.* AGARD CP-510.

Schlichting H, 1979. *Boundary-Layer Theory.* McGraw-Hill Publishing Company.
Schwab J R, 1992. *Navier-Stokes Solver.* Newsgroup 'sci/engr/mech', November.

Shadid J N, Eckert E R G, 1991. *The Mass Transfer Analogy to Heat Transfer in Fluids with Temperature-Dependent Properties.* ASME, Journal of Turbomachinery 113:27-.

Shkurikhin I B, 1969. *Investigation of Secondary Losses in Linear Turbine Cascades.* Izvestiya Vuzov - Seriya Mashinostroenie 6:83-87.

Sieverding C H, 1975. *Reduction of Secondary Losses in Turbines.* VKI course note 95.

Sieverding C H, 1985. *Recent Progress in the Understanding of Basic Aspects of Secondary Flows in Turbine Blade Passages.* ASME, Journal of Turbomachinery 107:248-257.

Sieverding C H, van den Bosche P, 1983. *The Use of Coloured Smoke to Visualize Secondary Flows in a Turbine-Blade Cascade.* Journal of Fluid Mechanics 134:85-89.

Sieverding C H, Wilputte Ph, 1981. *Influence of Mach Number and End-wall Cooling on Secondary Flows in a Straight Nozzle Cascade.* Journal of Engineering for Power, ASME 103:257-.

Smith L H Jr, Yeh H, 1963. *Sweep and Dihedral Effect in Axial-Flow Turbomachinery.* ASME Journal of Basic Engineering 85:401-416.

Spalding D B, 1972. *A Novel Finite Difference Formulation for Differential Expressions Involving Both First and Second Derivatives.* International Journal for Numerical Methods in Engineering 4:551-559.

Squire L C, 1962. *The Motion of a Thin Oil Sheet under the Boundary Layer on a Body.* AGARD-AG-70, 39-49.

SU1089-282/3, 1989. *Turbine Guide Apparatus with Partitions between Blades, Turbine Guide Apparatus Blade.* Leningrad Ship Building patents.

Tennekes H, Lumley J L, 1972. *A First Course in Turbulence.* MIT Press.

Tong S S, Gregory B A, 1990. *Turbine Preliminary Design using Artificial Intelligence and Numerical Optimization Techniques.* ASME 90-GT-148.

Topunov A M, Chernysh A A, 1982. *Improving the Effectiveness of Cooled Turbine Cascades.* Teploenergetika 29 (3):36-39.

Topunov A M, Nikolaev N E, 1975. *Increasing the Operating Economy of HP Steam Turbine Stages.* Izvestiya Vuzov Seriya Energetika 5:57-62.

Unsworth R G, Parker G L M, 1991. *A Two-Stage Air Turbine Test Facility for the Development of High Pressure/Intermediate Pressure Steam Turbine Blading.* IMechE paper C423/024.

Wang Zhongqi, Han Wanjin, Cai Daying, Xu Wenyuan, 1989. *Influence of Blade Leaning on the Flow Field behind Turbine Rectangular Cascades with Different Incidences and Aspect Ratios.* ISABE 89-7013.

Walsh J A, 1987. *Secondary Flow and Inlet Skew in Axial Flow Turbine Cascades.* PhD thesis, University of Durham.

Walsh J A, Gregory-Smith D G, 1987. *The Effect of Inlet Skew on the Secondary Flows and Losses in a Turbine Cascade.* Proceedings I Mech E Turbomachinery - Efficiency Predictions and Improvement, Paper C275/87, pp 15-28.

Walsh J A, Gregory-Smith D G, 1990. *Inlet Skew and the Growth of Secondary Losses and Vorticity in a Turbine Cascade*. Journal of Turbomachinery, ASME 113(4):633-642.

Wegel S, 1969. *Strömungsuntersuchungen an Beschleunigungsgittern im Windkanal und in der Axialturbine*. PhD thesis, University of Darmstadt.

Welua H, Daklberg D E, Heiser W H, 1969. *Investigation of a Highly Loaded Two-Stage Fan Drive*. AFAPL - TR-69-92.

Winter K G, Squire H B, 1951. *The Secondary Flow in a Cascade of Airfoils in a Non-Uniform Stream*. Journal of Aerodynamic Science 18:271-277.

Yamamoto A, Kondo Y, Murao R, 1990. *Cooling Air Injection into Secondary Flow and Loss Fields within a Linear Turbine Cascade*. ASME 90-GT-141.

Zienkiewicz O C, 1971. *The Finite Element Method in Engineering Science*. McGraw-Hill.